University of California

Los Angeles

High Frequency Faraday Rotation Observations of the Solar Corona

A dissertation submitted in partial satisfaction

of the requirements for the degree

Doctor of Philosophy in Earth and Space Sciences

by

Elizabeth Annah Jensen

2007

The dissertation of Elizabeth Annah Jensen is approved.

_____

Mark Moldwin

_____

Roger Ulrich

_____

Robert Strangeway

_____

Christopher T. Russell, Committee Chair

University of California, Los Angeles

2007

To...

Deborah Larkey Jensen, Science Fiction Enabler & Disciplinarian

Edward James Jensen, Miracle-Worker & Comedian

Patricia Elise Chapela, Vacation Overlord & Comedian

Jose Chapela, Computer Genius & Comedian

And most especially. . . Jeremy Scott and Carrie Joye Schoech

Beloved & Beguiling and Apple of my Eye & Mischief Minx

"The Italian Familiy"–Carrie Belle Traugh Larkey, 1917-2004

"Truly Peculiar"–Joyce Beaudry Holloway, 1928-2006

∞

The scientists, engineers, artists, and bureaucrats

Blasted our way to the space age

And blazoned trails of auroral lights

Brightening our steps into the infinite night

∞

"Drinking from the firehose." Both metaphorically and literally, I have.

TABLE OF CONTENTS

LIST OF TABLES

Vastano, Beryl-Lynn Strong-Caylor, and Dale Morgan

1975   Born, Albuquerque, New Mexico

1998   B. S., Geophysics

University Honors

Texas Agricultural and Mechanical University

College Station, Texas

1999   S. M. Geosystems

Massachusetts Institute of Technology

Cambridge, Massachusetts

1999-2006   Graduate Student Researcher

University of California, Los Angeles

2001-2004   National Aeronautic and Space Administration Graduate Student Research Program Fellow

2002   M. S. Space Science

University of California, Los Angeles

2004   Teaching Excellence Award

Department of Earth and Space Science

University of California, Los Angeles

Publications and Presentations

Jensen E.A. (1997). Satellite Observations of Oceanic Shelf-Slope Exchange. University Graduate Research Fellows Thesis, 1997. Texas A&M University. College Station, Texas.

Vilas F., Jensen E.A., and McFadden L.A. (1997). Extracting Spectral Information about 253 Mathilde Using the NEAR Photometry. Icarus, 129 (2):440-449.

Vilas F., Jensen E. A., Domingue D. L., McFadden L. A., and Coombs C. R. (1998). An Unusual Photometric Signature Detected on Lunar Complex Crater Rims at the South Pole. In Lunar and Planetary Science XXIX, Lunar and Planetary Institute, Houston, Texas (CD-ROM).

Jensen E.A. (1999). A Comparison of Short-Circuited Streaming Potentials in Westerly Granite From Changes in the Rock's Volume, Shape, Saturation, and Fracture Under Unconfined Uniaxial Compression. Geosystems Masters Thesis, 1999. Massachusetts Institute of Technology. Cambridge, Massachusetts.

Jensen E.A. (2001). Thermal Constraints to Callisto's Internal Structure. In Lunar and Planetary Science 32nd, Lunar and Planetary Institute, Houston, Texas (CD-ROM). 2001.

Asmar S.W., Resch G.M., Armstrong J.W., and Jensen E.A. (2001). Decadal Study for Radio Science Investigations Using the Deep Space Network. In 33rd Meeting of the AAS Division for Planetary Sciences, New Orleans, Louisiana.

Jensen E.A., Bird M.K., Paetzold M., Asmar S.W., Anderson J.D., Iess L., and Russell C.T. (2002). Initial Results from the Cassini Solar Conjunction Faraday Rotation Experiment. In 2002 Fall Meeting of the American Geophysical Union Section SH00, San Francisco, California.

Jensen E.A., Russell C.T., and Mulligan T. (2003). A Simple Method for Determining the Time of Closest Approach to the Center of a Magnetic Fluxrope. In 2003 Fall Meeting of the American Geophysical Union Section SH02, San Francisco, California.

Jensen E.A., Russell C.T., and Mulligan T. (2003). Using Vector Analysis to Reveal Interplanetary Coronal Mass Ejection Orientation. In Solar, Heliospheric and Interplanetary Environment Meeting, Mailea, Maui, Hawaii.

Coles D., Vichabian Y., Fleming F., DesAutels C., Briggs V., Vermeesch P., Arrell J.R., Lisiecki L., Kessler T., Hooper H., Jensen E., Sogade J., and Morgan F.D. (2004). Spatial decision analysis of geothermal resource sites in the Qualibou Caldera, Saint Lucia, Lesser Antilles, Geothermics, 33 (3):277-308.

Jensen E.A., Bird M.K., Paetzold M., Asmar S.W., Anderson J.D., Iess L., and Russell C.T. (2004). The Cassini Solar Conjunction Faraday Rotation Experiment. In 2004 Committee on Space Research (COSPAR) 35th Scientific Assembly Scientific Commission D, Paris, France.

Jensen E.A., Bird M.K., Asmar S.W., Iess L., and Russell C.T. (2004). The Cassini Faraday Rotation Experiment. In Solar Heliospheric and Interplanetary Environment Workshop, Big Sky, Montana.

Jensen E.A., Bird M.K., Paetzold M., Asmar S.W., Anderson J.D., Iess L., and Russell C.T. (2005). The Cassini Solar Conjunction Faraday Rotation Experiment. Advances in Space Research, 36:1587-1594.

Jensen E.A. and Russell C.T. (2005). Modelling CME effects on Faraday Rotation. In Solar Heliospheric and Interplanetary Environment Workshop, Kona, Hawaii.

Jensen E.A., Iess L., Asmar S.W. and Russell C.T. (2005). Cassini Measurement of the Coronal Electron Density. In Solar Heliospheric and Interplanetary Environment Workshop, Kona, Hawaii.

Jensen E.A., Bird M.K., Asmar S.W., Iess L., and Russell C.T. (2005). The Cassini Faraday Rotation Experiment 2002 Results. In Solar Heliospheric and Interplanetary Environment Workshop, Kona, Hawaii.

Jensen, E.A., Bird M.K., Paetzold M., Asmar S.W., Anderson J.D., Iess L., and Russell C.T. (2005). Solar Polar Electron Density Lower Than Equator in 2002, presented at the Spring Meeting of the American Geophysical Union Section SH32A-01, New Orleans, Louisiana.

Jensen, E.A., Bird M.K., Paetzold M., Asmar S.W., Anderson J.D., Iess L., and Russell C.T. (2005). Faraday rotation measurements over 3 Cassini Conjunctions, presented at the Fall Meeting of the American Geophysical Union Section SH31A-02, San Francisco, California.

Jensen, E.A. (2006). The "Invisible" Solar Corona, presented at the Space Science Seminar, Department of Earth and Space Science, University of California, Los

Angeles.

High Frequency Faraday Rotation Observations of the Solar Corona

by

Elizabeth Annah Jensen

Doctor of Philosophy in Earth and Space Sciences

University of California, Los Angeles, 2007

Professor Christopher T. Russell, Chair

The million degree solar corona generates the solar wind that in turn controls the Earth's "space weather". The solar coronal magnetic field within 0.25AU (60 solar radii) plays a critical role in the acceleration but is largely "invisible", and can presently only be measured by the Faraday rotation of high frequency electromagnetic radiation. Faraday rotation is the observed rotation in the plane of polarization of an EM wave as it traverses a magnetized medium. The amount of observed Faraday rotation is the integration along the propagation direction of the product of the component of the magnetic field parallel to the propagation vector and the electron density.

Faraday rotation is clearly useful for measuring the solar coronal magnetic field. As a remote observation, Faraday rotation measurements require careful consideration of the medium in the analysis. This thesis details the theory of Faraday rotation, previous experiments observing Faraday rotation using the carrier signal from a spacecraft in superior conjunction, the equipment used for the Cassini Faraday rotation observations, the signal analysis and steps taken to acquire a Faraday rotation observation from radio frequency data, the model used to fit the observations, all

ancillary data required for these steps, and all the code created for this purpose. The data and code are provided in the attached DVD media.

All previous Faraday rotation experiments observed coronal mass ejections (CMEs) producing either 'W' or sigmoid features. These observations are reproduced herein using a Taylor-state flux-rope model crossing the line of sight at different sizes, twist, and orientations, showing that Faraday rotation can be used to measure the magnetic field of CMEs.

Using a forward model to fit Faraday rotation and columnar electron density observations, a first order investigation into force balance in the solar corona was conducted. From these fits, the gradients in the magnetic and thermal pressure and the gravitational force per volume were calculated. For the solar wind to escape the gravitational force of the Sun, the magnetic and thermal pressure gradients must dominate. We show from the fits on 2002 June 20 that small adjustments to the PFSS model can provide the necessary magnetic field strengths to supply the needed pressure for solar wind flow; however, the fits from June 21st cannot. The closest approach of the June 21st measurements were all below the source surface of 2.5 solar radii indicating a problem in the use of the PFSS model to determine the structure of the coronal magnetic field below the source surface.

Large amplitude 4 minute period Alfven waves have been observed in Helios and Cassini Faraday rotation observations. Using a simple open-ended box model through which magnetohydrodynamic waves can propagate, it is demonstrated that the combination of Faraday rotation and columnar electron density observations can distinguish Alfven waves due to their lack of fluid perturbation. It is also shown that the 2nd harmonic in the Faraday rotation observations is the result of the electron density fluctuation in the magnetosonic (fast and slow) modes. This demonstrates that

previous Helios observations producing the 2nd harmonic were MHD magnetosonic waves. Cassini's observation of an Alfven wave is modeled to determine the amplitude of the magnetic perturbation. If we assume that these waves are continuously generated in all directions then the wave energy flux is $1.6 \times 10^{19} W$; for comparison, the kinetic energy flux of the solar wind at 1AU is $1.7 \times 10^{20} W$.

With better technology and the maturity of 3D tomography, the solar radioscience community is experiencing a resurgence of interest in the phenomenon of Faraday rotation. This thesis demonstrates that Faraday rotation can be used to determine the magnetic structure of CMEs, the solar wind, and MHD waves propagating from the solar corona. These observations enable us to predict the geoeffectiveness of a CME, study force balance in the solar wind, and measure magnetic energy flux in important regions such as the solar wind acceleration region.

CHAPTER 1

Introduction

The expression "the vacuum of space" ill defines the heliosphere. The plasma of
the solar corona streams away from the Sun, accelerating to become the supersonic
solar wind, and carrying with it the interplanetary magnetic field. At the orbit of
the Earth, the solar wind encounters the obstacle of the Earth's magnetosphere,
where it decelerates with the aid of a standing bow shock, behind which the plasma
and interplanetary magnetic field interacts with the geomagnetic field at the mag-
netopause. Reconnection of the interplanetary magnetic field with the geomagnetic
field couples the momentum flux of the solar wind to the magnetosphere. As a
result, the Earth's geomagnetic environment is very sensitive to changes in the so-
lar wind's properties. Strong magnetospheric convection occurs when an intense
southward interplanetary magnetic field (in geocentric solar magnetospheric coor-
dinates) is present leading to a magnetic storm. The strongest geomagnetic storms
associated with the strongest southward fields are often caused when coronal mass
ejections reach the Earth. Coronal mass ejections are the generally rapid releases of
large scale magnetic structures containing a central magnetic flux rope.

The solar cycle variability of geomagnetic activity is caused by the changes in the
occurrence rate and strength of coronal mass ejections, the changes of the inter-
planetary magnetic field and solar wind flow, and other solar phenomena such as,

solar energetic particle events, that evolve in the course of the Sun's 11 and 22 year cycles. As shown in Figure 1.1, the frequency of coronal mass ejections increases at solar maximum by a factor of four over solar minimum (Webb & Howard, 1994). As a result, the geomagnetic environment was perturbed more in 1981 near solar maximum than in 1985 near solar minimum. Coronal mass ejections can affect the Earth's magnetic field both through an increase in the dynamic pressure on the magnetosphere and a strong and changing north-south magnetic orientation as the flux rope passes. When the mass density in or velocity of the CME is greater than the ambient solar wind, the magnetosphere is compressed from the enhanced dynamic pressure of the fast solar wind (Kivelson & Russell, 1997). The magnetic structure of the coronal mass ejection nearly always produces a changing north-south component of the magnetic field (Mulligan *et al.*, 1998). A strong southward magnetic field in a coronal mass ejection that persists for several hours will generate a magnetic storm in the Earth's magnetosphere (Walker, 2000).

Predicting the effect of a coronal mass ejection as it is approaching the Earth presents two problems. The magnetic field cannot be measured until it passes a spacecraft in the vicinity of the Earth, and when the CME does cross the spacecraft the measurements consist of a single line through the coronal mass ejection limiting the interpretation of its overall structure (Mulligan, 2002). Thus it is of great interest to be able to measure remotely the magnetic field in the solar corona, long before a disturbance produced there, reaches the Earth.

1.1   The Heliosphere

At times during the solar cycle when the magnetic structure is only slowly evolving, coronal holes and streamers can last many months; as a result, the Earth can observe
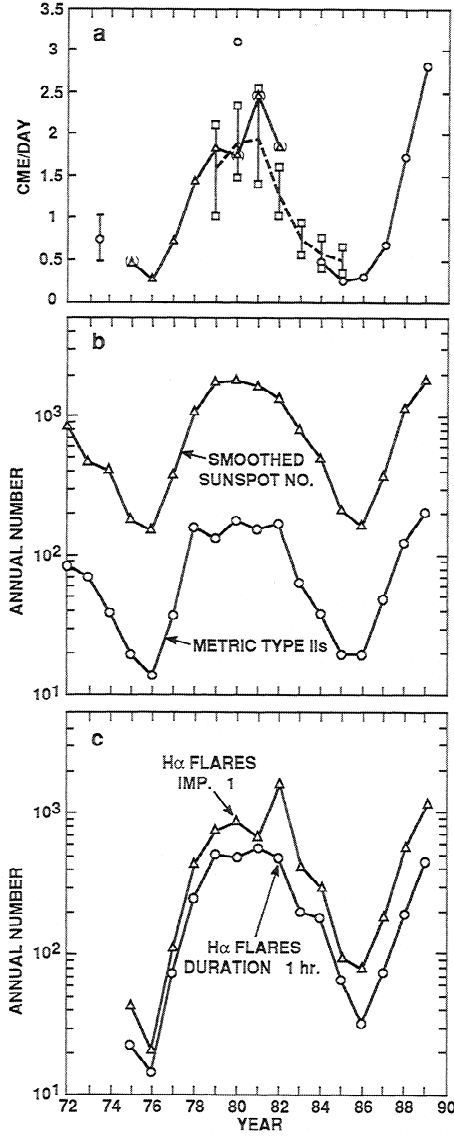
Figure 1.1: *a) The rate of occurrence of CMEs from the Skylab and SMM (circles) coronagraphs, P28-1 satellites (squares) coronagraph, and the Helios 1 and 2 (triangles) photometers; b) the annual numbers of smoothed sunspot numbers (triangles) and metric type II bursts; and c) Hα "grouped" flares of Importance $\geqslant 1$ (triangles) and duration $\geqslant 1$ hour (circles). The occurrence of coronal mass ejections is greatest at solar maximum when the number of sunspots is highest (Webb & Howard, 1994).*

3

the same structure approximately 27 days later when the same structure again rotates past the Earth. Note that one solar rotation relative to the stars occurs in close to 25 Earth days; however, due to the motion of the Earth around the Sun to an observer on the Earth, will see the Sun rotating over approximately 27 days. Additionally, the rotation rate of the Sun varies with solar latitude; the poles rotate slower than the equator. This variation in rotation with latitude is weaker in the corona than in the photosphere and corresponds to a 28 day period at the poles (as observed by the Earth) (Fisher & Sime, 1984).

Between 3 and 10 solar radii, the solar wind accelerates to supersonic and then superAlfvenic speeds as it flows away from the Sun. Below the critical radius around 3-5 solar radii, the solar wind is subsonic, the acceleration of the solar wind is outward, and the flow speed is small, and above the critical radius the solar wind is supersonic, the acceleration remains outward, and the dynamic pressure of the solar wind is greater than the thermal (Parker, 1958).

The solar wind originates from coronal holes, coronal streamers, coronal mass ejections (5%), and coronal areas that are neither streamers nor holes (Bird & Edenhofer, 1990). A schematic picture of the sources of the solar wind is shown in Figure 1.2. The characteristics of the solar wind are dependent on the magnetic topology of the corona; to estimate the magnetic field in the corona, photospheric magnetic field measurements are extrapolated into the corona using MHD or Potential Field Source Surface models (Luhmann *et al.*, 2002). Magnetic field lines with both footpoints on the solar surface are "closed" and therefore do not contribute to the solar wind; these are visible in coronagraphs as high-brightness "loops". The fast solar wind originates from coronal holes; however there are two sources of slow solar wind. The slow solar plasma originates from the boundaries between streamers and coronal holes and the plasma sheet above the cusps of streamers (Antonucci *et al.*,
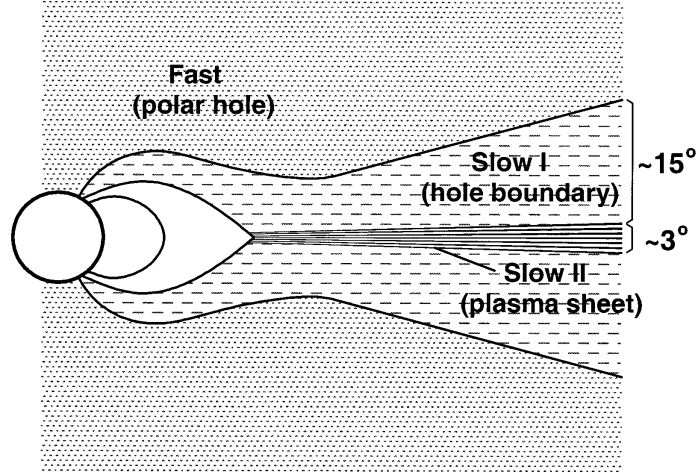
Figure 1.2: *Schematic illustration of the sources of the slow solar wind from a) the boundaries between streamers and coronal holes and b) the plasma above the cusps of streamers. The fast solar wind originates from coronal holes. (Wang* et al.*, 2000)*

2005).

1.2   The Solar Corona

When the moon is directly between the Sun and the Earth, it can block all the light from the photosphere over a small region on the surface of the Earth. Here observers can clearly see the solar corona for a brief period of time. The solar corona was probably seen by ancient cultures but the corona's physical linkage to the Sun was not correctly understood until recently. Only during the 19th century, was the solar corona shown to be part of the Sun, rather than terrestrial in origin, with photographs taken of the 1860 eclipse by De la Rue and Secchi. The helium-yellow and iron-green lines indicating the chemical composition of the corona was discovered by Janssen, Lockyer, Harkness, and Young. The coronal variability between the "quiet" and "active" Sun at sunspot minimum and maximum was observed

from the differences between the 1871 and 1878 eclipses. In 1930, Lyot invented the coronagraph allowing continuous observations of the corona. In 1939, Grotrian and Edlén proved that the iron "forbidden" lines were due to a million degree plasma. Beginning in the 1940s, time lapse movies of the corona by the High Altitude Observatory, Sacramento Peak Observatory, and McMath-Hulbert Observatory allowed the observation of large scale motions of dense coronal plasma (Golub & Pasachoff, 1997).

The Sun is a main sequence star of average radius 696,000 km, mass 1.989×10^{30} kilograms, and an escape velocity from the surface of 618 km/sec. It has an average surface temperature of 5800 Kelvin and radiates 3.83×10^{26} Watts. The plasma at the surface of the Sun has an electron density of $2 \times 10^{23} m^{-3}$ and magnetic field magnitude of 500 G; therefore the plasma is highly collisional with a high beta. Through the chromospheric thickness of approximately 700 km, the plasma temperature increases by an order of magnitude, electron density decreases by 8 orders of magnitude, and the magnetic field decreases by two orders of magnitude. The chromosphere is a region of low plasma beta; the plasma energy density becomes magnetically dominated in the chromosphere in contrast to the thermally dominated energy density in the photosphere as shown in Figure 1.3 (Aschwanden, 2004).

The corona begins above the transition region; it is where the temperature profile of the solar atmosphere begins to change slowly. This region varies with activity and thus position on the Sun, it is on average located around 2700 km above the photosphere. The region between 2700 km and 1.5 million km above the photosphere or approximately 2 solar radii where the solar wind begins is referred to as the inner corona; above this region is the outer corona. From the bottom to the top of the inner corona, the average temperature increases by 2 orders of magnitude while the electron density steadily decreases (but not by the same order) causing a steady
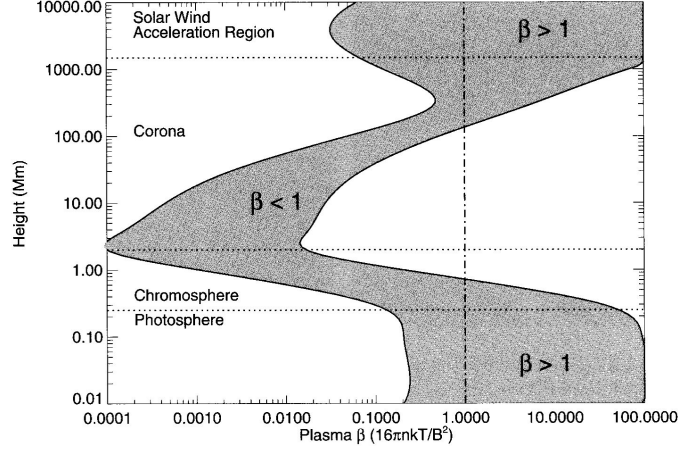
Figure 1.3: *Plasma beta as a function of height in the solar atmosphere. Plasma beta is a ratio of thermal pressure to magnetic pressure. Beta equals one is indicated by a dashed-dot line. The heating problem of the corona is how to achieve the great increase in thermal pressure observed between 1 and 1000 Mm. Dotted lines delineate the regions of the solar atmosphere (Aschwanden, 2004).*

increase in thermal pressure. There is no observed increase in magnetic pressure through this region; therefore, the plasma beta increases.

Current theories of the solar corona use the dissipation in current systems (DC heating) and the dissipation of waves (AC heating) to heat the corona (Aschwanden, 2004). The definition of DC heating mechanisms are those that could heat the corona through footpoint motions of the magnetic field. AC heating wave modes include acoustic, Alfven, fast and slow magnetosonic, torsional, kink and sausage. "It is widely accepted that mechanical motions in and below the photosphere are the ultimate source of [coronal heating] energy" (Klimchuk, 2006). One coronal heating theory depends on the nonlocal heat transport that would occur due to a suprathermal tail in the electron particle distribution (Scudder, 1992). A coherent coronal heating theory that includes the energy source, heating mechanism, plasma response, and expected observables does not exist. Faraday rotation measurements allow observation of waves over a limited frequency range ($\leqslant$200 mHz demonstrated

7

by Helios) and could help in assessing the contributions of waves to coronal heating.

The change in the plasma characteristics from the chromosphere and through the inner corona is poorly understood. The Cassini Faraday rotation experiment has obtained measurements of the coronal magnetic field between 1.16 and 2 solar radii within this region of changing plasma characteristics. Beyond 2.5 solar radii, the magnetic field lines of the Sun are generally assumed to be open on average; however, this distance at which they become open is variable. In fact the flux ropes in interplanetary coronal mass ejections often appear to be closed, even at 1AU (Bird & Edenhofer, 1990).

1.3 The Coronal Magnetic Field

The structure of the coronal magnetic field makes itself apparent in white light coronagraphs taken in clear air at high altitude. The electron density on closed field lines is higher than on open field lines; the higher densities scatter more sunlight through Thompson scattering. On open field lines, electrons escape the Sun leading to lower densities and lower scattering. An exception to this observation are streamers where the electrons are very dense even though the field lines appear to be open; the outflow speed of the plasma in streamers is slower and more plasma collects on the magnetic field lines.

The dynamics of the solar magnetic field is dominated by energy release and mass loss processes. The magnetic field lines of the ambient solar wind are generally considered to be open if they extend past 2.5 solar radii. Field lines are opened by the accelerated solar wind that drags the coronal magnetic field lines as the solar wind escapes the solar gravity as shown in Figure 1.4. At the polar regions near

8

Table 1.1: *Advanced Technology Solar Telescope near-infrared spectral lines used for solar magnetic field measurements.*

Spectral Line	Wavelength (nm)	Solar Region
FeI	1654.8	photosphere
TiI	2200	sunspot umbra
HeI	1038.0	chromosphere
FeXIII	1074.7	corona below 1.2 solar radii

solar minimum the magnetic field is open in large coronal holes. At solar maximum, the polar coronal holes occupy a smaller area and have a weaker magnetic field strength; additionally, coronal holes occur at lower latitudes (Belenko, 2001).

In active regions where the plasma radiates, the coronal magnetic field can be measured through the combined use of Zeeman splitting (magnetic field component along the line of sight) and the Hanle effect (magnetic field component in the plane of the sky) (Keil & Avakyan, 2003); Table 1.1 lists infrared spectral lines used by the Advanced Technology Solar Telescope to measure the solar magnetic field. Outside of active regions, the coronal magnetic field is largely "invisible" and only affects electron density structure and passing electromagnetic radiation. Because measurements of the structure of the coronal magnetic field can only be made in situ by spacecraft or inferred where the electron density is large enough, models must be constructed for the magnetic field between the photosphere and where the magnetic field can be directly measured.

Three empirical models have been derived for the magnitude of the radial magnetic field from Type 3 burst data (Dulk & McLean, 1978), two Helios inverted Faraday rotation data sets (Volland *et al.*, 1977), and all the Helios inverted Faraday rotation and in situ data ($\geqslant$62Rs) ((Patzold *et al.*, 1987)). Although these models only consider one component of the magnetic field; this is sufficient outside of 2 solar radii and will be compared to inverted data in this region. Figure 1.6 compares the
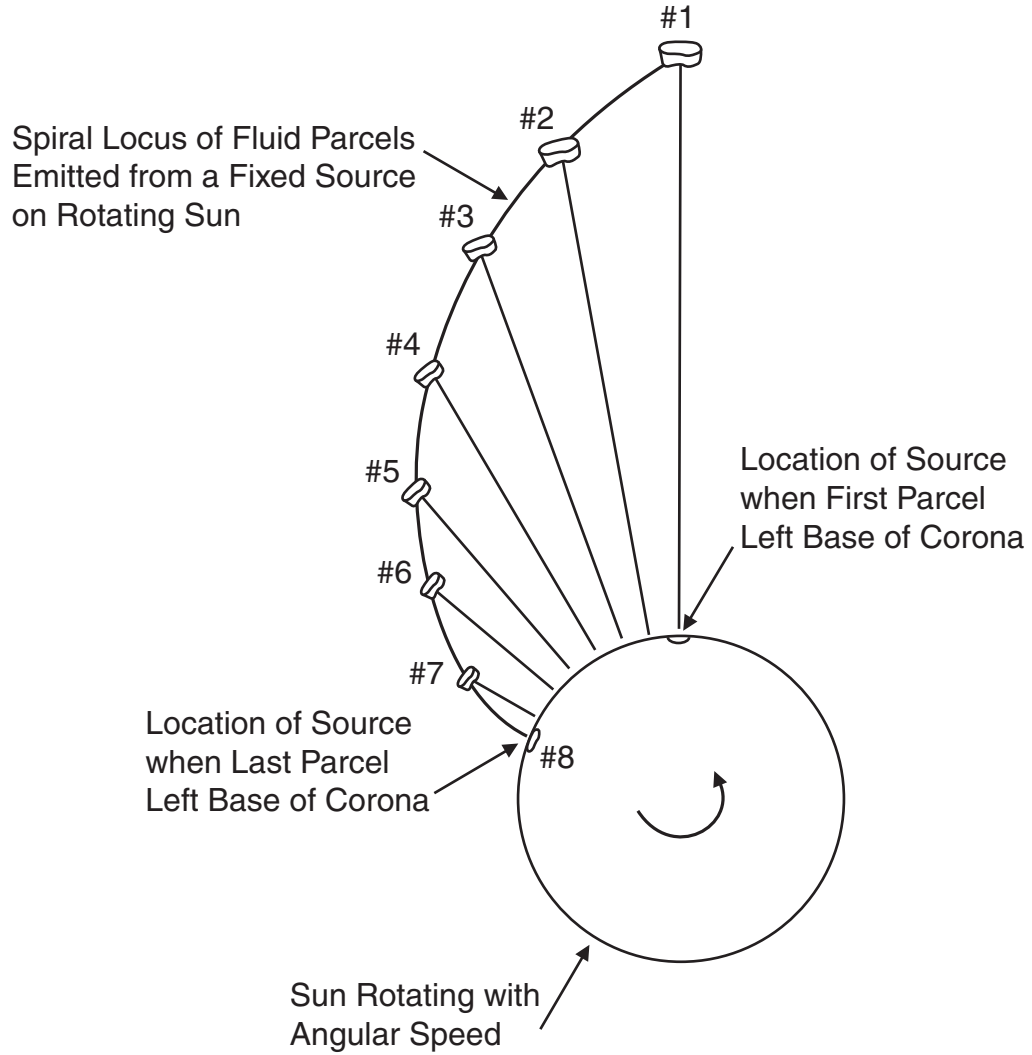
Figure 1.4: *Schematic showing the positions of parcels of solar wind plasma originating from the same source region on the Sun over eight time steps as the Sun rotates counterclockwise through an angle of about 60 degrees (Russell, 2000). As a parcel of coronal plasma streams away in the solar wind, it remains magnetically connected to the region from which it originated in the solar corona. This draws the interplanetary magnetic field out along an Archimedian spiral.*

Solar Minimum
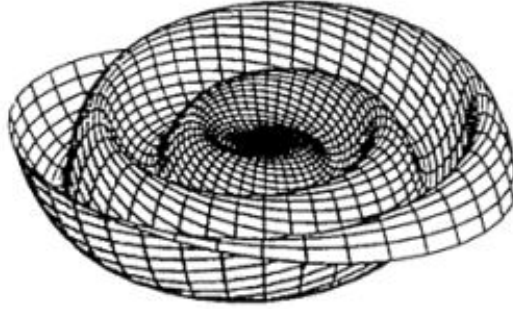
Figure 1.5: *The current sheet between the inward and outward directed interplanetary magnetic fields. The solar dipole is tilted with respect to the solar rotational axis causing a periodic variation in the location of the current sheet as the Sun rotates. As the Sun rotates the Earth moves back and forth across this current sheet (Kallenrode, 2001).*

behavior of these models.

The National Science Foundation's Center for Integrated Space Weather Modeling (CISM) is combining solar, coronal, heliospheric, near Earth, magnetospheric, ionospheric and atmospheric models together to predict the conditions in the solar wind at the Earth (Center for Integrated Space Weather Modeling, 2002). The baseline solar wind model at CISM against which other solar wind models will be compared is the Wang-Sheeley-Arge model (WSA) which uses the Potential Field Source Surface model for the coronal magnetic field (Owens *et al.*, 2005). The PFSS model assumes that the corona is current-free between the boundaries of the photosphere and the 2.5 solar radii source surface; as a result the magnetic field vector field can be represented by a potential field. It is described in greater detail in Section 1.3.1 below. The WSA model is capable of predicting the solar wind speed at the Earth with an error of $\pm 15\%$ and the correct polarity of the interplanetary magnetic field

75% of the time (Arge & Pizzo, 2000).

1.3.1   Steady State Magnetic Field Model

There are a limited number of models that are used to model the structure of the coronal magnetic field. The two types of coronal models used are the Potential Field Source Surface (PFSS) and Magnetohydrodynamic (MHD) models. The PFSS model assumes that the corona is current-free between the boundaries of the photosphere and the 2.5 solar radii source surface. The source surface is usually set at 2.5 solar radii because electron density observations indicate that stable closed magnetic field lines do not extend past this boundary; the magnetic field beyond this boundary is assumed to be purely radial. In contrast, the MHD-only model assumes that the plasma can be treated as a "fluid" described by its moments density, velocity, and temperature. A full MHD study of the solar corona requires more information than a single Faraday rotation observation over a spacecraft occultation can provide and will be the topic of future research when more lines of sight are acquired simultaneously. Chapter 4 of this thesis will use the PFSS model and test whether a simple adjustment to the model is sufficient to produce the observed Faraday rotation.

The PFSS model's current-free assumption allows the magnetic field to be expressed by a scalar potential.

Recalling the relation between current and twisted magnetic field

$$\nabla X \vec{B} = \mu_o \vec{J}$$

if $\vec{J} = 0$ then
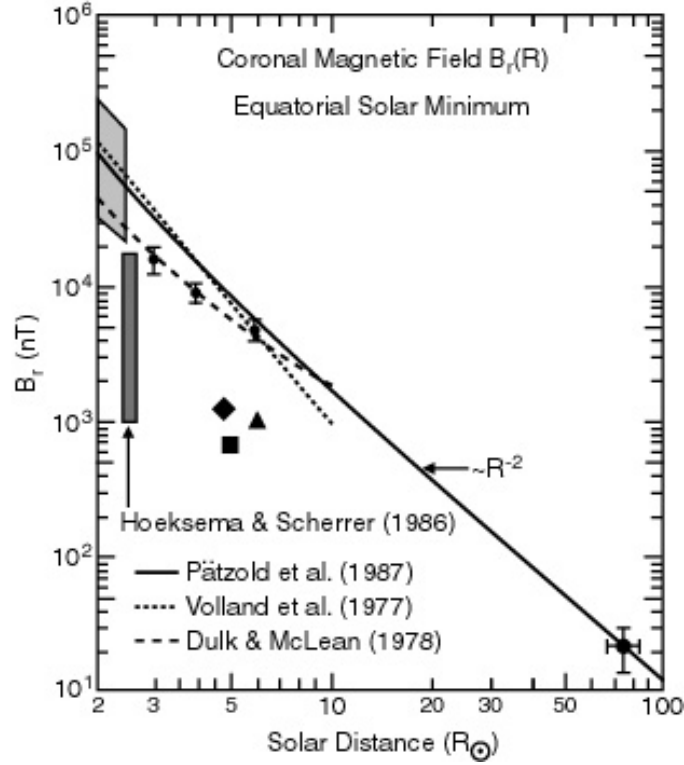
Figure 1.6: *The range of radial magnetic field strengths obtained through varying methods. Magnetic field observations are interpreted from radio bursts transmitted along field lines using an electron density model (dotted region), gyrosynchrotron radiation (filled circles and dashed line), Potential Field Source Surface model extrapolation (hatched region), Faraday rotation (solid square, triangle, diamond, thick solid line, and dotted line), and direct measurement with the Helios magnetometer (solid star, bottom right corner) (Bird & Edenhofer, 1990). The magnetic field in quiet regions of the solar corona can only be measured by Faraday rotation.*

$$\vec{B} = -\nabla\psi$$

Because the magnetic field must conserve flux $\nabla \cdot \vec{B} = 0$, then Laplace's equation is

$$\nabla^2\psi = 0$$

therefore, the magnetic field can be described by Laplace's equation. The solution to which is Legendre polynomials. In order to solve for the coefficients to the Legendre polynomials, boundary conditions must be applied. The inner boundary condition specifies that the magnetic field on the surface of the Sun is given by the Zeeman splitting measurements. The outer boundary condition is loosely defined; the most common definition is a purely radial magnetic field at the "source surface". The source surface is commonly set at 2.5 solar radii; however, it can be 3.25 Rs or as far as 30 Rs (Jackson *et al.*, 2003). The source surface was set at 2.5 Rs in the model discussed in Chapter 4.

The Faraday rotation forward model uses the Community Coordinated Modeling Center (CCMC) PFSS code for calculating magnetic field vectors from their dataset (Luhmann, 2002); this code uses the Wilcox Solar Observatory (WSO) coefficients for its calculations. The WSO uses the FeI line for its Zeeman splitting measurements which occurs in the photosphere. Zeeman splitting measurements are also made in the NaI line (ie at Mount Wilson Observatory (MWO)). The MWO data has higher resolution and is measured from above the photosphere where the current free assumption is a little more valid (Tran *et al.*, 2005); however, the line is generated over a larger range of height than the Lyman-alpha line so that the inner boundary condition is not as well defined. Additional differences are present geometrically with respect to synoptic versus snapshot maps which will be discussed in the coordinate systems section. For additional comparisons between observatories,

see Svalgaard (Svalgaard, 2005).

The WSO Legendre polynomials are a special variety, normalizing the polynomial values so that the varying degrees (monopole, dipole, quadrupole, etc) can be compared directly (Chapman & Bartels, 1940). The WSO data, used in the forward model, consist of the coefficients of the polynomials from the 2.5 Rs source surface boundary condition. Outside of the source surface, the radial magnetic field is calculated from the source surface (ss) as $B_{ss}\left(\frac{R_{ss}}{r}\right)^2$ thus conserving magnetic flux through the surface of a sphere of radius r. The points of closest approach for all of the Cassini Faraday rotation observations from 2002 (June 18-22) and 2003 (June 30-July 1) were within 10 solar radii; using the equation below, the Archimedian spiral curvature to the magnetic field ϕ was small. We note that we have adjusted the field strength of the CCMC output by a factor of two to adjust it to agree with published values of the field.

The high frequencies used in the Cassini Faraday rotation experiment were sensitive to electron densities in the experiment's range of 10 solar radii (in 2002). The Archimedian spiral curvature to the magnetic field ϕ in this region is small.

$$\phi = \frac{\omega_{sun}}{v_{sw}}(r - R_{sun})$$

where v_{sw} was assumed to be on average 250km/s, gives a spiral angle of approximately 4 degrees. Therefore, the curvature in the interplanetary magnetic field is negligible for modeling these Faraday rotation observations.

The WSO spherical harmonics solutions are continuously calculated from Zeeman splitting observations in the FeI line giving the component of the magnetic field

along the line of sight. For each calculation, a full solar rotation is centered on a time period ranging the 360 degrees longitude; when the next day of observations are made, they replace the longitude's observations from the previous rotation, the center is shifted by a day, and the spherical harmonics are recalculated. For the forward model, the spherical harmonics calculations that were chosen were centered near the time period of closest approach and had the lowest monopole value. As discussed in subsection 1.3.1, the WSO harmonics have a special normalization allowing comparison of the magnetic field in different regions; Table 1.2 shows that the dipole contribution is significantly larger than the monopole.

Note that the spherical harmonics provide by the WSO are usually "phase" shifted by the longitude of the Sun along the Earth-Sun line at the "End Time" of the data used in the harmonics calculations (Hoeksema, 2006). For example, the Carrington longitude along the Earth-Sun line on the day the "End Time" measurement for the spherical harmonics centered on the day of conjunction in 2002 was 160 degrees. Therefore, any magnetic field vector calculated from the spherical harmonics is similarly shifted by 160 degrees in longitude. This effect was accounted for in the model described in Chapter 4.

The WSO harmonics are calculated from a synoptic map using measurements over a full solar rotation centered on the time of conjunction. Note that this timescale is longer than the timescale on which minor solar phenomena occur. However as a result of changes occurring on smaller timescales, the dipole can shift slightly over the period of a rotation which leaves a monopole term in the coefficients. At solar maximum when the dipole is weakest, this monopole term can become sizable. In addition to this, the monopole term can arise when different measurement quality was taken between the poles (ie clouds present when one pole was visible). For this study, we simply dropped the monopole term from our calculations because the

Table 1.2: *Time period of PFSS model calculations and corresponding monopole and dipole coefficients. Note that the model also used the quadrupole coefficients in calculating the magnetic field vectors.*

	2002 WSO Harmonics	2003 WSO Harmonics
start of time period	2002 June 07 23h 01m 47s	2003 June 17 23h 51m 56s
center of time period	2002 June 21 14h 19m 58s	2003 July 01 15h 10m 07s
end of time period	2002 July 04 20h 32m 39s	2003 July 14 21h 22m 48s
monopole (l=0,m=0)	6.53	-0.55
dipole (l=1,m=0) (g10)	-62.32	-100.85
dipole (l=1,m=1) (g11)	-23.55	-67.13
dipole (l=1,m=1) (h11)	-27.68	-51.36

term was significantly smaller than the dipole term as shown in Table 1.2. In 2003, when the line of sight was closer to the Sun, the monopole term is still negligible because it is significantly smaller than the quadrupole terms.

Zeeman Effect

In 1896, Zeeman discovered that spectral emission lines split up into polarized components with the presence of a strong magnetic field at the emission source. While the normal Zeeman effect could be explained by classical physics; the anomalous Zeeman effect could not be explained until the discovery of electron spin in 1925 (Gamow, 1966). The magnetic quantum states of an atom which were formerly degenerate may become separated when subjected to an external magnetic field. The changes produced in the energy levels can be regarded as resulting from the magnetic moment of the electron to have a different orientation with respect to the rotation vector of the electron's orbit (Dicke & Wittke, 1960). The number of split energy levels depends on the state of the electron. For instance, an electron in the 2P angular quantum state in a magnetic field will assume one of 3 possible magnetic quantum states depending on the relative spin and angular momentum moments as
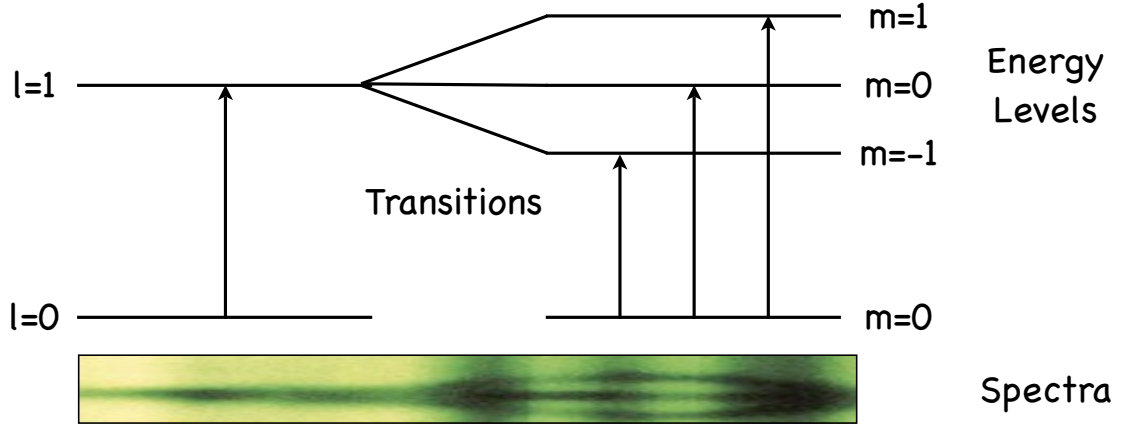
Figure 1.7: *Schematic showing the energy level split that occurs in the presence of a magnetic field. Given a particular angular quantum state, an electron changing energy levels from the ground state to the next energy level will absorb an amount of energy depending on its precession with respect to the nucleus and the atom's precession with respect to the background magnetic field (Dept. Physics & Astronomy, University of Tennesee, 2006; Lang, 2003). A sample absorption spectrum is shown as the field of view changes from a region of weak to strong magnetic field from left to right.*

shown in Figure 1.7.

The center line in the split spectra is the π component while the two "wings" or σ components are the resultant normal energy level superposed with a $\pm\Delta$ energy. The Wilcox Solar Observatory uses a Babcock magnetograph to measure the σ components of the FeI absorption line (Beckers, 1968; Scherrer *et al.*, 1977). This allows the measurement of the magnitude and direction of the component of the magnetic field along the line of sight. The σ components are circularly polarized with opposite polarizations; therefore, they constitute the portion of the wave in the Stokes V parameter (Unno, 1956). The Stokes I parameter is a measure of the power of the signal, while the Stokes V parameter is the signal power in a particular circular polarization. In general, Stokes parameters are used to express the sum of different polarizations in a signal. The magnetic field strength can be determined
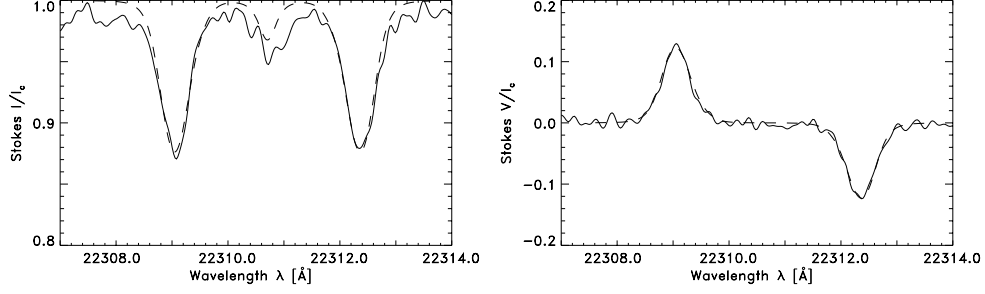
Figure 1.8: *The Stokes I and V measurements of the split Ti 2.2µ m absorption line in a large sunspot umbra. The observations (solid line) have been fit (dashed line) with a radiative model (Rueedi et al., 1998). The Stokes V parameter shows that the left circularly polarized component V>0 is at a shorter wavelength than the right circularly polarized component V<0 indicating that the magnetic field is oriented anti-parallel to the line of sight.*

from the relative strength of the Stokes V and I parameters.

$$\frac{V_\sigma - V_\pi}{I_\pi} = kB_p$$

where I is the intensity of the wave (Stokes I parameter), k is a constant, and B_p is the parallel component of the magnetic field to the line of sight. Figure 1.8 shows the Stokes I and V parameters in the Titanium 2.2μm line. The magnetic field measured by the magnetograph in the figure is oriented anti-parallel to the line of sight ($\lambda_{lcp} > \lambda_{rcp}$) (Ramaprakash, 1998).

1.4   Coronal Electron Density

The electrons and ions in the heliosphere have different behaviors. The solar ions provide the mass and momentum of the supersonic, superAlfvenic solar wind. Bi di-

rectional electrons on the interplanetary magnetic field of the solar wind are subsonic and ensure the charge neutrality of the solar wind. Solar corona electron density measured by Faraday rotation, Thompson scattering, Doppler shifting, group velocity travel times, and scintillation are assumed to apply to the ion fluid through charge neutrality.

Coronal electron density models are much more developed than the magnetic field models because of their greater ease of measurement (radio techniques and Thompson scattering) and the fact that electron density is a scalar quantity. White light coronagraphs use Thompson scattering polarization brightness in order to determine the electron density. Inside 2 solar radii, the K or Kontinuum corona brightness is dominated by Thompson scattering of light by electrons. Outside of this boundary, the F or Fraunhofer corona brightness is dominated by dust grains and must be removed from the electron density calculations. Figure 1.9 illustrates how the coronal brightness varies with distance from the Sun at the poles and the equator.

The other methods for measuring electron density include Type 2 and 3 radio bursts, scintillation measurements from natural sources and spacecraft, and in situ data ($\geqslant$62Rs). Radio scintillation studies observe the change in flux from a radio source (either natural or spacecraft) that results from the scattering effects of the coronal electron density; the amount of scattering varies with the electron density, the relative velocity of the scattering medium, and the frequency of the scattered signal (Erickson, 1964).
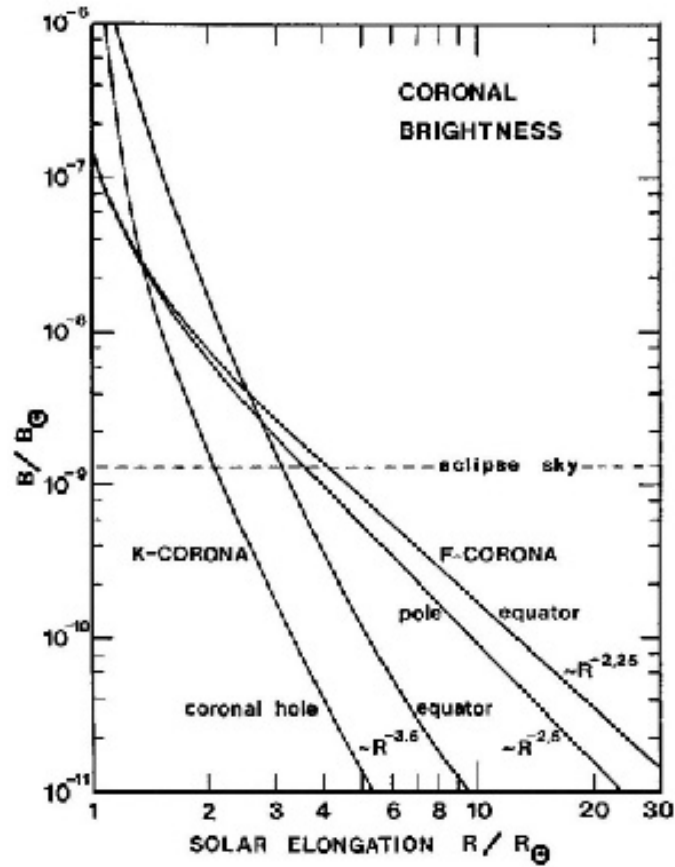
Figure 1.9: *The coronal brightness with distance. The upper solid black lines on the left in the figure represent the K corona brightness at the equator and pole, and the upper lines on the right represent the F corona brightness at the equator and pole. Between 2 and 3 solar radii, the brightness observed is dominated by dust in the F corona which can be modeled and removed from the data due to its relatively uniform distribution. The scattering of light by the terrestrial atmosphere dominates the brightness observed by terrestrial coronagraphs beyond 4 solar radii.*

1.4.1   Steady State Electron Density

The Solar Heliospheric Observatory (SOHO) was capable of collecting white light information out to 30 solar radii; the ground based observatories such as HAO's Mark IV Coronagraph on Mauna Loa can only observe out to 2 solar radii. Additionally, ground based coronagraphs are dependent on clear observing conditions. During the 2003 conjunction the source for appropriate white light images, SOHO, was under maintenance and not collecting data. Therefore it was not possible to use the best coronal electron density models which are those that are constructed using the white light coronagraph images and photospheric magnetographs.

During both the 2002 and 2003 solar conjunctions, Interplanetary Scintillation (IPS) data was collected from Nagoya, Japan at 327 MHz and used to construct 3D electron density maps from 22-323 Rs. Within the 22 Rs sphere, either the 3D structure was extrapolated or the Tyler electron density model (Tyler *et al.*, 1977) was used. The electron density model is a general global empirical model constructed from radio occultation and white light data.

1.5   Overview of Transients

1.5.1   Coronal Mass Ejections

Coronal Mass Ejections (CMEs) are associated with large flux ropes that erupt from the Sun and maintain much of their structure as they expand in the solar wind. While it is clear in the white-light images of CMEs that the density structure is controlled by the magnetic structure, the precise correlation between density structure and magnetic field structure remains an open question. Three-dimensional

Table 1.3: *The significant characteristics of coronal transients that can be measured by Faraday rotation.*

Transient	LOS Transit Time Scale	Density Characteristics	Magnetic Characteristics
Coronal Mass Ejection	2-8 hours	increase above the background	associated flux rope
Streamer	multiple solar rotations	2 orders of magnitude increase	planar around current sheet
Waves:			
Magnetosonic or Slow	0.1-0.5 hour period	periodic; anticorrelated with B	periodic; anticorrelated with N
Fast	0.1-2 hour period	periodic; correlated with B	periodic; correlated with N
Alfvenic or Intermediate	0.1-0.5 hour period	no signature in linear approximation	periodic

MHD models show the CME expansion as taking on the form of a "pancake" due to the greater expansion in the azimuthal direction over the radial (Odstrčil & Pizzo, 1999). However, most flux rope reconstructions from ICME crossings fit a cylindrical model to the magnetometer observations; Mulligan showed that with multiple spacecraft observations, the ICMEs can be fit with either elliptically or axially stretched cylinders (Mulligan, 2002).

Table 1.3 lists the properties of CMEs and other transients that have significant effects on the Faraday rotation measurement. Each transient is unique in its transit time scale and affects on the plasma electron density and magnetic field through which the Faraday rotation observation is made. The only exception as will be discussed in Chapter 6 is the ambiguity in distinguishing fast and slow mode MHD waves; the phase correlation between the magnetic field and electron density fluctuations depends on the line of sight through the wave.

A simple flux rope model is the constant alpha Bessel function flux rope. The model is cylindrically symmetric with the currents from twist in the magnetic field

balancing the magnetic field pressure. Thus magnetic "bubble" or "cloud" is often used to describe CMEs which exhibit similar structure to the model. If it is assumed that a flux rope magnetic configuration is "force-free", then from the momentum equation

$$\vec{J} X \vec{B} = 0$$

Using Ampere's Law $\nabla X \vec{B} = \mu_0 \vec{J}$, the equation becomes

$$\frac{1}{\mu_0} \vec{B} X (\nabla X \vec{B}) = 0$$

which in cylindrical coordinates is

$$
\begin{aligned}
B_z &= B_0 J_0(\alpha R) \\
B_\phi &= B_0 H J_1(\alpha R) \\
B_r &= 0
\end{aligned}
\tag{1.1}
$$

where J_0 and J_1 are the Bessel function solutions, α is the constant determining twist of the flux rope, and H is the handedness of the rope ($+1$ for right and -1 for left).

1.5.2 Streamers

Coronal streamers are prominent quasi stationary structures in the solar corona that span neutral lines. The standard mode of the structure of a streamer as derived from
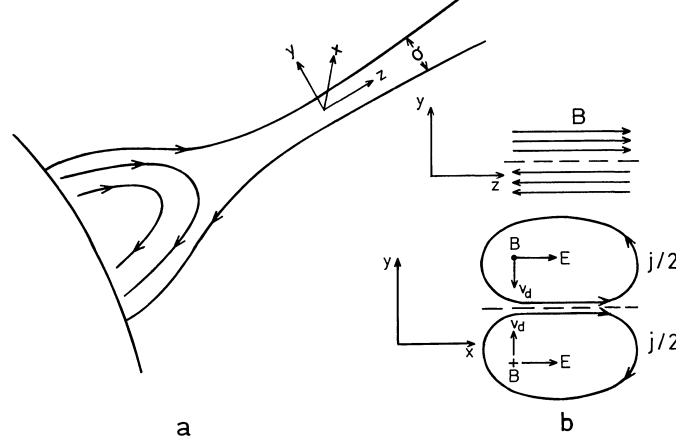
Figure 1.10: *a) The idealized magnetic field structure in a streamer. b) The current sheet begins at the cusp and continues radial outward along the z-direction; as shown in the bottom diagram, the current is flowing in the x-direction (Koutchmy & Livshits, 1992).*

polarization observations is shown in Figure 1.10. Below 2.5 solar radii, the streamer is wide with some closed magnetic loops; beyond this point, the outer magnetic field lines stretch out into the solar wind as a stalk. With distance from the Sun, the stalk of the streamer occupies a smaller solid angle indicating that the magnetic field within is not purely radial; this structure is supported by the central current sheet along the z-axis (current flows in the x-direction) causing the plasma to drift towards the x-axis as shown in part b of Figure 1.10. Although the streamer densities are approximately 2 orders of magnitude higher than mean equatorial densities, they are not a large contributer to the solar wind (Koutchmy & Livshits, 1992).

The electron density of a streamer is described by

$$N(r) = N(R_s) \exp\left\{ -\left(\frac{0.6 m_e g R_s}{kT} \right)\left(\frac{1}{R_s} - \frac{1}{r} \right) \right\}$$

where N is the electron density, r is the radius from the Sun, R_s is the radius of the Sun, g is the gravitational acceleration of the Sun at the surface, and T is the

temperature of the corona (usually between 1.3 and 1.6 MK).

1.5.3 Waves

Helios Faraday rotation data revealed that "generally the appearance of periodicities ... are quite variable" (Samoznaev & Bird, 1997) between 3 and 20 solar radii. Waves observed below 2 solar radii occur in the subsonic region of the corona where upwardly propagating waves from the transition region constitute an important observable for coronal heating. Between 10 and 20 solar radii, the solar wind accelerates by approximately a factor of 4 possibly due to nonlinear Alfven wave damping (Stelzried & Seidel, 1982).

1.6 Faraday Rotation

Faraday rotation occurs when an electromagnetic wave passes through circularly birefringent media. The index of refraction in the medium is not the same for the two modes of circular polarization parallel to the magnetic field in the medium. An electromagnetic wave passing through the medium with a wave vector component parallel to the magnetic field of the medium will experience a rotation of the plane of polarization. This birefringent property of the medium can be studied using time perturbation theory on the effects of electromagnetic radiation interacting with the electrons of the magnetized medium (Halpern *et al.*, 1964). General Faraday rotation is discussed in Appendix A.

1.6.1 High Frequency Faraday Rotation in Plasma

While Faraday rotation will occur over a wide range of frequencies, we will employ only the high frequency regime where the signal frequency is much greater than either the plasma or gyrofrequencies ($\omega \gg \omega_{ce}, \omega_{pe}$). A high frequency electromagnetic wave passing through a plasma has four modes: right (R), left (L), extraordinary (X), and ordinary (O). Only the ordinary mode is independent of the magnetic field in the media; the extraordinary mode is a wave that propagates perpendicular to the magnetic field (Swanson, 1989). The X mode is also capable of affecting the plane of polarization; however, it is 4 orders of magnitude smaller than the R and L mode effects. The Faraday rotation equation in the high frequency regime in a plasma is:

$$\frac{d\phi}{ds} = \frac{1}{2}\frac{\omega}{c}(n_L - n_R)\left[\frac{radians}{m}\right] \tag{1.2}$$

where $n_{R,L}$ is the index of refraction

$$n_{R,L}^2 = \left[1 - \frac{\omega_{pe}^2}{\omega^2(1 \mp \omega_{ce}/\omega)}\right]$$

where ω is the signal frequency, $\omega_p^2 = \frac{Ne^2}{\epsilon_o m_e}$ is the plasma frequency, $\omega_c = \frac{eB}{m_e}$ is the cyclotron frequency, and N is the electron density. A Taylor expansion of the 2nd term gives

$$n_R^2 = \left[1 - \frac{\omega_{pe}^2}{\omega^2(1-\omega_{ce}/\omega)}\right] \approx \left[1 - \left(\frac{\omega_{pe}^2}{\omega^2} + \frac{\omega_{pe}^2}{\omega^2}\frac{\omega_{ce}}{\omega}\right)\right]$$
$$n_L^2 = \left[1 - \frac{\omega_{pe}^2}{\omega^2(1-\omega_{ce}/\omega)}\right] \approx \left[1 - \left(\frac{\omega_{pe}^2}{\omega^2} - \frac{\omega_{pe}^2}{\omega^2}\frac{\omega_{ce}}{\omega}\right)\right]$$

and s Taylor expansion of $n_{R,L}$ gives

27
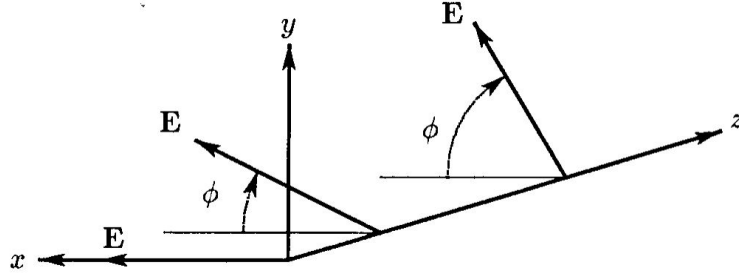
Figure 1.11: *Schematic showing that if the background magnetic field in a plasma is oriented in the z-direction, as a linearly polarized EM wave propagates in the z-direction, the electric field vector of the wave will rotate in the right handed direction (Swanson, 1989). A linearly polarized EM wave is comprised of equal amplitude left and right circularly polarized waves. Because a plasma is circularly birefringent, the phase velocities of the left and right circularly polarized waves are different which causes the rotation in the plane of polarization.*

$$n_R = 1 - \frac{1}{2} \frac{\omega_{pe}^2}{\omega^2} \left(1 + \frac{\omega_{ce}}{\omega}\right)$$

$$n_L = 1 - \frac{1}{2} \frac{\omega_{pe}^2}{\omega^2} \left(1 - \frac{\omega_{ce}}{\omega}\right)$$

because $n_L > n_R$, the relative phase velocities of the left and right polarizations through a magnetized medium $v_{ph} = c/n$ is $v_{ph,L} < v_{ph,R}$. Therefore, as shown in Figure 1.11, if the magnetic field is oriented along the z-axis, the rotation of the electric field vector from Faraday rotation is in the positive (RCP) direction. At the Earth, the Faraday rotation angle measured is the integrated quantity of the amount of rotation along the line of sight.

$$FR = \int_{SC}^{\oplus} \frac{\omega_p^2 \omega_c}{2c\omega^2} ds \, [radians]$$

which becomes ($\omega = 2\pi f \left[\frac{radians}{second}\right]$)

$$FR = \tfrac{A}{f^2} \int_{SC}^{\oplus} N\vec{B} \cdot d\vec{s} \quad [radians] \tag{1.3}$$

where A is the constant $\tfrac{q^3}{8\pi^2\epsilon_o m_e^2 c}$, f is the frequency of the signal in Hz, SC is the spacecraft, E is the Earth, N is the electron density in $[m^{-3}]$, s is the path of the signal in meters, q is the electron charge in Coulombs, m_e is the mass of an electron in kg, and c is the speed of light in meters/second.

1.7 Faraday Rotation Measurements

In the high frequency regime, four sets of coronal Faraday rotation measurements using spacecraft radio frequency carriers have been published. Spacecraft Faraday rotation measurements are particularly difficult to obtain because of the competing phenomena of increasing noise from greater electron densities and the basic limits on power available to the spacecraft radio communications (Staelin, 2003). High frequency measurements require large antennas to collect enough radiation to overcome these problems. In the frequency regime around 300MHz, where less expensive technology is required to obtain measurements, there are regular observation campaigns conducted. However, the low frequency regime is unable to measure closer to the Sun than 60 solar radii.

1.7.1 Pioneer 6

The 1968 Pioneer 6 occultation of the corona began on October 26 and ended on December 9 with the line of sight passing equatorially behind the Sun (Figure 1.12). Using the linearly polarized signal at 2292 MHz, the Faraday rotation measurements
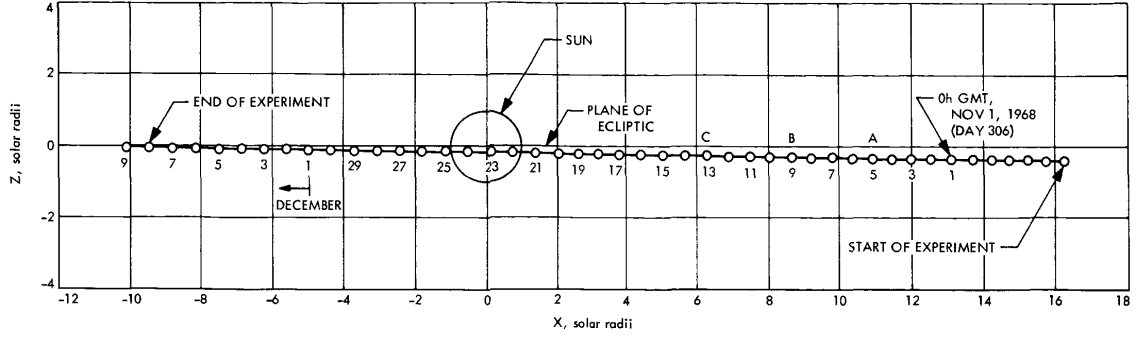
Figure 1.12: *The position of the line of sight (LOS) in the plane of the sky of Pioneer 6 during the 1968 solar conjunction from October 26 to December 9. Each dot marks the position at 0000 UT each day as the LOS moves from right to left across the plane of the sky. The latitude of the LOS remained equatorial throughout the experiment (Stelzried, 1968).*

were obtained through the physical rotation of quarter-wave plates to determine the direction of the plane of polarization (Stelzried, 1968). Stelzried compared the early version of the PFSS model (Figure 1.13) to the extrapolation of Explorer 33 Earth orbiting data (Figure 1.14) to the solar corona using the Faraday rotation measurements. To do the comparison, Stelzried tested several electron density models and found a best fit. The Explorer 33 magnetometer data was increased by R^{-2} along the Parker spiral to the Sun and reconstructed the sector structure at the time of the Faraday rotation measurements. Stelzried also showed that the maximum Faraday rotation that could be measured occurred when a current crossing was near the point of closest approach. Stelzried's observations also found three 'W' features measured November 4, 8, and 12 lasting approximately 3 hours and ranging over 40 degrees that have remained unexplained. It will be shown in Chapter 5 that these signatures are probably due to CME flux ropes.

30
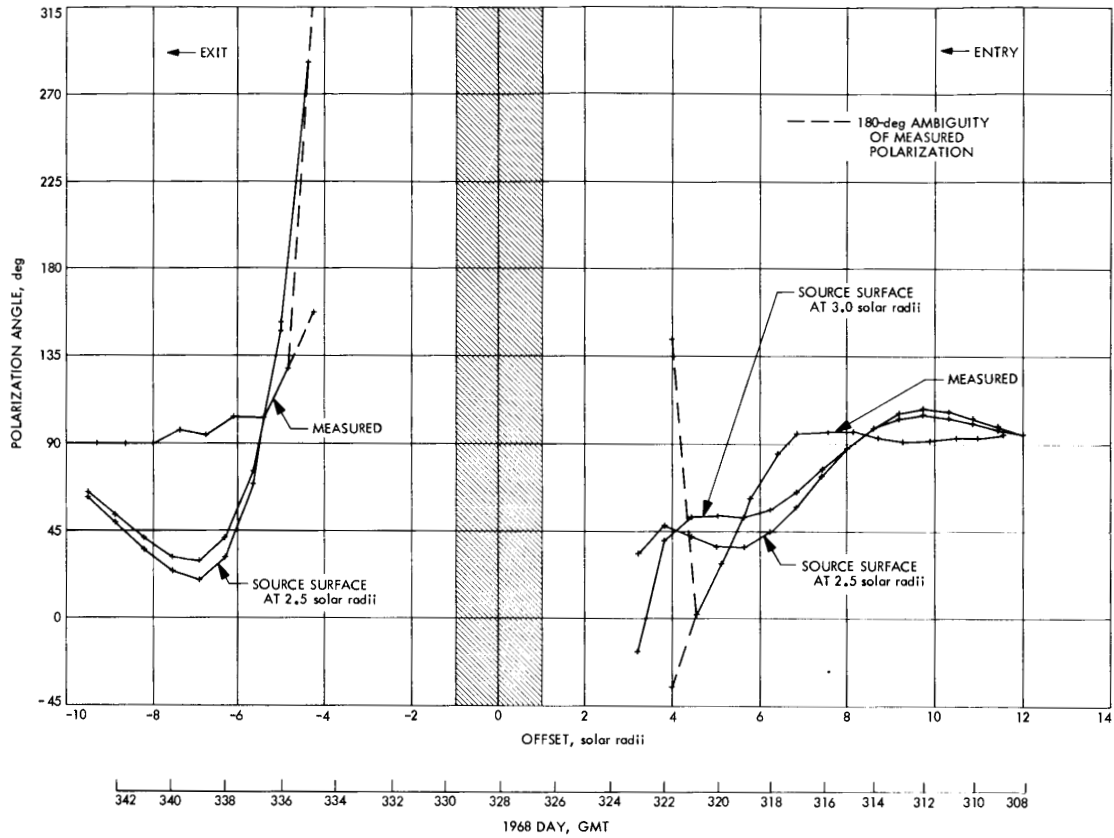
Figure 1.13: *The comparison between Pioneer 6 measured and PFSS modeled Faraday rotation. The hatched area in the center marks the time period and the position of the solar surface at 1 Rs. The curve ('measured') connects to 2 dashed curves where the signal has rotated enough that the plane of polarization is ambiguous ±180 degrees. The two other curves labeled 'source surface' are generated using the Potential Field Source Surface model (source surface set at 2.5 and 3 solar radii as marked) and a modified spherically symmetric Allen-Baumbach electron density model. The zeroth order similarity between the curves is due to the accuracy of the sector structure prediction. The PFSS model was constructed from Mt. Wilson Solar Observatory Zeeman splitting measurements by K.H. Schatten; the classic line of sight source surface error in predicting the sector structure of the corona contributed to the differences between the model and the FR data (Stelzried, 1968).*
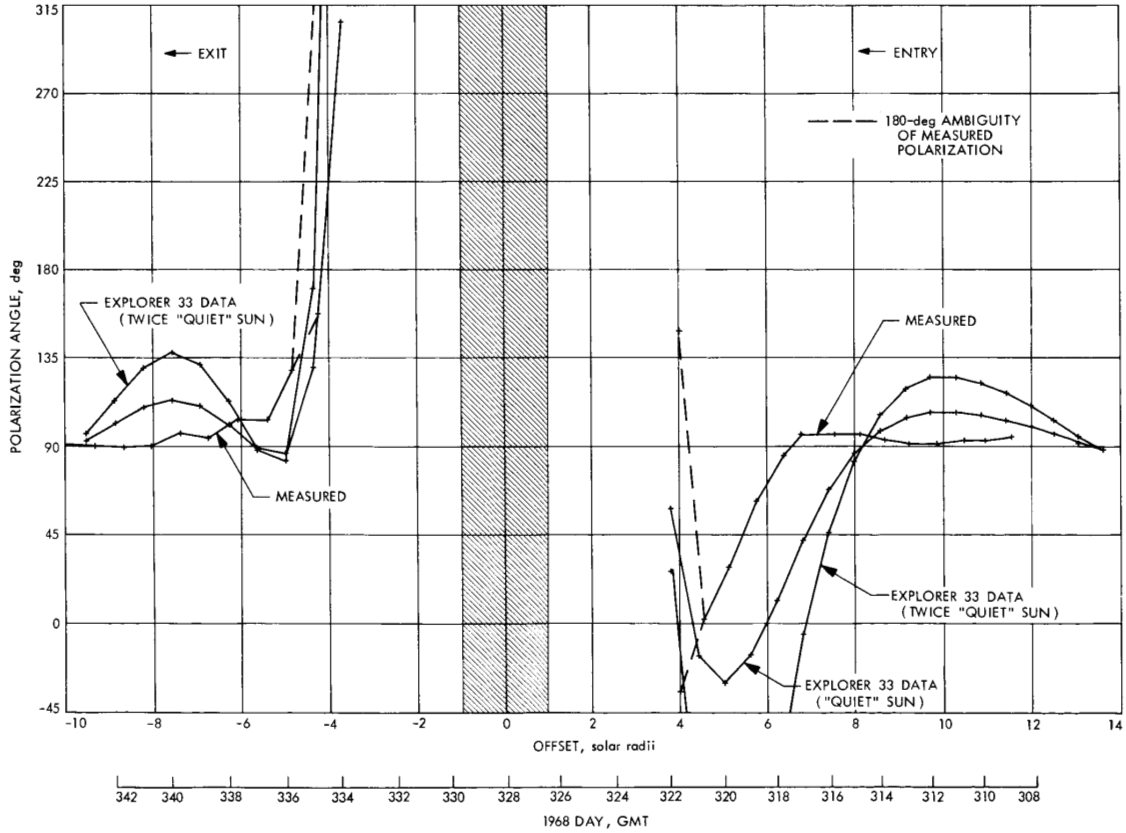
Figure 1.14: *The comparison between Pioneer 6 measured Faraday rotation and modeled Faraday rotation using a heliospheric magnetic field structure reconstruction from the Explorer 33 magnetometer measurements. The hatched area in the center marks the time period and the position of the solar surface at 1 Rs. The curve ('measured') connects to 2 dashed curves where the signal has rotated enough that the plane of polarization is ambiguous ±180 degrees. The two other curves labeled 'Explorer 33' are constructed using the modified Allen-Baumbach model for electron electron density; however, the magnetic field model was a reconstruction from a Carrington rotation of Explorer 33 magnetometer observations outside of the Earth's magnetosphere. The Explorer 33 magnetic field measurements for a full solar rotation were extrapolated inward along the ideal Parker spiral for a constant 400 km/s solar wind speed (Stelzried, 1968). Cannon later showed that the fit improves with electron density and velocity measurements in conjunction with the magnetometer observations.*
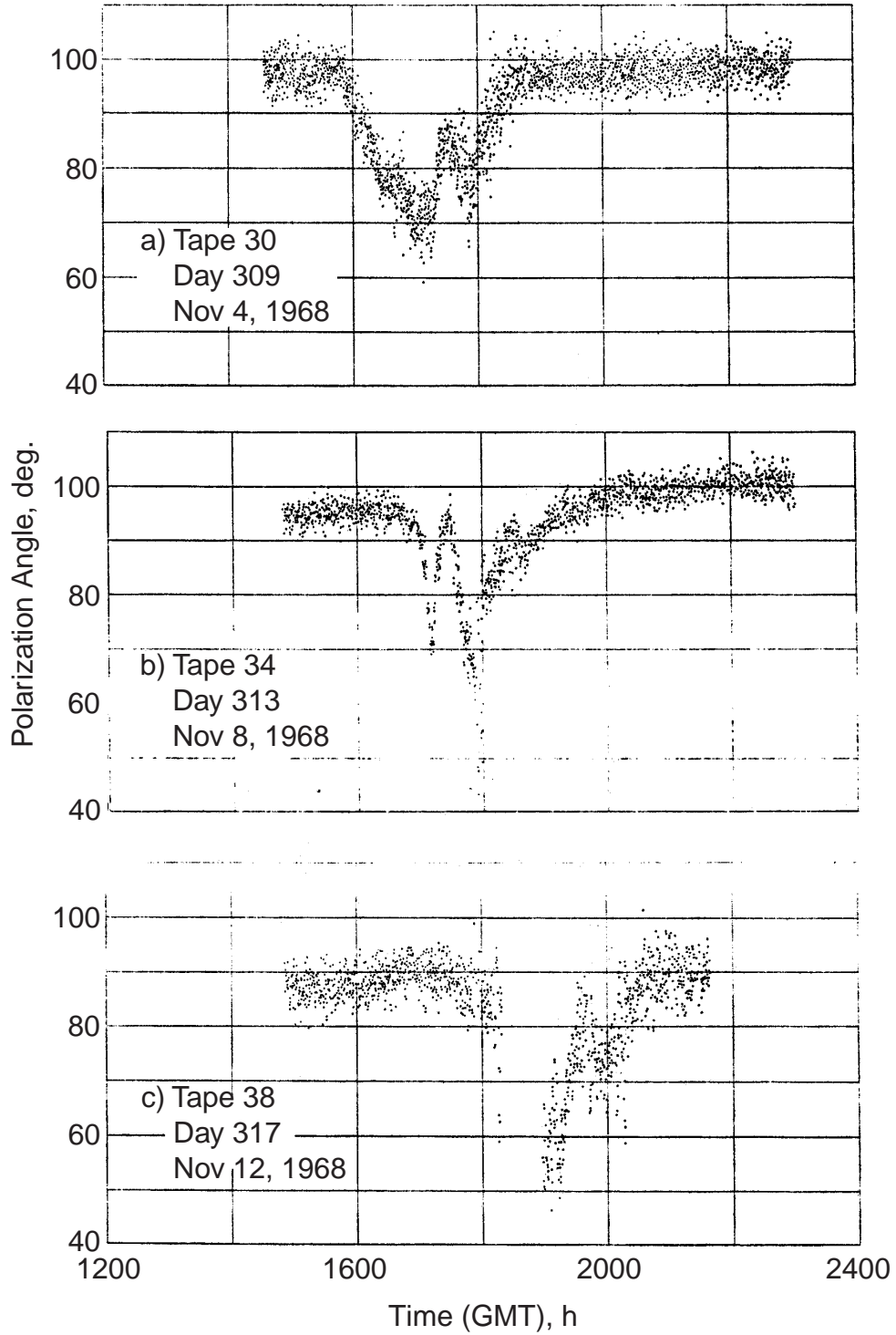
Figure 1.15: *The Faraday rotation observations from Pioneer 6 during the crossing of 3 CMEs on 1968 November 4, 8, and 12. The 'W' features last approximately 3 hours and range over 40 degrees (Stelzried, 1968).*

33
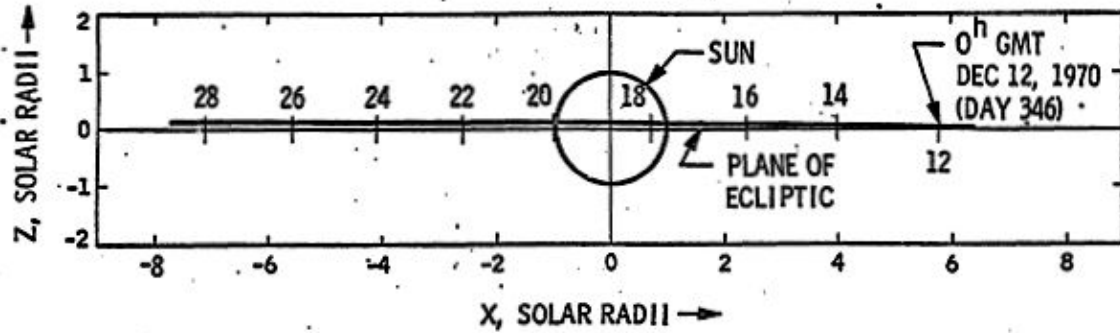
Figure 1.16: *The position of the line of sight (LOS) in the plane of the sky of Pioneer 9 during the 1970-1 solar conjunction from October 2 to January 28. Each vertical dash marks the position at 0000 UT each day as the LOS moves from right to left across the plane of the sky. The latitude of the LOS remained equatorial throughout the experiment (Cannon, 1976).*

1.7.2 Pioneer 9

The Pioneer 9 Faraday rotation observations began 1970 October 2 and ended 1971 January 28. Using the same 2292 MHz signal and quarter-wave plate technology as the Pioneer 6 experiment, the Pioneer 9 experiment was sensitive to a minimum line of sight closest approach of 4 solar radii (Figure 1.16) (Cannon, 1976). Cannon observed that the sector structure reconstructed from satellite magnetic field, electron density, and solar wind velocity data predicted the Faraday rotation measurements. During the observing period two transients were observed; the first appeared to be an initial 'W' feature on December 11. The second transient on December 26 was more sigmoidal in shape (Figure 1.17) lasting 5+ hours and rotating over a range of 15 degrees; this also will be shown to be interpretable as a CME flux rope crossing the line of sight.

PIONEER 9 SIGNAL POLARIZATION

DAY 360, 1970   -6.2 SOLAR RADII
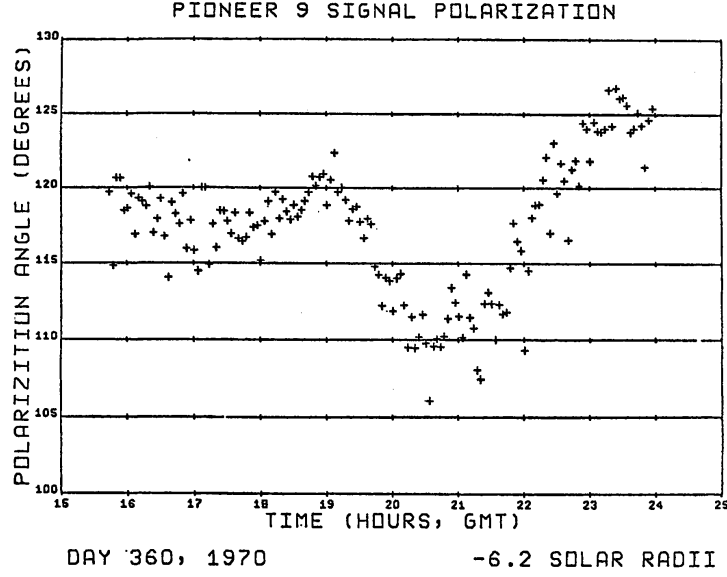
Figure 1.17: *The Faraday rotation observation from Pioneer 9 during the crossing of a transient on 1970 December 26. The Pioneer 9 transient was sigmoidal in shape (Cannon, 1976).*

1.7.3   Helios 1 and 2

Helios had a unique configuration with the two Helios spacecraft orbiting the Sun in elliptical orbits inside of 1 AU and passing behind the solar corona regularly at low latitudes. Faraday rotation measurements were made using the spacecraft from 1975 to 1984 from solar minimum to maximum. The 2292 MHz Helios radio signal was linearly polarized and used similar equipment to that of the Pioneer 6 and 9 experiments. The envelope for maximum Faraday rotation for a particular point of closest approach occurs when there is one sector boundary very close to the solar limb; Figure 1.18 shows the slope of the envelope from 460 hours of Faraday rotation data at solar minimum. Paetzold statistically determined the radial falloff of magnetic field at solar minimum using the maximum Faraday rotation envelope shown in Figure 1.6 (Patzold *et al.*, 1987).
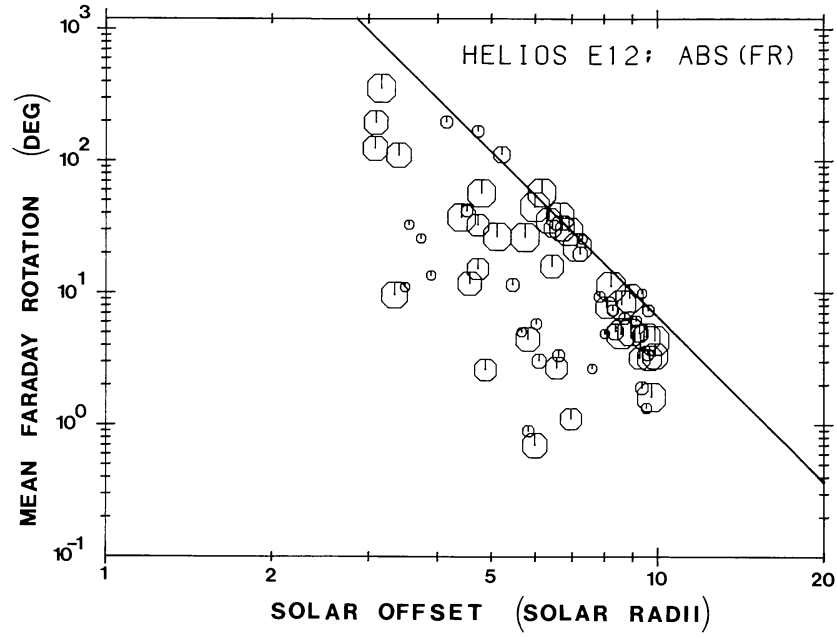
Figure 1.18: *The mean Faraday rotation from Helios 1 and 2 during time periods with little variability relative to the distance of the point of closest approach. The size of the points gives the error in the measurement. Paetzold shows that there is an envelope that varies with the impact parameter of the line of sight using 460 hours of Helios data. Because the envelope occurs when the current sheet crossing is located near the point of closest approach, the magnetic field as a function of distance can be determined empirically (Patzold et al., 1987).*
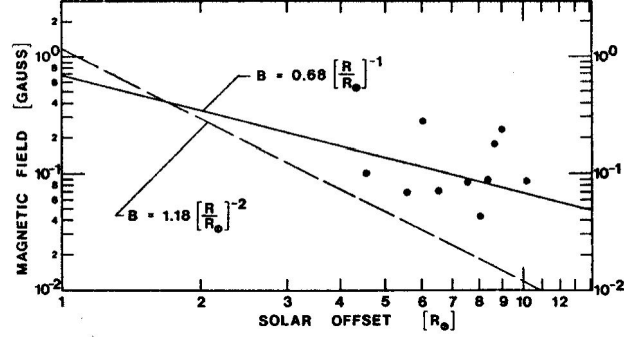
Figure 1.19: *The background magnetic field inferred from Helios 1 and 2 Faraday rotation RMS deviation assuming that the RMS deviation is purely the result of electron density fluctuations with respect to the impact parameter of the line of sight. The expected slope from an R^{-2} extrapolation of Helios magnetometer data is shown (dashed line). Hollweg produced a model predicting the effect that Alfven waves would have on the magnetic field calculation shown by the solid black line (Hollweg* et al., *1982). Hollweg did not evaluate the effects of compressive mode MHD waves on the magnetic field calculation.*

Helios data were also used to detect periodic fluctuations in the root mean square (rms) Faraday rotation fluctuations. Hollweg compared the RMS deviation in ranging data to the Faraday rotation data assuming that any difference would be due to magnetic field fluctuations in Figure 1.19 (Hollweg *et al.*, 1982). Assuming that Alfven waves are the primary source of the fluctuations, Hollweg developed an expression for the expected Faraday rotation RMS deviation and found that it reasonably compared to observations.

During the numerous Helios conjunctions, several CMEs were observed to intersect the line of sight (LOS) to the Helios spacecraft (Bird *et al.*, 1985). Bird reported on the best 4 observations occurring on 1979 October 23, 24, 27 and November 16. The CMEs on the 23rd and 24th (Figure 1.20) appeared to produce similar 'W' features in the Faraday rotation measurements as observed by Stelzried. The CME observed on the 27th appears to have have missed the Helios LOS; however, the
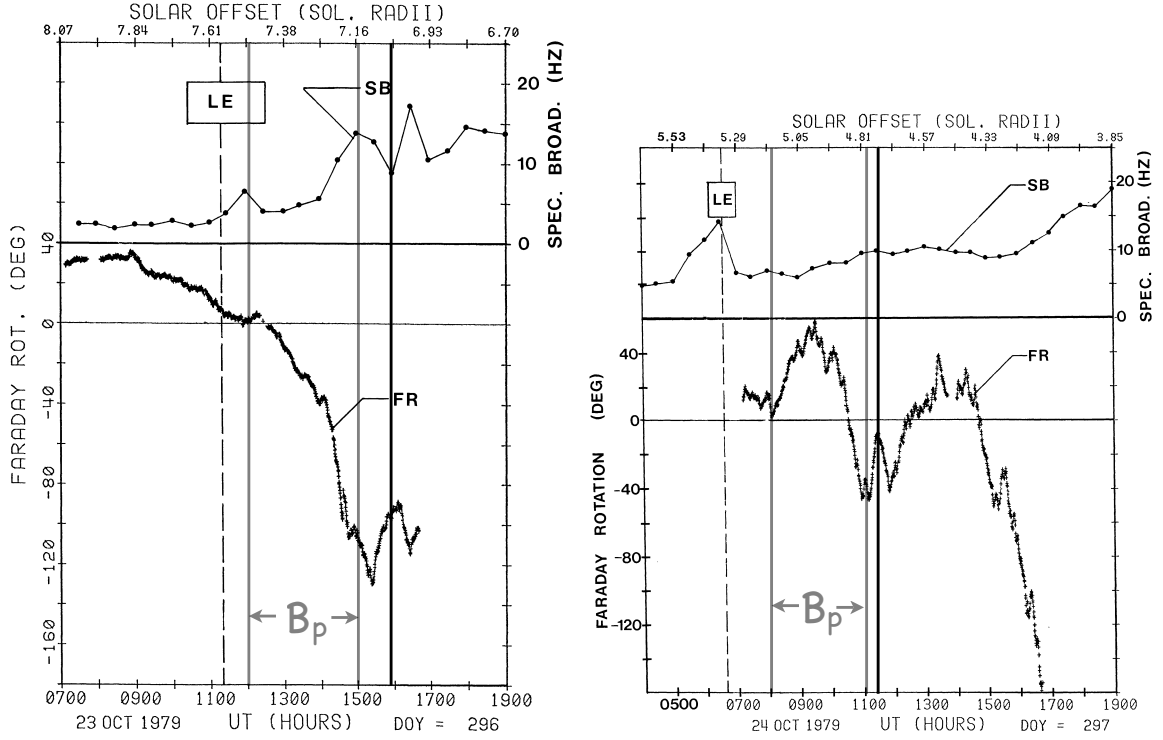
Figure 1.20: *The Faraday rotation observations (FR) and spectral broadening (SB) of the signal during a CME crossing measured by the Helios spacecraft on 1979 October 23 (left) and 24 (right). The leading edge (LE) of the CME crossing and the spectral broadening (SB) of the signal are shown. The parallel magnetic field could only be calculated in the range Bp (Bird et al., 1985).*

Faraday rotation measurements indicate a possible oblique crossing of the plasma surrounding the CME. Finally, the November 16 CME (Figure 1.21) appeared to have produced a reverse sigmoid in the Faraday rotation. Using Solwind columnar electron density measurements, Bird estimated the electron density weighted average magnetic field along the line of sight to the 23rd and 24th CMEs to be in the range of 10 to 25 mG or approximately 1000 nT.
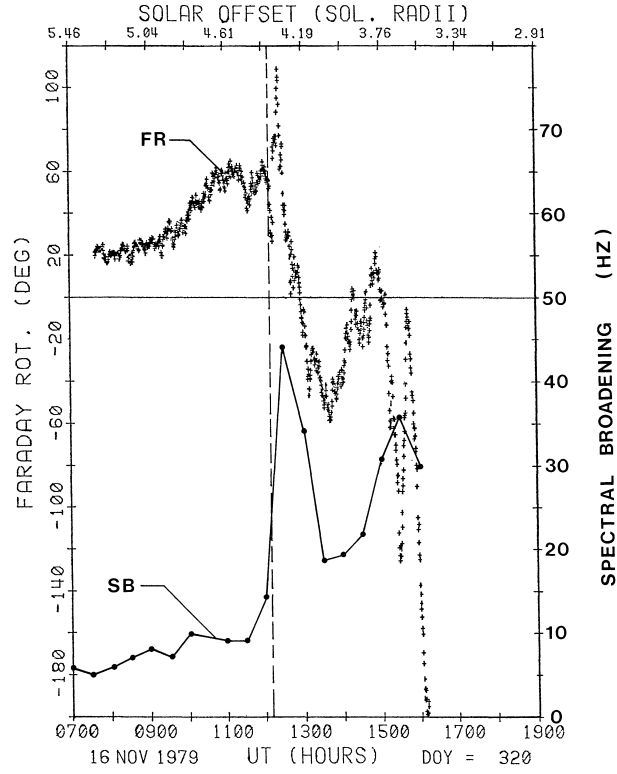
Figure 1.21: *The Faraday rotation observations (FR) and spectral broadening (SB) of the signal during a CME crossing measured by the Helios spacecraft on 1979 November 16. The leading edge of the CME crossing occurred around 1200UT. The spectral broadening (SB) of the signal increased throughout the CME crossing with a peak around 1230UT (Bird et al., 1985).*

39

1.7.4 Magellan

In 1992, dual frequency (S- and X-band) dual polarization data were collected using the coronal occultation of the Magellan spacecraft (Asmar, 1996). The data collection system used Digital Sampling Processing equipment for the data collection requiring new methods for obtaining Faraday rotation measurements. Unfortunately, the data were corrupted by a sampling error in the DSP which has not yet been corrected (Johnston, 2005).

1.8 Electron Density Measurements

Faraday rotation is the rotation observed in the plane of polarization of an electromagnetic wave passing through a magnetized medium. In a plasma, the amount of rotation is proportional to the integrated product of the electron density and the component of the magnetic field parallel to the wave vector of the electromagnetic wave. The Cassini Faraday rotation experiment uses the phenomenon of Faraday rotation to estimate the coronal magnetic field. This requires the coronal electron density to be independently determined using any one of a variety of methods. These include ranging, Doppler, or scintillation of the radio signal.

1.8.1 Ranging

DRVID

Differenced Range Versus Integrated Doppler (DRVID or "ranging") measures the total columnar electron density of the solar corona using the radio signal from a

spacecraft near conjunction. The technique has high spatial resolution in the plane of the sky, but it has the lowest overall coverage of the solar corona because few spacecraft are in the appropriate orbits and have ranging capability. A two way link to the spacecraft must be maintained in order to make the measurements. The uplink carrier is modulated with "a sequence of square waves varying from 2 MHz to as low as 1 Hz." (Moyer, 2000) The lowest frequency is determined based on the expected error in the time it would take for the signal to reach the spacecraft because of plasma. The modulations travel at the group velocity through the plasma resulting in a time delay that increases with increases in columnar plasma density (Total Electron Content or TEC). The measurement is the integrated plasma density along the line of sight from the spacecraft to the Earth.

The time that it takes for a packet of waves traveling at the group velocity to travel from a source to a receiver is

$$t_g = \int_0^s \frac{ds}{v_g} \; [seconds]$$

where s $[meters]$ is the distance traveled, and v_g $[meters/second]$ is the group velocity.

$v_g = \frac{d\omega}{dk} = cn$ $[meters/second]$ (where $c = 3 \times 10^8$ $[meters/second]$ is the speed of light, and n is the dimensionless index of refraction) and the index of refraction is

$$n^2 = \frac{c^2 k^2}{\omega^2} = 1 - \frac{\omega_{pe}^2}{\omega^2}$$

where ω_{pe} $[radians/second]$ is the plasma frequency, and ω $[radians/second]$ is the signal frequency. The plasma frequency is

$$\omega_{pe}^2 = \frac{Ne^2}{\epsilon_o m_e} \; [radians^2/second^2]$$

where electron density N $[meters^{-3}]$, charge $e = 1.6022 \times 10^{-19}$ $[Coulombs]$, permittivity of free space $\epsilon_o = 8.8542 \times 10^{-12}$ $[Coulombs^2/Newton/meters^2]$, and electron mass $m_e = 9.1095 \times 10^{-31}$ $[kilograms]$. In the high freq regime, $\omega \gg \omega_{pe}$ so the index of refraction is approximated using a Taylor expansion as

$$n \sim 1 - \frac{1}{2}\frac{\omega_{pe}^2}{\omega^2}$$

which gives a group travel time of

$$t_g = \frac{1}{c}\int_0^s (1 - \frac{1}{2}\frac{\omega_{pe}^2}{\omega^2})^{-1}ds \ [seconds]$$

This can also be approximated using a Taylor expansion to

$$t_g \sim \frac{1}{c}\int_0^s (1 + \frac{1}{2}\frac{\omega_{pe}^2}{\omega^2})ds \ [seconds]$$

Therefore the total columnar electron density from the group travel time is

$$t_g = \frac{s}{c} + \frac{1}{2}\frac{e^2}{\epsilon_o m_e 4\pi^2 f^2}I \ [seconds]$$

where signal frequency $f = \frac{\omega}{2\pi}$ $[Hz]$ and

$$I = \int_0^s N ds \ [meters^{-2}]$$

Cassini range data available were infrequently obtained and limited to 2002. It was used to compare to the Doppler variable electron density measurements and the scintillation electron density columnar integrations.

1.8.2   Previous Ranging Measurements

The technique of ranging was first developed by Kelso who also considered the advantages of dual frequency ranging (Kelso, 1959). Pioneer 6, 7, 8, 9, Mariner 5, Viking Orbiter, Helios 1&2, Ulysses, and Voyagers 1&2, all measured the solar corona or coronal transients using ranging.

Koehler conducted a study using the ranging data from Pioneer 7 to observe 3 transient events (Koehler, 1968). The transients were observed on 1966 October 24, November 10, and 1967 January 25. It is difficult to distinguish whether the transients are CMEs crossing the line of sight or streamers crossing the Earth's orbit, because the events have not been correlated with geomagnetic activity. Croft et al. (below) determined that the rotation period of the sun could be used to identify streamer crossings; based on the distance of the spacecraft from the Earth, an increase in columnar electron density should take a fixed period of time before the onset of geomagnetic activity. CMEs were identified because the time difference was too small. Figure 1.22 shows the orbital geometry between the Earth and Pioneer 7 when the transients were passing.

On 1972 August 3 and 9, two possible CMEs were observed crossing the line of sight between Pioneer 9 and the Earth (Croft, 1973). The August 3rd event peaked at a concentration of $40/cm^3$ followed by a geomagnetic effect at the Earth on August 4th. A cavity was observed with densities under $1/cm^3$ on August 6. Another increase was observed again on August 9 to $15/cm^3$. Pioneer 9 was approximately 1AU from the Sun trailing the Earth by about 4 days of solar wind co-rotation when the events occurred. High densities were also observed on the following two solar rotations, on August 31 and September 20, indicating that the CMEs were probably associated with a helmet streamer. The August 3rd event can be ruled
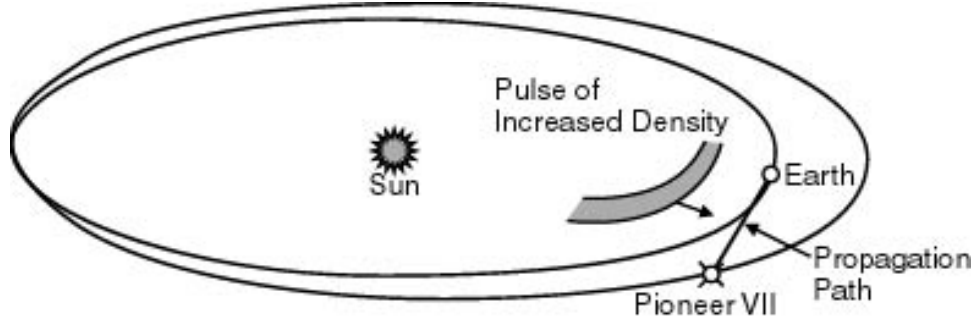
Figure 1.22: *The position of the Earth and Pioneer 7 in orbit about the Sun during either a streamer or CME crossing. When the 1966-7 transients intersected the line of sight between Pioneer 7 and Earth, Pioneer 7 led the Earth in orbit around the Sun by approximately 50×10^6 km (Koehler, 1968).*

out as a streamer due to its geomagnetic manifestations taking only 1 day to reach the Earth rather than four.

Landt describes several possible CMEs crossing lines of sight between the Earth and Pioneers 6, 7, 8, and 9 and Mariner 5 (Landt, 1974). Using the combination of Earth orbiting plasma measurements and the ranging measurements from the spacecraft to the Earth, Landt attempts to reconstruct the fronts of the intersecting CMEs shown in Figure 1.23. The dates of the CMEs include 1966 July 9, December 22, 1967 January 12, January 25, March 2, March 31, April 4, May 1, 1968 May 7, 1969 February 26, and March 19. From these measurements and attempts to model CME size, an anticorrelation is derived between cloud size and and density shown in Figure 1.24. The carrier frequencies were at 50 and 423 MHz. The columnar electron content was accurate to within $3 \times 10^{16} m^{-2}$ while the change in content was accurate to $4 \times 10^{14} m^{-2}$

The Helios, Ulysses, Voyager, and Viking Orbiter ranging experiments all fit the ranging electron density data with modified Allen-Baumbach formulas. The model which combined the most empirical data for a global electron density was developed
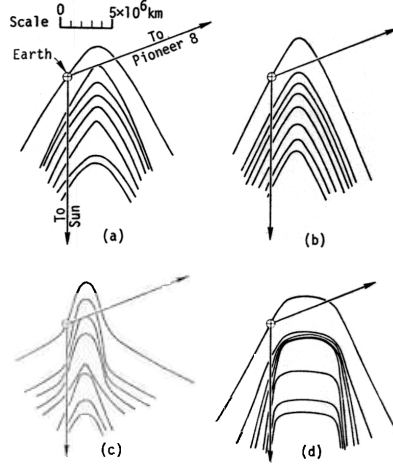
Figure 1.23: *A variety of CME shapes that can produce the observed increase in electron density on 1968 May 7. The fits from combining Earth orbiting plasma measurements with the ranging observations to model the front of the plasma cloud include: a) best fit b) uniform thickness shells c) center line 2×10^6 km from the Earth d) center line 4×10^6 km from the Earth (Landt, 1974)*
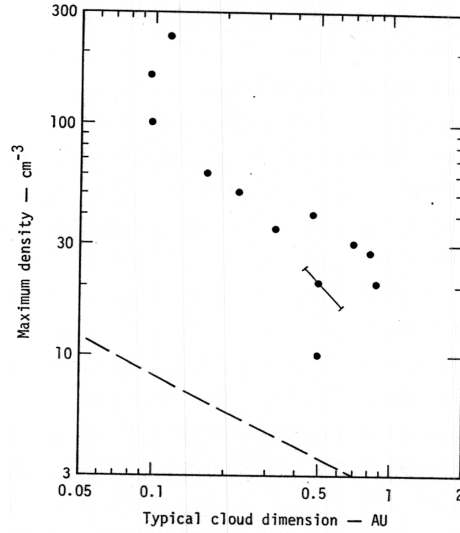
Figure 1.24: *The relationship between CME cloud size and average electron density as determined from ranging measurements. The error bar shows 20 % uncertainty in electron density. The dashed line shows the lower sensitivity of the ranging instrument. The radius of curvature of the plasma cloud is inversely related to the average electron density (Landt, 1974)*

by Tyler et al (Tyler *et al.*, 1977). Tyler et al combined empirical models from other methods of measuring the electron density into a single model and then compared that to the Viking Orbiter electron density data. Viking was in conjunction on 1976 Nov 26 and observations were measured as far out as 60 solar radii using the S and X bands at 13 and 3.5 cm wavelengths. The transmissions were detected as close as 1.8 and 1.3 solar radii; however, differential ranging measurements were obtained only as close as 2 solar radii. The electron density model is a combination of the Baumbach-Allen model at the equator, and a ρ^{-2} term to account for the 7.5 cm^{-3} electron density of the solar wind at the Earth. Finally, the latitudinal factor is "heuristic" approximating the results from work on solar effects on radio observations of pulsars.

$$N_e \left[\left(\frac{2.99}{\rho^{16}} + \frac{1.55}{\rho^6} \right) \times 10^{14} + \frac{3.44}{\rho^2} \times 10^{11} \right] (cos^2\theta + \frac{1}{64} sin^2\theta)^{1/2} \left[m^{-3} \right]$$

where θ is solar latitude. Note that the ρ^{-6} and ρ^{-2} terms are equal at just under 5 solar radii. Using dual ranging, the standard error in columnar density was $70 \times 10^{16} \left[m^{-2} \right]$.

Croft presents the data from DRVID measurements from Pioneer 6,7,8, and 9 and Mariner 5 at frequencies of 49.8 and 423 MHz (Croft, 1979). However, the data presented is only correlated with time and solar longitude. If the data are still located at the National Space Science Data Center in its modern day form, then a limited data recovery may be possible for further analysis.

Global electron density models were constructed from ranging experiments using Ulysses, Viking, and Voyager 2. The models for Viking and Ulysses included a latitudinal component due to the significantly varying latitude of the line of sight.

However, the latitude was in solar geographic coordinates rather than solar dipole coordinates. In Appendix D, the method to compare current ranging data to previous ranging models is presented.

1.8.3   Doppler

The Doppler equation

While ranging gives a measurement of the total columnar electron density, it has a low time resolution, generally on the order of 10 minutes. Because of the relative motions of the Earth and Cassini, this translates to a resolution on the order of 10^5 km spatially. High resolution columnar electron density data can be obtained using a Doppler effect that is caused by the deflection of the radio signal by the plasma of the corona; however, only the change in electron density is measured from the Doppler effect. Figure 1.25 shows a comparison between the resolution of the two techniques on 2002 June 25.

Doppler shifting is the frequency change that occurs when wavefronts of a signal apparently compress (frequency increases) or rarefact (frequency decreases) due to the relative motions of the source and observer. The Doppler shifting that is present in the Cassini radio frequency data is due to the fractional deflection of the component of the propagation vector along the path between the spacecraft and the ground antenna as shown in Figure 1.27. The antenna at the Earth acquires the signal from Cassini using ephemeris predictions; once the signal is received, the antenna adjusts its position to measure the signal where it is strongest. The plasma effects the direction the antenna must point because it deflects the signal inwards towards the Sun as shown in Figure 1.26; however, fluctuations in the plasma around the
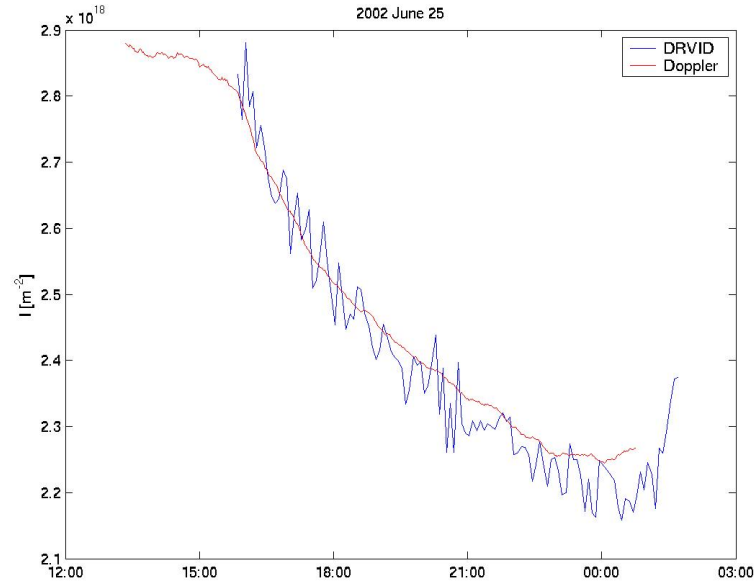
Figure 1.25: *Comparison between the columnar electron density from ranging (blue) and Doppler (red) over the 12 hour period of observation on 2002 June 25. The initial columnar electron density is unknown in the Doppler measurement and was set to 2.88×10^{18} m^{-2}. The variability in electron density was due to the integration of electron density through the solar corona following a coronal mass ejection on the 24th.*
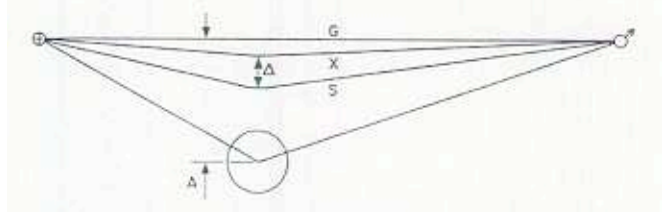
Figure 1.26: *Schematic of the effect of the radial distribution of electron density affecting the index of refraction on EM waves propagating from a spacecraft ⊙ to the Earth ⊕. Between the spacecraft and the Earth, the visual line of sight (G) is deflected towards the Sun by the coronal plasma depending on frequency ($X(8GHz) > S(2GHz)$). Δ is the distance separating the deflected S- and X-band waves (Tyler* et al., *1977).*

mean background cause a small shift in frequency. The component of the incoming wave parallel to this established line of sight is passed to the subreflector near the focus; as a result, an apparent decrease in frequency is observed in the measured signal.

The frequency shift is proportional to the change in the index of refraction along the line of sight (Bertotti & Giampieri, 1997).

$$\frac{\Delta f_p}{f} = \frac{d}{dt} \int_{LOS} \frac{n}{c} ds$$

Substituting the index of refraction for a plasma and $I = \int N ds$ gives

$$\Delta f_p = \frac{-e^2}{8\pi^2 f c \epsilon_o m_e} \Delta I \tag{1.4}$$

The component of the frequency shift due to plasma can be isolated using two frequencies. The change in frequency of the signal is the sum of the effect of Doppler
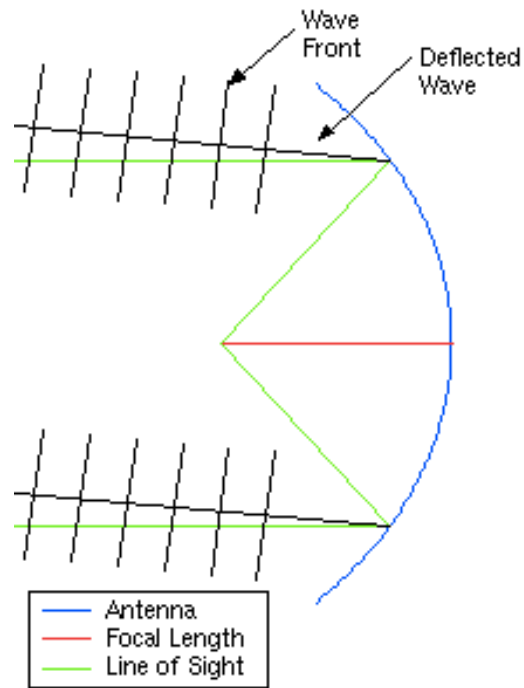
Figure 1.27: *How the bending of the ray with respect to the visual line of sight (green) affects the raypath (black) arriving at the antenna; the wavefronts are the regular perpendicular lines on the raypath. The component of the incoming deflected wave parallel to the line of sight of the antenna is passed to the subreflector near the antenna focus causing a Doppler shift. The antenna acquires the signal from a spacecraft and adjusts its position to maximize the signal power. Fluctuations in electron density cause the signal to deflect about this mean position causing a decrease in the signal frequency.*

shifting due to the relative motions of the Earth and the Spacecraft (f_{nd}) and the as deflection of the signal by the coronal plasma (generally f_p, uplink f_{pu}, downlink f_{pd}. In the case of the two way link to and from Cassini

$$\Delta f_x = \Delta f_{nd} + \Delta f_{pu} + \frac{\Delta f_{pd}}{\alpha_x^2}$$
$$\Delta f_{ka} = \Delta f_{nd} + \Delta f_{pu} + \frac{\Delta f_{pd}}{\alpha_{ka}^2}$$

$$(1.5)$$

Where $\alpha = \frac{f_d}{f_u}$ is the turnaround ratio between the downlink and uplink frequencies. The change in columnar electron density is solved from equations 1.5 and 1.4

$$\frac{-e^2}{8\pi^2 c\epsilon_o m_e}\Delta I = \frac{1}{f_x - f_{ka}}\frac{\Delta f_x - \Delta f_{ka}}{\frac{1}{\alpha_x} - \frac{1}{\alpha_{ka}}}$$

Doppler variable columnar electron density data is summed to give the total columnar electron density data starting at zero; the initial TEC (I_o) is unknown.

$$I(t) - I_o = \sum_t \Delta I(t)\Delta t$$

The analysis of MHD waves intersecting the line of sight uses the Doppler TEC data in combination with the Faraday rotation data (Chapter 6).

1.8.4 Ionosphere Removal

The columnar electron density (Total Electron Content or TEC) measured by ranging and Doppler includes the ionosphere. The ionosphere has an average columnar electron density of the order 10^{17} m^{-2}. As a radio frequency source rises above the horizon, transits and sets, the signal passes through the ionosphere at varying an-
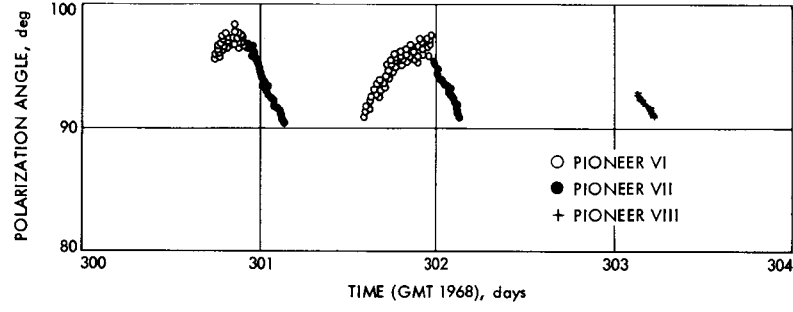
Figure 1.28: *The Faraday rotation that occurs in the S-band due to the changing line of sight through the ionosphere during the course of spacecraft rise and set times. The Faraday rotation polarization change caused by the ionosphere increases with the longer path length of the line of sight through the ionosphere occurring when the Pioneer 6 pass ends and the Pioneer 7 pass begins (Stelzried, 1968). Because of the orientation of the terrestrial magnetic field with respect to the line of sight, the Faraday rotation could not drop below the 90 degree plane of polarization of the signal. The ionospheric rotation in the X-band is 1/16th of that in the S-band.*

gles causing a variable TEC; the TEC along the line of sight through the ionosphere tangent to the surface of the Earth is on the order of 10^{18} m^{-2}.

The Cassini Faraday rotation measurements were insensitive to the ionosphere because of the high signal frequency in X- and Ka-bands (8 and 32 GHz). For example, Figure 1.28 shows the ionospheric contribution to Faraday rotation in S-band (2 GHz) of approximately 8 degrees (Stelzried, 1968). Because Faraday rotation scales as f^{-2}, the X-band would rotate by approximately 0.5 degrees; this rotation was not observed in the smoothed time series and was too small to detect in the raw time series.

Due to the rough calibration of the Cassini Faraday rotation data, only passes with rotations greater than 5 degrees were significant. Therefore, the Doppler columnar electron density measurements were dominated by the solar corona, and the ionospheric correction was not necessary.

Detailed ionospheric removal from lower frequency radio frequency data requires either an accurate ionospheric model or regularly obtained transionospheric radio propagation. The International Reference Ionosphere 2000 (IRI) model is used by the International Union of Radio Science for ionospheric radio propagation analysis (Bilitza, 2001); however, for accurate determination of the ionospheric electron density, transionospheric radio propagation data is necessary. The data is obtained using Global Positioning Satellites transmitting ranging signals to receivers in the vicinity of the antenna (Yizengaw, 2004).

1.8.5   Interplanetary Scintillation

Ranging and Doppler have reasonably high resolution in time; however, only a single line through the corona is measured. Electron density values for the three dimensional solar corona have been obtained using tomographic modeling on interplanetary scintillation measurements of the RF spectrum from natural sources (Jackson *et al.*, 2003).

Interplanetary Scintillations (IPS) can be used to infer the electron density of a medium by measuring the scintillation level (m) of a radio signal passing through the medium. Scintillation is the frequency and angular broadening of a signal that arises from changes in the index of refraction causing scattering of the passing wave. The scattering is small for high frequency (RF >> plasma and cyclotron frequencies) waves allowing the Born approximation to hold. The amount of scattering is modeled using the Born approximation to construct a weighing factor to the contribution of the variable index of refraction along the line of sight (W) from perpendicular thin surfaces of index of refraction (Jackson *et al.*, 1997).

$$m^2 = \int_{LOS} (\Delta N_e(s))^2 W(f, k, s) ds$$

where k is the wave vector and

$$W = \int_k \sin^2\left(\frac{k^2 sc/f}{4\pi}\right) \exp\left(-\frac{\theta^2 k^2 s^2}{2}\right) k^{-3} dk$$

where θ is the average angular size of a radio source at the frequency of the signal.

The scintillation level is measured from the ratio of the mean and the variance of the intensity of the radio signal (Bird & Edenhofer, 1990).

$$m^2 = \frac{< [I(t) - < I >]^2 >}{< I >^2}$$

In order to solve for the electron density along the lines of sight from the scintillation level of several sources, tomographic techniques have been developed.

3D Modeling

Electron density tomography is the method of constructing a grid of "pixels" with fixed electron density through which signals pass integrating the TEC at different angles allowing for the value of each individual pixel to be determined through inversion. As shown in Figure 1.29 for the two dimensional tomographic problem, the integration of electron density (I) along the line of sight (i) is broken up into several pixels (d) of fixed density (n).
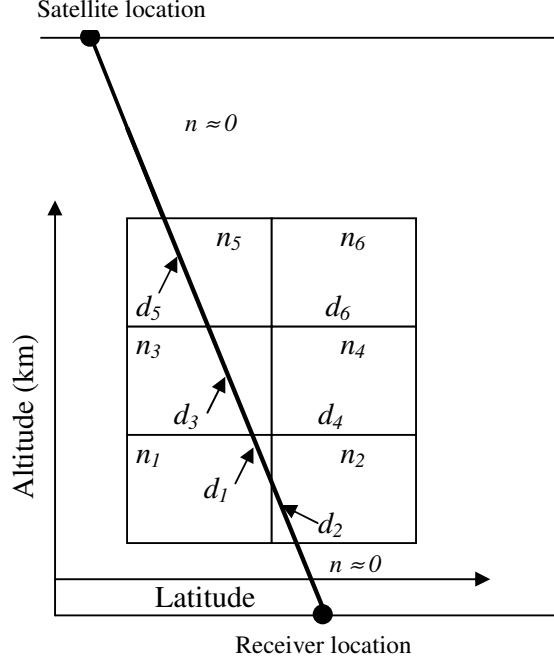
Figure 1.29: *Schematic showing the matrices for an ionospheric tomographic inversion relative to the satellite and receiver locations. The matrices include the electron density for each pixel (n) and a binary determination of whether the signal passed through a particular pixel (d) (Yizengaw, 2004).*

$$I_i = \sum_{j=1}^{M} n_j d_{ij} + e_j$$

where M is the number of pixels and e is the error (Yizengaw, 2004).

The plasma moves during the 3 to 5 hour time period that TEC measurements are made requiring velocity information in the tomographic technique. The cross-correlation between interplanetary scintillation spectra from two antennas in the same region gives a time difference due to plasma velocity. Addtionally, Jackson assumes that the variations in electron density scale proportionally with the total electron density to further simplify the inversion (Jackson *et al.*, 2003).
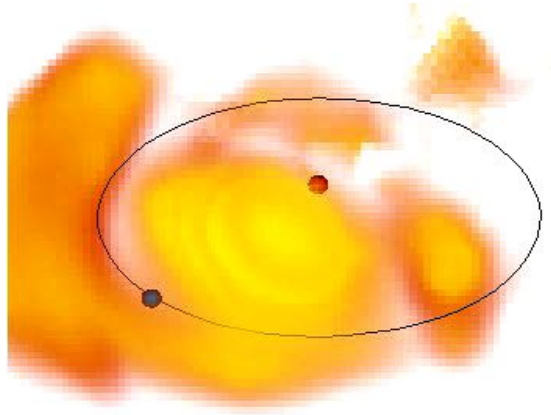
Figure 1.30: *The relative positions of the Earth and Sun during the 2000 July 14 CME. The electron density enhancement between 10 and 30 cm^{-3} (at 1AU) is shown in yellow with an r^{-2} density gradient removed. Interplanetary scintillation observations were inverted for determining the 3D electron density structure (Jackson, 2006).*

$$\Delta N_e = AR^p N^q$$

The variables A, p, and q are fit using least squares minimization of a kinematic model. The kinematic model propagates density outward through the tomographic pixels using velocity data obtained by antennas separated by relatively small distances. The kinematic model conserving mass and momentum is approximately consistent with in situ spacecraft measurements (Jackson *et al.*, 2003). For example, Figure 1.30 shows the enhanced electron densities from the Bastille Day coronal mass ejection.

1.9   Concluding Remarks

Because of the effects of the solar wind can have on the geomagnetic field, solar wind prediction is important. With the Potential Field Source Surface and Wang-Sheeley models, the predicted speed of the solar wind has an error of ± 15 % and the polarity of the interplanetary magnetic field is correct 75% of the time. This can be improved with MHD modeling that requires magnetic field measurements of the corona. In active regions, the photospheric magnetic field can be measured from multiple methods including Zeeman splitting, the Hanle effect, and radio burst frequency spectra. The quiet corona can only be measured by Faraday rotation, the columnar integration of the electron density and the line of sight parallel magnetic field. Previous Faraday rotation experiments include Pioneer 6, 9, and Helios 1 and 2 which found that Faraday rotation is most sensitive to the magnetic structure of the corona and that transient structures would cross through the line of sight over the period of hours.

We now know much more about the solar disturbances and can use this knowledge to reinterpret the 'W' and sigmoidal transient measurements in terms of a flux rope model as we do in Chapter 5. The Cassini Faraday rotation experiment builds on these previous experiments and addresses the issues that will be faced by future spacecraft, carrier-signal, Faraday-rotation experiments. The measurement system for Cassini, the method for data processing, and the results from the Cassini Faraday rotation model fitting and analysis will be discussed in the following chapters.

CHAPTER 2

Hardware

The Faraday rotation measurements that form much of the basis for this dissertation used the radio frequency signal from the Cassini spacecraft, transmitting through the corona to antenna receivers on the Earth for measurement. Details of this communication system that affect our measurements include the design of the Cassini radio system and antenna, the Earth receiving antenna, receiver package design, and the signal acquisition and digitization methods.

As discussed in the previous chapter, quarter-wave plate technology was used to measure the plane of polarization of the signal from Pioneer 6, Pioneer 9, Helios 1 and Helios 2 Faraday rotation experiments. The Cassini Faraday rotation data was collected using Digital Signal Processor (DSP) technology with In-phase Quadrature (IQ) demodulation capability. The use of this new technology required the development of new data processing techniques to obtain plane of polarization data from the signal. With the exception of improvements in signal amplification technology, the receiver package design used to filter, polarize, and convert the incoming signal is the same as in previous experiments.

2.1 Cassini

2.1.1 The Cassini Spacecraft

The Cassini Saturn orbiter mission was launched on October 15, 1997 and inserted into orbit in July 2004. During the solar conjunctions in 2002 and 2003 as Cassini flew out to Saturn, Faraday rotation data were collected.

Cassini is a 3-axis stabilized spacecraft carrying a high gain antenna, 3 radioactive thermal generators, and 12 instruments (excluding the Huygens probe). Spacecraft pointing was controlled by the Attitude and Articulation Control Subsystem through its sensors (Sun Sensor Assembly, Stellar Reference Unit, Z-axis accelerometer, and 3-axis gyro) (Russell, 2005).

In 2002, the spacecraft used its reaction wheels for stable pointing; however, this was not the case in 2003 when the pointing was being maintained by thrusters (Media Relations Office, 2003).

The High Gain Antenna was capable of transmitting S (2.3 GHz), X (8.4 GHz), Ka (32 GHz), and Ku (13.78 GHz) bands. X-band and Ka-band data were collected in 2002 and 2003, but S-band data were not collected until after the Huygens probe was deployed in 2004.

2.1.2 The Cassini Antenna System

The radio science subsystem (RSS) was designed to measure the rings, atmospheres, and ionosphere(s) during occultations, and gravity fields on flybys using their effects on the radio signal being emitted from the High Gain Antenna (Russell, 2005).
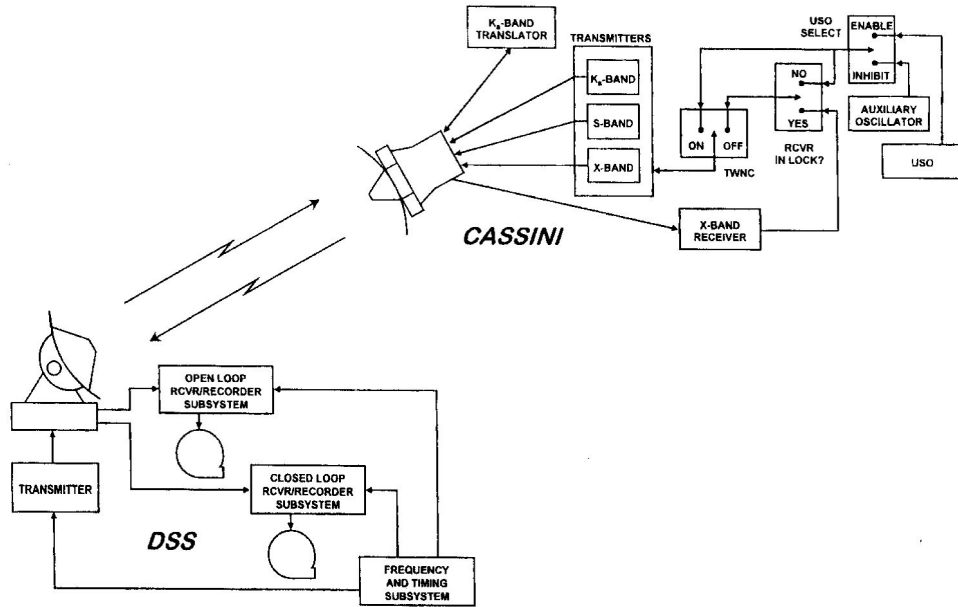
Figure 2.1: *Schematic illustration of the ground antenna system and the Cassini antenna system with its 1-way (USO) and 2-way (X-band Receiver, Ka-band Translator) capabilities. When the system is 2-way, the Cassini receiver is locked and the USO is disabled. When the receiver loses lock, the USO is enabled (Russell, 2005).*

The RSS can be operated in one-way, two/three-way noncoherent, or two/three-way cooherent with the uplink phase modes. In one-way and two/three-way noncoherent modes, the signal is generated from the on-board ultra-stable oscillator, mixed with the appropriate frequency for transmitting S, X, or Ka-bands. In two/three way coherent modes, the received signal is used to generate the transmitted signal. As a result of this transmission mode, any scintillation effects on the uplink signal are multiplied by a ratio of 240/749 for X-up S-down, 880/749 for X-up X-down, 3344/749 for X-up Ka-down, and 294/315 (or 14/15) for Ka-up Ka-down.

The Cassini Deep Space Transmitter is capable of locking onto a signal as weak as -155.8 dBm. The X-band was amplified to 15.8W, the S-band to 13.5W, and the Ka-band to 7.2W (when operated in a single mode) or 5.7W (when operated in dual X-up Ka-down and Ka-up Ka-down modes). Because of its higher frequency, the Ka-band could be operated with less power while delivering a similar quality baud rate as the X-band. Additionally to further reduce the power required by the radio antenna, all transmitted frequencies were circularly polarized (right circular polarization) (Staelin, 2003). This, of course, is counter to the optimum (linear) polarization needed by Faraday rotation. Linear polarization consists of equal right and left handed power.

2.2 Earth Receiving System

The construction of an electromagnetic wave communication system is dedicated to improving the signal to noise ratio as much as possible through a variety of electrical engineering techniques. Electromagnetic noise is created by a variety of sources including inefficiencies in the transmitting system, scattering properties of the medium through which the wave travels, and inefficiencies in the receiving sys-
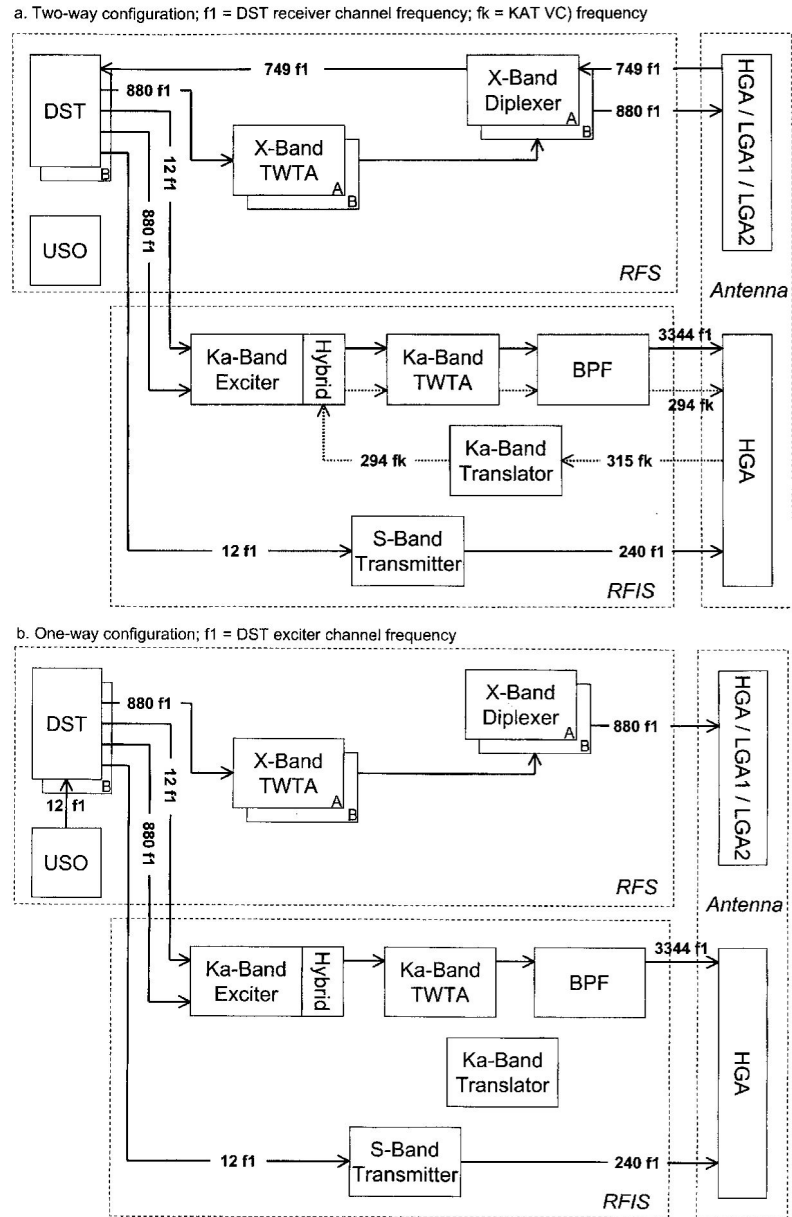
Figure 2.2: *Schematic block diagram of the Cassini antenna system. The 2- and 1-way configurations are shown in the top and bottom flow charts. The X-band system is in the upper box of each flow chart, while the Ka-band is in the bottom box. The low gain antennas (LGA) are only capable of receiving/transmitting X-band. The Ka-band system is capable of being phase-coherent with the X-band and Ka-band signals (Russell, 2005).*
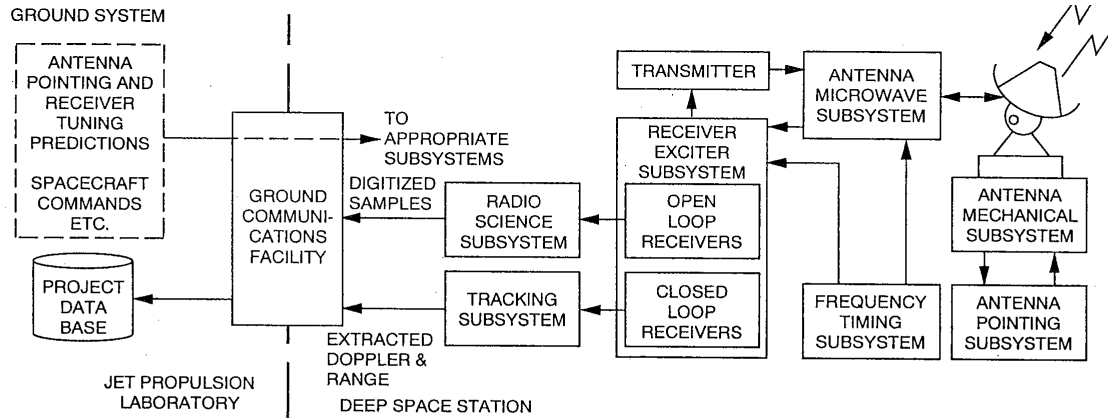
Figure 2.3: *Schematic block diagram of the different subsystems that make up the ground antenna system. The signal received from the spacecraft at the antenna is passed through the receiver subsystem to the radio science subsystem where it is measured (Kliore et al., 2004).*

tem. Engineering components that affect the signal include the antenna itself, conversion between an EM wave and a TE wave, conversion between circular and square wave, transmission through polarizers/mixers/isolators, amplification, and thermal noise throughout (Staelin, 2003).

The following sections describe the system in use for Cassini with particular emphasis on the Radio Science Subsystem used in the Faraday rotation experiment. Figure 2.3 illustrates the ground system supporting the signal measurement.

2.2.1 Antennas

The Deep Space Network is comprised of three deep space communications complexes located at approximately equilongitude separations around the Earth in California, Spain and Australia. All Faraday rotation data were collected at the Goldstone, California complex at approximately 116 degrees W longitude and 35 degrees N latitude. Each antenna is designated as a Deep Space Station (DSS) with a num-

ber. From Spain, the uplink signals were transmitted only in the X-band from DSS 54 and 63. DSS 25 was the only antenna capable of transmitting Ka-band. From Goldstone, the uplink signals were transmitted from stations DSS 25, 26 and 15. All the Faraday rotation data were collected from signals received at DSS 13. The antennas used were either Beam Wave Guide (BWG) or High Efficiency (HEF) types which are both altitude-azimuth antennas rotating on two axis to achieve full sky measuring capability.

A diagram of the Beam Wave Guide antenna is shown in Figure 2.4. The signal passes into the dish of the antenna and is focused onto the subreflector; the difference between BWG and HEF antennas is that the primary dish and the subreflector are modified to allow more uniform illumination between the two in an HEF antenna. The subreflector passes the signal into the base of the antenna where it is reflected by a mirror positioned to focus the signal toward the radio receivers. In the case of dual frequency measurements, the radio receivers have a dichroic plate positioned over the longer wavelength, and a mirror over the shorter wavelength receivers. The dichroic plate consists of a metal plate with hexagonal grids larger than the shorter wavelength but smaller than the longer wavelength. Gravitational deformation of the antenna can be as great as 7cm, and therefore affects the 1 and 4cm signals from Cassini (Russell, 2005).

Network Operations Control Center (NOCC) Monitor and Control Subsystem transmits predictions for antenna pointing, tracking, and receiving. Pointing is computed by NOCC Support System from ephemerides provided by the Cassini Flight Project. The Antenna Pointing Assembly transforms the predicts to Azimuth-Elevation coordinates. The coordinates are interpolated between time intervals with polynomial coefficients provided by the predicts. The Antenna Control System (ACS) corrects the predicts for refraction and subreflector position. The ACS sends position com-

Shaped-Surface
Subreflector

Quadropod

34-meter Shaped
Surface Reflector

Beam Waveguide

Azimuth Track

Pedestal Room

Dichroic Plate

Ka-Band   X-Band
Feedhorn Feedhorn

Beam Waveguide Structure
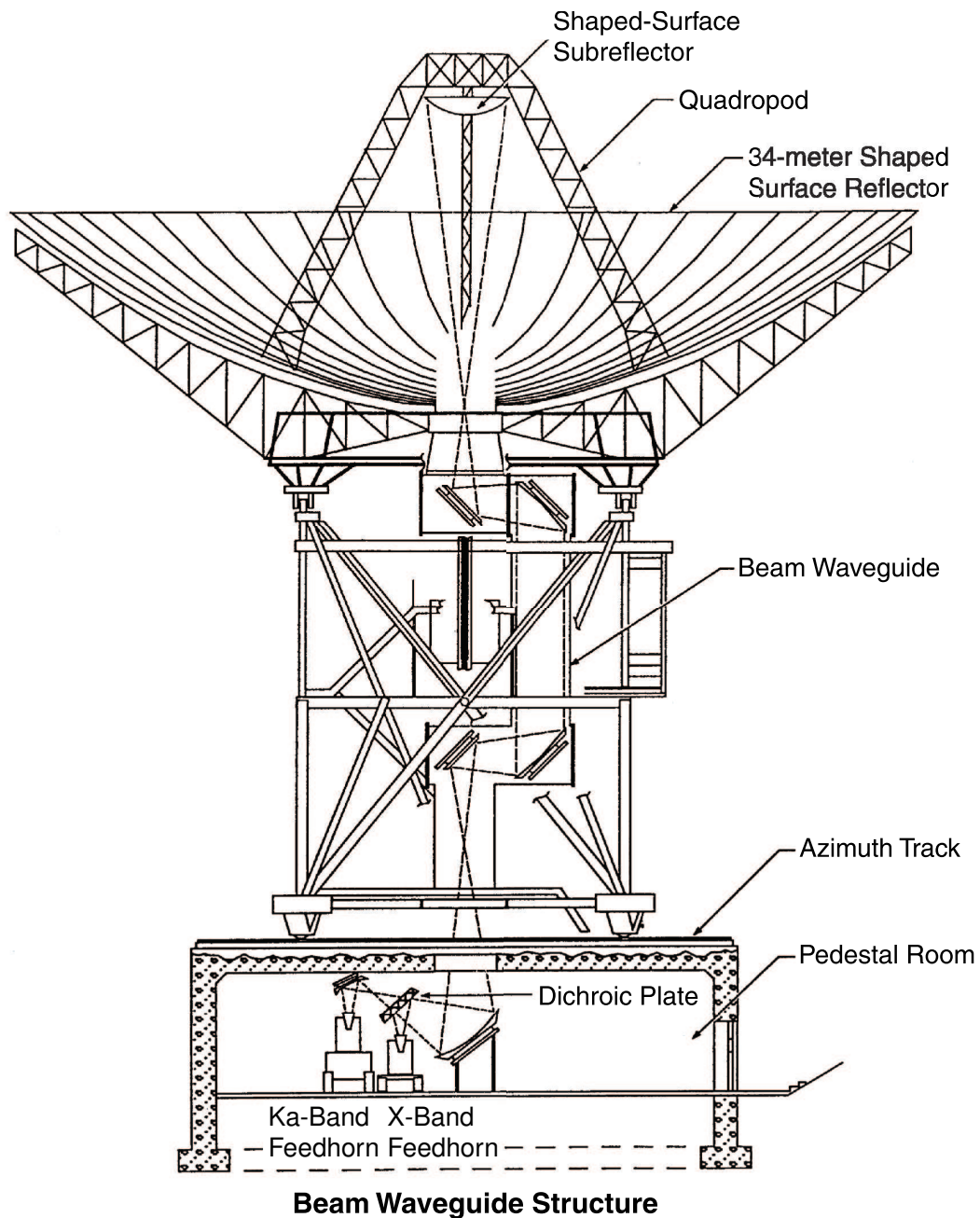
Figure 2.4: *Schematic of the internal structure of a beam wave guide (BWG) antenna showing the path of the signal. The BWG antenna focuses in the incoming signal and passes it internally to receivers in the base. Because the receivers are fixed while the antenna is allowed to track the source of the signal across the sky, an apparent rotation occurs in the polarization called the "parallactic effect" (Imbriale, 2003).*

mands every second.

DSS-13 Antenna

The Deep Space Station 13 (DSS 13) antenna is unique among the Deep Space Network allowing radio astronomy scientists to experiment with cutting edge technology. The antenna is a Beam Wave Guide with 5 positions in the pedestal room for radio receiver packages. A Radio Science Receiver (RSR) is located at DSS 13 allowing measurement of two narrowband signals. In 2002 and 2003, KARCP and KaLCP (Ka-band Right/Left Circularly Polarized signals) were measured by the DSS 13 RSR. The X-band signals were passed to the fiber optic lines connecting DSS 13 to Signal Processing Center 10 where the rest of the RSRs are located. In 2005, only the X-band was measured, and this was by the DSS 13 RSR.

2.3   Receivers

The radio receiver is designed to convert an incoming electromagnetic wave in free space to a TE wave, amplify the signal in the frequency band of interest, and downconvert the signal to a frequency that can be transmitted with little loss in coaxial cables for measurement by the post receiver system. The free space signal entering the radio receiver includes noise from the transmitter system, the intervening medium, and the receiving antenna. Additional sources of noise are introduced by the conversion of the EM wave to a TE wave by the feed horn, and by the separation of the polarizations in the polarizer. A dewar encloses the front end of the receiver and is kept at cyrogenic temperatures to reduce the addition of thermal noise from all the components to the signal. The back end of the receiver consists
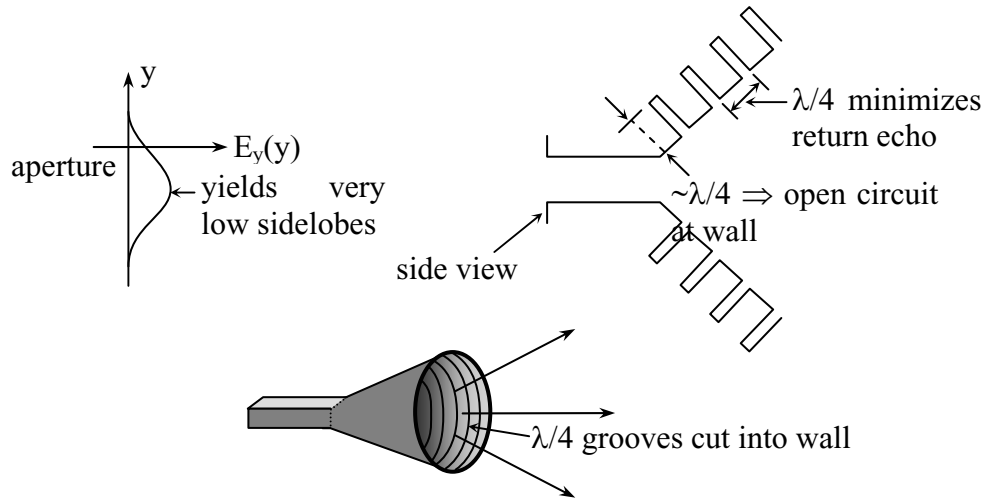
Figure 2.5: *Design elements of a feed horn. The bottom picture shows the external appearance of the feed horn. The top left plot shows the electric field inside the feed horn and how it varies across the diameter of the cone; it tapers to zero on the edges. The top right schematic shows the groves cut into the feed horn that make the electric field profile possible. Radially flowing currents and the energy returned to the throat of the horn are cancelled by the $\lambda/4$ deep slots and $\lambda/4$ slot separations respectively. Feed horns are designed to receive and transmit EM waves with the smallest possible sidebands in the conversion to or from the TE mode (Staelin, 2003).*

of the equipment necessary to downconvert the signal for sampling. Figure 2.5 illustrates the general shape of the feedhorn designed to minimize the EM interference in the conversion process.

The component of the receiver that splits the circular polarizations is called the diplexer or polarizer; the type of polarizer used for the Ka-band Cassini Faraday rotation measurements is an orthomode transducer which separates the two orthogonal polarizations using a septum polarizer. The X-band polarizer is a hybrid taper orthomode transducer.

The inefficiency of the polarizer with respect to splitting the two signals is described

by (Myers, 2004):

$$\vec{E'} = \overleftrightarrow{J}\, \vec{E} = \overleftrightarrow{G}\overleftrightarrow{D}\overleftrightarrow{P}\overleftrightarrow{T}\, \vec{E} \tag{2.1}$$

where $\overleftrightarrow{J}$ is the Jones matrix describing the polarization effects. This matrix is equal to the product of $\overleftrightarrow{G}$, the gain of the respective channels, $\overleftrightarrow{D}$, the leakage inefficiency of the polarizer, $\overleftrightarrow{P}$, the parallactic angle, and $\overleftrightarrow{T}$, the tropospheric effect (Ka-band only). Specifically

$$\overleftrightarrow{G} = \begin{bmatrix} g_R & 0 \\ 0 & g_L \end{bmatrix}$$

$$\overleftrightarrow{D} = \begin{bmatrix} 1 & d_L \\ d_R & 1 \end{bmatrix}$$

$$\overleftrightarrow{P} = \begin{bmatrix} e^{i\chi} & 0 \\ 0 & e^{-i\chi} \end{bmatrix}$$

$$\overleftrightarrow{T} = \begin{bmatrix} t & 0 \\ 0 & t \end{bmatrix} \qquad \text{Ka-band only}$$

$$\begin{bmatrix} E'_R \\ E'_L \end{bmatrix} = \begin{bmatrix} g_R(E_R e^{i\chi} + d_L E_L e^{-i\chi}) \\ g_L(E_L e^{-i\chi} + d_R E_R e^{i\chi}) \end{bmatrix} \tag{2.2}$$

where $E'_{L,R}$ is the measured electric field, $E_{L,R}$ is the electric field passing into the receiver, and χ is the source position of the polarized radiation. The Cassini Faraday rotation experiment uses the leakage inefficiency of the Cassini radio system to measure Faraday rotation. The Cassini spacecraft is transmitting Right Circular Polarization; however, it "leaks" Left Circular Polarization with a power of 20dB less than the RCP.

After splitting the signal into opposite polarizations, each channel is amplified by a High Electron Mobility Transistor (HEMT) amplifier. The HEMT is a Gallium-Arsenide-Metal Semiconductor Field Transistor capable of amplifying high frequencies. The amplifier increases the power of the target bandwidth or the gain.

$$G_I = \frac{P_{w/amp}}{P_{w/o}}$$

For calibration purposes a mixer precedes the amplifier to allow a gaussian noise source signal to pass into the signal channel. The ratio of the power of the noise with the amplifier turned on to the power when the amplifier is turned off allows the measurement of the gain. This is called the insertion gain.

For these measurements, we want the noise in the signal to be dominated by the plasma. The transducer noise is the result of the amplification of the system noise (Staelin, 2003). The noise resulting from the system is insignificant at -120 dB in comparison to the plasma noise around 70 dB.

$$N_T = kT_{sys}G$$

The stability of the receiver is measured by its power gain. When the noise source is turned on, a fixed temperature load (T_L) is placed over the feed horn. The power of the signal measured by the receiver is

$$P = k(T_L + T_{sys})GB$$

Where B is the bandwidth of the bandpassed signal and k is Boltzmann's constant. The bandwidth of the X- and Ka-band receivers is 1.3 and 2 GHz respectively.
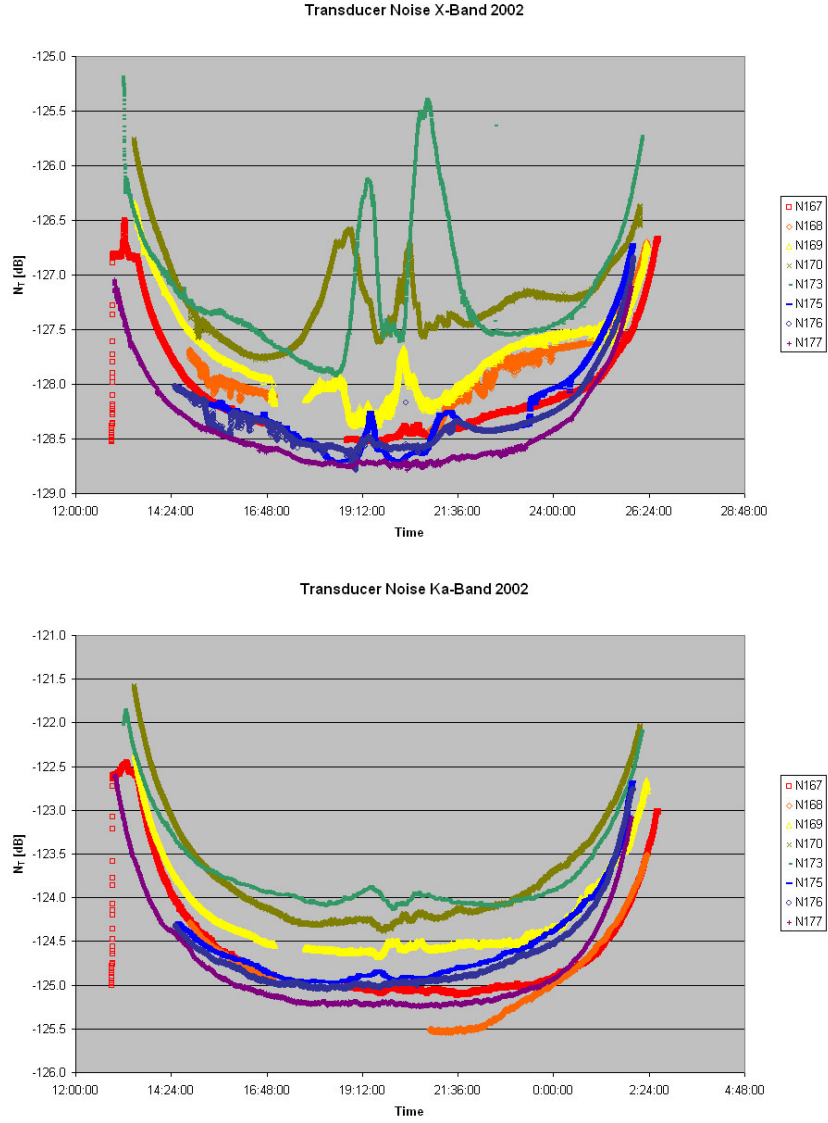
Figure 2.6: *The transducer noise in the X- and Ka-bands versus universal time during the period in which radio frequency measurements were made. The transducer noise is a measure of the system noise. As the scales on the plot indicate the noise is less in the X-band (left) than in the Ka-band (right). At both frequencies, the system noise is significantly less than the signal power. Each pass on which an observation was made has a unique color; day of year 167 corresponds to June 16.*

X-band Receiver

The X-band receiver is shown below in Figures 2.7 and 2.8. The signal enters from the top of the receiver and passes through the circular waveguide in the center to the box shown. One of the HEMT amplifiers is shown (Berkshire Technologies piece) in Figure 2.7. Figure 2.8 shows the LCP and RCP HEMTs of the receiver; the polarizer is not clearly visible. The connecting strips of metal keep the attached parts at relatively the same cool temperature to reduce sources of thermal noise. The tubes connecting to the base of the receiver can be clearly observed to pass through the metal plate and connect to the HEMTs; these carry the polarized and amplified X-band waves out of the dewar to the back end.

Ka-Band Receiver

The difference between the Ka-band and X-band receivers is shown in Figure 2.9. The signal is amplified again and mixed with a local oscillator to downconvert to X-band in the back end of the receiver. The components listed in Figure 2.9 are shown in Figures 2.10 and 2.11.

2.3.1   Downconversion System

Figure 2.9 shows an example of the system in place for the signal downconversion and acquisition. At X-band frequencies, the signal requires waveguides for transmission. Upon entering the downconversion system, the signal is mixed with a Local Oscillator to further reduce the frequency to the 300 MHz Intermediate Frequency (IF). The IF signal can then be transmitted with little noise loss through coaxial
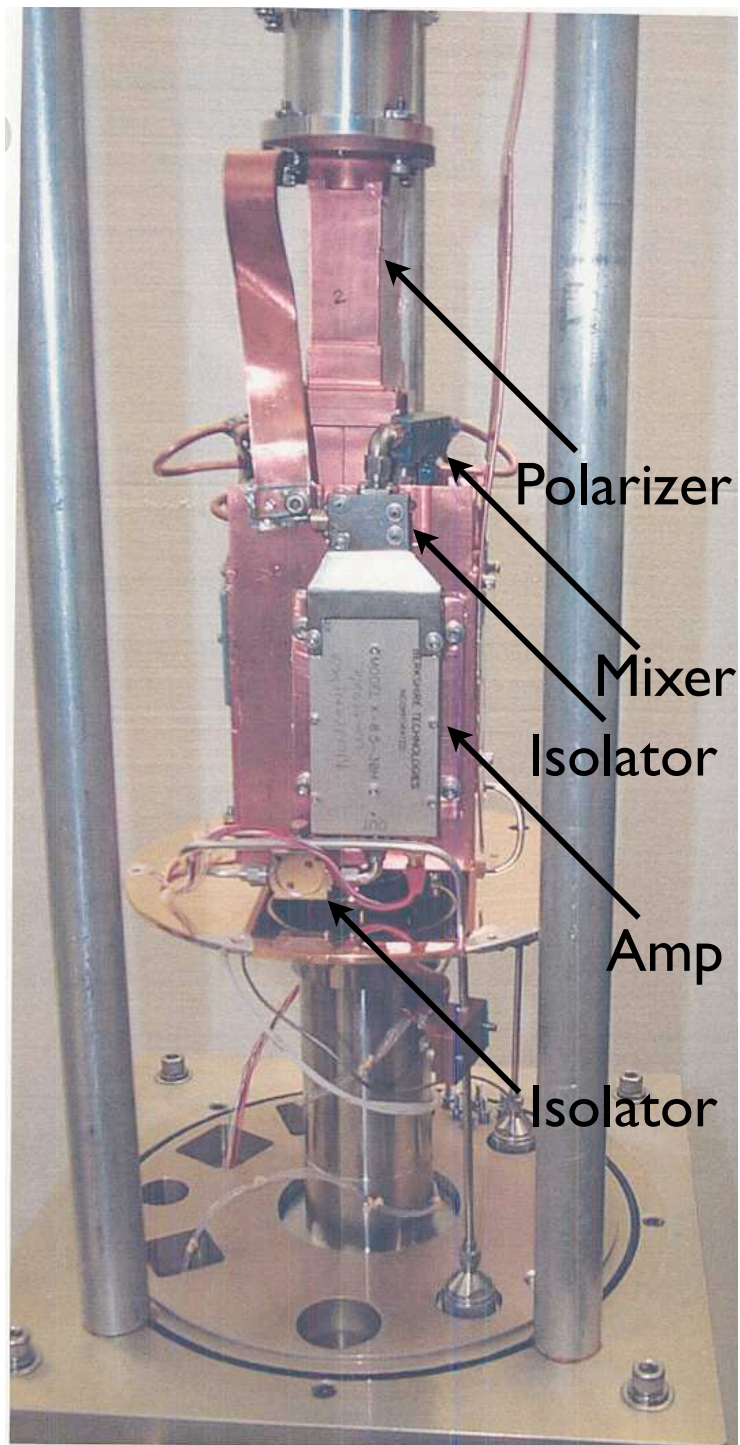
Figure 2.7: *The X-band receiver (front view).*
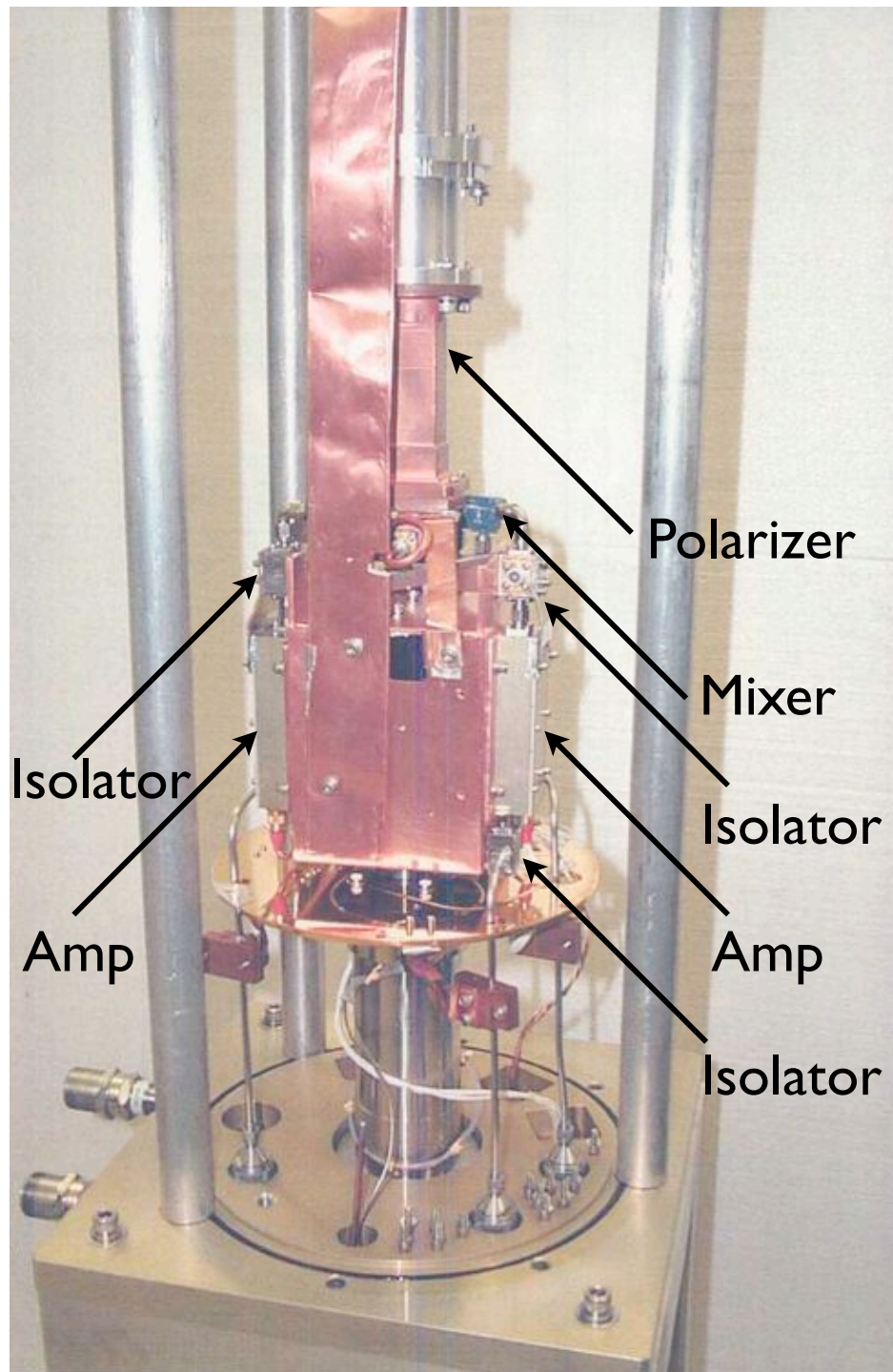
Figure 2.8: *The X-band receiver (side view).*

Figure 2.9: *Schematic block diagram of the X- and Ka-band receivers. Outside of the Ka-band dewar, the signal is downconverted to the X-band before passing to the local oscillator.*
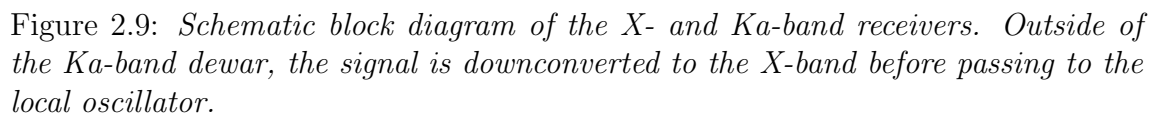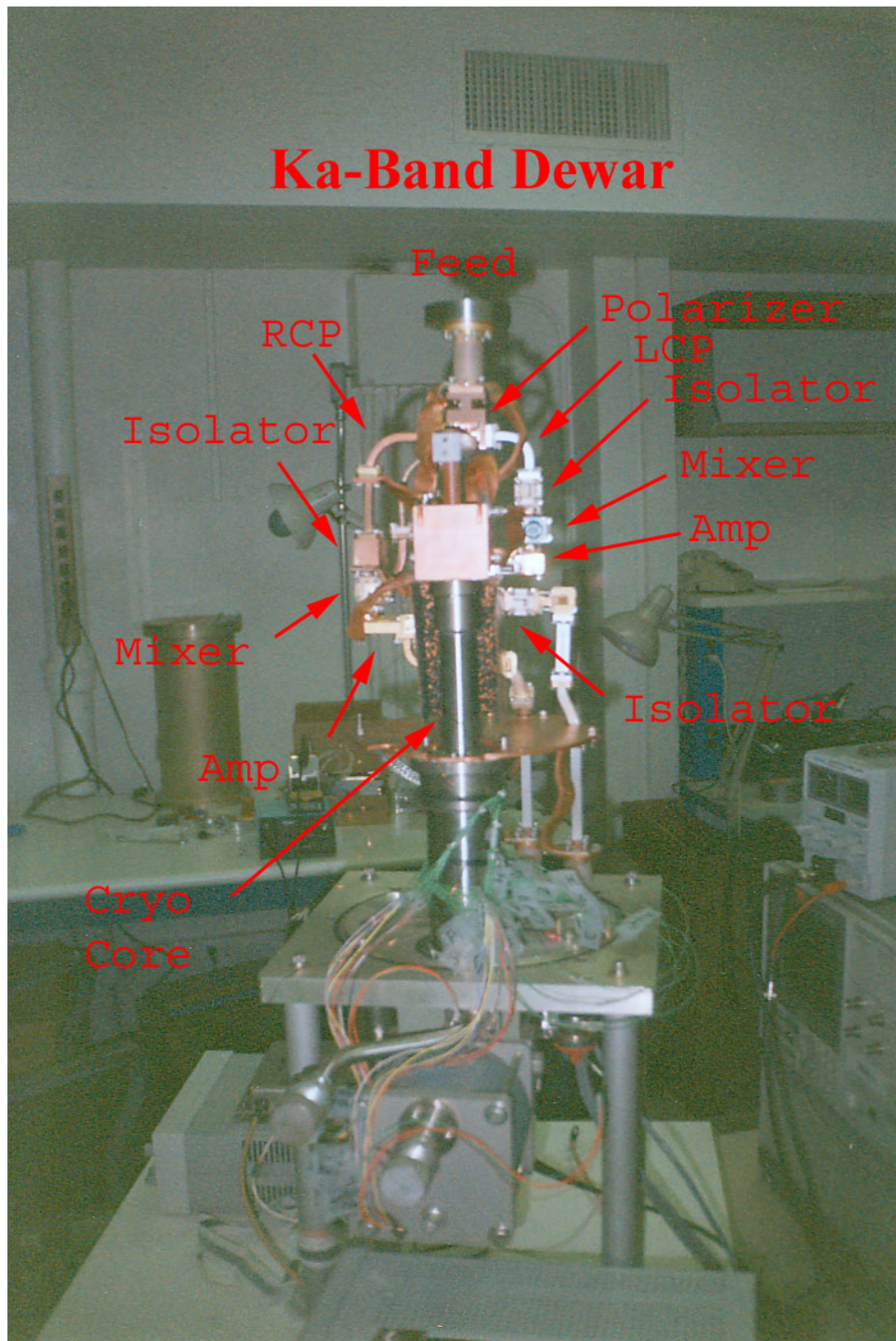
Figure 2.10: *The Ka-band receiver (rear view) with labeled component parts.*
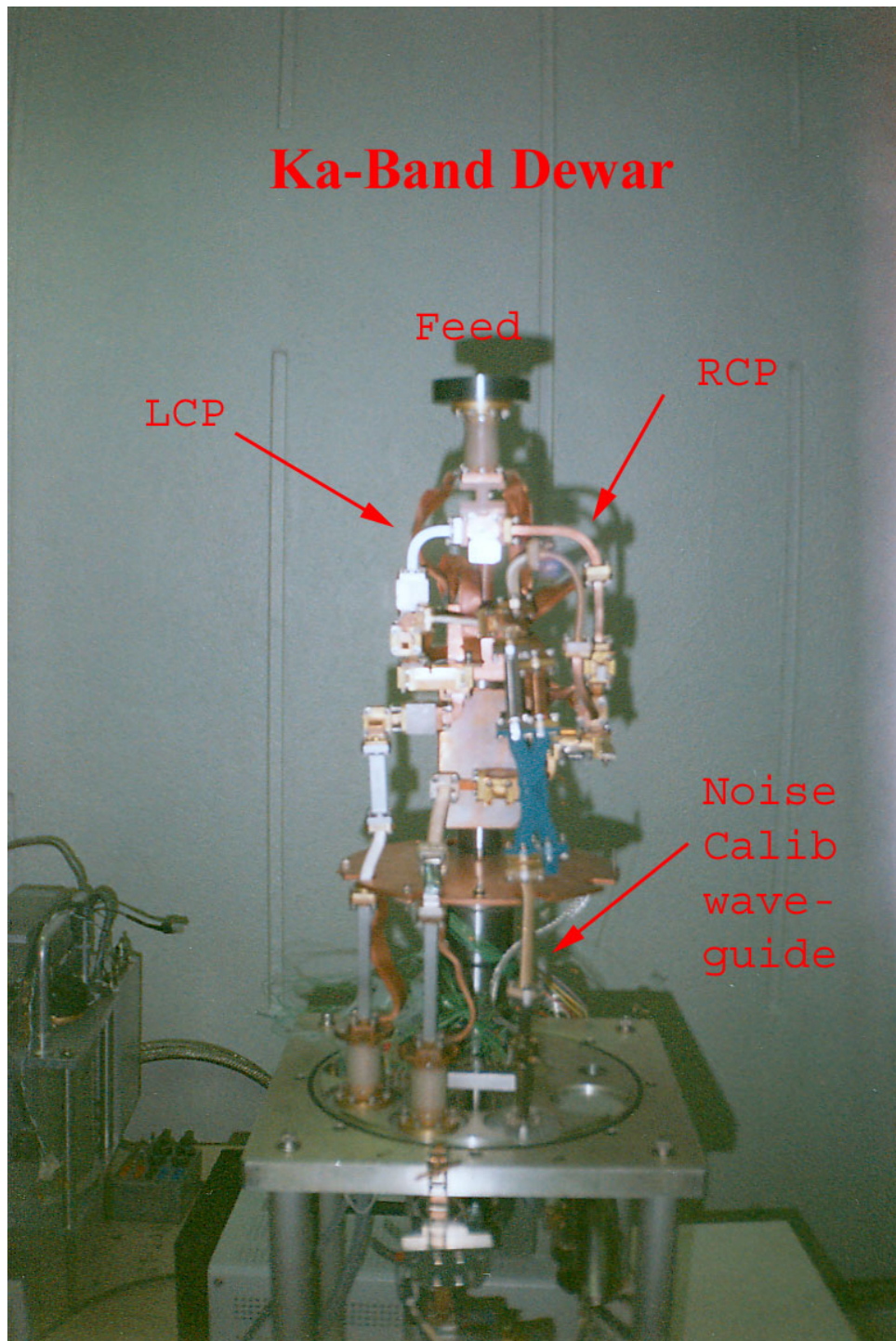
Figure 2.11: *The Ka-band receiver (front view) with labeled component parts.*

cables to the appropriate switches for passing to the Radio Science Receivers.

2.3.2 Radio Science Receivers

Figure 2.12 shows the process that is performed on the incoming signal inside the RSR. In the digitizer (DIG) portion of the RSR, the analog IF signal is bandpass filtered to the range from 256 to 384 MHz, downconverted from 320 to 64 MHz and digitized at 256MHz into a complex (real plus imaginary) data stream. The samples are then passed to the digital downconverter (DDC) which uses modeled frequency predictions to downconvert the data frequency inside a 1kHz bandwidth around the modeled frequency. These are the raw data samples used for the plane of polarization measurements. (Tinto & Sniffin, 2000)

Figure 2.13 shows how the complex data stream is generated ideally. The mixing wave on either side of the split are 90 degrees out of phase with each other. This allows the measurement of the in-phase (I) and quadrature-phase (Q) of the signals, or equivalently the real and imaginary components of the incoming wave. The model predicted frequencies were chosen to reduce the signal frequency down to a few Hz. Usually, this was in the range of 1-5Hz; however sometimes the signal frequency was larger, usually when Madrid was transmitting or the signal was one-way (Kirkhorn, 1999).

The reconstruction of the original wave is different for the RCP versus the LCP I and Q samples. In the case of the RCP wave, $x(t) = I + i * Q$. Because the Q samples are asymmetric with respect to polarization, $sin(-\theta) = -sin(\theta)$, the LCP wave is reconstructed as $x(t) = I - i * Q$. An example of the RCP and LCP waves is shown in figure 2.14.

ANALOG IF

0   100   200   300   400   500

256   320   384

DIGITIZED BAND

128-MHz (nominal), samples at 256 Ms/s, 8-bit samples

Variable, 1-MHz steps

0   128

BASEBAND CHANNEL

16-MHz (nominal) samples at 16 Ms/s, I & Q, 8-bit samples

−8   0   +8

Variable, < 1-Hz steps
with Doppler Compensation

0

SUBCHANNELS (Up to 4)

Variable width, 1 kHz – 16 MHz
Variable Samples, I & Q, 1-bit – 16-bit
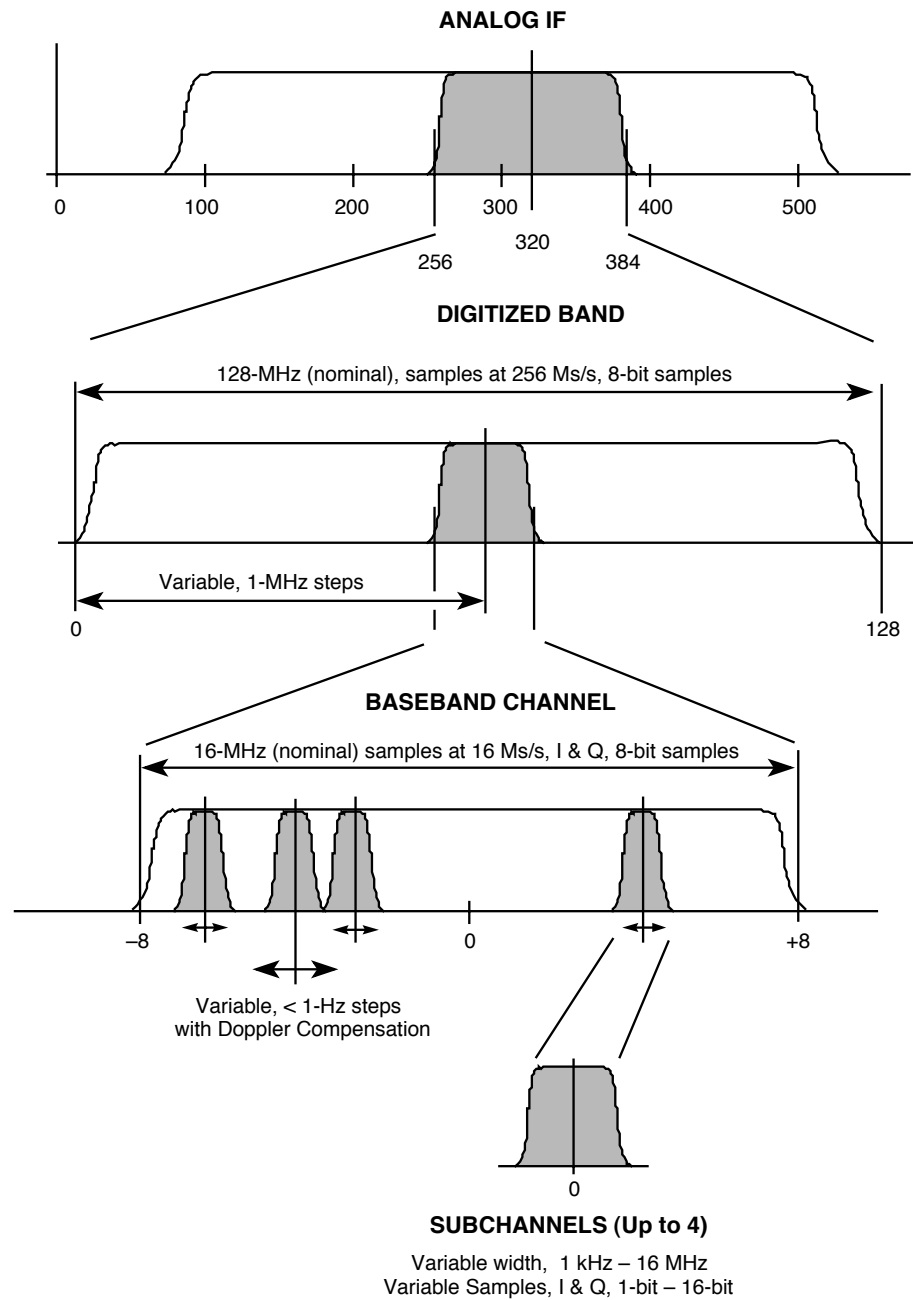
Figure 2.12: *The radio passband filters used as the signal is digitized from the intermediate frequency (IF) and filtered using the frequency predictions into subchannels (Tinto & Sniffin, 2000).*
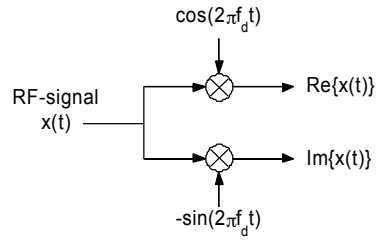
Figure 2.13: *The schematic of the splitting of a radio frequency (RF) signal into two channels and its mixing with sine and cosine waves to separate the real and imaginary components to the wave (Kirkhorn, 1999).*
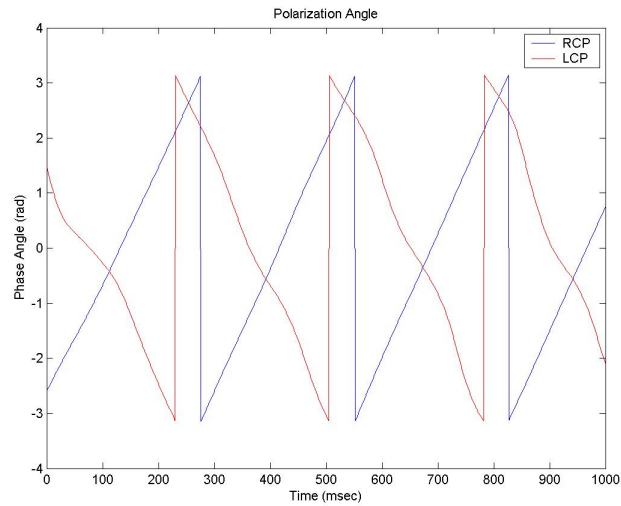
Figure 2.14: *The phases of the right and left circularly polarized (RCP and LCP) waves calculated from the real and imaginary data samples are shown; the RCP wave advances in the positive angular direction while the LCP wave advances in the opposite direction.*

2.4 Closing Remarks

The method of radio frequency data acquisition and its effects on the measurement requires comprehension for the next step of data processing. The signal transmitted from the Cassini antenna system traverses the solar corona and is received by the ground system in Goldstone, California. The crucial component of the ground system for polarization effects is the antenna microwave subsystem; these effects and their correction will be discussed in detail in the next chapter.

CHAPTER 3

Signal Processing

The raw plane of polarization measurements described in Chapter 2 contain both Faraday rotation effects from propagation through a magnetized plasma and the effects introduced by the receiving equipment. These latter effects need to be corrected in order to begin to interpret the geophysical causes of the Faraday rotation. These effects include the parallactic angle and polarizer leakage which will be defined below. This chapter details how the Faraday rotation observations are reduced by discussing each of the steps in the data processing procedure. These steps and their corresponding sections are given in Table 3.1.

Table 3.1: *Steps in the data reduction procedure.*

Method for obtaining the plane of polarization measurements from low signal to noise ratio radio frequency data (Section 3.1.3)
Construction of the Jones matrix for polarization effects on the plane of polarization due to the antenna (Section 3.2.2)
Calibration of the plane of polarization measurements for leakage in the polarizer using the Parallactic Effect (Section 3.2.5)
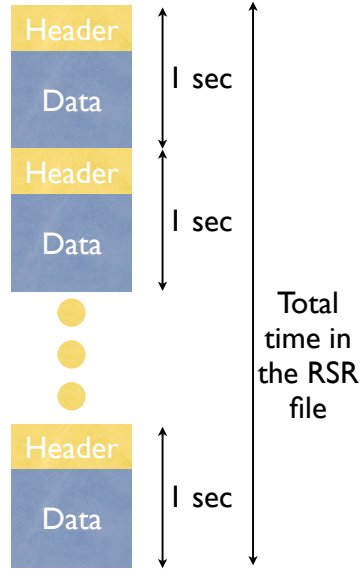
Figure 3.1: *The structure of the Radio Science Receiver file format. A header precedes each second of radio data in the file.*

3.1 Obtaining Plane of Polarization Measurements

3.1.1 Radio Science Receiver Files

The Radio Science Receiver (RSR) file is a binary formatted file with a new header for every second of data shown in Figure 3.1. For example, if the sample rate is 1000 samples per second, there is a header leading every 1000 samples in the single file of several hours of data. Appendix F includes the Matlab codes used to process these files, and how to interpret a sample header.

Each RSR file was aligned in time with the RSR files from the other polarizations and frequencies, then separated into header and data files. The standard header consists of 71 descriptions of the dataset including frequency predictions and downconversion calculations allowing the user to reconstruct the original sky frequency from the

Table 3.2: *List of times (UT) Faraday rotation observations were collected.*

	2002		2003	
	Start Pass	End Pass	Start Pass	End Pass
	June 16 16:22:45	June 17 02:34:23	June 26 13:38:03	June 26 00:57:36
	June 17 19:08:50	June 17 23:33:46	June 27 14:03:03	June 27 18:19:51
	June 18 16:11:44	June 19 02:18:42	June 28 13:50:50	June 29 01:33:07
	June 19 14:28:35	June 20 01:41:30	June 29 13:45:50	June 30 01:52:38
	June 20 13:36:50	June 21 01:29:50	June 30 13:45:50	July 1 01:04:20
	June 21 13:50:13	June 22 02:02:45	July 1 03:22:00	July 2 01:58:57
	June 22 13:30:03	June 23 02:03:49	July 2 13:35:50	July 3 01:57:45
	June 23 13:33:31	June 24 01:58:10	July 3 13:35:50	July 4 01:56:07
	June 24 13:18:34	June 25 01:23:15	July 4 13:22:50	July 5 00:57:49
	June 25 13:20:20	June 26 00:45:09	July 5 13:17:30	July 6 01:37:49
	June 26 13:17:25	June 26 23:57:56	July 6 13:25:50	July 7 01:38:47
			July 7 13:45:50	July 8 01:33:51

data. This was not done in the data processing because the change in the plane of polarization is independent of the downconversion process.

Two operations were performed on the data. First of all, the data were bandpass filtered; the left hand side of Figure 3.2 shows the raw samples. Through iterative tests of sensitivity and consistency, the best bandpass filter range was $\pm 0.5 \times 10^{-3}$ Hz around the frequency of the signal; the right hand side of Figure 3.2 shows the filtered samples. The second operation was the determination of the plane of polarization through cross-correlation which will be discussed in Section 3.1.3.

3.1.2   The Fourier Transform Tool

The Fourier transform calculates the Fourier coefficients for the trigonometric terms of a Fourier series representing the periodic function of the radio frequency carrier. Note that the following material is adapted from Tolstov (Tolstov, 1962).
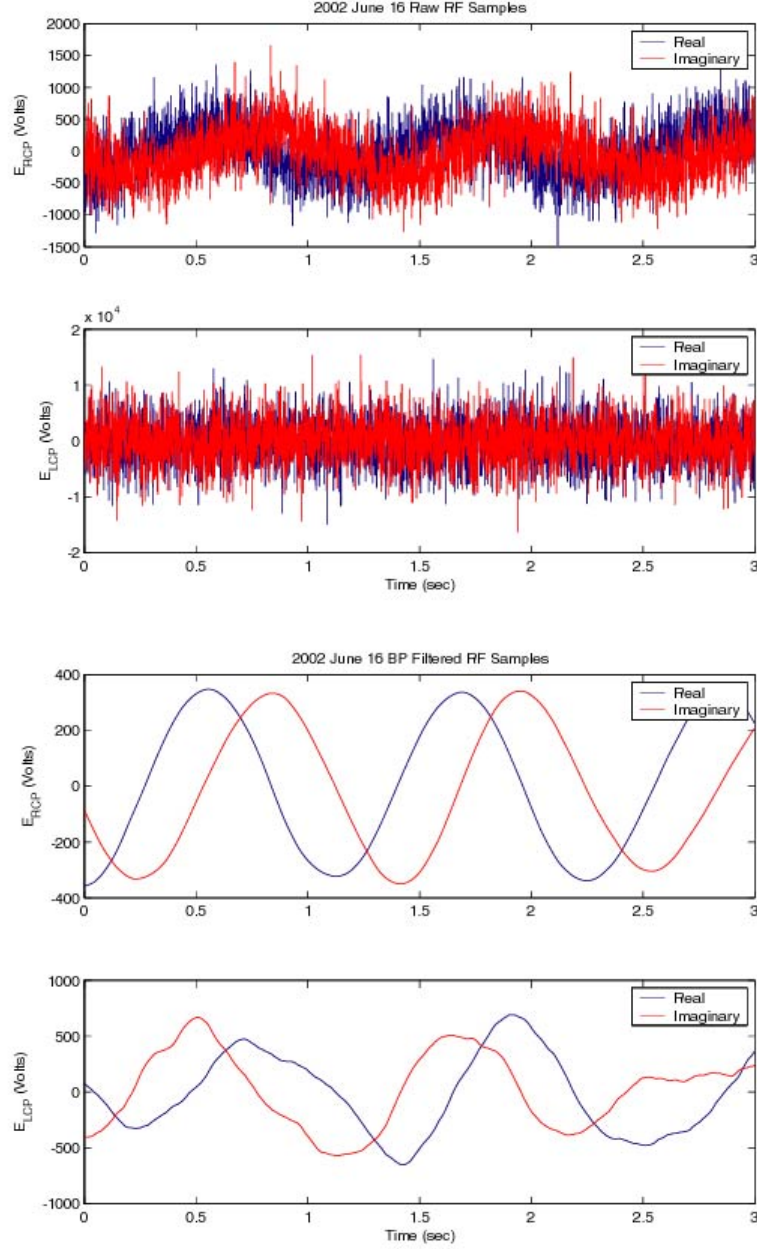
Figure 3.2: *The raw radio frequency samples from Cassini's X-band carrier in the RCP and LCP polarizations on the top two plots and the bandpass filtered values of the samples on the bottom two plots. The different amplitudes are a result of the different amplifier gains on the polarizations.*

If the monochromatic function f(t) is given by

$$f(t) = A\sin(\omega t + \phi)$$

then using the identity $\sin(m+n) = cos(m)sin(n) + sin(m)cos(n)$, it becomes

$$f(t) = a\cos(\omega t) + b\sin(\omega t)$$

where $a = A\sin\phi$ and $b = A\cos\phi$. Note that this allows the calculation of the phase of the wave from

$$\tan\phi = \frac{a}{b} \tag{3.1}$$

Similarly, a general function f(t) consisting of waves of many frequencies can be represented can be represented by the sum

$$f(t) = \frac{a_0}{2} + \sum_{\omega=1}^{\infty}(a_\omega\cos(\omega t) + b_\omega\sin(\omega t))$$

The coefficients a_ω and b_ω can be solved by integration over the phase step 2π, because of the following trigonometric formulas

$$\int_{-\pi}^{\pi} \cos(nt)dt = 0 \quad \Bigg| \quad \int_{-\pi}^{\pi} \cos^2(nt)dt = \pi$$

$$\int_{-\pi}^{\pi} \sin(nt)dt = 0 \quad \Bigg| \quad \int_{-\pi}^{\pi} \sin^2(nt)dt = \pi$$

$$\int_{-\pi}^{\pi} \cos(mt)\cos(nt)dt = 0$$

$$\int_{-\pi}^{\pi} \sin(mt)\sin(nt)dt = 0 \qquad (3.2)$$

$$\int_{-\pi}^{\pi} \sin(mt)\cos(nt)dt = 0$$

So

$$\int_{-\pi}^{\pi} f(t)dt = \frac{a_0}{2} \int_{-\pi}^{\pi} dt + 0 = \pi a_0$$

Note that with this particular form of Fourier series, the integral and the sum do not need to be performed in a particular order. And similarly for the other coefficients, the equation can be more generally expressed as

$$\pi a_\omega = \int_{-\pi}^{\pi} f(t)\cos(\omega t)dt$$

$$\pi b_\omega = \int_{-\pi}^{\pi} f(t)\sin(\omega t)dt \qquad (3.3)$$

The wave period producing the greatest correlation with the radio frequency (RF) carrier time series has the greatest amplitude and produces a peak in the frequency spectrum (ω on the abscissa and its corresponding coefficient $a_\omega^2 + b_\omega^2$ on the ordinate) as in Figure 3.3. The noise in the frequency spectrum is generally flat or downward sloping with increasing frequency and is caused by a variety of effects including small angle diffraction from changes in velocity and electron density and the thermal radiation of the individual antenna components. Except for 2003 July 1, the Fourier
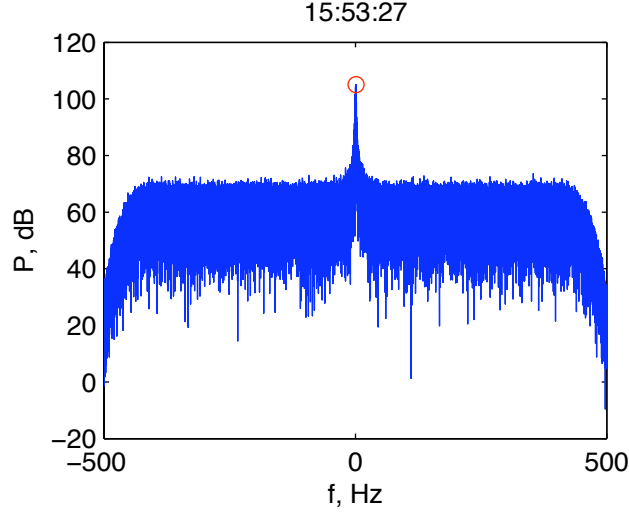
Figure 3.3: *The Fourier series amplitudes of the X-band RCP signal for a 100 second time period (100K points); the signal frequency is circled in red. Note that the plot is of the frequency residuals after the downconversion process.*

transform is used to find the frequency of the signal from the right hand circularly polarized (RCP) component of the RF carrier. One important assumption made when using the frequency result from a Fourier transform is that the apparent RCP and LCP frequencies are the same in magnitude. This is equivalent to the change in phase of the LCP and the RCP due to Faraday rotation being small. Checking this assumption with our forward model indicates that it is valid. Using the phase results from the Fourier transform (Equation 3.1), the plane of polarization (P) can be calculated with Equation 3.4. The result for 2002 June 16 is shown in the top panel of Figure 3.6; however, the calculations of P from the Fourier transform became too noisy when the impact parameter of the line of sight was less than 20 solar radii. Therefore, the technique described below was developed.

$$P = \frac{\phi_{RCP} + \phi_{LCP}}{2} \tag{3.4}$$

3.1.3 Standard Data Processing Method

As discussed earlier in Section 1.8.5, the phase calculations from the Fourier transform become significantly worse the greater the scintillation becomes. As a result, new techniques were developed to obtain the plane of polarization. It was found that calculating a plane of polarization angle every 100 seconds using the method described below delivered the best results for the following reasons:

a) Faraday rotation should not be rotating faster than 90 degrees every 100 seconds at any point in the passes.

b) The calculations of the plane of polarization significantly increase computation time for finer time resolutions.

c) The calculations of the plane of polarization significantly increase computation time for larger time steps; each 100 second time period has 100,000 samples.

The top panel of Figure 3.4 shows the LCP and RCP waves as calculated from the I&Q samples; the angles vary from -180 to 180 degrees and therefore have the appearance of a saw tooth wave. Remembering the assumption that the LCP and RCP frequencies have the same magnitude, then the slope (frequency) of the "saw" should be similar in magnitude and opposite in direction. As shown in the top panel of Figure 3.4, there are two phase angles through which the RCP and LCP waves intersect; one is between 0 and 100 while the other is between -180 and -100. This is the $\pm\pi$ ambiguity. Applying Equation 3.4 to the curves plotted will usually give the positive plane of polarization; however, for a fraction of the time (ie between 1 and 1.5 seconds), the negative polarization will result. In order to fix on a particular plane of polarization, the slope of the saw teeth of both waves was set to a positive slope. The results of this method are shown in Figure 3.4. After reversing the sign of the angle of the sine components of the LCP samples, the waves were compared by cross correlation. As shown in the bottom panel of

Figure 3.4, the RCP wave precedes the LCP in time; if we look at the roll-over from positive to negative 180 degrees on the RCP curve, the LCP wave is in the vicinity of 100 degrees. The phase difference is approximately 80 degrees, which is confirmed in Figure 3.5 showing the cross-correlation. The method for converting the time lag in the cross correlation analysis to phase difference is as follows. Over a single sawtooth period, the functions for the RCP and LCP phases can be represented by a linear function.

$$\phi_{rcp} - \phi_{lcp} = \left(\frac{\partial \phi}{\partial t} t + \phi_{rcp_i ntercept} \right) - \left(\frac{\partial \phi}{\partial t} t + \phi_{lcp_i ntercept} \right) = \phi_{rcp_i ntercept} - \phi_{lcp_i ntercept}$$

Note that the slope of the phase curve is the carrier frequency $f = \frac{\partial \phi}{\partial t}$. If we want to calculate the time difference between two equal phases, then:

$$ft(\phi_{rcp} = \pi) + \phi_{rcp_i ntercept} = ft(\phi_{lcp} = \pi) + \phi_{lcp_i ntercept}$$

And finally we can solve for $\phi_{rcp} - \phi_{lcp}$

$$\phi_{rcp} - \phi_{lcp} = \phi_{rcp_i ntercept} - \phi_{lcp_i ntercept} = f \left(t(\phi_{lcp} = \pi) - t(\phi_{rcp} = \pi) \right)$$

The cross correlation gives the LCP time lag behind the RCP phase curves, specifically $(t(\phi_{lcp} = \pi) - t(\phi_{rcp} = \pi))$. Finally, the phase difference is divided by two to give the plane of polarization; in this case, approximately 40 degrees. Figure 3.6 shows the plane of polarization as determined from Fourier analysis and this method.
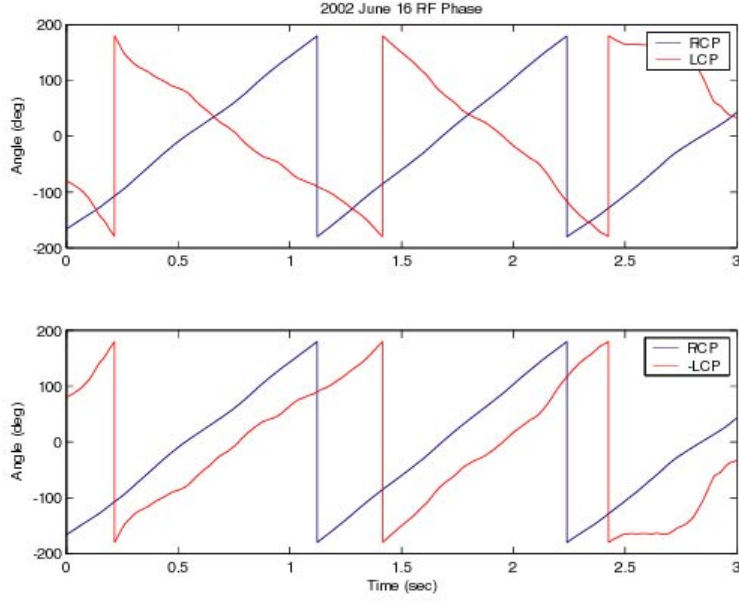
Figure 3.4: *The phase angles from the bandpass filtered samples shown in Figure 3.2 in the top plot. The bottom plot shows the same values with the LCP angles effectively multiplied by -1.*

$$P = \frac{\phi_{rcp} + \phi_{lcp}}{2} = \frac{\phi_{rcp} - (-1)\phi_{lcp}}{2}$$

3.1.4   Before 1600UT 2003 July 1 Processing Method

On 2003 July 1, the one way signal from Cassini was observed in both the X- and Ka-bands; however, the signal would periodically lose power and increase in bandwidth. In the Ka-band the effect was diffuse; the power in the cross correlation determination of the plane of polarization would periodically strengthen and weaken with the thruster activity while the plane of polarization remained relatively constant as shown in Figure 3.8.
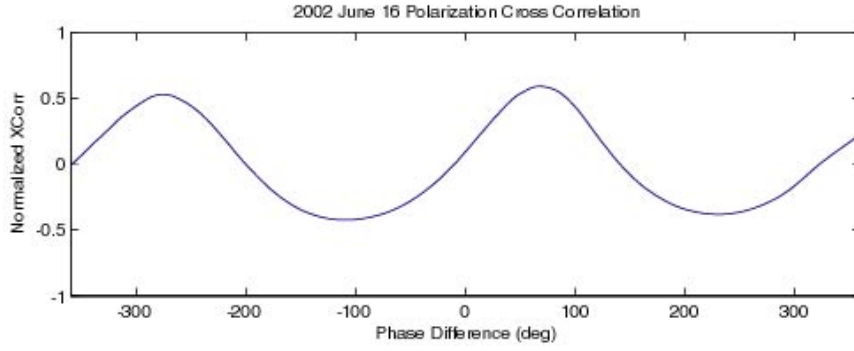
Figure 3.5: *The cross correlation of the LCP and RCP angles for a 100 second time period (including the portion plotted in Figure 3.4). Notice that the phase difference is approximately 80 degrees.*
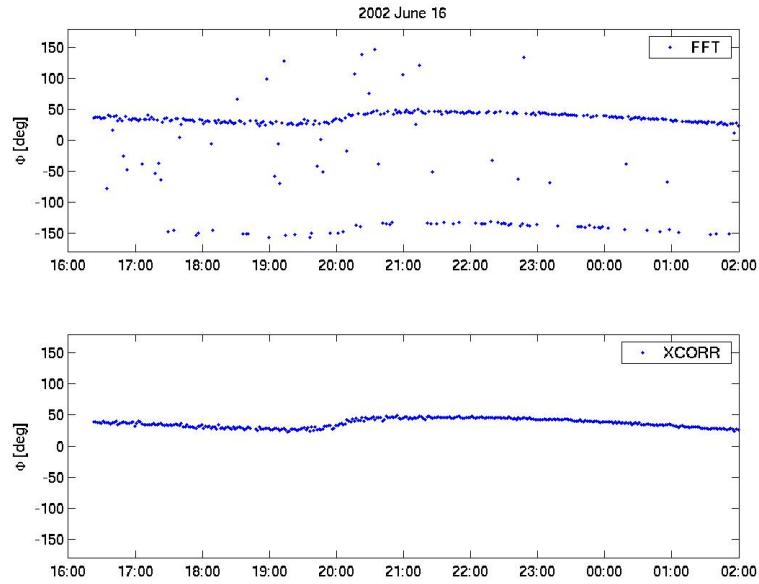
Figure 3.6: *The plane of polarization calculated using Equation 3.4 on the phase angles from the FFT calculation in the top plot. The bottom plot shows the plane of polarization calculated using the method described in section 3.1.3.*
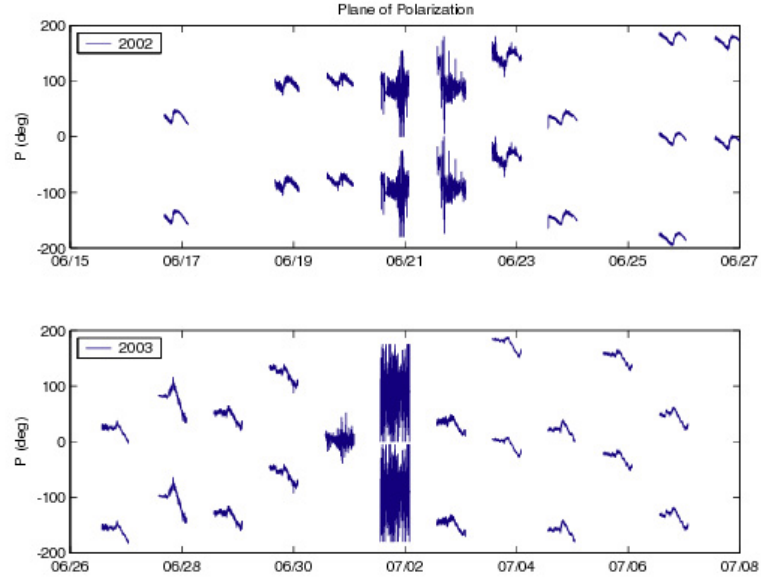
Figure 3.7: *The raw plane of polarization measurements in the X-band. The diurnal variability in the measurements are primarily due to the ground antenna.*

In the X-band, the noise on the signal was very large as shown in Figure 3.9. Determination of the frequency of the signal about which to filter was not consistent. To determine the plane of polarization of the X-band signal prior to 1800UT, the cross correlation method was adapted to determine which frequency resulted in curves which most resembled the one shown in Figure 3.5; specifically, the curve is bimodal, symmetric, and separated by 360 degrees peak to peak (or 180 degrees after the step of dividing by 2). Scanning through the frequencies produced the new plane of polarization calculation shown in the 1400UT to 1600UT portion of the bottom panel of Figure 3.8.
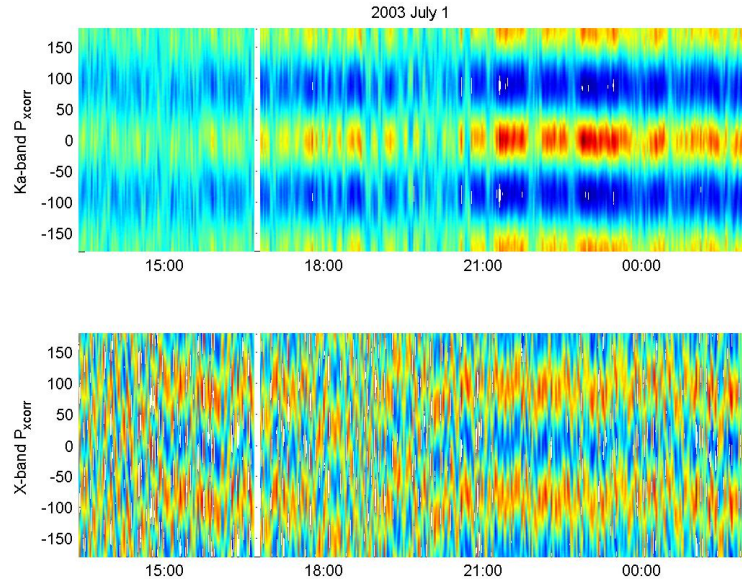
Figure 3.8: *The cross correlation curves for each 100 second time period with the colors indicating the correlation values for the phase difference. Note that the phase difference has been divided by 2 in comparison with Figure 3.5. The top panel shows the Ka-band values using the standard method. The bottom panel shows the X-band values using the technique described in Section 3.1.4.*
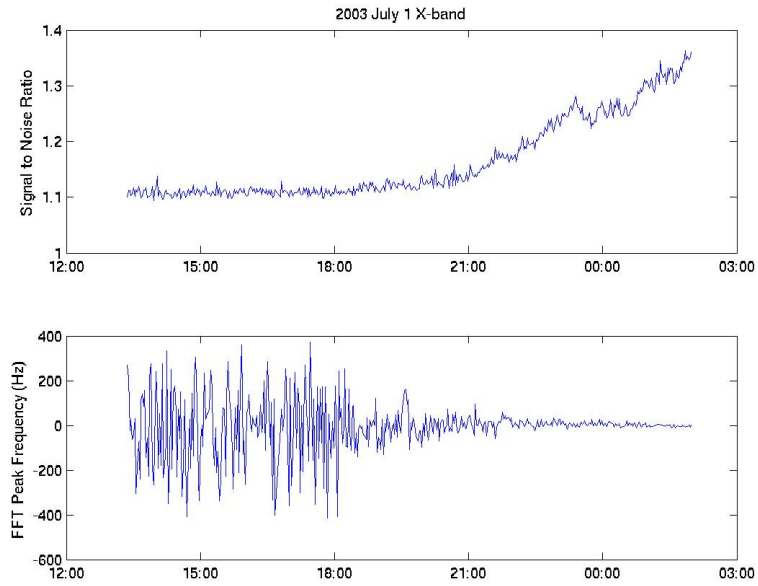
Figure 3.9: *The X-band signal to noise ratio in the top panel for comparison to the variability in signal frequency determined by FFT in the bottom panel as the RF carrier undergoes strong scintillation as the beginning of the pass.*

3.2 Effects on Signal Power

As will be discussed in Section 3.2.2, the signal power received from the spacecraft affects the plane of polarization through leakage in the polarizer. The frequency of the uplink signal and the pointing accuracy were found to have effects on the signal power in the different polarizations.

Because the carrier was constructed to minimize the amount of power required for a signal transmission while maintaining a reasonable baud rate through solar wind, this also means that the signal to noise ratio of the carrier is greatly degraded. Figure 3.10 shows the degradation that occurs in the SNR over the 2002 conjunction; the Ka-band with its higher frequency displays a better SNR only when the mode is Ka-up to Ka-down. X-up to Ka-down mode multiplies the noise on the X-band by four. Tables 3.3 and 3.4 list the operational modes of the carrier frequencies throughout the 2002 and 2003 conjunctions.

The diurnal variation of the plane of polarization angles show that the polarization of the signal was affected by the azimuth and elevation of the antenna which is consistent with parallactic rotation discussed later in Section 3.2.4. As shown in Figure 3.11, the Ka-band (Ka-up to Ka-down) shows a clear discontinuity as the alt-az antenna rotates through the highest point in the sky reached by the line of sight. This was around approximately 1900UT. The X-band (X-up to X-down) shows a similar rotation; however, it is not as large in angular rotation. As shown in Figure 3.11, the X- and Ka-bands (X-up to Ka-down) rotate through the discontinuity over the same period of time and with the same degree of rotation. The change in the Ka-band curve between Ka-up and X-up is correlated with the signal to noise ratio as shown in Figure 3.10. This indicates that the leakage function d_R changes with the signal to noise ratio.
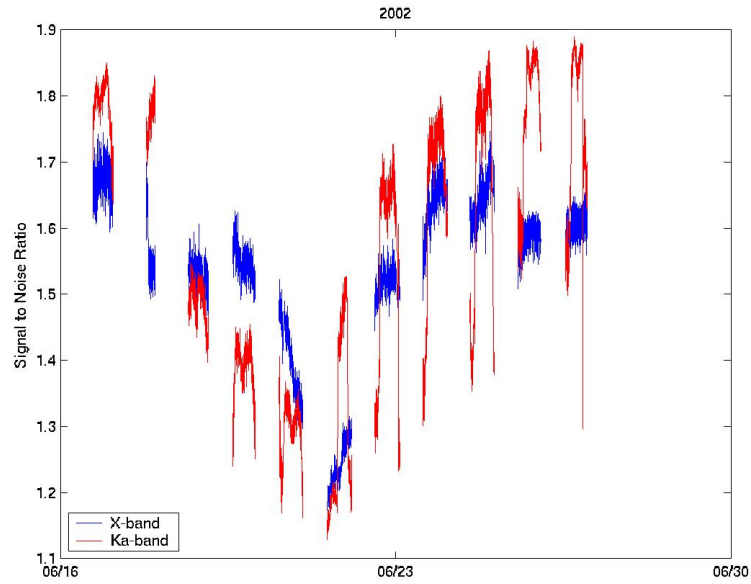
Figure 3.10: *The signal to noise ratio in the X-band (blue) and Ka-band (red) throughout the 2002 conjunction. When the Ka-band SNR is greater than the X-band, the operational mode of the Ka-band is Ka-up Ka-down; when the SNR is less, the mode is X-up Ka-down. Noise on the X-band is increased by a factor of four on the downlink.*

Table 3.3: *2002 Transmission Modes and RSR Channel Polarization*

Start	Stop	Uplink	Downlink	Transmit	RCP RSR
June 14 18:14:35	19:37:36	X,K	X,K	25	4A,1A
June 16 16:21:55	June 17 2:36:7	X,K	X,K	25	4A,1A
June 17 19:8:0	19:31:40	X,K	X,K	25	4A,1A
June 17 19:32:4	19:54:32	X,K	X,K	25	4B,1A
June 17 19:57:26	20:3:45	X,K	X,K	25	4A,1A
June 17 20:3:48	23:35:14	X,K	X,K	25	4B,1A
June 18 16:10:54	June 19 2:19:59	X,K	X,K	25	4B,1A
June 19 14:27:45	16:4:47	X,X	X,K	65	4B,1A
June 19 16:9:0	June 20 1:43:53	X,X	X,K	25	4B,1A
June 20 13:36:0	15:43:59	X,X	X,K	65	4B,1A
June 20 16:9:0	June 21 2:4:59	X,X	X,K	25	4B,1A
June 21 13:49:23	16:4:59	X,X	X,K	65	4B,1A
June 21 16:8:0	18:57:59	X,X	X,K	25	4B,1A
June 21 19:1:33	23:40:8	X,K	X,K	25	4B,1A
June 22 0:6:55	2:4:59	X,X	X,K	25	4B,1A
June 22 13:29:13	15:54:54	X,X	X,K	65	4B,1A
June 22 16:8:20	June 23 1:18:26	X,K	X,K	25	4B,1A
June 23 1:21:19	2:4:59	X,X	X,K	25	4B,1A
June 23 13:32:41	15:49:59	X,X	X,K	65	4B,1A
June 23 15:53:36	June 24 1:59:59	X,K	X,K	25	4B,1A
June 24 13:14:24	15:50:29		X,K		4B,1A
June 24 15:52:37	June 25 0:53:47	X,K	X,K	25	4B,1A
June 25 1:0:45	1:26:11	X,X	X,K	25	4B,1A
June 25 13:19:30	15:45:31	X,X	X,K	54	4B,1A
June 25 15:50:59	June 26 0:47:22	X,K	X,K	25	4B,1A
June 26 13:16:35	16:0:58	X,X	X,K	65	4B,1A
June 26 16:6:15	21:56:40	X,K	X,K	25	4B,1A
June 26 21:58:46	23:59:59	X,X	X,K	25	4B,1A

Table 3.4: *2003 Transmission Modes and RSR Channel Polarization*

Start	Stop	Uplink	Downlink	Transmit	RCP RSR
June 24 16:46:16	16:52:46	X,X	X,K	65	2B,1A
June 24 16:59:26	22:29:59	X,X	X,K	25	2B,1A
June 26 13:37:13	16:40:45	X,X	X,K	54	2B,1A
June 26 16:53:26	June 27 0:59:59	X,X,	X,K	25	2B,1A
June 27 14:2:13	18:20:59		X,K		2B,1A
June 27 18:37:32	June 28 1:59:59	X,X	X,K	25	2B,1A
June 28 13:49:60	16:37:4		X,K		2B,1A
June 28 16:38:57	June 29 1:59:59	X,X	X,K	25	2B,1A
June 29 13:45:0	16:32:29		X,K		2B,1A
June 29 16:33:28	June 30 1:59:59	X,X		2B,1A	
June 30 13:45:0	16:32:39		X,K		2B,1A
June 30 16:33:30	July 1 1:59:58	X,X	X,K	25	2B,1A
July 1 13:21:10	July 2 1:59:58		X,K		2B,1A
July 2 13:35:0	16:22:45		X,K		2B,1A
July 2 16:23:35	July 3 1:59:58	X,X	X,K	25	2B,1A
July 3 13:35:0	16:22:45		X,K		2B,1A
July 3 16:23:37	July 4 1:57:6	X,X	X,K	25	2B,1A
July 4 13:22:0	16:22:49		X,K		2B,1A
July 4 16:23:39	July 5 0:59:59	X,X,	X,K	25	2B,1A
July 5 13:15:0	16:12:53		X,K		2B,1A
July 5 16:13:39	July 6 1:39:58	X,X	X,K	25	2B,1A
July 6 13:25:0	20:50:48	X,X	X,K	65	2B,1A
July 6 20:52:57	July 7 1:39:58	X,X	X,K	25	2B,1A
July 7 13:45:0	16:32:55		X,K		2B,1A
July 7 16:33:1	July 8 1:34:59	X,X	X,K	25	2B,1A
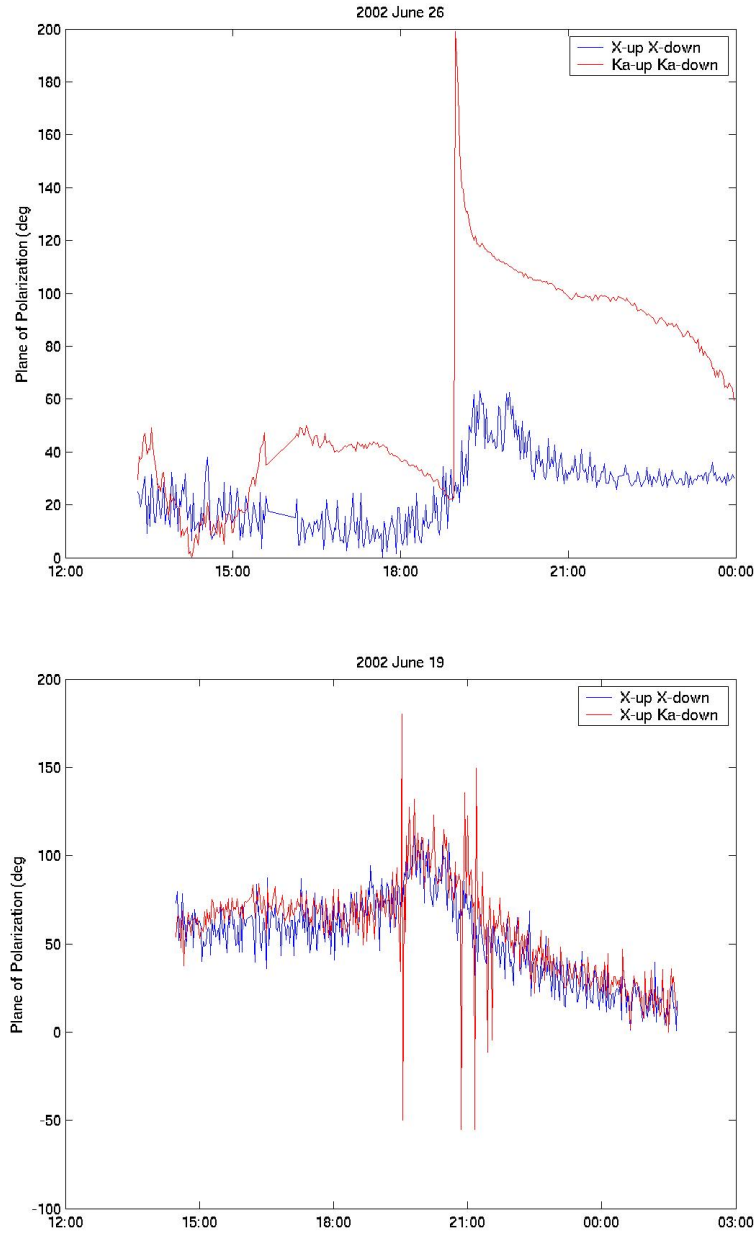
Figure 3.11: *The plane of polarization of the X- and Ka-bands throughout a pass. The figure on the top shows the X-up X-down and Ka-up Ka-down operational mode, while the figure on the bottom shows the X-up X-down and X-up Ka-down modes. The signal to noise ratio drops significantly in the Ka-band (red line) when the mode changes from Ka-up (top panel) to X-up (bottom panel).*

3.2.1 Antenna Pointing

In 2002 when Cassini pointing is controlled by reaction wheels, it can be assumed that the signal transmitted from Cassini does not vary. This is because the system was designed to be unusually stable to measure gravity waves when the reaction wheels are being used (Ekelund & Roth, 2004). Specifically, the change in distance between Cassini and the Earth can be measured to within 3cm for 10K second integration times (Iess *et al.*, 1999).

In 2003, the pointing of Cassini was controlled by thrusters rather than reaction wheels in order to conserve the slowly degrading wheels for the primary mission. As shown in Figure 3.12, the 2003 dataset has time periods which clearly show the thruster effects on the signal (the irregular dips at 1630, 1830, 1930, and 2200 UT) that are not present in the reaction wheel time series. As the signal pointing changes, the resulting amplitude of the signal changes which in turn effects the amount of leakage in the polarizer and the final resulting plane of polarization measurement. The leakage is discussed below.

3.2.2 Jones Matrix

As discussed in Section 2.3, the Jones matrix quantifies the variables for antenna effects on a polarized signal where $\overleftrightarrow{J}$ is the Jones matrix for polarization effects, $\overleftrightarrow{G}$ is the gain of the respective channels, $\overleftrightarrow{D}$ is the leakage inefficiency of the polarizer, and $\overleftrightarrow{P}$ is the parallactic angle. Specifically

$$\vec{E'} = \overleftrightarrow{J}\,\vec{E} = \overleftrightarrow{G}\overleftrightarrow{D}\overleftrightarrow{P}\overleftrightarrow{T}\,\vec{E} \tag{3.5}$$
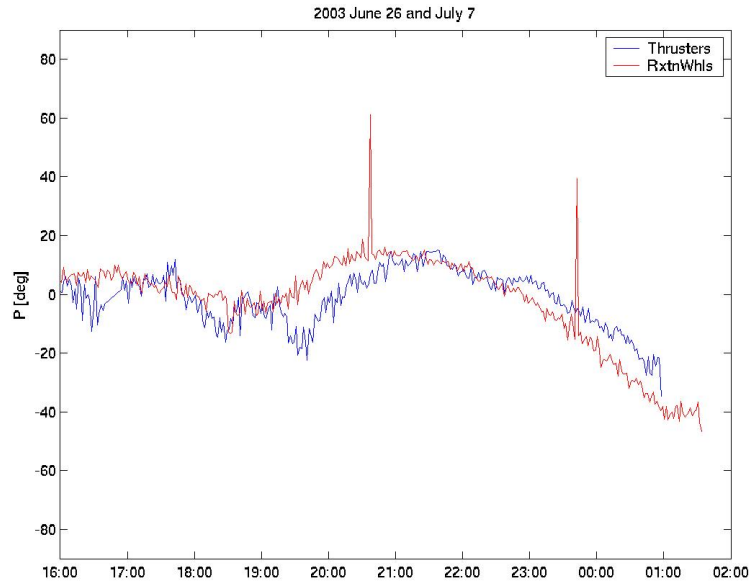
Figure 3.12: *The X-band plane of polarization from the 2003 June 26 and July 7 passes when the Cassini spacecraft was controlled by thrusters and reaction wheels respectively. The thruster effect on the signal is visible in the polarization drops at 1630, 1830, 1930, and 2200 UT which are not present in the other pass.*

On the Earth the received signal is strongly right circularly polarized; this allows us to simply equation 2.2 to

$$E'_R = g_R(E_R e^{i\chi})$$
$$E'_L = g_L(E_L e^{-i\chi} + d_R E_R e^{i\chi})$$
(3.6)

where g is the gain of the antenna, χ is the position angle, and d is the leakage from the opposite polarization in the polarizer. Combining the equations in 3.6, we obtain

$$E'_L = g_L E_L e^{-i\chi} + \frac{g_L}{g_R} d_R E'_R$$
(3.7)

3.2.3 Polarizer Leakage

Unfortunately there is a problem with directly applying equation 3.7 to the RF data; d_R is unknown. As a result, it is necessary to apply an approximate equivalent to equation 3.7.

Remembering that equation 3.7 is derived from the Jones matrix, the parallactic angle term $e^{-i\chi}$ can be dropped temporarily while focusing on the change in plane of polarization due to leakage. It can be rewritten as

$$\frac{g_L E_L}{E'_L} = \tan(\epsilon_d) = 1 - d_R \frac{E'_R}{E'_L} \frac{g_L}{g_R}$$

This gives the relationship between the polarization due to leakage ϵ_d and the ellipticity of the RF signal.

101

$$\epsilon_d = -\arctan\left(1 - d_R \frac{E'_R}{E'_L} \frac{g_L}{g_R}\right) \tag{3.8}$$

The plane of polarization is the sum of the plane of polarization from the Cassini line of sight ϕ, the parallactic angle χ, and the leakage from the variable signal power ϵ_d.

$$P = \phi + \chi + \epsilon_d \tag{3.9}$$

3.2.4 The Parallactic Effect

Setting the initial plane of polarization to zero, then the plane of polarization $P - \chi = \epsilon_d$. This is accomplished by shifting all all of the plane of polarization calculations to zero at the point when Cassini was in the highest point in the sky (Figure 3.13). As an Alt-Az antenna tracks a polarized source in the sky, the coordinate system of the antenna changes with the hour angle of the source causing an apparent rotation of its plane of polarization. Figure 3.14 shows the expected parallactic rotation at DSS 13 as it tracks Cassini; it is calculated as

$$\chi = \arctan\left(\frac{cos(l)sin(h(t))}{sin(l)cos(\delta) - cos(l)sin(\delta)cos(h(t))}\right)$$

where l is the latitude, δ is the declination of the object, $h(t) = LST - RA$ is the hour angle, LST is the local sidereal time, and RA is the right ascension of the object.

This adjustment is appropriate because the plane of polarization variation between
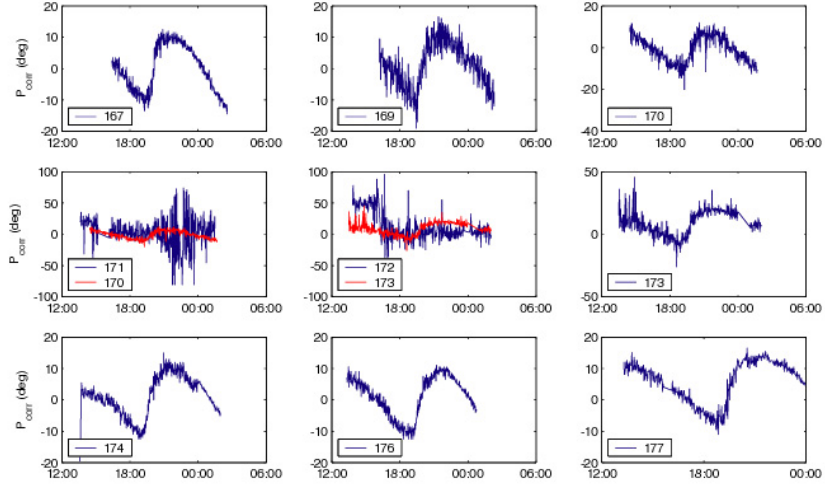
Figure 3.13: *The plane of polarization measurements adjusted to zero degrees at the time of lowest hour angle (Cassini at the highest point in the sky).*

passes during most of the conjunction is entirely dependent on the antenna system. As shown in Figure 3.13, the time when Cassini was highest in the sky (when the plane of polarization is shown crossing zero), occurs when the maximum change in slope occurs in the plane of polarization. There is some error with this method on the two passes of significant Faraday rotation; however, as shown from the red curves (of the previous and following days) during these time periods, the correction occurs when the variation in the plane of polarizations are similar.

3.2.5 Calculating d_R Using χ

The calibration method consists of calculating d_R for time periods when the line of sight was farthest from the Sun, determining a function for how d_R varies throughout the pass, and to use it to remove the antenna effects from the dataset for measuring Faraday rotation during the time periods when the point of closest approach was
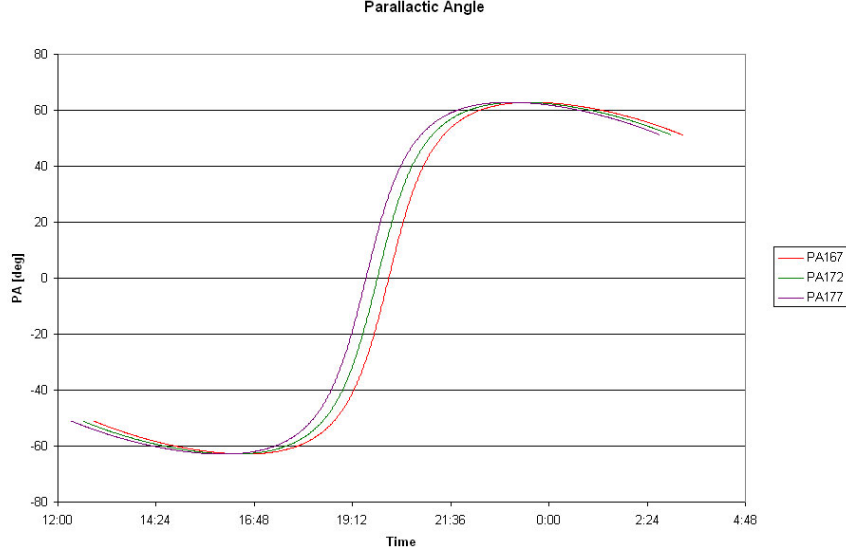
Figure 3.14: *The Parallactic Angle. The change in the plane of polarization is caused by the non-inertial coordinate system of the alt-az antenna rotating on the Earth observing a fixed source in the sky.*

closer to the Sun.

The function for d_R can be determined from the calculation of $\epsilon_d = P - \chi$. Specifically,

$$d_R = 1 - \tan(\chi - P)\frac{E'_L}{E'_R}\frac{g_R}{g_L}$$

The results from the calculation of d_R in the X-band are shown in Figure 3.15. Note that the d_R values in 2003 were calculated from angles reduced by a factor of two in order to remain continuous; the factor was removed before the Faraday rotation calculations were made. This was necessary because the tan function becomes discontinous at 90 degrees, and the difference between the parallactic angle and the observed plane of polarization often spanned this discontinuity in 2003.

104

The Ka-band values always spanned the discontinuity. In every dataset, the leakage function was sufficiently modeled to closely resemble the observed change in the plane of polarization at large distances from the sun.

The red curve in all the plots in Figure 3.15 is the fit to the d_R values from 2002 June 25 and 2003 July 7. 2002 June 16 and 25 have identical d_R values indicating the antenna contribution to the rotation of the plane of polarization can be determined using the fit (red curve) from the 25th.

A comparison of the ϵ_d observations from the 16th and 26th show a secondary fluctuation about the point of the smallest hour angle in Figure 3.16; this is very similar between the two passes and is assumed to be an unaccounted secondary antenna effect. The secondary fluctuation from the two calibration passes (the 16th and 26th of June) were averaged and removed from all the observations. Figure 3.16 shows the low pass filter curves that result from two different pass bands. The lower pass band indicates that the general trends used for forward model fits are within the noise below 1.5 degrees; this eliminates the 2002 June 18 time series. However, the error level shown depends on the passband. Attempting to produce a timeseries with greater resolution increases the error to 4 degrees. Because the Faraday rotation forward model described in Chapter 4 is based on the large scale configuration of the magnetic field, the data were filtered using the lower passband, so the general trend of the observations can be compared to the model. Attempting to determine finer structure in the magnetic field requires that the data be filtered with a higher passband; however, the higher passband increases the size of the error in the observation. Figure 3.17 shows the final Faraday rotation values for use in the model.
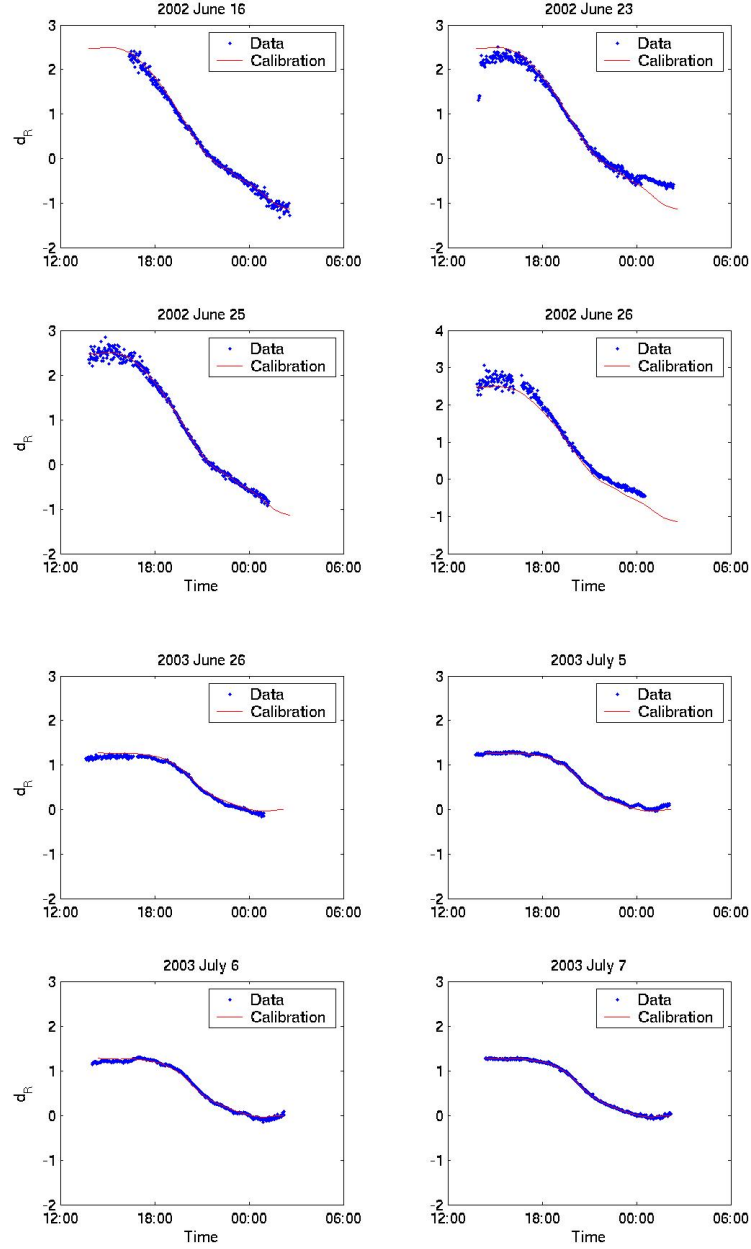
Figure 3.15: *The d_R values for the four time periods at largest impact parameters from the Sun with the least amount of electron density in 2002 (top 2 rows) and 2003 (bottom 2 rows). The red curve is the fit to 2002 June 25 (2nd row, 1st column) and 2003 July 7 (bottom right); this curve was used as the model for d_R.*
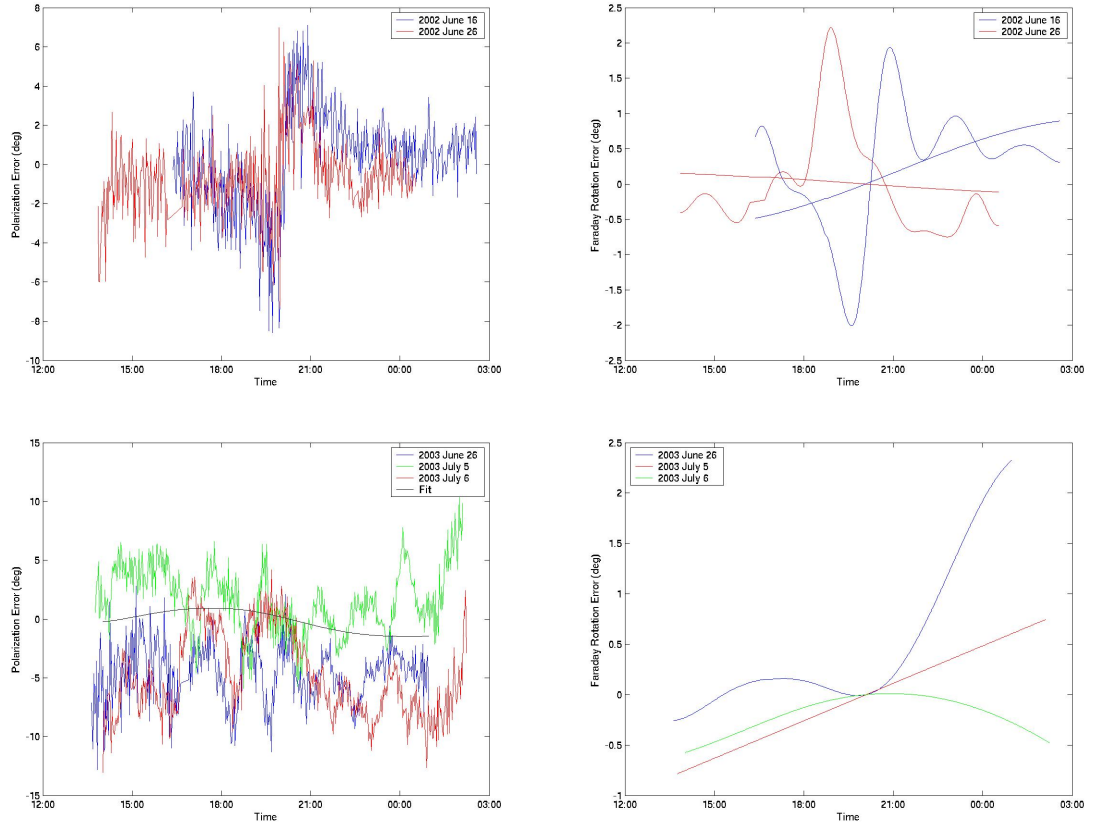
Figure 3.16: *The net error in the Faraday rotation after removal of the d_R effects on the left and net error after removal of the curves on the left (plotted on the right) (2002 on the top row, 2003 on the bottom). The curves on the left show the remaining rotation of the plane of polarization following the removal of the polarizer leakage on the two passes at greatest distance from the sun. These curves were averaged together and removed from all the passes. The remainder (in the two passes following the removal of the plane of polarization average) has been plotted to the right after applying a low pass filter with a high and low passband.*
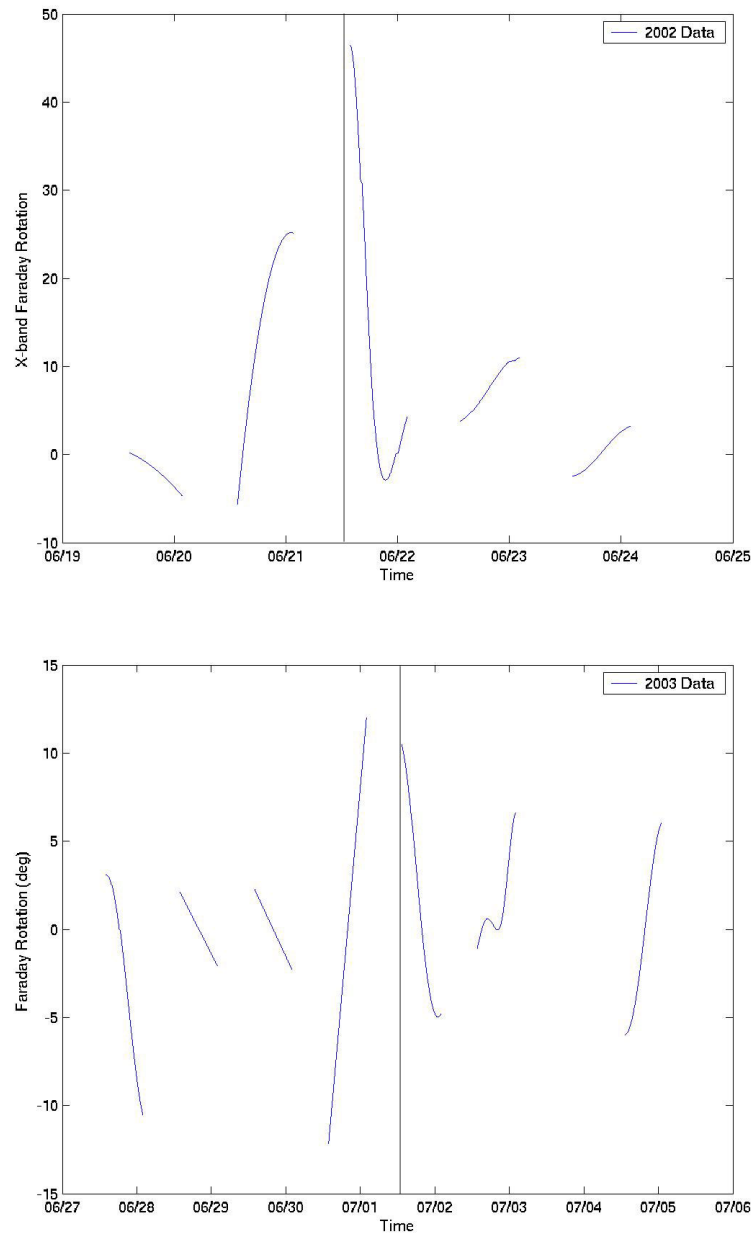
Figure 3.17: *The 2002 (top) and 2003 (bottom) Faraday rotation values after removal of the d_R effects and the net fluctuation left over.*

108

Table 3.5: *Amount of rotation observed (corrected for ground effects) and associated closest approach impact parameters. The values indicate that in 2003 spacecraft induced rotation probably caused by the thrusters is present.*

Date	Total Rotation (deg)	Closest Approach (Rs)
2002 June 19	5	5.6
2002 June 20	30	2.8
2002 June 21	42	2
2002 June 22	7	4.4
2002 June 23	5	7.4
2003 June 27	14	11.0
2003 June 28	5	7.9
2003 June 29	5	4.8
2003 June 30	24	2.1
2003 July 1	15	1.3
2003 July 2	8	3.5
2003 July 4	12	9.7

3.2.6 2003 Faraday Rotation Values

As shown in Table 3.5, the total amount of rotation of the plane of polarization at X-band was significant during time periods when the line of sight was at large impact parameters from the Sun. The change in columnar electron density for these time periods was not extraordinarily high indicating that either the magnetic field strength is significantly greater than predicted or the spacecraft itself is slowly rotating as it maintains its pointing with thrusters. It is probably not the magnetic field because large rotation measures (FR/λ^2) in the vicinity of 10 solar radii have not been observed. This indicates that the 2003 data set requires additional processing to attempt to remove spacecraft motion; this can be done with the Ka-band observations once they have been appropriately calibrated.

3.3 Data Processing Summary

The radio frequency data from Cassini consists of real and imaginary components stored in RSR files. FFTs were calculated using the complex wave on the stronger right circularly polarized signals to determine the downconverted frequency of the signal. Assuming that Faraday rotation is small, the left circularly polarized signal should have the same frequency. Therefore, this frequency was used to band pass filter both polarizations. The phase angles were calculated from the filtered real and imaginary waves, and the plane of polarization was determined using cross correlation.

The antenna system was observed to cause two known effects in the plane of polarization: parallactic rotation and polarization leakage. The amount of expected parallactic rotation was used in combination with the observed plane of polarizations during passes that the line of sight was at large distances from the Sun to calculate a function for the leakage. It is unknown why the leakage function is asymmetrical and variable during the pass. However, the leakage function did model the observed plane of polarization for passes during which the line of sight was closer to the Sun.

Following the removal of the expected antenna effects on the plane of polarization, the passes that were at significant distances from the Sun were then used to remove any consistent trends and estimate the error in the resulting Faraday rotation measurement; in 2002, this was ± 1 degrees and in 2003 ± 2 degrees in the X-band. In the Ka-band, the maximum expected rotation during both conjunctions never exceeded the error in the measurement. The resulting Faraday rotation measurements above the error were then inspected for anomalous behavior relative to the impact parameter of the point of closest approach. The 2003 observations showed significant rotation in the vicinity of 10 solar radii where there should be none ob-

served in the X-band indicating that another effect is present in the antenna system that was not accounted for. In this case, it was the motion of the spacecraft as it pointed towards Earth using thrusters. In 2002, the pointing was controlled by reaction wheels keeping the spacecraft stable. The thruster motion clearly induced a rotation of about 15 degrees or less throughout a pass.

CHAPTER 4

Faraday Rotation Forward Model

In this chapter we present the forward model used to fit the Faraday rotation observations, the method of fitting, and the results of the fits. The forward model is constructed using spacecraft navigation ephemerides (Acton, 1996), the electron density model from Tyler et al (1977) and differential Doppler, and the Community Coordinated Modeling Center Potential Field Source Surface model (Luhmann, 2002) for the magnetic field. The forward model is first tested under the ideal conditions of a simple dipole magnetic field. We then discuss the full model, its sources of error, and the methods employed to obtain a fit to the observations. The ideal PFSS magnetic field solution is combined with a magnetic field vector which allows the model to reproduce the observations.

4.1   The Ideal Faraday Rotation Model

In order to model the expected Faraday rotation through the solar corona, the Faraday rotation equation can be rewritten as

$$FR = \frac{A}{f^2} \sum_i N_i \vec{B}_i \cdot \hat{n} \Delta s_i = \frac{A}{f^2} \sum_i N_i |B|_i \cos\theta_i \Delta s_i$$

where $\cos\theta = \hat{B} \cdot \hat{n}$. Notice that Δs is variable. Specifically,

$$\Delta s_i = kR_i$$

where R_i is the distance from the Sun at the point along the line of sight specified by i and $k = 10^{-3}$. The constant k was determined by calculating the Faraday rotation along the line of sight with $k = 0.1$ and comparing it with the same calculation using $k = 0.01$. k was progressively reduced until the difference in Faraday rotation was negligible. Specifically, $FR(k = 10^{-3}) \sim FR(k = 10^{-4})$.

4.1.1 SPICE

The Faraday rotation forward model requires that the line of sight from Cassini to the Earth be determined with the highest accuracy possible. This was achieved using the JPL Navigation and Ancillary Information Facility (NAIF) Spacecraft Planet Instrument C-matrix Events (SPICE) kernels. The SPICE files include "spacecraft orbiter, rover, or natural body trajectory" (SPK), "target body size, shape and orientation" (PcK), "instrument field of view geometry" (IK), "orientation of spacecraft or rover or any articulating structure" (CK), "Events information: Science Plan, Sequence of Events, and Experimenter's Notebook" (EK), "reference frame specifications" (FK), "leapseconds" (LSK), and "spacecraft clock coefficients" (SCLK) (Acton, 1996). The SPICE toolkit software allows the determination of the coordinates of a signal traveling from Cassini to Earth with the appropriate light time correction in Carrington coordinates (IAU_SUN) and performs all matrix calculations appropriately. The forward model code is printed in Appendix H.

4.1.2   Coordinate Systems

There are two coordinate systems used in the forward model: Geocentric Equatorial Inertial System (J2000) and Carrington Heliographic (IAU_SUN). The J2000 system is used to calculate the positions of the signal as it passes through the corona with an appropriate light time correction. These coordinates are rotated into IAU_SUN coordinates for the calculation of the magnetic field vector at a particular point.

The J2000 coordinate system is an Earth-centered inertial system. The X-axis is aligned from the origin at the center of the Earth to the first point of Aries (the direction of the Sun at the fall equinox); this corresponds to the intersection of the ecliptic and Earth equatorial planes. The Z-axis is aligned with the Earth's rotational axis, and the Y-axis completes the right-handed rectangular coordinate system. This system is fixed at the epoch of J2000.

The IAU_SUN coordinate system is defined by the International Astronomical Union as a Sun centered rotating coordinate system with the fixed period of 25.38 days. The X-axis is aligned from the center of the Sun to the ascending node of the solar equator on the ecliptic plane on 1854 January 1 at 12 UT. The Z-axis is aligned with the Sun's rotational axis, and the Y-axis completes the right-handed rectangular coordinate system (Parthasarathy & Papitashvili, 1995).

As the signal from Cassini travels to the Earth, its travel time is approximately 90 minutes in 2002 and 120 minutes in 2003. The Sun is approximately 8 minutes light time from the Earth. The position of the signal in the corona is calculated accounting for the light time correction in J2000 coordinates. To convert to IAU_SUN coordinates, the following steps are taken in SPICE:

1) Obtain the vector for the path of the signal from Cassini to the Earth in light-time corrected J2000 coordinates

2) Obtain the vector for the path of the signal from the Sun to the Earth in light-time corrected J2000 coordinates

3) Calculate the vector for the light-time corrected path of the signal from Cassini to Sun by subtracting the two vectors $\vec{L}_{C \rightarrow \odot} = \vec{L}_{C \rightarrow \oplus} - \vec{L}_{\odot \rightarrow \oplus}$

4) Obtain the transformation matrix from J2000 coordinates to IAU_SUN

5) Calculate the vectors above in IAU_SUN coordinates

Note that this calculation needs to be made for every point in time of a Faraday rotation datum point ($\Delta t = 100 sec$); the positions of the Earth and Cassini are changing while the Sun is rotating.

4.1.3   The Signal Path from Cassini to Earth

The amount of Faraday rotation is proportional to the component of the coronal magnetic field parallel to the line of sight, therefore $\hat{k}_{cf} \cdot \hat{B}$ reversals affect the amount of Faraday rotation measured. As shown in the schematic in Figure 4.1, the impact parameter and structures such as sector boundaries reverse the parallel component of the magnetic field. The reversal at closest approach in Figure 4.1 is purely the effect of the geometry of the assumed radial field; therefore, the Faraday rotation measured at the Earth is a measurement of the net magnetic field direction. In other words, the Faraday rotation in Figure 4.1 decreased to the closest approach where it began to increase because of the parallel magnetic field reversal; once the signal crossed the current sheet, it began to decrease again. The measured Faraday rotation from this signal path is the final angle that is achieved. The magnitude of the Faraday rotation depends on the product of the possibly asymmetrical electron

density (i.e. increases in streamers by as much as one order of magnitude over equatorial densities) and the magnitude of the parallel component of the magnetic field. Therefore, the measured Faraday rotation from a sector boundary will vary with the position of the boundary varying along the path of integration. Interpreting Faraday rotation data requires the use of 3D models of both electron density and magnetic field. Figure 4.2 shows the location of the sector boundary with respected to the path of the signal from Cassini on both the ingress and the egress passes.

4.1.4 Ideal Faraday Rotation

The orientation of a magnetic dipole is given by the g11, h11, and g10 Legendre polynomial coefficients. The h11 direction is from the center of the Sun outward at zero degrees IAU_SUN longitude (x-direction), g10 is along the rotational axis of the Sun (z-direction), and g11 (y-direction) completes the right handed xyz coordinate system. When the forward model uses these dipole coordinates, Figure 4.3 shows the resulting Faraday rotation. The top panel shows that the g10 component contributes to positive Faraday rotation due to the asymmetric orientation of the line of sight relative to the sun (illustrated in more detail in the bottom figure). Because the strength of a dipole magnetic field varies with colatitude ($B = Mr^{-3}\sqrt{1 + 3\cos^2\theta}$, M is the dipole moment), the changing position of the point of closest approach introduces an asymmetry in the magnetic field strength along the line of sight relative to its contribution to the Faraday rotation as shown. The h11 plot shown in the 3rd panel from the top shows that it is a relatively (25%) minor contributor to the overall observed Faraday rotation. The 2nd plot from the top shows the Faraday rotation that occurs because of a dipole magnetic field oriented in the direction towards the Earth; the Faraday rotation is negative and of a comparable magnitude to the g10 contribution. This figure indicates that only the time period between
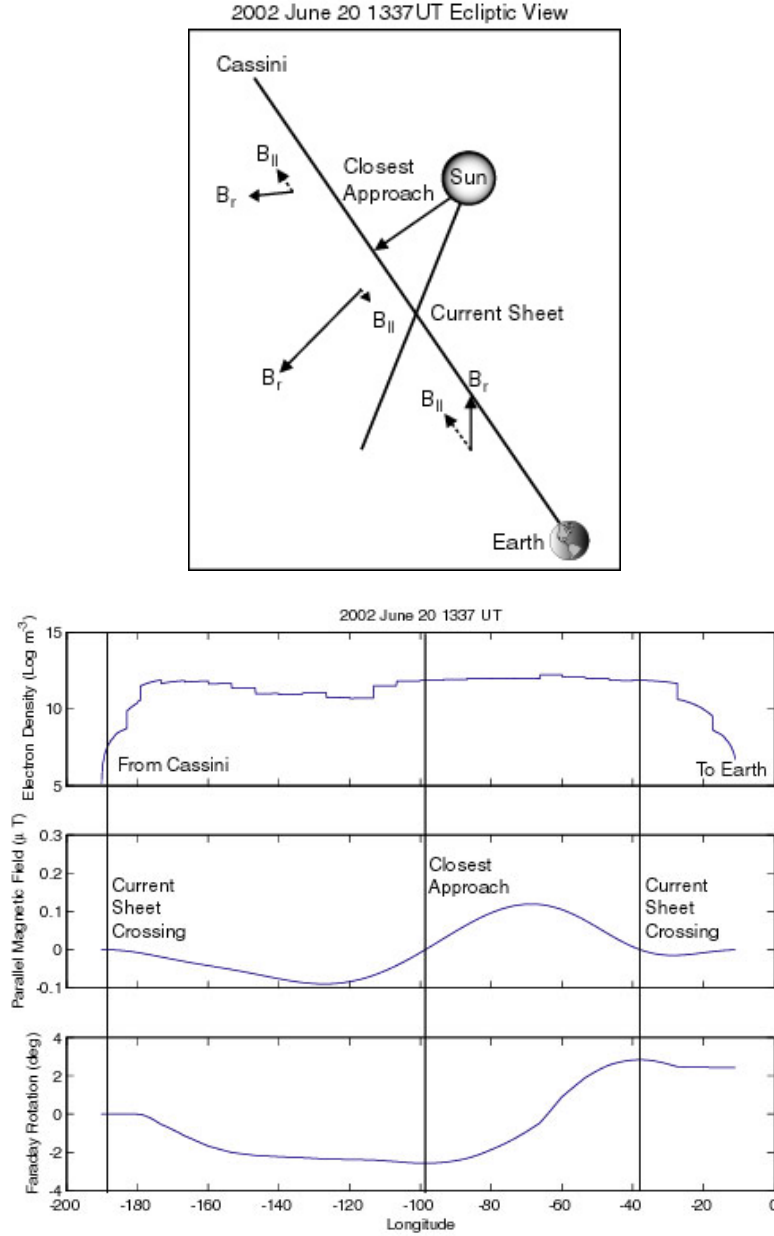
Figure 4.1: *Schematic for the line of sight between Cassini and the Earth on 2002 June 16 (top) and Faraday rotation along the line of sight (bottom figure, bottom plot). The structure of the electron density (bottom figure, top plot) and magnetic field (bottom figure, middle plot) through which the radio wave passes is important to consider when interpreting Faraday rotation data. A current sheet is located approximately 60 degrees Earthward of the point of closest approach. The radial magnetic field reverses across this current sheet.*
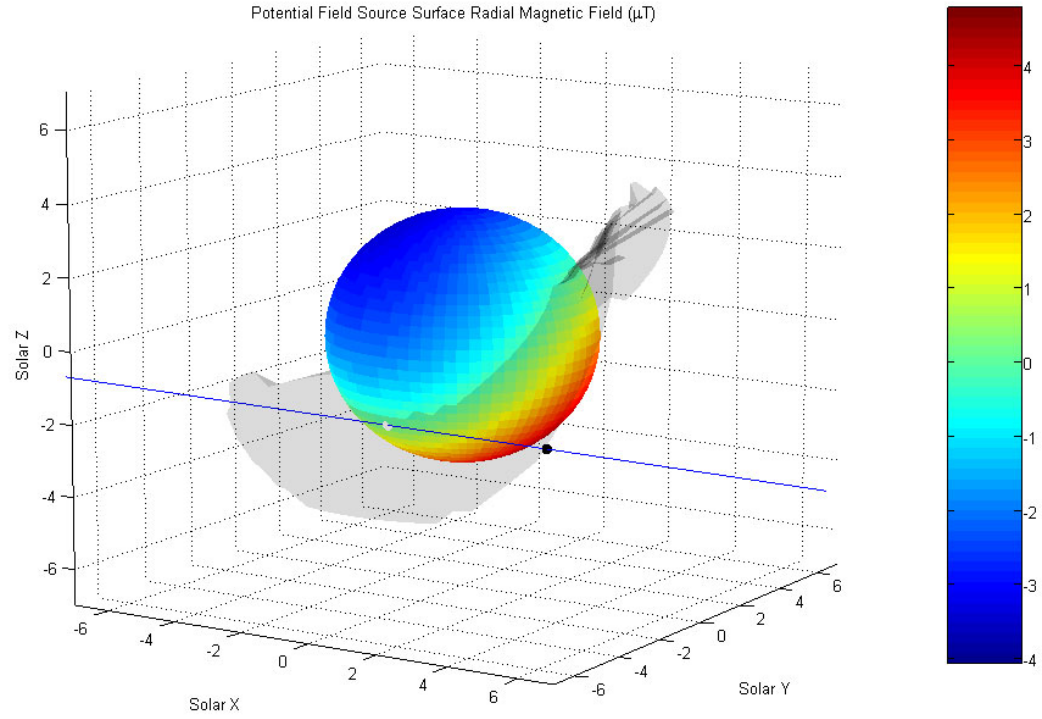
Figure 4.2: *The line of sight between Cassini and the Earth during the 2002 conjunction plotted against the radial magnetic field on a sphere at closest approach. A current sheet exists at the sector boundary shown as the grey plane projection from the sphere between the positive and negative poles. The radial magnetic field reverses across the minimum in the path (the point of closest approach) and again across this boundary (current sheet crossing).*

June 21 and 22 in 2002 should produce significant Faraday rotation.

4.2   The Equation for Fitting

The Faraday rotation equation used for the forward model fit is as follows:

$$FR_{obs} + \epsilon = \frac{A}{f^2} \sum_i^s (N_i + \eta_i)\beta(\kappa)|B|_i \cos(\theta_i + \kappa)\Delta s_i \tag{4.1}$$

where $-1 < \epsilon < 1$ is the error in the Faraday rotation observation (as determined from Chapter 3), η_i is the error in the electron density model value at point i, κ is the change in the angle between the $\vec{B}_{PFSS}$ solution and the line of sight, and β is a function of κ being the scaling factor to the rotated vector to fit the observations. Note that this equation is used for a single point in time; the position of the spacecraft changes with time affecting the N values, $\vec{B}_{PFSS}$ solutions, and Δs values along the line of sight. Therefore, every component to the equation (with the exception of the constant A and frequency f) changes with time. And

$$\begin{aligned} \beta(\kappa)|B|_i \cos(\theta_i + \kappa) &= \vec{B}_{PFSS} + \vec{B}_{corr} \\ \vec{B}_{PFSS} &= |B|_i \cos\theta_i \\ \vec{B}_{corr} &= \beta(\kappa)|B|_i \cos(\theta_i + \kappa) - |B|_i \cos\theta_i \end{aligned} \tag{4.2}$$

As shown in Figure 4.4, the PFSS solution to the magnetic field vector is adjusted by $\vec{B}_{corr}$ in the following manner. If we set $\beta = 1$, then it is apparent that $\cos\theta + \cos\kappa$ is restricted to real space such that $-1 < \cos\theta + \cos\kappa < 1$. If we remember that Faraday rotation depends on the parallel component of the magnetic field
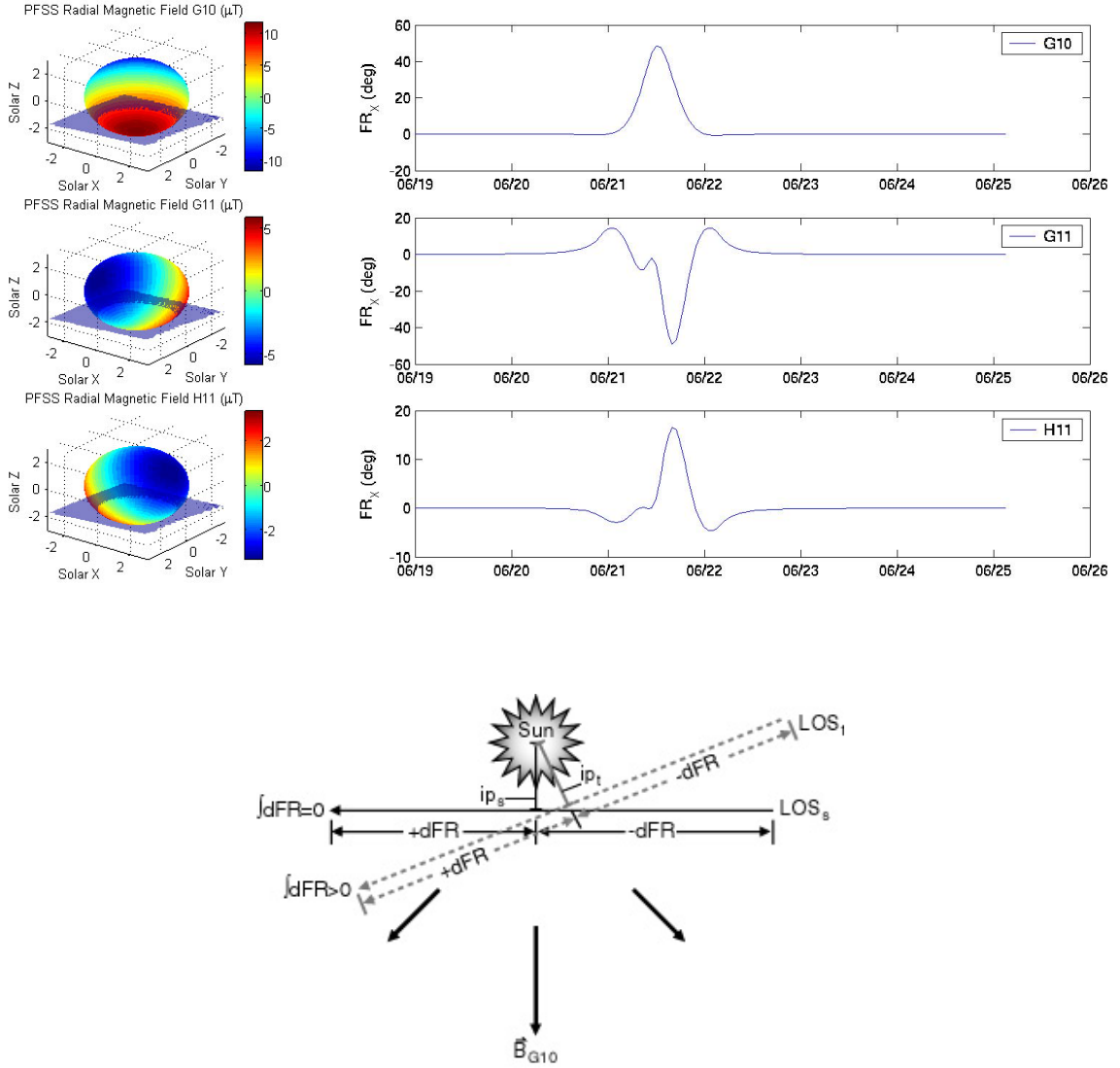
Figure 4.3: *The effects that various orientations of the dipole magnetic field have on the Faraday rotation measurement. On the right hand side in the top panel the magnetic moment is along the Sun's rotation axis. In the middle panel the dipole axis is pointing toward the Earth. In the bottom panel the dipole magnetic moment is perpendicular to the Sun-Earth line. Note that in this example the field on the equator of the dipole at the surface of the Sun was 67 μT, producing 0.5 μT at 5Rs. The density model used was that generated by Tyler et al (1977) that produced a density of $6.7 \times 10^{15} cm^{-3}$ at 5 Rs. The plots on the left hand side show the radial magnetic field on a sphere at 2.5 solar radii used in the Faraday rotation calculations. The line of sight is shown as the grey plane passing through the sphere. The bottom figure shows the geometry of the Faraday rotation measurement in the plane containing the Earth, the Sun, and the spacecraft.*
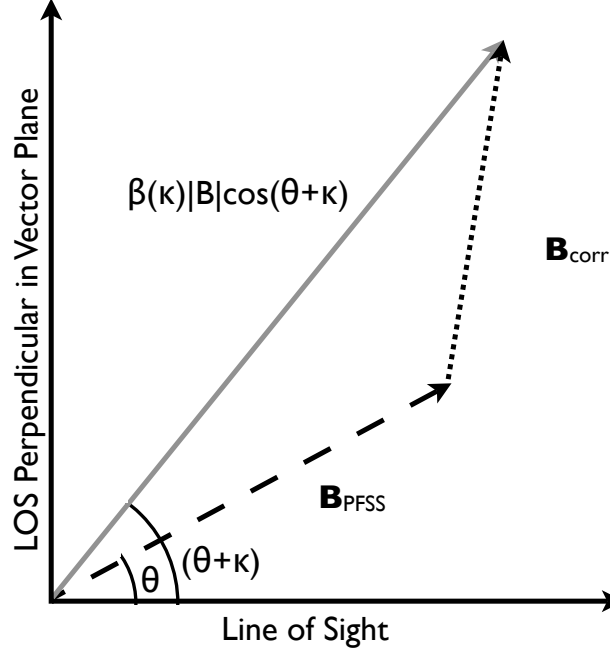
Figure 4.4: *The method for adjusting a single PFSS magnetic field vector along the line of sight when fitting the Faraday rotation model to the observations. A "correction" magnetic field vector is summed to the PFSS solution. Note that $\beta(\kappa)$ and κ are kept constant for every vector along the line of sight within the region of interest around the point of closest approach.*

vector being either parallel or anti-parallel to the line of sight, then there is an additional restriction to $0.5 < \cos\theta + \cos\kappa < 1$ (for example) in that the sign of the Faraday rotation must remain the same. For each angle through which the $\vec{B}_{PFSS}$ can be rotated within these restrictions, the magnitude of the resulting vector $|\vec{B}_{PFSS} + \vec{B}_{corr}|$ must be similarly adjusted in order to fit the Faraday rotation observations. This is done through the parameter β in the $\vec{B}_{corr}$ vector.

As this equation is set up, the Faraday rotation problem is still an underdetermined system. A range of solutions are possible for κ where β is a function of κ. This will be discussed in Section 4.3.1.

4.2.1 $N_i + \eta_i$

The electron density component to the Faraday rotation equation $N_i + \eta_i$ requires the combination of two datasets to evaluate. The UCSD 3D electron density tomographic solutions from interplanetary scintillation (IPS) measurements are publicly archived as they are generated; however, they are limited to the region between 22 Rs and 3 AU (approximately 600 Rs). Another tomographic technique is currently being developed for inverting white-light observation from SOHO (Frazin, 2000) which would be more appropriate to this study; however, the technique is not yet ready for regular data analysis. Additionally, SOHO was inoperable during the 2003 Cassini superior conjunction; therefore, an ideal electron density model (Tyler *et al.*, 1977) was chosen for now.

As discussed previously, differential Doppler measurements from the X- and Ka-band (8 and 32 GHz) Cassini carrier frequencies provide a measurement of the change in columnar electron density along the line of sight. The challenge in modeling the electron density is to develop a method to combine the 3D structure from the model and the change in the line of sight integration of electron density.

4.2.2 Adjusting 3D Electron Density

The total columnar electron density was measured on only the last two days over the 2002 June 19-23 time period. A comparison between the change in columnar density during the pass and the initial total columnar electron density indicated that the total columnar density should be greater than the change in columnar density; in other words, electron density cannot be negative. This result was used to estimate the total columnar electron density for the other passes. Specifically,

Table 4.1: *The estimated columnar electron density vlaues for 2002 (and the range of acceptable values). June 22 and 23 have negligible error in comparison the other passes because they were acquired through ranging measurements.*

Date	TEC (m^{-2})
June 19	$9.6(6.4 - 12.8) \times 10^{19}$
June 20	$4.1(2.7 - 5.5) \times 10^{21}$
June 21	$6.8(4.5 - 9.1) \times 10^{21}$
June 22	4.9×10^{20}
June 23	1.6×10^{20}

the total columnar electron density for the June 22nd pass was 2 times greater than the change in electron density between the beginning and the end of the pass. The total columnar electron density for the June 23nd pass was 4 times greater than the change in electron density between the beginning and the end of the pass. The total columnar electron density was 4.9×10^{20} m^{-2} on the 22nd and 1.6×10^{20} m^{-2} on the 23rd with errors on the order of 10^{17} m^{-2}. For these two days, the slope varied over approximately a third of the total columnar electron density; the maximum Doppler value was about 2.2×10^{20} and 0.4×10^{20} m^{-2} for these days respectively. The initial columnar electron density (TEC) for 2002 was therefore assumed to be 3 times the maximum of the differential Doppler value with the error bars from 2 to 4 times. Figure 4.5 shows the profile of the electron density along the line of sight for 2002 June 20 1337 UT.

With these columnar electron density adjustments, the ideal Faraday rotation can be calculated. Figure 4.6 shows the Faraday rotation measurements versus the model for 2002. The plot shows that a better fit could be obtained by either a 12 hour displacement in time or a 7 degree rotation of the sun. The observations were obtained in UTC; we have studied the code used to produce the model and find that it is also initialized in UTC. Therefore we investigated the effect of a 7 degree error in longitude of the solar magnetic field and found that it could possibly explain the
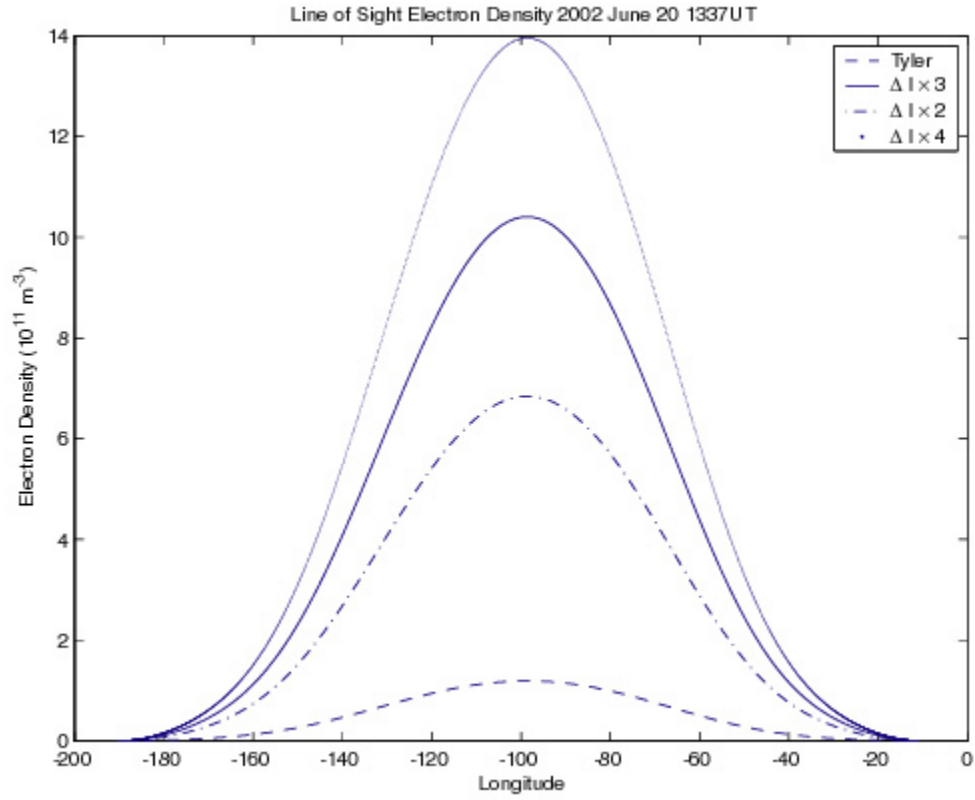
Figure 4.5: *The N values from the Tyler model (dashed) along the line of sight. The scaled values using the columnar electron density estimates for the time period (solid), and the error on those estimates (dash dotted and dotted) for 2002 June 20 at 1337UT.*

difference.

4.3 Magnetic Field Vector Fits

The PFSS magnetic field solutions from Equation 4.1 are summed with a correction vector $\vec{B}_{corr}$ (Equation 4.2) to produce a fit to the Faraday rotation observations. The range of possible solutions for the magnetic field vector are addressed in this section. Specifically, $-1 \geqslant \cos(\theta_i + \kappa) \leqslant 1$, and the range of κ is further restricted to maintain the same sign $(+/-)$ for Faraday rotation as the Faraday rotation observation. Within these boundaries, β is varied until a fit is made.

4.3.1 PFSS Solutions

Figure 4.7 shows the magnetic field vectors determined by the PFSS model along the line of sight. When the component parallel to the line of sight is calculated, notice that there is a reversal across the point of closest approach shown in the top panel on the right side. The other two reversals coincide with current sheet crossings; the boundaries of the vector plot were set at the current sheet crossings which were both located within 10 solar radii of the Sun.

In determining how best to fit the model to the observations, several assumptions are made. Note that because the region within 20 solar radii of the Sun has the greatest effect on the Faraday rotation measurement, the only corrections applied are within this region. First of all, it is assumed that the PFSS model accurately predicts the locations of the current sheet boundaries. This is confirmed by the 75% accuracy the WSA model has for predicting the N-S orientation of the interplanetary magnetic
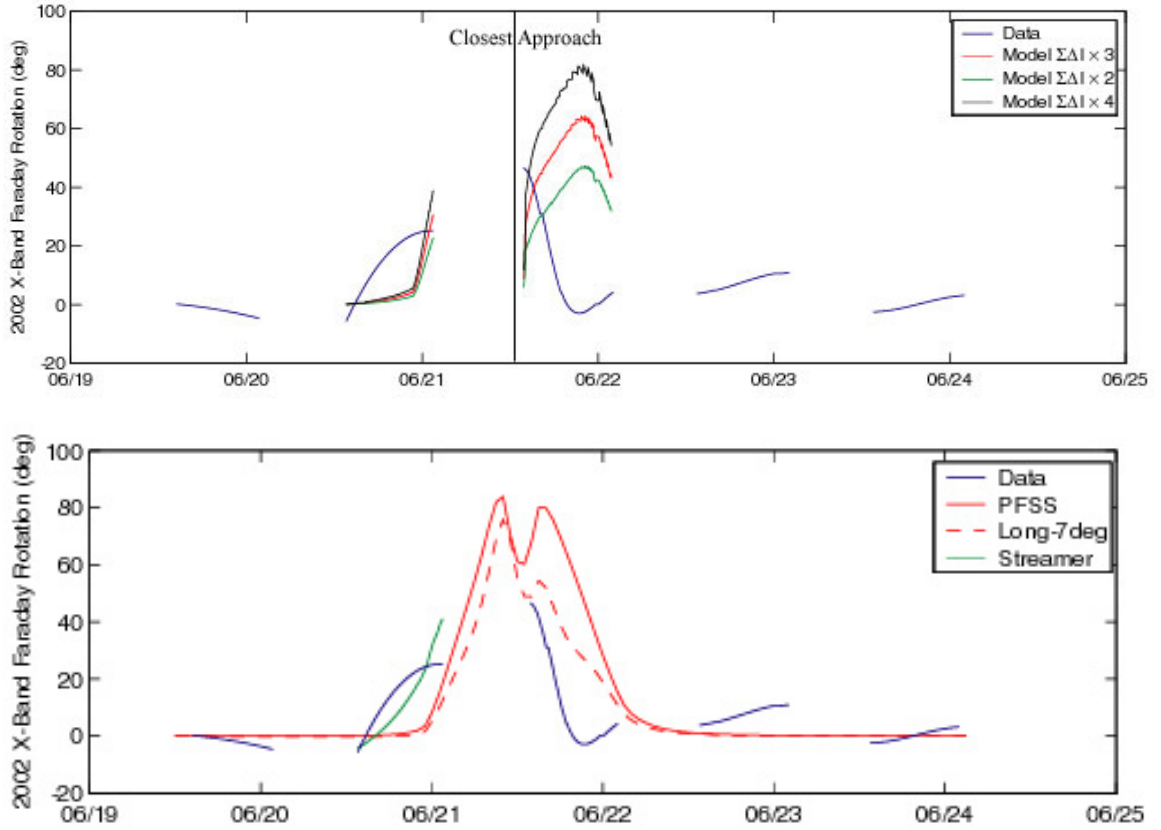
Figure 4.6: *The Faraday rotation observations for 2002 (blue), the model Faraday rotation (red), and the error in the model from the error in the electron density estimates (green and black) on the top plot. The bottom plot shows the Faraday rotation observations for 2002 (blue), the model Faraday rotation (red solid line), the model Faraday rotation with the solar dipole adjusted by seven degrees in longitude (red dashed line), and the model Faraday rotation accounting for the enhanced density due to a streamer in the line of sight on June 20th.*
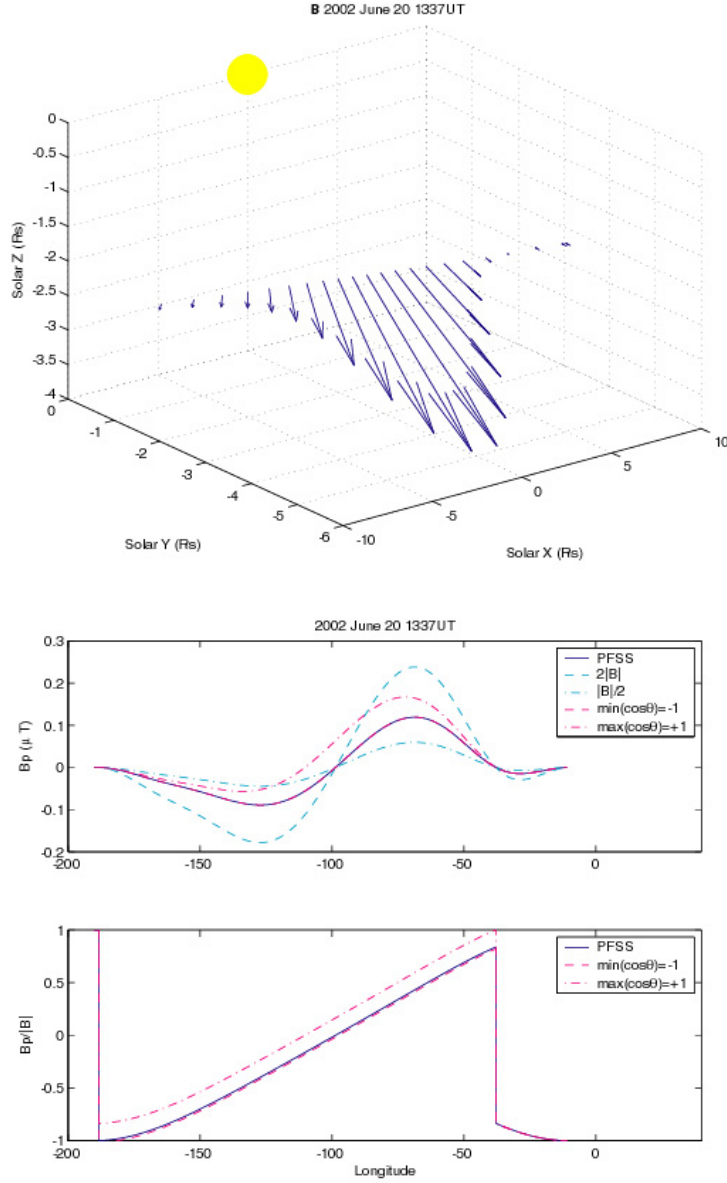
Figure 4.7: *The magnetic field vectors in solar coordinates relative to the line of sight (LOS) from Cassini to the Earth in the vicinity of 4 solar radii (top). The PFSS magnetic field component parallel to the line of sight (Bp) (middle). Cosine of the angle between $\vec{B}_{PFSS}$ and the LOS $\cos\theta = Bp/|B|$ (bottom). As shown in the middle panel, adjustments in the magnitude of $\beta|B|_i$ (cyan) cause Bp to increase or decrease proportionally, while adjustments in $\cos\theta + \cos\kappa$ (magenta) cause Bp to shift up or down. Note that the ratio of $Bp/|B|$ is limited to ± 1 as shown in the bottom plot.*

field (Arge & Pizzo, 2000). Therefore, the current sheet crossing boundaries are considered immovable.

We define $Bp = |B| \cos \theta$ as the magnetic component to the Faraday rotation observation. The bottom panel on the right side of Figure 4.7 shows the value of $\cos \theta = \frac{Bp}{|B|}$ along the line of sight. The current sheet crossings are clearly visible where $\cos \theta$ reverses sign. The 2nd assumption is that $\cos \theta$ can be erroneous and therefore is allowed to be adjusted. While the adjustment must stay within the range of -1 to 1, the amount and manner of the adjustment is not so clear. The 20 solar radii radius and current sheet crossings are used for boundaries in the adjustment; whichever is closer to the point of closest approach on either side of closest approach. These boundaries are used because the Faraday rotation difference is assumed to originate from close to the Sun, and there is not enough information to be more selective.

The range of acceptable $\cos(\theta + \kappa)$ values between -1 and 1 is further restricted by the sign of the integrated Faraday rotation calculation. For instance on 2002 June 19 1428 UT, the Faraday rotation calculation is 0.0373 deg while the observation is 0.2013 deg. If $\cos(\theta + \kappa)$ is adjusted to -1, the calculation then becomes -0.2567, and there is no possibility of a fit by adjusting β. Therefore, the $\cos(\theta + \kappa)$ parameter can only be adjusted by 3 degrees downward before the sign changes and there are no more possible solutions.

While it would be reasonable to assume that large electron density gradients are probably the regions most fit for adjustments in Bp, this concept must first be tested by assuming the electron density gradients are a separate variable. The rest of this chapter will be concerned with testing the correlation between the magnetic field and the electron density by attempting to fit an ideal Faraday rotation model

to the observations.

The last assumption regards the β component to the Faraday rotation observation. The PFSS model's photospheric observations for calculating $|B|$ can be erroneous by as much as a factor of 2. Therefore, changes in $|B|$ between $1/2$ and 2 can be assumed to be caused by measurement error; however, beyond this is significant. The top panel on the right side of Figure 4.7 shows the range of Bp values between $1/2 < \beta < 2$.

The range of acceptable $\beta(\kappa)|B|_i$ fits is much more flexible than $\cos\theta$. Theoretically, β can vary over the full range from 0 to infinity; however, there are some reasonable limits that can be placed on β. β values that are smaller than 0.3 give virtually flat Bp values which stand out in stark contrast to the PFSS solutions for large distances from the Sun; the usefulness of the PFSS model in predicting the interplanetary magnetic field strength indicates that this is not reasonable. Similarly, β values that are greater than 10 are not reasonable. Values for β greater than 0.5 and less than 10 are possible and will be included in the range of possible solutions.

Figures 4.8 and 4.9 show the β multiplying values necessary to accomplish a fit to the Faraday rotation values across the range of possible columnar electron density and Faraday rotation values.

4.4   Forward Model Fits

The solutions shown in Figures 4.8 and 4.9 indicate that a simple adjustment to the PFSS model can only be made for a fraction of the time. On June 20th for example, there is no small adjustment that can be made to the PFSS model to agree with
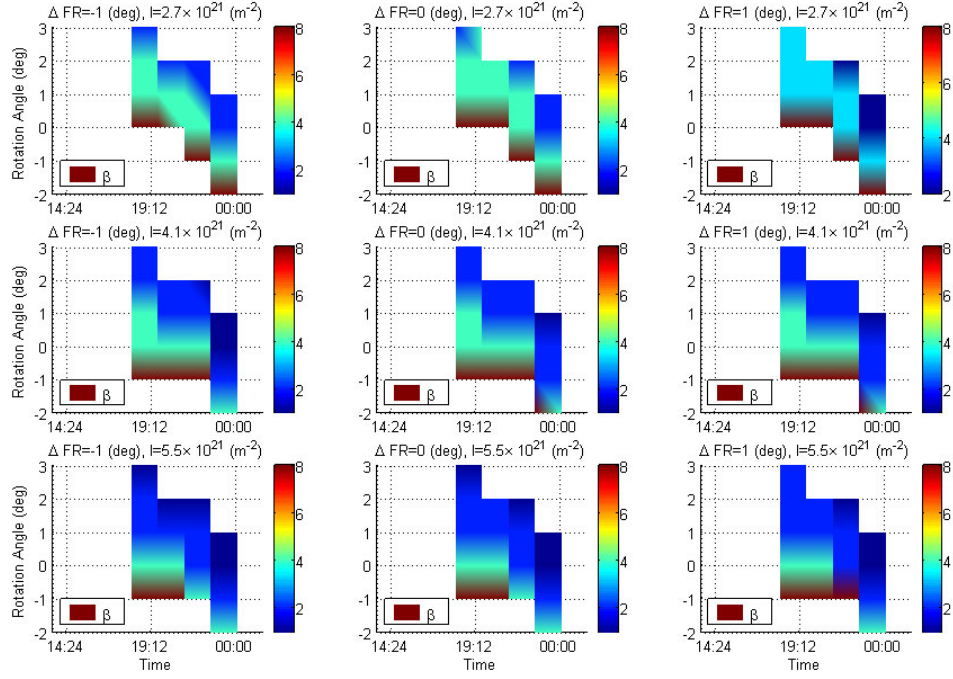
Figure 4.8: *The June 20 multiplying factor β required for the Faraday rotation calculation to fit the observations for the given change in* $\cos\theta + \cos\kappa = Bp/|B|$. *The step sizes are in 1 degree steps. This plot shows the multiplying factors between 0.5 and 10 for each possible κ within the columnar electron density and Faraday rotation errors.*
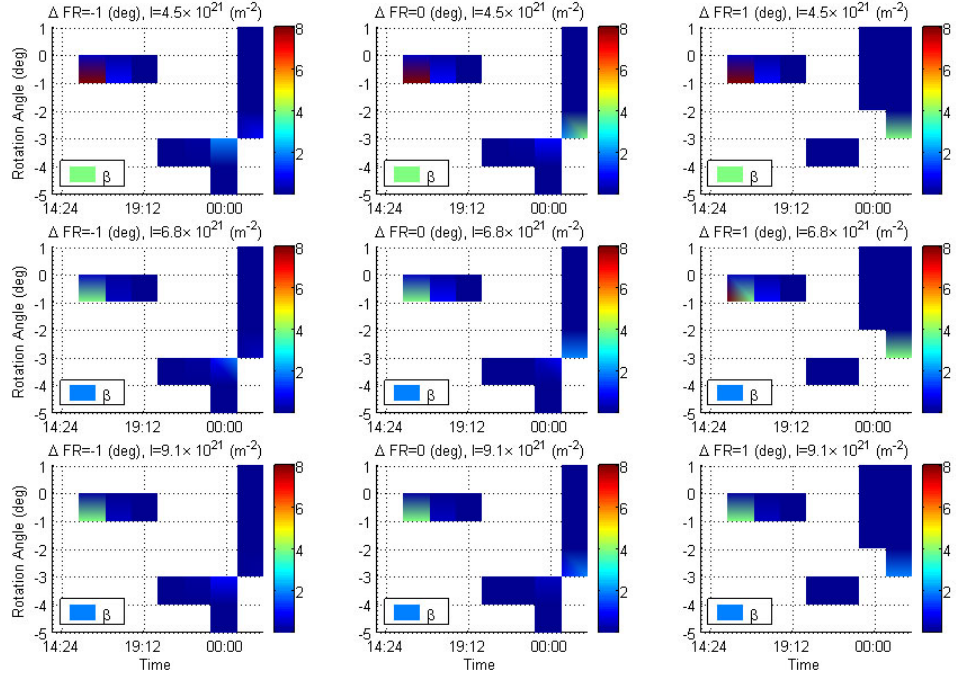
Figure 4.9: *The June 21 multiplying factor β required for the Faraday rotation calculation to fit the observations for the given change in* $\cos\theta + \cos\kappa = Bp/|B|$. *The step sizes are in 1 degree steps. This plot shows the multiplying factors between 0.5 and 10 for each possible κ within the columnar electron density and Faraday rotation errors.*

the observations prior to 1800UT and after 0000UT the following day. In contrast, on June 21st the model can be moderately adjusted to fit the observations for much of the time period. However, a significant portion of the time between 2000UT and midnight requires that the direction of the magnetic field vectors be adjusted. It is important to note that within the error in electron density and Faraday rotation measurements, the solution space shown in Figures 4.8 and 4.9 are consistent with some moderate variability at midnight on the 22nd.

The solutions shown on the 20th have a general trend of decreasing magnitude with time. For the initial estimates of magnetic pressure, the solution for zero rotation ($\kappa = 0$) was used. On the 21st, the zero rotation solution also was used except within the 2000UT to midnight time period when the -3 degree solution was used.

Figures 4.10 and 4.11 show the gradient in the magnetic pressure in the radial direction $-\nabla_r P_B$ associated with these solutions in the top plot. The next plot down in the figures shows the radial gradient in the thermal pressure $-\nabla_r P_T$. The thermal pressure is calculated from the 3D Tyler electron density values that were fit to the changing columnar electron density measurements from the Doppler data. Additionally, the temperature was assumed to be a constant $1 \times 10^6 K$. The 3D electron density values can also be used to determine the force of gravity in the region; this is presented as the gravitational force per volume NF_g shown in the 3rd plot from the top.

Finally, the UCSD/IPS electron density 3D tomographic values do not apply within the region being measured; however, they do contain information about the presence of streamers and the general distribution of electron density in the solar wind. For June 20, the UCSD/IPS data was extrapolated inward and normalized for comparison to the magnetic pressure plots (N_{rel}). These plots are shown in the bottom
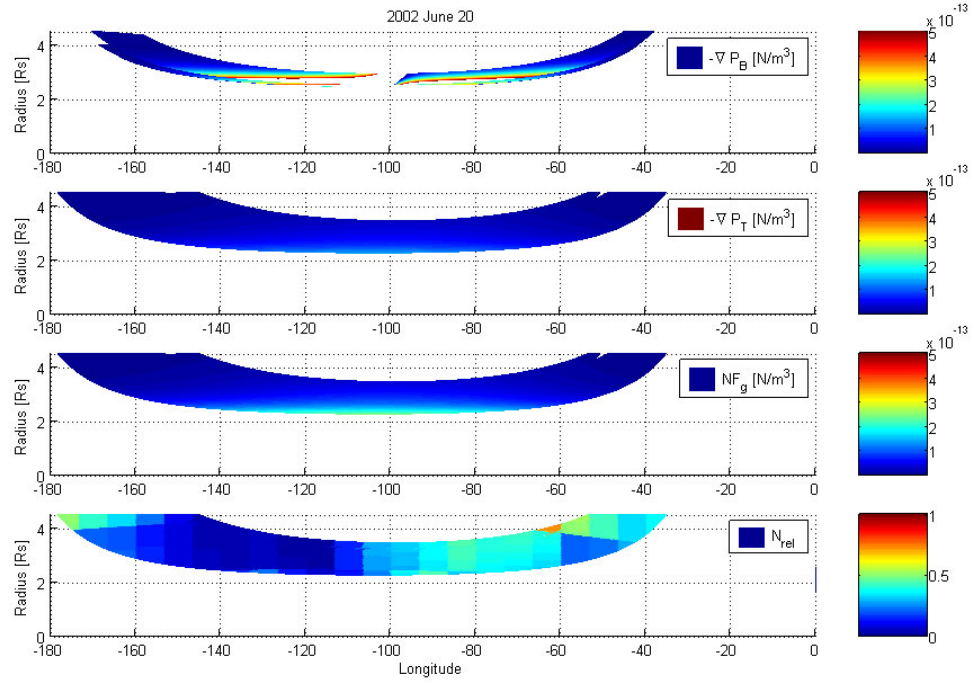
Figure 4.10: *The magnetic pressure gradient* $-\nabla_r P_B$ *from the Faraday rotation observation fit compared to the thermal pressure gradient* $-\nabla_r P_T$ *and the gravitational force per volume* NF_g *for 2002 June 20. The UCSD/IPS data* (N_{rel}) *has been extrapolated into the region and normalized to provide a visual comparison for the actual distribution of electron density in the region from a streamer.*
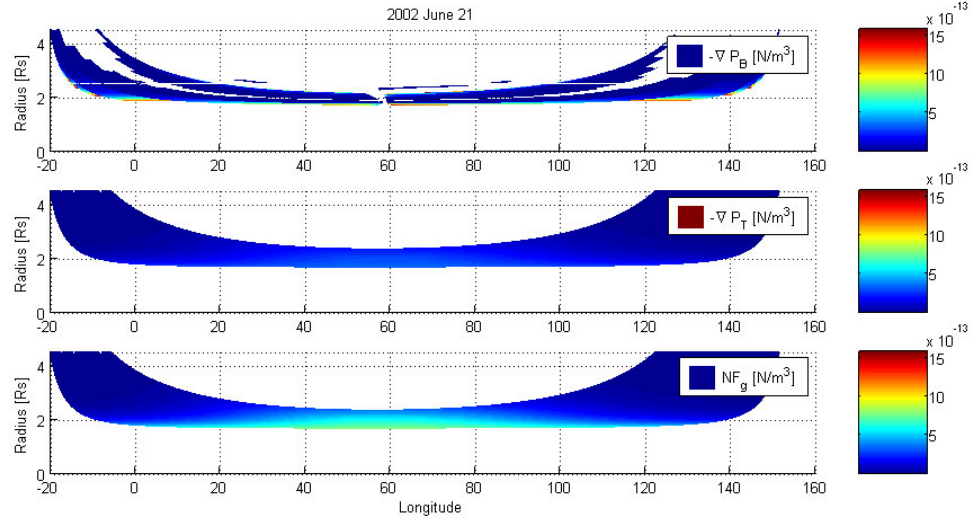
Figure 4.11: *The magnetic pressure gradient* $-\nabla_r P_B$ *from the Faraday rotation observation fit compared to the thermal pressure gradient* $-\nabla_r P_T$ *and the gravitational force per volume* NF_g *for 2002 June 21.*

plot. Unfortunately, the June 21 pass occurred in a region where there was a data gap in IPS observations.

On June 20th, the limited coverage given by the magnetic pressure is used in the estimates of the forces in the region. The gradient in the magnetic pressure varies between $10^{-13} - 10^{-12} N/m^3$ in the vicinity of the point of closest approach, the gradient in the thermal pressure varies from 3-14 $\times 10^{-14} N/m^3$ (the error contribution from the electron density error gives the range of 2-10 $\times 10^{-14} N/m^3$ assuming low density and 4-17 $\times 10^{-14} N/m^3$ for high), and the gravitational force per volume varies from 1-25 $\times 10^{-14} N/m^3$ (1-20 low and 1-30 high). This indicates that the PFSS model solutions initializing a fit to Faraday rotation observations can potentially provide a realistic model of the forces acting on the region. The SMEI plot for June 20th indicates that the electron density is variable in the longitudinal direction. We performed an initial investigation into the effect of asymmetrical electron density distribution and found that the magnitude of the magnetic pressure did not vary significantly while its symmetry varied in conjunction with the electron density distribution.

On June 21st within the 2.5 solar radii source surface, the magnetic pressure force varies between $10^{-15} - 10^{-9} N/m^3$ at the point of closest approach. The thermal pressure force varies from 20-35 $\times 10^{-14} N/m^3$ (the error contribution from the electron density error gives the range of 15-25 $\times 10^{-14} N/m^3$ assuming low density and 25-50 $\times 10^{-14} N/m^3$ for high) and the gravitational force varies from 30-80 $\times 10^{-14} N/m^3$ (30-50 low and 40-100 high). Once again the thermal pressure is weaker than the gravitational pressure; however, it's clear that the PFSS model initialized fits cannot model the magnetic pressure in the region. The fall off with radius is absent, and the small pressures calculated in the regions where the forward model Faraday rotation values were significantly greater than the data demonstrate that a small

adjustment to the PFSS model is insufficient.

4.5   Closing Remarks

The Faraday rotation observations obtained by the line of sight integration of the electron density and the component of the coronal magnetic field parallel to the line of sight provide a remote sensing measurement of the coronal magnetic field. Using the potential field source surface model for the magnetic field and the Tyler model for the electron density, the expected Faraday rotation measurement was calculated along the line of sight. Using the changing columnar electron density values determined from Doppler measurements, the Tyler model values were adjusted to reproduce these observations. Because Faraday rotation is sensitive only to the component of the magnetic field along the line of sight, the solution for the PFSS magnetic field vector can be both rotated and adjusted in magnitude. To address these, the PFSS vectors were rotated through all possible orientations en masse, and the necessary magnitude of the magnetic field vectors was adjusted to fit the Faraday rotation observations through a single scaling factor applied to all the vectors en masse.

As a result of the fitting calculations, a solution space was determined. The solution space occasionally did not cover the entire pass indicating that the PFSS model magnetic field solutions could not be used to perform the fits. The scaling factor values from minimum rotation were used in the calculation of the magnetic pressure for the region. In general, the gravitational force per volume dominated the thermal pressure gradient; however, the sum of the thermal and magnetic pressure gradients was shown to be sufficient to overcome the gravitational force per volume for 2002 June 20. The fits from 2002 June 21 clearly indicated that a simple adjustment to

the PFSS model cannot reproduce the Faraday rotation measurements; the closest approach of the lines of sight for the entire June 21 pass were below the 2.5 solar radii source surface.

This chapter is an initial investigation into comparing the forces acting on the solar wind. It is clear from these results that the radial gradient in the thermal pressure is not large enough to overcome the gravitational force per volume the Sun exerts on the plasma. The PFSS model assumes that $\vec{J}X\vec{B} = 0$ in the momentum equation below the source surface; the results from 2002 June 21 show that unless $\vec{J}X\vec{B} \neq 0$, then there would be no solar wind. Finally, more information is necessary using 3D tomography with more lines of sight. A full MHD analysis to the region can allow a better estimate of the force balance.

CHAPTER 5

Faraday Rotation Observations of CMEs

During the solar occultation radio observations of Pioneer 6, Pioneer 9, and Helios 1 and 2, solar transient crossings lasting several hours were observed. The Helios events were identified as coronal mass ejections (CMEs) by simultaneous observations of the Solwind coronagraph. Using these cases, Bird et al provided the first measurements of the CME magnetic field in the region between 3 and 10 solar radii. However, Bird et al could not infer the magnetic field structure of the CME. Since then we have determined using in-situ magnetometer measurements at 1AU that the magnetic field structure in an interplanetary CME (ICME) is a flux rope. This chapter tests the hypothesis that this flux rope structure is present in the CME at the Sun. Using the simple flux rope model developed for modeling the 1AU ICMEs we fit the Helios observations, and we present the information that can be determined from the flux rope fits on the CME size, orientation, and expansion velocity capable of reproducing the observations. Finally, we show that the Pioneer transients have the signature of flux rope crossings, indicating that they were caused by CME passages.

5.1 Faraday Rotation Transient Observations

Pioneer 6 and 9 and Helios 1 and 2, equipped with 2.3 Ghz (S-band) radio frequency carriers, observed solar transient crossings in 1968, 1970, and 1979. These transient crossings lasted several hours and ranged from 15 to 120 degrees in amplitude. This section discusses the observations in detail.

5.1.1 Pioneer 6

Pioneer 6 measured three 'W' shaped transients (Figure 5.1 left side) in 1968 which were clearly due to distances in the solar wind rather than in the Earth's ionosphere. If we remember that the plane of polarization from the spacecraft will be rotated in a positive or negative sense depending on the direction of the magnetic field and that the electron density only affects the magnitude of that adjustment, the Faraday rotation effect of the Earth's magnetic field is positive because the field is directed towards the ground in the northern hemisphere (i.e. at Goldstone, CA). Further, the line of sight from the spacecraft is at its most parallel to the Earth's magnetic field at the smallest hour angle (around noon). This is shown clearly in the diurnal Faraday rotation signature shown in Figure 5.1 (top right). Thus ionospheric effects would have increased the angle of the plane of polarization, rather than decrease it. The transit time of the transients were around 3 hours, the maximum $|FR|$ was around 40 degrees, and they occurred at solar offsets of 11.5, 9, and 6.5 solar radii.
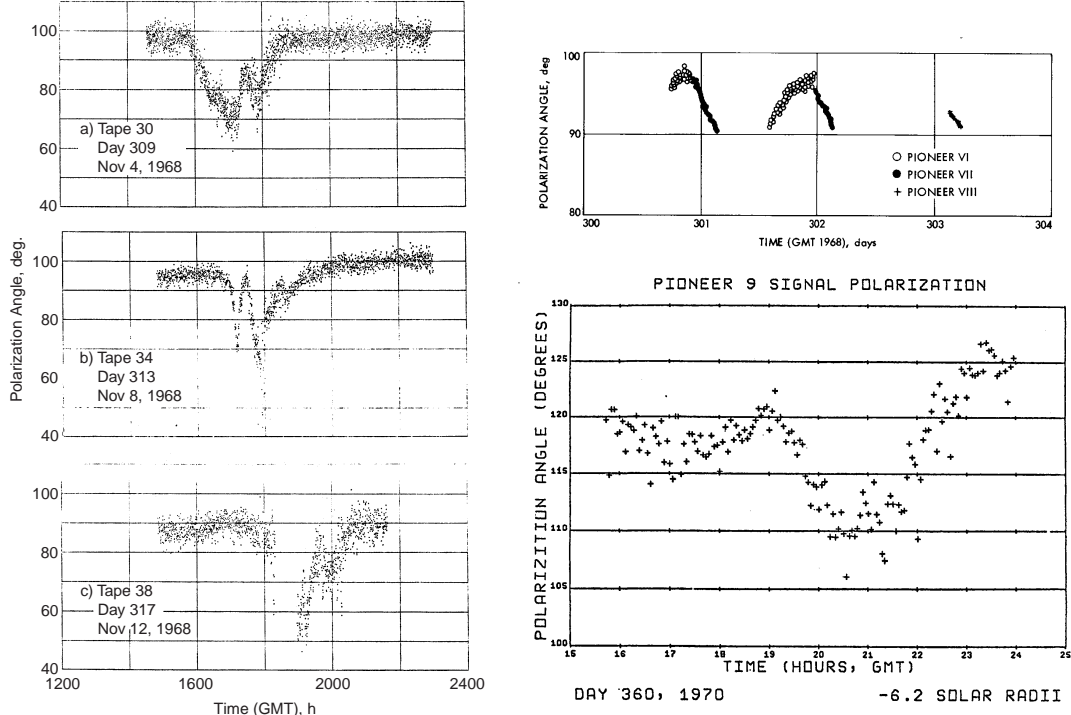
Figure 5.1: *Pioneer 6 Faraday rotation transients (left) observed on 1968 November 4, 8, and 12. The transients were 'W' shaped, lasted approximately 3 hours, and ranged over 40 degrees (Stelzried, 1968). The top right plot shows the Faraday rotation caused by the Earth's magnetic field and ionosphere. On the bottom right, the sigmoidal transient observed by Pioneer 9 on 1970 December 26. The transient signature is incomplete, and started around 1900 UT. The feature ranges over approximately 15 degrees and lasts longer than 5 hours (Cannon, 1976).*

5.1.2 Pioneer 9

Pioneer 9 measured a sigmoidal transient (Figure 5.1 bottom right); the transit time of the structure was around 6 hours, the maximum $|FR|$ was around 10 degrees, and the impact parameter of the point of closest approach was 5.8 solar radii.

140

5.1.3 Helios CMEs

The CMEs observed by the Solwind coronagraph and measured by the Helios S-band (2.3 GHz) radio frequency carrier are distinct from previous transient measurements because the coronagraph observations were used to select the intervals of Helios Faraday rotation measurements to be analyzed. Both observations in Figure 5.2 were on the west-limb, the angular extent of the CMEs were 40 and 20 degrees respectively, and the observed velocities were 115-145 km/sec and 120-160 km/sec. The first CME observation was incomplete; however, it appears to have lasted 8 hours and rotated a maximum of 120 degrees. The second CME lasted 6 hours and rotated a maximum of 60 degrees. As will be discussed in the last section, the 1979 October 24 CME appears to be twisted past the point where the axial field reverses (Figure 5.4 at α(r/R)=2.4).

The October observation in Figure 5.3 was either a halo CME with strong limb brightening on the east-limb or an east-limb eruption with an angular range of approximately 20 degrees with Helios passing over rather than through the CME, while the November CME was on the west-limb. The velocity in the plane of the sky falls in the range of 60-370 km/sec. The November 16 CME is clearly moving out of the plane of the sky with an angular range of 110 degrees. The time period of the October CME is not clear; however, the November CME appears to have a 3 hour transit time based on the changes in Faraday rotation scatter at the leading edge around 1200 UT and the trailing edge around 1500 UT. This time period is difficult to define against the general background Faraday rotation expected in the vicinity of 3 solar radii for a 2.3 GHz signal as it approaches the local plasma frequency at the point of closest approach. The velocity could not be determined from the coronagraph images, and the ultimate value used ($1000 km/s$) will be discussed in Section 5.5.
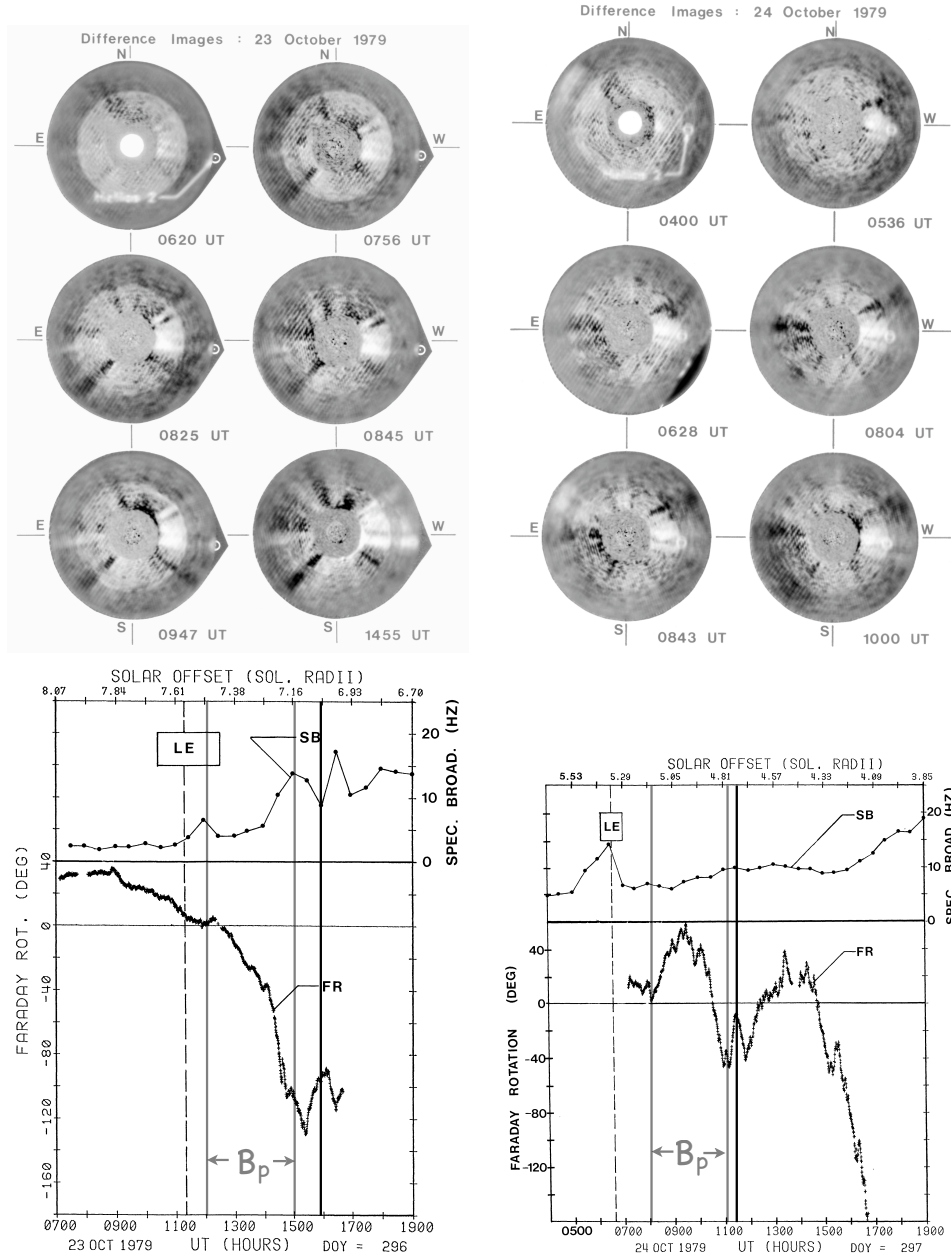
Figure 5.2: *Difference coronagraph images from Solwind during the 1979 October 23 and 24 CMEs and the associated Helios Faraday rotation signatures. The Faraday rotation (FR) and spectral broadening (SB) curves are marked in the plots. The Faraday rotation 'W' signatures for both events are similar to the Pioneer 6 transients in shape. Note that the density enhancements shown are with respect to the previous time period. Magnetic field measurements were obtained for the range marked (Bp) following the leading edge (LE) of the CME using the electron density enhancements observed by Solwind (Bird et al., 1985).*
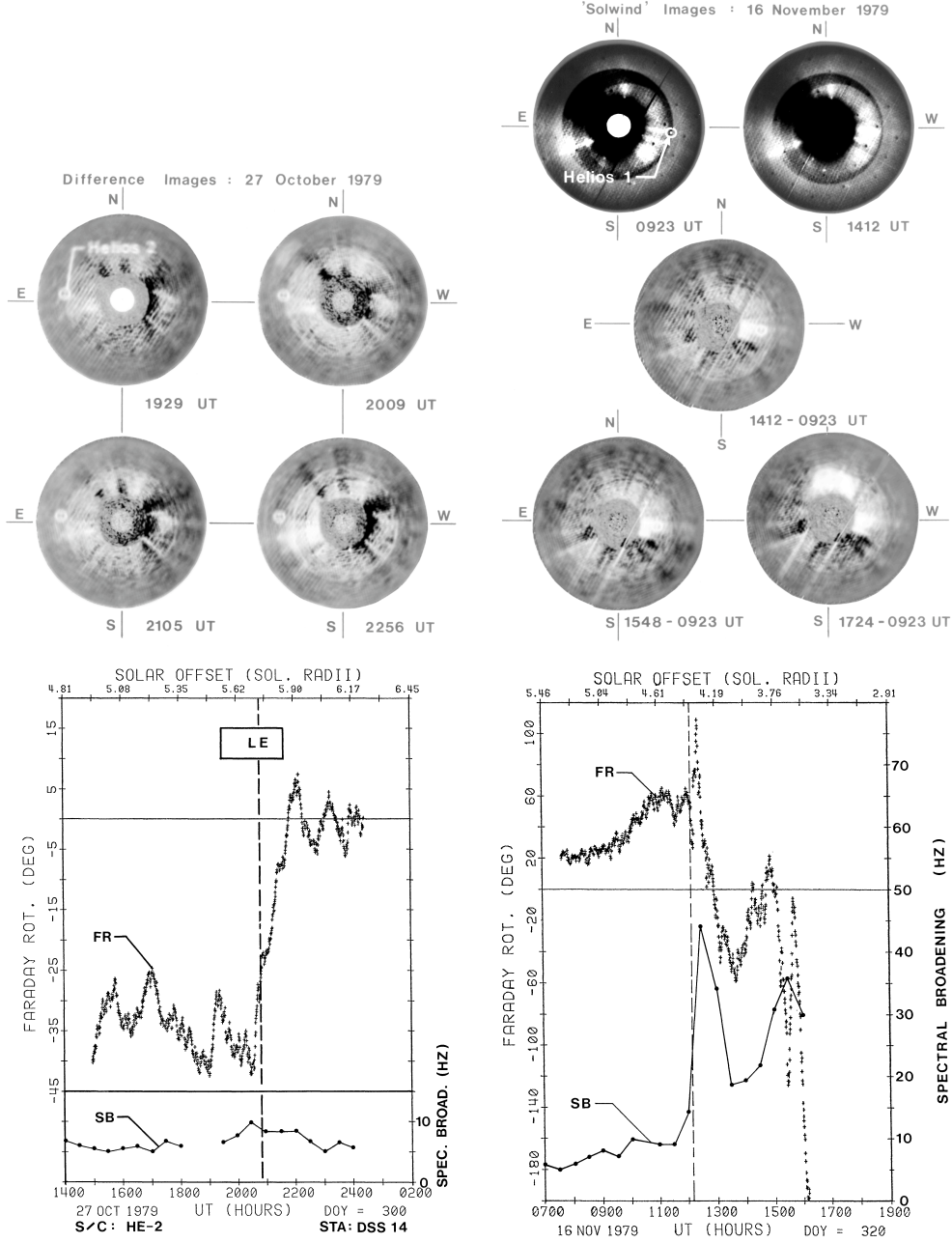
Figure 5.3: *Difference coronagraph images from Solwind during the 1979 October 17 and November 16 CMEs and the associated Helios Faraday rotation signatures. The Faraday rotation (FR) and spectral broadening (SB) curves are marked in the plots. The October event is unusual and will be discussed later. The Faraday rotation reverse sigmoid signature for the November event is similar to the Pioneer 9 transient in shape. Note that the density enhancement for November is with respect to the 0923 UT time period. The leading edge (LE) of the CMEs are marked (Bird et al., 1985).*

5.2 Modeling a CME

When a Coronal Mass Ejection crosses the line of sight, some properties of the CME can be determined using the combination of radio frequency data and velocity information from coronagraphs or the time difference between the start of a CME crossing and the time of increased solar activity (Section 5.5). The electron density distribution and the flux rope magnetic field strength can be separated with the use of ranging data; however, this was unavailable during all CME crossings. The orientation of a CME can be determined by the shape of the Faraday rotation signature it produces; however, the ϕ angle is ambiguous with the handedness without magnetic field observations of the handedness prior to eruption. Finally, the velocity and orientation of the CME can provide information on the CME size and expansion rate. Therefore, there is enough information to construct a simple flux rope model for a Coronal Mass Ejection using the set of variables for location, size, orientation, velocity, expansion velocity, magnetic field magnitude (B_0), twist (α), and electron density. Note that excepting the 1979 October 23 and 24 flux ropes for which there are magnetic field and electron density data, the two variables (N and B) cannot be separated in the remaining flux ropes.

5.2.1 The Taylor State Flux Rope Model

The Taylor state flux rope model discussed in Section 1.5.1 is constructed using the magnetic field magnitude of the central axis of the rope $|B|$, the Bessel function constant α, handedness ($H = \pm 1$, where +1 is right-handed), and radius size (R) for inputs. Recalling Equation 1.1

$$B_{axis} = B_0 J_0(\alpha r/R)$$

$$B_{tor} = B_0 H J_1(\alpha r/R)$$

$$B_r = 0$$

The Bessel function is shown in Figure 5.4 where the magnetic field configuration at a particular radius within the flux rope (r) is given by $\alpha(r/R)$. For instance, as shown in Figure 5.5 the field lines near the center have very little twist. At $\alpha(r/R) = 0.61$ in Figure 5.4, the axial magnetic field J_0 is 4-5 times greater than the toroidal magnetic field J_1; Figure 5.5 shows this as a field line with very little twist. At the edge of the flux rope, $\alpha = 1.84$ and $r = R$, the field line is strongly twisted; this is shown in Figure 5.4 where J_0 is approximately half the value of J_1. In the Taylor state flux rope model, flux ropes with different α's have different amounts of twist in the magnetic field configuration on their outer edges and distribution of twist as a percent of radius (Russell & Mulligan, 2003).

5.2.2   Determining the Position of the CME in Space

The inputs for determining the position of the CME as it crosses the line of sight are the time the crossing starts and stops, the time the axis of the flux rope intersects the line of sight, the velocity of the CME, an estimate of the orientation of the CME relative to the line of sight, and an estimate of the angle the trajectory of the CME is out of the plane of the sky (CA). The time the CME axis intersects the line of sight and the velocity of the CME allow an estimate of the location of the axis of the CME at the start and stop times. The minimum distance between the CME axis and the line of sight allow the determination of the radius of the flux rope at the crossing start and stops times (Figure 5.6, described in detail below). If the radius is different between the two positions then the difference is used to calculate
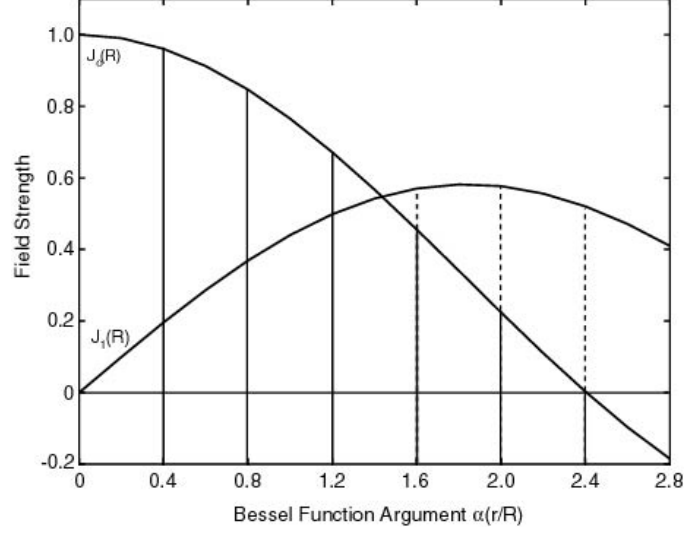
Figure 5.4: *Bessel function solutions for a constant α (Taylor state) flux rope. The axial field is given by $B_{axis} = B_0 J_0(\alpha r/R)$ and the toroidal field is given by $B_{tor} = B_0 H J_1(\alpha r/R)$ where r is the radius within the rope of radius R (Russell & Mulligan, 2003). Note that $H = \pm 1$ is for the handedness of the rope; +1 is right-handed and -1 is left-handed.*

the expansion velocity of the CME.

Without columnar electron density data, the magnetic field magnitude and electron density variables cannot be separated, so the magnitude of the variation of the Faraday rotation through the transient per se can provide no information on the magnetic field magnitude. Since the direction of the magnetic field determines the sign of the Faraday rotation while the magnitude of the electron density and magnetic field parallel to the line of sight determines the magnitude of the Faraday rotation response, only the relative magnitudes of the Faraday rotation response contain useful information; all solutions that satisfy, $N \times |B| = constant$ are acceptable. For the purposes of fitting as a consequence of this, the Faraday rotation measurements and model calculations were normalized. The change in columnar electron density in the 2002 October 23 and 24 CMEs was measured allowing a
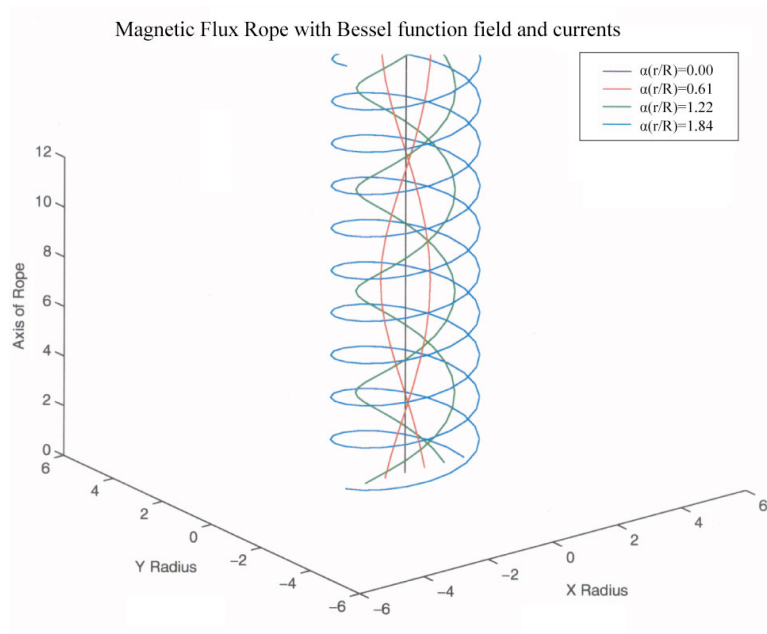
Figure 5.5: *The magnetic field line configuration of a Taylor state flux rope with Bessel function constant $\alpha = 1.84$ where r is the radius within the rope of radius R (Russell & Mulligan, 2003).*

measurement of $|B|$; in these two cases, the normalized fit was performed to determine CME orientation, and then the total electron density was adjusted to fit the observations allowing the determination of the total electron density. Note that velocities measured from decametric bursts (Section 5.5) and coronagraphs are in the plane of the sky ($V_{apparent}$) and required adjusting by the cosine of the angle of displacement from the point of closest approach (CA) to determine the actual velocity (V).

$$V_{apparent} = V\cos(CA)$$

The position of Cassini is given by $\vec{rc}$, the signal path is given by $\widehat{rsp}$, and the center of the CME is given by $\hat{c}$. Note that the center is the center point of the rope axis in the center of the rope. At the time of the center of the flux rope crossing the line of sight, the calculation is

$$\vec{rc} + \alpha\widehat{rsp} - \delta\hat{c} = 0 \tag{5.1}$$

Using the initial guess for the orientation of the CME, this is an over-determined system with unknowns α and δ solved using 3 equations. Note that the center of the rope is not allowed to be displaced from the Sun-spacecraft-Earth plane.

At the times the rope crossing starts and finishes, the $\vec{rc}$ and $\widehat{rsp}$ vectors are in a different position, while $\hat{c}$ remains constant. As shown in Figure 5.6 for a CME oriented perpendicular to the line of sight as the crossing starts, the shortest distance from the line of sight to the central axis of the CME is perpendicular to both (labeled $\hat{v}$) which gives the size of the CME radius. Note that the CME length is set to twice

148
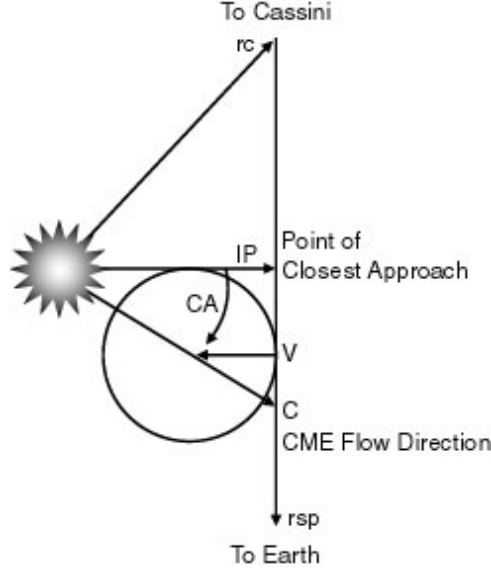
Figure 5.6: *The geometry of a CME crossing at initiation. The position of Cassini (rc), the signal path (rsp), the CME track (c), the perpendicular to the axis of the CME and the signal path (v), the vector to the point of closest approach (ip), and the angle from ip to c (CA) are shown.*

the size of the radius. This was an arbitrary setting to limit the size of the rope that is crossing the line of sight at parallel and anti-parallel orientations based on the fact that real CME flux ropes are curved and have footpoints located back on the Sun with only a finite part of the structure crossing the line of sight.

With the calculation of the CME radius as the crossing starts and finishes, the expansion velocity is simply the quotient of the difference in radius and the length of time of the crossing. Changes in the orientation and position (CA angle) of the CME affect its size and expansion velocity; as the fit minimizes the difference between the model and data, all these parameters are recalculated.

5.2.3 CME Orientation

The orientation of the CME relative to the line of sight determines the response of the Faraday rotation observation. Therefore, a coordinate system is constructed relative to the line of sight; the x-axis is pointed towards the source, the z-axis to the normal of the Earth-Sun-Spacecraft plane, and the y-axis completes the right handed coordinate system.

Using the direction of closest approach (away from the Sun) ($\widehat{ip}$) and the signal path ($\widehat{rsp}$), then the orientation of the flux rope relative to the line of sight can be calculated (coordinate system C1 in Figure 5.7). Note that the x-axis in the C1 system is oriented in the negative direction to the signal path ($\widehat{rsp}$).

$$
\begin{aligned}
\widehat{rope}_z &= \frac{\widehat{ip} X \widehat{rsp}}{|\widehat{ip} X \widehat{rsp}|} \\
\widehat{rope}_z &= \widehat{rope}_z b_{limb} \\
\widehat{rope}_x &= -\widehat{rsp} \\
\widehat{rope}_y &= \frac{\widehat{rope}_z X \widehat{rope}_x}{|\widehat{rope}_z X \widehat{rope}_x|}
\end{aligned}
\tag{5.2}
$$

where b_{limb} is the binary value of 1 (east-limb) or -1 (west-limb); remember that the east-limb is on the left and the west-limb is on the right for spacecraft and northern hemisphere coronagraphs. Finally, the rotation matrix to convert from solar to rope coordinates is:

$$
\overset{\leftrightarrow}{S2C_1} =
\begin{bmatrix}
\widehat{rope}_{x_i} & \widehat{rope}_{x_j} & \widehat{rope}_{x_k} \\
\widehat{rope}_{y_i} & \widehat{rope}_{y_j} & \widehat{rope}_{y_k} \\
\widehat{rope}_{z_i} & \widehat{rope}_{z_j} & \widehat{rope}_{z_k}
\end{bmatrix}
\tag{5.3}
$$
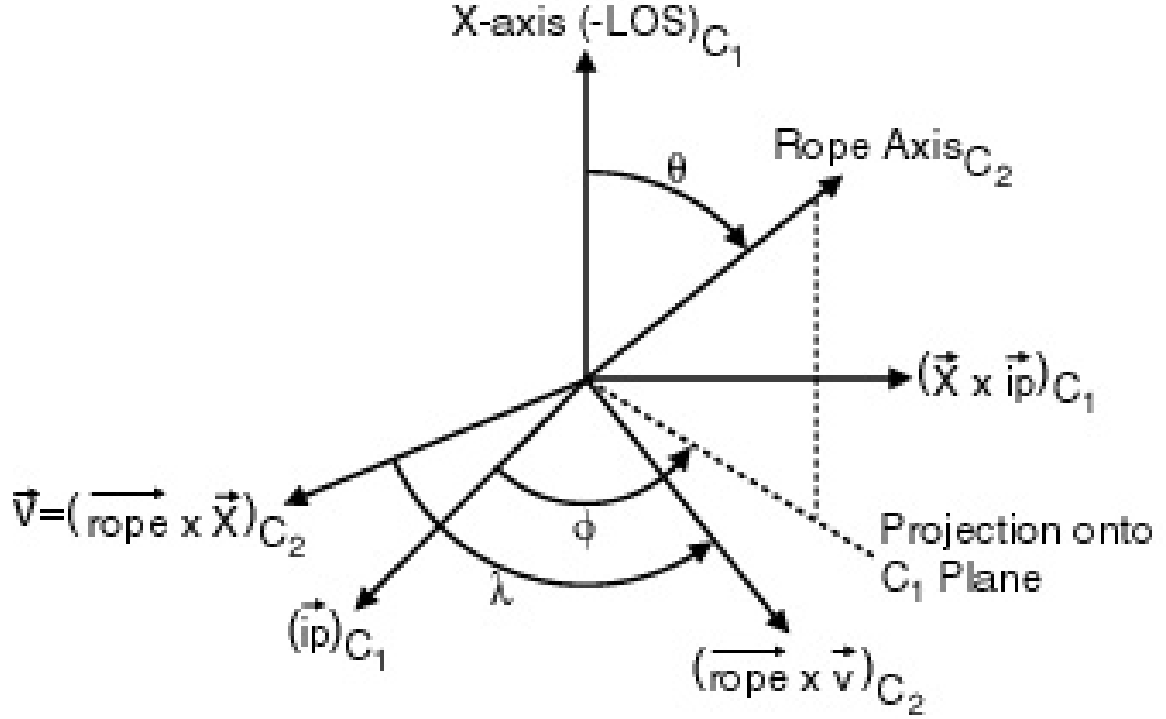
Figure 5.7: *The coordinate system in the frame of the observation geometry (C1): signal path (LOS), closest approach (ip), and the perpendicular to complete the right handed coordinate system. Note that closest approach (ip) is directed away from the Sun. The coordinate system of the flux rope relative to this system is shown (C2): rope axis (rope), perpendicular (v) to rope and signal path, and perpendicular to complete the right handed coordinate system. ϕ and θ are the azimuthal and cone angles respectively. The angle λ is used to determine the direction of the toroidal magnetic field in cartesian coordinates.*

The input parameters for the azimuthal angle (ϕ) and cone angle (θ) of the rope relative to the line of sight are defined in this $\widehat{rope}$ (C1) coordinate system. Note that the clock angle is $90 - \phi$; where ϕ is the angle from the y- to the z-axis, the clock angle is the angle from the z- to the y-axis. The cone angle is the tilt angle from the x-axis.

The internal magnetic field coordinate system that is used (system C2 in Figure 5.7) is defined by the axis of the rope for the z-axis ($\widehat{rope}$), the $\widehat{v}$ vector for the x-axis, and the y-axis is is the cross product of the two ($\widehat{rope}X\widehat{v}$). This is accomplished with the input ϕ and θ angles. Note that λ in Figure 5.7 is an angle that is used to determine the direction in which the toroidal component of the magnetic field points.

$$
C_1\overset{\leftrightarrow}{2}C_2 =
\begin{bmatrix} 0 & 1 & 0 \\ 0 & 0 & 1 \\ 1 & 0 & 0 \end{bmatrix}
\begin{bmatrix} \sin\theta\cos\phi & \sin\theta\sin\phi & \cos\theta \\ \frac{\sin\theta\sin\phi}{|\sin\theta|} & \frac{-\sin\theta\cos\phi}{|\sin\theta|} & 0.0 \\ \frac{\sin\theta\cos\theta\cos\phi}{|\sin\theta|} & \frac{\sin\theta\cos\theta\sin\phi}{|\sin\theta|} & \frac{(-\sin\theta)^2}{|\sin\theta|} \end{bmatrix}
\tag{5.4}
$$

5.2.4   Orientation

Multiple modeling runs over the full range of possible azimuthal and cone angles were used to develop a template for the shape of the expected Faraday rotation structures. The template was used to determine the orientation with which to initialize the fit. CME crossings with a very small cone angle as shown in Figure 5.8 produced a dip in Faraday rotation as shown in Figure 5.9. Note that the runs used to produce the template used a variable electron density (increased with radius) in order to better view the asymmetry between different azimuthal angles. The rest of the template is shown in Figures 5.10 and 5.11. Because the figures were generated for
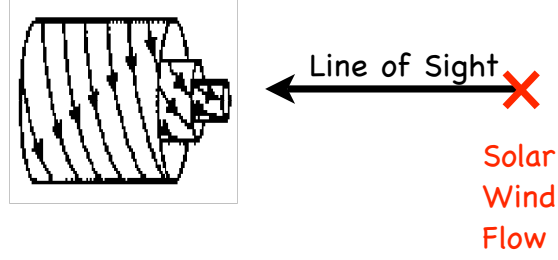
Figure 5.8: *The antiparallel flux rope orientation relative to the line of sight. Note that the rope is convecting into the page with the solar wind. The Faraday rotation will decrease as the crossing starts, reach a minimum when the axis passes, and then increase to the (original) background Faraday rotation when the crossing ends.*

right-handed CMEs on the east-limb, the proper initialization depends on making the appropriate adjustment to the template for left-handed and west-limb ropes. A left-handed east-limb rope would produce the same signatures reversed with respect to the abscissa. A right-handed west-limb rope would produce the same signatures reversed with respect to the abscissa. Finally, this template requires no correction for a left-handed west-limb rope.

5.2.5 Electron Density

The only magnetic field measurements that were previously obtained of CMEs were the Helios 1979 October 23 and 24 Faraday rotation observations shown in Figure 5.12 for the period of time labeled 'Bp' in Figure 5.2 (Bird *et al.*, 1985). Figure 5.9 illustrates that these estimates were obtained from a quasi antiparallel axial magnetic field configuration relative to the line of sight. Therefore, the magnetic field estimates are accurate for modeling purposes. For the rest of the transients and CMEs, we do not have independent electron density data so the electron density was kept constant throughout the flux rope.
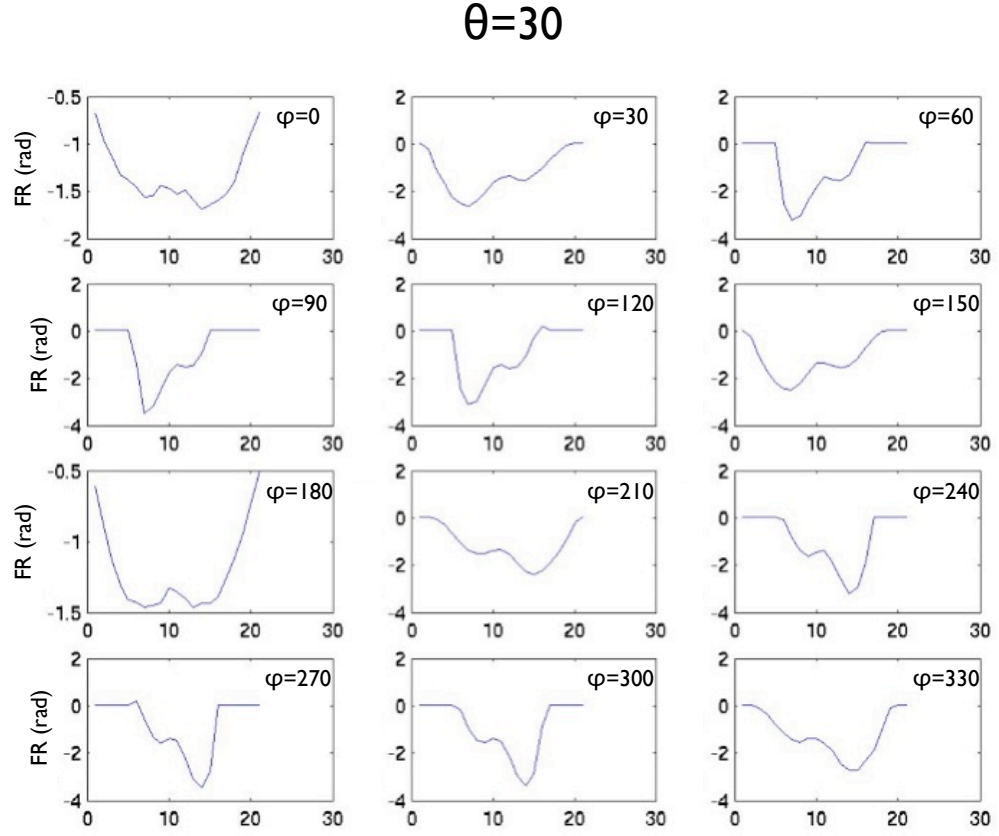
Figure 5.9: *Modeled Faraday rotation in a flux rope of varying azimuth for a quasi antiparallel CME ($\theta = 30$). Note that these plots apply to an east-limb, right-handed (or west-limb, left-handed) flux rope, and the electron density increases with radius in the rope.*
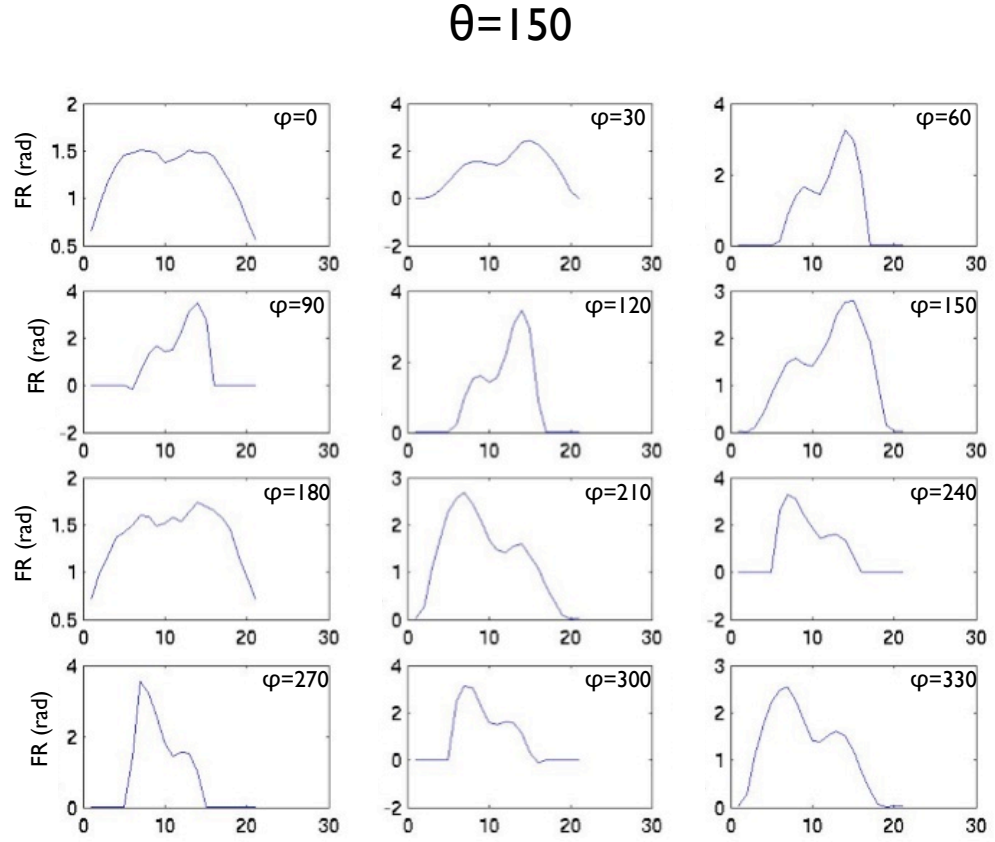
Figure 5.10: *Modeled Faraday rotation in a flux rope of varying azimuth for a quasi parallel CME ($\theta = 150$). Note that these plots apply to a east-limb, right-handed (or west-limb, left-handed) flux rope, and the electron density increases with radius in the rope.*
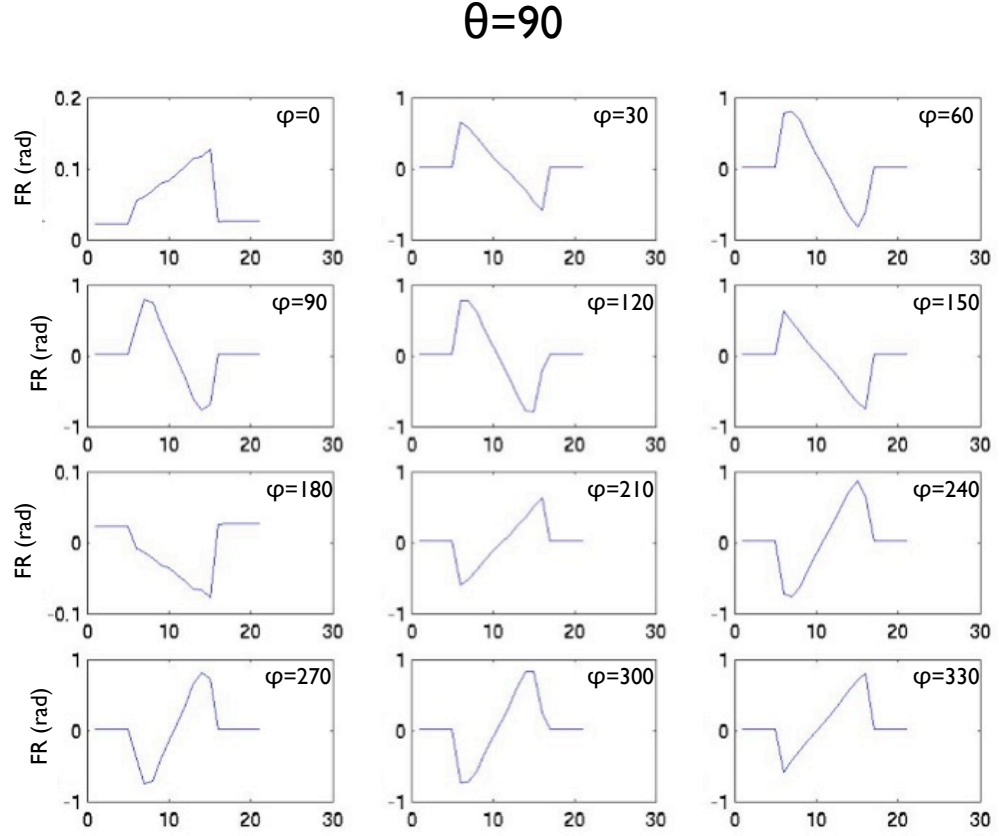
Figure 5.11: *Modeled Faraday rotation in a flux rope of varying azimuth for a perpendicular CME ($\theta = 90$). Note that these plots apply to an east-limb, right-handed (or west-limb, left-handed) flux rope, and the electron density increases with radius in the rope.*
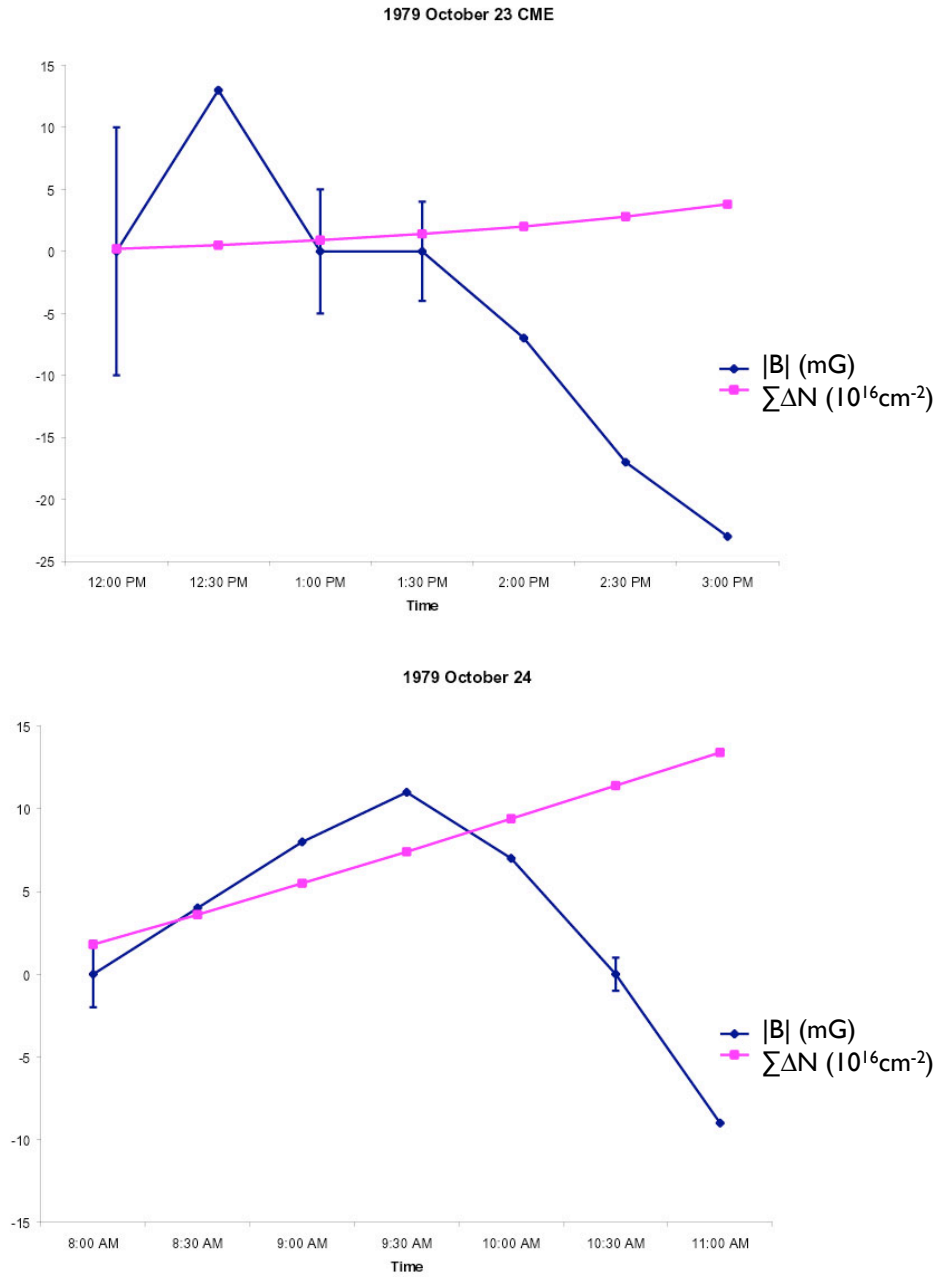
Figure 5.12: *Bird et al (1985) measurements of CME magnetic field from Helios Faraday rotation and Solwind Coronagraph observations. Note that the initial columnar electron density is unknown; the Solwind data was only of sufficient quality to determine the change in electron density.*

The axial magnetic field strength determined by Bird for the 1979 October 23 and 24 CMEs varied between 0.3-1.3 μT. The change in columnar electron density varied between 10 and 25 $\times 10^{20}$ m^{-2} indicating that the electron density contribution to Faraday rotation is the dominant component of the Faraday rotation equation. Therefore, the rest of the CMEs were assumed to be approximately 1 μT in axial field strength. With this assumption the total columnar electron density for the other CMEs was approximated as shown in Table 5.2.

5.3   Fit Analysis

The flux rope fits shown in Figure 5.13 indicates that the Taylor state flux rope model performs well in modeling the observed Faraday rotation fluctuations. Table 5.1 gives the orientation cone (θ), azimuthal angle (ϕ), and angle of displacement from closest approach (CA, Figure 5.6) which were used to produce the fits. The determination of the CME orientation thereby led to the calculation of the other parameters, CME size (R), expansion velocity (V_e), and columnar electron density (I) in the case of 1979 October 23 and 24 (Table 5.2). Because CMEs expand as they move out in the solar wind and therefore decrease in density, the distance the CME was from the Sun (IP) is given.

5.3.1   Helios

The 1979 October 23 CME measured by Helios (Figure 5.2) is distinct from previous measurements because the large rotation is observed entering the structure, but the central peak does not rise more than 1/4th of the rotation in the first indicating that the electron density variability in the structure is not proportional to its density. The

Table 5.1: *The orientations of the flux rope fits to the observed Faraday rotation transients assuming left hand ropes.*

Date	limb	θ (deg)	ϕ (deg)	CA (deg)
1968 November 4	west	0.5	-11.4	±32.3
1968 November 8	west	33.6	25.9	±61.8
1968 November 12	west	28.9	-9.0	±8.1
1970 December 6	east	104.7	82.2	±29.0
1979 October 23	west	-27.8	19.8	±35.1
1979 October 24	west	28.6	28.6	±28.6
1979 October 27	east	98.9	83.5	±88.7
1979 November 16	west	55.8	86.1	±50.6

Table 5.2: *The impact parameters and radii of the flux rope fits in solar radii (IP), observed velocities (V_{app}) (over the error range) and expansion velocities (V_{exp}) of the fits in km/s, and (for 1979 October 23 and 24) columnar electron densities (I) of the observed CMEs.*

Date	I $10^{20}m^{-2}$	IP Rs	V_{app} km/s	R_{CME} Rs	V_{exp} km/s
1968 Nov 4	*1.3*	11.5	930 (450,1170)	4.7 (2.3,6.0)	190 (91,240)
1968 Nov 8	*0.9*	9.0	1400	4.7	13
1968 Nov 12	*1.3*	6.5	640 (440,820)	2.3 (1.6,3.0)	-150 (-10,-190)
1970 Dec 6	*1.2*	5.8	120	1.5	-15
1979 Oct 23	4.4 (4.1 , 4.4)	7.0	150 (60 , 220)	1.0 (0.17 , 1.6)	-6.5 (-0.95 , -11)
1979 Oct 24	2.7 (2.2 , 3.7)	4.8	160 (80 , 210)	1.8 (0.73 , 2.4)	-18 (-7.8 , -25)
1979 Oct 27	*3.7*	5.8	260 (60 , 370)	7.5 (4.9 , 15)	2000 (790 , 3400)
1979 Nov 16		3.4	1000		
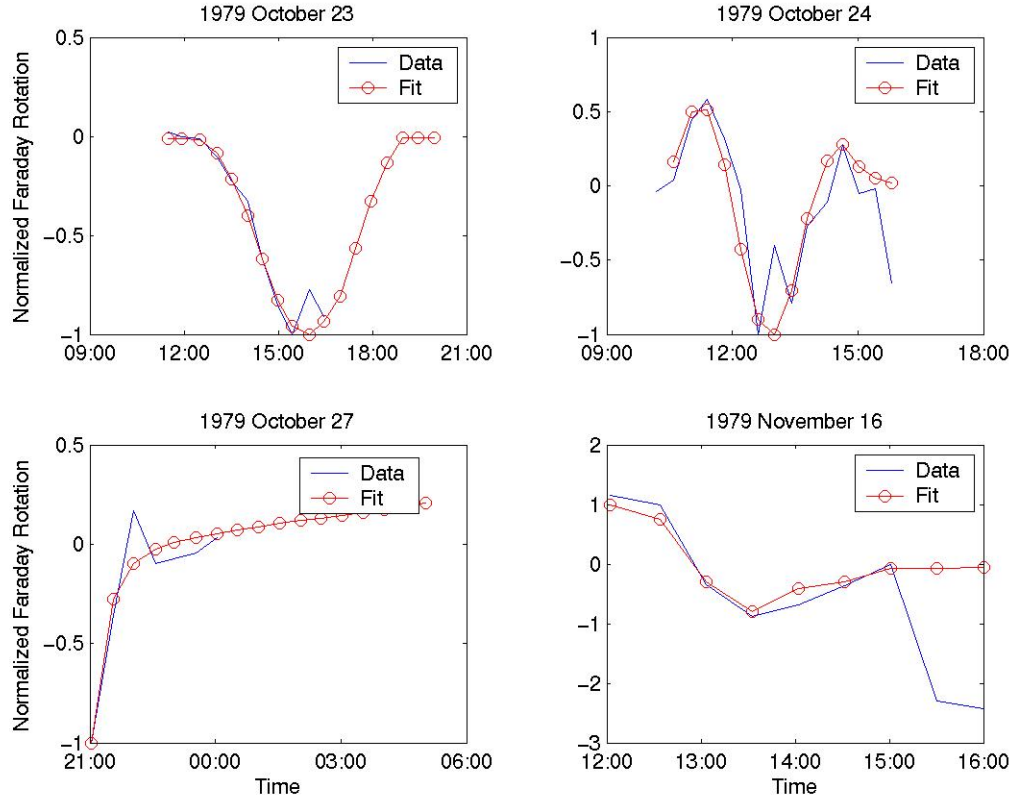
Figure 5.13: *The normalized Faraday rotation CMEs and their flux rope fits for the Helios CMEs.*

1979 October 24 CME closely resembles the Pioneer 6 transients; Bird determined that the electron density variability in the October 24 CME was greater than the 23rd. The fits indicate that the columnar electron density of the 24th CME is less than the 23rd; this suggests that there may be an inverse relationship between the total columnar electron density and the electron density variability through a structure.

The rise on either side of the October 24 CME can easily be produced by increasing alpha past the axial field reversal point as shown in Figure 5.13. Twisted flux ropes of these types have been observed in Venus' ionosphere (Elphic & Russell, 1983), and there is little physical evidence to suggest another cause of the reversals. For instance, the flux rope is too close to the Sun and moving too slowly to develop forward and reverse shocks. Because the flux rope was oriented along the line of sight in these CMEs, the longitudinal magnetic field components provided a good measurement of the magnetic field magnitude.

The October 27 CME shown in Figure 5.3 is included in the analysis to demonstrate that all the CME measurements can be modeled with flux ropes. However, the FR measurements would be similar for a sector boundary change along the line of sight. The Solwind coronagraph observations clearly indicate that a CME erupted; however, it is not clear that the measurements obtained were in fact within the CME. The fit that was produced and the coronagraph observations suggest that the CME which erupted was propagating towards the Earth.

Figure 5.3 shows a Faraday rotation inverse sigmoid similar to the Pioneer 9 measurement except that it varies over 160 degrees while Pioneer 9 ranged over 10. The exact details of the reverse sigmoid are difficult to determine; however, the structure appears to be moving at slow velocity with respect to the LOS (it is mostly moving

Earthward).

5.4   Pioneer Transient Identification

As mentioned previously, the Pioneer 6 Faraday rotation 'W' transients are very similar in structure to the Helios 1979 October 23 and 24 CME crossings which have been shown to be caused by an anti-parallel flux rope crossing the line of sight. Unfortunately, the electron density measurements could not be obtained for the time period when the Faraday rotation magnitude decreases forming the central peaks to the 'W'.

Spectral broadening observations are presented to illustrate the relationship between their intensity and the observed Faraday rotation. A sample of spectral broadening is shown in Figure 5.14 where the half-power width of the signal carrier frequency increases with time as the signal crosses the 1968 November 8 Pioneer 6 transient. Notice that the greatest width occurs at 1752 UT during the maximum magnitude in Faraday rotation and that the half-power width at 1718 UT prior and 1810 UT after the maximum have similar widths corresponding to the main peak in the 'W' and the small peak on the trailing edge of the 'W'. Spectral broadening is generated by the scattering of the signal frequency through the turbulent solar wind; as a consequence, it is a complex function of electron density and velocity. It is also important to note that as a measure of electron density, it is only useful to approximately 9 solar radii; within this region, phase angle scattering or "angular" broadening should be used if electron density measurements are being obtained. This is the most probably explanation why the best anti-correlation between spectral broadening and Faraday rotation for the Helios measurements was for 1979 October 23 when the impact parameter of the point of closest approach of the line of sight was between 7 and 8

Sample spectrograms taken on 8 November 1968, showing the effects of a
solar event. Each spectrogram is the result of 15 minutes of averaging time.
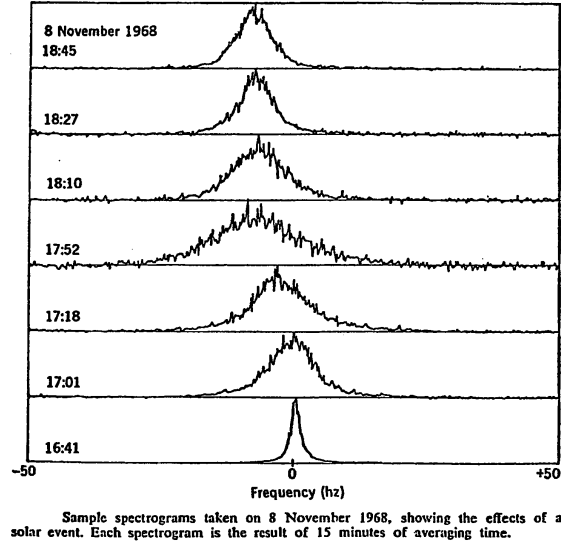
Figure 5.14: *Spectral broadening as measured by Cannon in the 1968 November 8
transient observed by Stelzried. The maximum broadening occurred at the time of
the largest dip in the 'W' (the 2nd one) (Cannon, 1976).*

solar radii. The rest of the Helios observations were closer to the Sun.

If we focus on the 1979 October 23 CME, the central peak in the Faraday rotation
'W' anti-correlates well with the spectral broadening curve above; the decrease in
the electron density associated with the decrease in spectral broadening is similarly
accompanied by a decrease in the magnitude of Faraday rotation. If we apply this
to the curves shown in Figure 5.14, it is reasonable to assume that the peaks at
November 4 1730 UT and November 12 1930 UT are probably the result of a local
decrease in electron density assuming that they include the time periods around
them with similar increases in electron density. In other words, the FFT time
windows were large and included large magnitude Faraday rotation time periods
with the weak magnitudes. If we assume that the large magnitude Faraday rotation
values correspond to the same electron density as the 1752 UT time period, then
only low electron density time periods could be successfully included in the FFT

calculation to produce the thinner half-power width values. Note that the half-power widths occurring at 1701 and 1827-1845 UT are located on the edges of the flux rope. The long duration of the exit signature is caused by the expansion of the transient.

There is clearly similar enough structure between the 1979 October 23 and 24 CMEs and the Pioneer 6 transients to indicate that the Pioneer transients are flux ropes. They all cross the line of sight over a period of hours, include large negative Faraday rotations, and when electron density observations over the structures can be inferred, deviate from the overall magnitude of the Faraday rotation trough with the change in electron density. As a result these Faraday rotation measurements can be modeled with the flux rope model described previously. The flux rope fits are shown in Figure 5.15 and the flux rope model parameters producing the fits are given in Tables 5.1 and 5.2.

The similarity in structure between the Pioneer 9 transient and 1979 November 16 CME indicates that this transient is probably a flux rope as well; the Pioneer 9 structure is also similar to the perpendicular CME plot for an east-limb, right-handed flux rope with an azimuthal angle of 270 degrees (or a 90 degree left-handed rope). The flux rope source is further supported in that similar to all the other CMEs measured, the Pioneer 9 transient crossing occurs over the period of hours. The flux rope fit for the Pioneer 9 CME is shown in Figure 5.15 and the model parameters producing the fit is given in Tables 5.1 and 5.2.
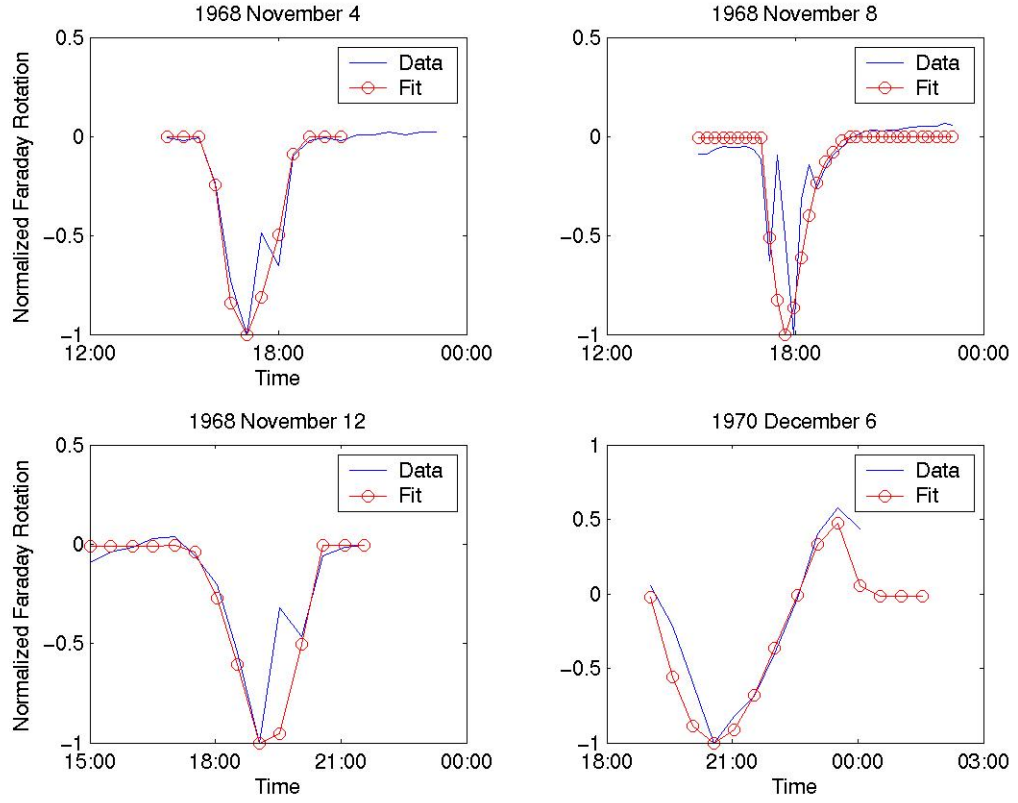
Figure 5.15: *The normalized Faraday rotation transients and their flux rope fits for the Pioneer 6 and 9 transients.*

5.5 Determination of Velocity

In order to perform the fits, velocity estimates were necessary. The Helios velocity estimates for the 1979 October CMEs were obtained from Solwind coronagraph observations of the eruptions. The velocity estimates for the Pioneer 6 flux ropes were obtained from the comparison of the crossing start time of the rope and decametric burst activity on the Sun. Both of these measurements produced large error bars in the velocity; however, the transient crossing period apparent from these two datasets indicate that the crossing time period is inversely related to velocity. The Pioneer 6 transient crossing periods are around 3 hours, and the 1979 October CME crossing periods appear to be twice as long. The velocities determined for the Pioneer 6 transients were approximately $1000km/s$ (Levy *et al.*, 1969), while the October CME velocities determined from coronagraph observations were around $150km/s$.

The decametric database (Coffey, 2005) is unclear when there are multiple bursts such as in the cases for 1979 October 23 and 24; however, 1979 October 27 transient only has one decametric burst that could correspond with the transient observed by Solwind and Helios giving it a velocity of $116km/s$ which is well within the coronagraph derived velocity range. The 1970 December 6 transient provides another test for the decametric derived velocities. The crossing time period is approximately 6 hours, similar to the 1979 October 23 and 24 transients, and the decametric burst database only shows one burst within the 5 hours of time before the crossing. The velocity that is calculated from the time of the burst to the start time of the transient crossing and the distance the closest approach of the line of sight from the Sun is $120km/s$; this number is well within the velocity range for the 1979 October 23 and 24 transients which have similar time periods of transient crossing.

The 1979 November 16 transient velocity could not be determined from the Solwind

coronagraph observations. However, the period of time for the transient crossing was approximately 3 hours similar to the Pioneer 6 transients. Using the reasoning above, it would appear that the transient velocity was approximately $1000km/s$. An inspection of the decametric burst database reveals that it is unclear which decametric burst could be attributed to the transient eruption; however among all the possible bursts listed, there is a burst that would correspond to a transient velocity of $870km/s$. Coincident with these observations, the magnetometer on Pioneer Venus Orbiter (in the vicinity of Venus) measured what could potentially be an interplanetary CME. As the Solwind coronagraph observations indicate, the 1979 November 16 CME erupted off the northwest limb, and the flux rope fits indicate it was out of the plane of the sky by approximately 50 degrees. As shown in Figure 5.16 of the relative orbital locations of the Earth and Venus at the time of the CME eruption, this could be either in the positive y- or negative x-directions. Venus was in the negative-y direction indicating that the PVO observations could only apply either to the forward shock of the CME or to another eruption occurring during the same time frame. If the PVO observations were the result of the same eruption, the velocity of the transient would be approximately $1000km/s$. Because strong evidence for the velocity of the transient could not be obtained, the 1979 November 16 transient velocity was set to $1000km/s$ for the fit and no error bars were placed; only the orientation of this flux rope could be determined.

5.6   Magnetic Flux

The magnetic flux across a circular cross section of a flux rope is $\Phi = \int \vec{B} \cdot \hat{n} dA$ where $\hat{n}$ is the direction of the axial field. The type of flux rope used in the model is a squat cylinder where the length is twice the radius $\Delta z = 2r$. Additionally, the radius is
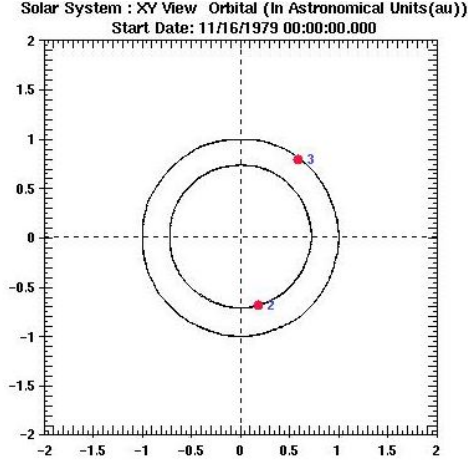
Figure 5.16: *The relative positions of Venus (2) and the Earth (3) in the ecliptic plane during the eruption of the 1979 November 16 event. The first point of Aries is to the right. The CME was moving out of the plane of the sky as viewed from the Earth in either the positive Y direction (earthward) or negative X direction (anti-earthward). Pioneer Venus Orbiter measured an ICME on the 17th.*

determined from the orientation of the flux rope and its velocity. Specifically, the largest radii are determined for flux ropes that are either oriented parallel to the line of sight or perpendicular to the line of sight and parallel to the normal of the Sun-spacecraft-Earth plane. All other orientations produce elliptical cross sections and whose radii are consequently smaller for a fixed velocity. The dependence of the length of the cylinder on its radius has a similar effect. A flux rope crossing the line of sight such that a point on its base is the first to cross and a point on its top crosses last will have a different radius depending on the relationship between Δz and r. If the cylinder is longer such that $\Delta z = 3r$, then the radius will necessarily be smaller in order for the crossing time period to remain the same for the same velocity. This dependence of the radius of the flux rope on the cylindrical flux rope model introduces significant uncertainty into any magnetic flux calculations. As a result of this, the magnetic flux for the observed CMEs will be presented as a ratio with respect to a 1 μ T axial magnetic field flux rope with a radius of 1 Rs.

Table 5.3: *The relative fluxes for the CME fits relative to a 1 μT flux rope with a radius of 1 Rs.*

Date	IP Rs	R_{CME} Rs	Relative Φ
1968 Nov 4	11.5	4.7	22.1
1968 Nov 8	9.0	4.7	22.1
1968 Nov 12	6.5	2.3	5.3
1970 Dec 6	5.8	1.5	2.3
1979 Oct 23	7.0	1.0	0.3
1979 Oct 24	4.8	1.8	4.2
1979 Oct 27	5.8	7.5	56.3
1979 Nov 16	3.4		

As mentioned previously, the Faraday rotation observations are ambiguous with respect to the total columnar electron density and magnetic field. Because the electron density varies significantly more than the magnetic field strength as observed both by the difference between the 1979 October 23rd and 24th CMEs and observations of Earth-passing CMEs, the magnetic field magnitude of the axial field was fixed. However, the magnetic flux varied between CMEs due to the variable radii observed. Table 5.3 gives the relative ratio of the different flux ropes.

5.7 Summary

Many observations of transient structures have been obtained during solar Faraday rotation observations. But not until 1979, did Bird et al show that these transients were associated with CMEs. This chapter shows that Faraday rotation calculations for a Taylor state flux rope model at various orientations are capable of reproducing the transient/CME signatures measured in previous Faraday rotation experiments indicating that the imbedded flux rope seen in ICMEs at 1AU has its origin back at the Sun and is not created by processes such as velocity shear in transit to the Earth.

CHAPTER 6

Magnetohydrodynamic Waves

Faraday rotation is produced by the different index of refraction in a magnetized plasma for right and left handed EM waves traversing the plasma in the high frequency regime ($\omega \gg \omega_{ce}, \omega_{pe}$) where only the electrons in the plasma interact with the waves. In this chapter we show how close to the Sun these waves can be used to probe the naturally generated waves in the lower frequency MHD regime ($\omega \ll \omega_{ci}, \omega_{pi}$) where both the ions and the electrons participate in the wave motion producing what are known as fast and slow magnetoacoustic and Alfven waves.

MHD waves have been observed in the corona during Faraday rotation measurements with the Helios mission. As shown in Figure 6.1, large amplitude long period ($\approx$ 4-5 min) waves were observed; such waves were observed every year of the Helios mission during ingress and egress and throughout the range of impact parameters of the point of closest approach based on the system sensitivity (3 to 15 solar radii) (Andreev *et al.*, 1997). The two spectra shown in the figure have the same magnitude of the perturbation on 1983 January 9 between the two stations (the Goldstone spectrum was shifted down by an order of magnitude). The time sequence of spectra observed by Canberra on 1983 January 7 show that the maximum amplitude was observed around 22:50 just before signals ceased presumably, because the wave train ceased to cross the line of sight. The fundamental frequency is often accompanied by a

second harmonic with a period of ≈ 2 minutes. The 2nd harmonic is difficult to explain because the frequency of the wave is near the ion gyrofrequency in the chromosphere (Chashei & Shishov, 1984); however, the corona absorbs little energy from MHD waves with periods of five minutes or above.

Waves near 5-minute period are to be expected in the corona. The solar surface "rings" with multiple modes in the band near five-minute periods. Figure 6.2 shows this multiple-mode structure near 5-minute periods. These waves may be the source of the energy for heating the solar corona; the acoustic waves in the Sun couple to MHD waves that propagate into the corona and damp (Klimchuk, 2006). The goal of this chapter is to determine the amplitude and modes of these MHD waves using the Faraday rotation data. Finally, we analyze the Cassini Faraday rotation observation of an MHD wave.

MHD waves can affect Faraday rotation through the perturbation of both the magnetic field and electron density. In order to test the effects that MHD waves would have on the Faraday rotation measurement, a simple box model was constructed in which the waves propagate (Figure 6.3). This chapter will also show that the 2-minute period harmonic can be produced in the Faraday rotation data by a 4-minute period magnetoacoustic wave thus explaining the unexpected appearance of the 2-minute period wave.

6.1 Model Equations

Recalling that Faraday rotation is the integrated product of the electron density and the magnetic field component parallel to the line of sight, distinguishing the types of waves present in Faraday rotation observations requires adjusting this equation
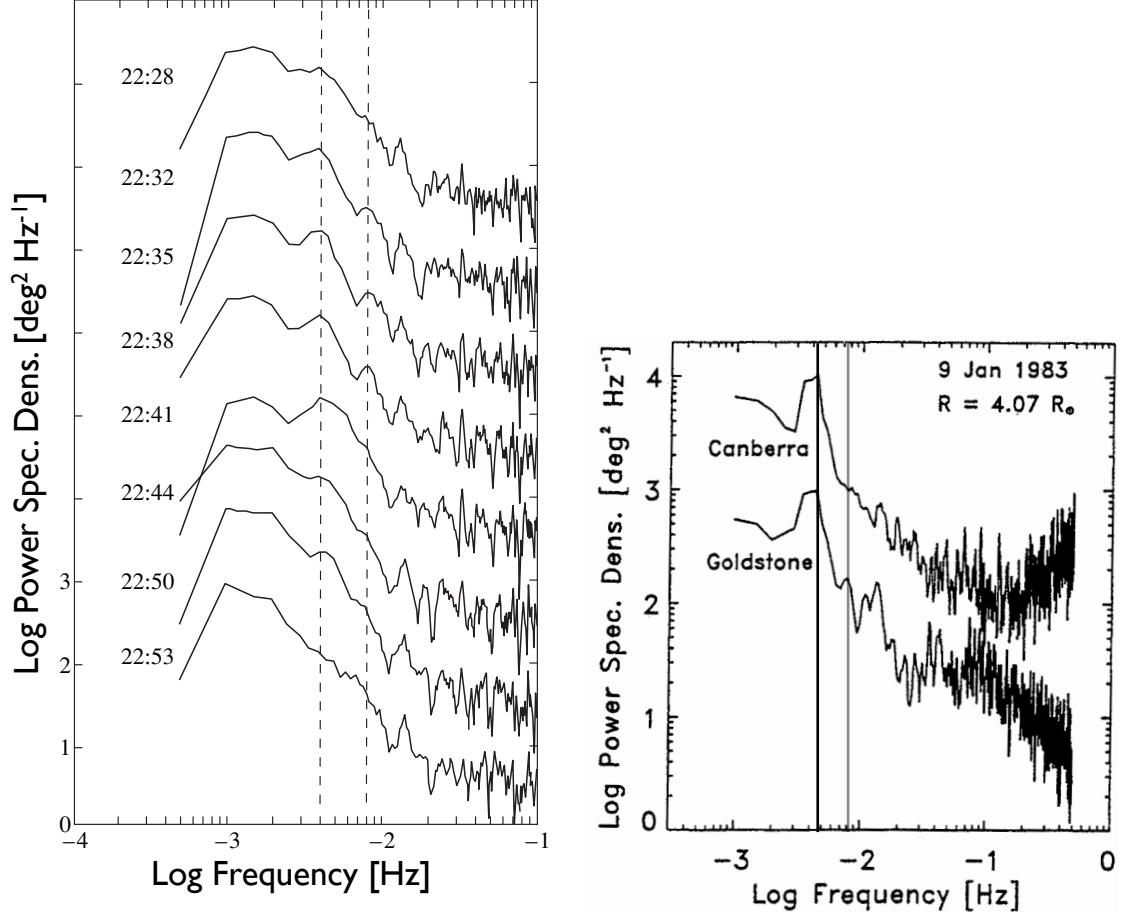
Figure 6.1: *A large amplitude MHD wave measured by Faraday rotation of the Helios carrier signal on 1983 January 7 (4.4 Rs) and 9 (4.1 Rs). The waves had a 4-minute fundamental period and a second harmonic with a period of 2 minutes. The left hand figure shows the evolution of the Faraday rotation wave spectrum with time from the Canberra 1983 January 7 observations (Efimov et al., 2000). The right hand figure shows that the amplitude of the signal was the same at Madrid, Spain and Goldstone, CA; note that the Goldstone spectrum is shifted down an order of magnitude (Samoznaev & Bird, 1997).*
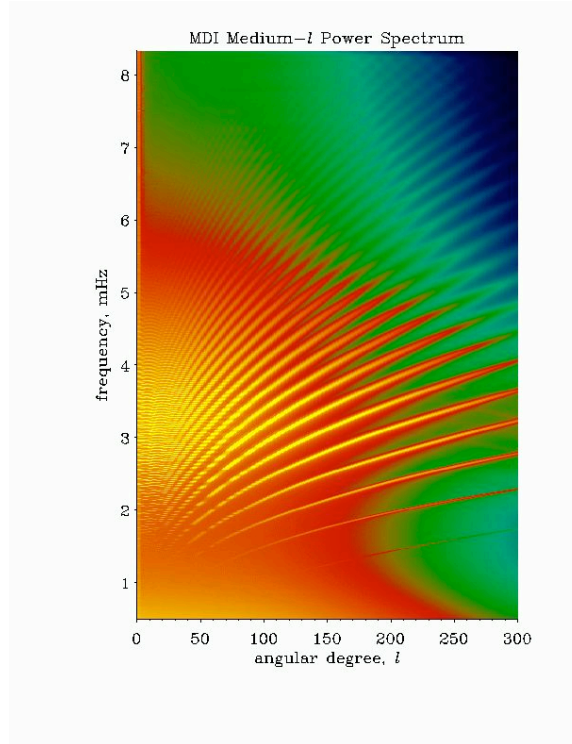
Figure 6.2: *The solar 5-minute resonance. The surface acoustic resonance consists of many resonant modes near 5-minute periods. This plot shows a range from 1 to 8 mHz. The abscissa refers to scale sizes in terms of spherical harmonics. Degree zero refers to the entire Sun, and the scale sizes get smaller with increasing degree. The lower the degree and the lower the frequency produces deeper resonances (Graps, 1998).*
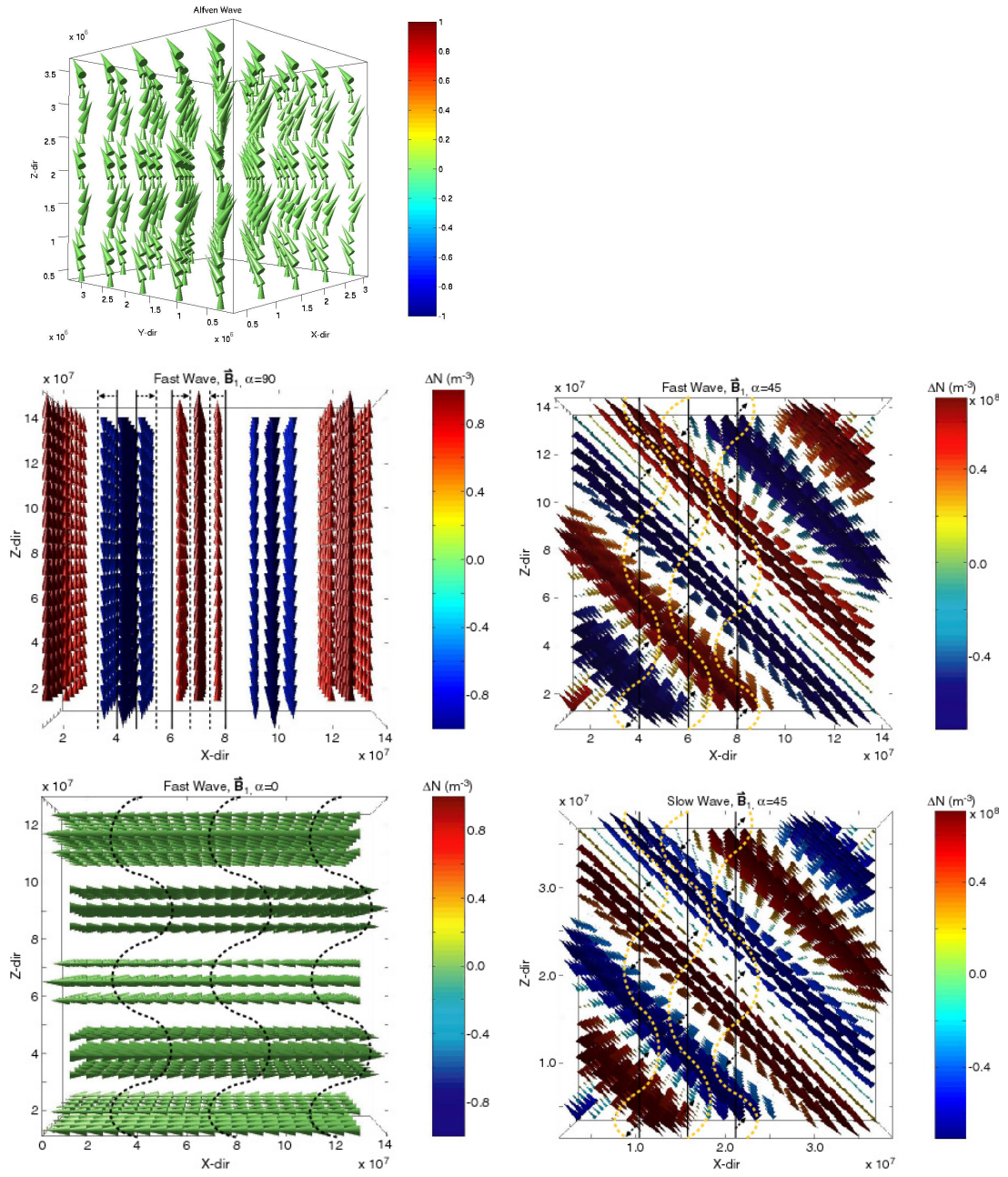
Figure 6.3: *The general characteristics of the box model. The model is a cube of user specified dimensions filled with MHD waves throughout. The colors indicate the change in electron density relative to the background. The line of sight along which Faraday rotation is calculated passes through the box; note that the line of sight can pass through the box at any angle. In our model, the MHD waves propagate while the line of sight remains fixed.*

174

with the linearization assumption for waves.

$$FR \propto \int_{sc}^{\oplus} (N_0 + N_1)(\vec{B}_0 + \vec{B}_1) \cdot d\vec{s} \tag{6.1}$$

This expands into:

$$
\begin{aligned}
FR \propto & \int_{sc}^{\oplus} N_0 \vec{B}_0 \cdot d\vec{s} + \int_{sc}^{\oplus} N(\omega) e^{i(\vec{k} \cdot \vec{s} - \omega t - \phi_N)} \vec{B}_0 \cdot d\vec{s} \\
& + \int_{sc}^{\oplus} N_0 \vec{B}(\omega) e^{i(\vec{k} \cdot \vec{s} - \omega t - \phi_B)} \cdot d\vec{s} + \int_{sc}^{\oplus} N(\omega) \vec{B}(\omega) e^{i(2\vec{k} \cdot \vec{s} - 2\omega t - \phi_N - \phi_B)} \cdot d\vec{s}
\end{aligned} \tag{6.2}
$$

Notice that the last term of the equation produces a fluctuation at two times the frequency of the wave. If $N(\omega)/N_0$ and $B(\omega)/B_0$ are both small, this term will be insignificant with respect to the two terms containing the fundamental frequency. The appearance of the second harmonic in Figure 6.1 suggests that at least occasionally the wave amplitudes are a large fraction of the DC levels.

The Doppler columnar electron density time series is

$$I \propto \int_{sc}^{\oplus} N_0 ds + \int_{sc}^{\oplus} N(\omega) e^{i(\vec{k} \cdot \vec{s} - \omega t - \phi_N)} ds \tag{6.3}$$

Using the box model, we analyze the components of these two equations.

Table 6.1: *The input parameters for modeling MHD wave propagation in the solar corona at 10 solar radii.*

Model Parameters
polytropic index $\gamma = 1$ for isothermal or turbulent flows (Baumjohann & Treumann, 1996)
temperature $T = 10^6$ Kelvin
electron density (at 10 Rs) $n_0 = 10^{10}$ m^{-3}
magnetic field magnitude (at 10 Rs) $B_0 = 10^{-6}$ T
pressure $P = n_0 k_B T = 1.38 \times 10^{-7}$ N/m^2
speed of sound $Cs = \sqrt{\gamma P/(m_i n_0)} = 0.91 \times 10^5$ m/s
Alfven speed $V_A = \sqrt{B_0^2/(\mu_0 n_0 m_i)} = 2.18 \times 10^5$ m/s
magnetosonic speed $C_{ms} = \sqrt{C_s^2 + V_A^2} = 2.36 \times 10^5$ m/s

6.1.1 Alfven, Fast, and Slow Waves

In the construction of an MHD model, the dispersion relations give the relationship between the frequency of the wave (ω) and its propagation vector (k). The dispersion relations for MHD Alfven (A), fast (f), and slow (s) waves are

$$
\begin{aligned}
k_A &= \frac{\omega}{v_A \cos \alpha} \\
k_f &= \sqrt{\frac{2\omega^2}{c_{ms}^2 + \sqrt{(v_A^2 - c_s^2)^2 + 4 v_A^2 c_s^2 \sin^2 \alpha}}} \\
k_s &= \sqrt{\frac{2\omega^2}{c_{ms}^2 - \sqrt{(v_A^2 - c_s^2)^2 + 4 v_A^2 c_s^2 \sin^2 \alpha}}}
\end{aligned}
\tag{6.4}
$$

where v_A is the Alfven velocity, α is the propagation angle with respect to the background magnetic field, c_{ms} is the magnetosonic speed, and c_s is the sound speed. Table 6.1 lists the input parameters used to calculate the propagation vectors for the region at 10 solar radii.

The magnetic field and electron density can be expressed in terms of the perturbed flow ($\delta\vec{v}$) (Baumjohann & Treumann, 1996) using the dispersion relations derived from Faraday's law and the continuity equation:

176

$$\frac{\partial \delta \vec{B}}{\partial t} = (\vec{B}_0 \cdot \nabla)\delta \vec{v} - \vec{B}_0 (\nabla \cdot \delta \vec{v})$$

$$\frac{\partial \delta n}{\partial t} = n_0 \nabla \cdot \delta \vec{v}$$

In the coordinate system with the background magnetic field in the z-direction, and the propagation vector in the x-,z- plane, the following expressions for the magnetic field and plasma velocity are derived for the shear wave:

$$\frac{\partial \delta n}{\partial t} = 0$$
$$\delta v_x = \delta v_z = 0$$
$$\delta v_y = \widetilde{v}_y \exp\left[i(\omega t - kz)\right] \tag{6.5}$$
$$\frac{\partial}{\partial t}\left(\frac{\delta B_y}{B_0}\right) = \frac{\partial \delta v_y}{\partial z}$$
$$\delta B_y = -B_0 \widetilde{v}_y \frac{k}{\omega} \exp\left[i(\omega t - kz)\right]$$

In contrast, the compressive mode solutions are:

$$\delta v_y = 0$$
$$\delta v_x = \widetilde{v}_x \exp\left[i(\omega t - kx \sin\alpha - kz \cos\alpha)\right]$$
$$\delta v_z = \widetilde{v}_z \exp\left[i(\omega t - kx \sin\alpha - kz \cos\alpha)\right]$$
$$\frac{\partial}{\partial t}\left(\frac{\delta B_x}{B_0}\right) = \frac{\partial \delta v_x}{\partial z}$$
$$\frac{\partial}{\partial t}\left(\frac{\delta B_z}{B_0}\right) = -\frac{\partial \delta v_x}{\partial x} \tag{6.6}$$
$$\delta B_x = -B_0 \widetilde{v}_x \frac{k}{\omega} \cos\alpha \exp\left[i(\omega t - kx \sin\alpha - kz \cos\alpha)\right]$$
$$\delta B_z = B_0 \widetilde{v}_x \frac{k}{\omega} \sin\alpha \exp\left[i(\omega t - kx \sin\alpha - kz \cos\alpha)\right]$$
$$\frac{\partial \delta n}{\partial t} = -n_0 + \frac{\partial \delta v_z}{\partial z}$$
$$\delta n = \widetilde{v}_z \frac{k}{\omega} \sin\alpha \, n_0 \exp\left[i(\omega t - kx \sin\alpha - kz \cos\alpha)\right]$$

Using a wave frequency 3×10^{-3} Hz, and setting the amplitude of the wave to $v_A \frac{k}{\omega}$, the magnetic field and electron density (compressive only) of the wave can be calculated for any point in the space. The line-of-sight step sizes used were no greater than 1/4 of a wavelength. The line of sight was then rotated through various angles (colatitude or azimuthal). For the following results, the box size was set to one wavelength. When analyzing the Cassini observations, the box size was set to the maximum size possible while still maintaining coherence; this will be discussed in greater detail later.

6.2   Model Results

Faraday rotation is capable of detecting MHD waves when the perturbations have a component along the LOS that integrates to a non-zero value. If we assume that the wave is propagating along the radial magnetic field and is composed of a single wave train, then the type of wave and its amplitude in the magnetic field can be determined.

6.2.1   Faraday Rotation Sensitivity to View Orientation

Figure 6.4 shows the magnetic field vectors in the top panel while the Faraday rotation along the line of sight for the perpendicular and parallel orientations of the waves with respect to the line of sight are shown in the bottom panel. This figure demonstrates that a component of the fluctuation of the wave must be oriented along the line of sight in order for it to be detectable by Faraday rotation. The geometry of the coronal sounding measurements is advantageous in this respect: the magnetic field is mostly radial, waves tend to travel along the magnetic field

lines from the Sun, and the Faraday rotation measurement is most sensitive to the region of closest approach which is perpendicular to the radial magnetic field. Faraday rotation is unable to measure those wave only where the perturbation is purely in the perpendicular to the line of sight and the radial directions.

6.2.2 FFT Analysis

As noted above when the time series of MHD waves are Fourier transformed, the fast and slow magnetosonic waves produce a secondary peak in the Faraday rotation intensity spectrum at 2ω where ω is the frequency of the fundamental harmonic shown in Figure 6.5. As the 4th term in Equation 6.2 demonstrates, the 2nd harmonic is the result of the product of the electron density and magnetic field perturbations in the index of refraction.

In contrast, the Alfven wave lacks the second harmonic because it only perturbs the magnetic field perpendicular to its wave vector; the plasma does not compress. As shown in Figure 6.5, the Alfven wave produces a single peak in the Faraday rotation intensity spectra.

6.3 Orientation

Figure 6.6 shows how the box orientation of the MHD wave fits in the general coronal sounding experiment. If we assume that the background magnetic field is oriented in the radial direction, then the z-direction of the box lines up with the radial field. The x- and y-directions of the box depend on the orientation of the perturbed magnetic field relative to the line of sight. The wave shown in the figure has its
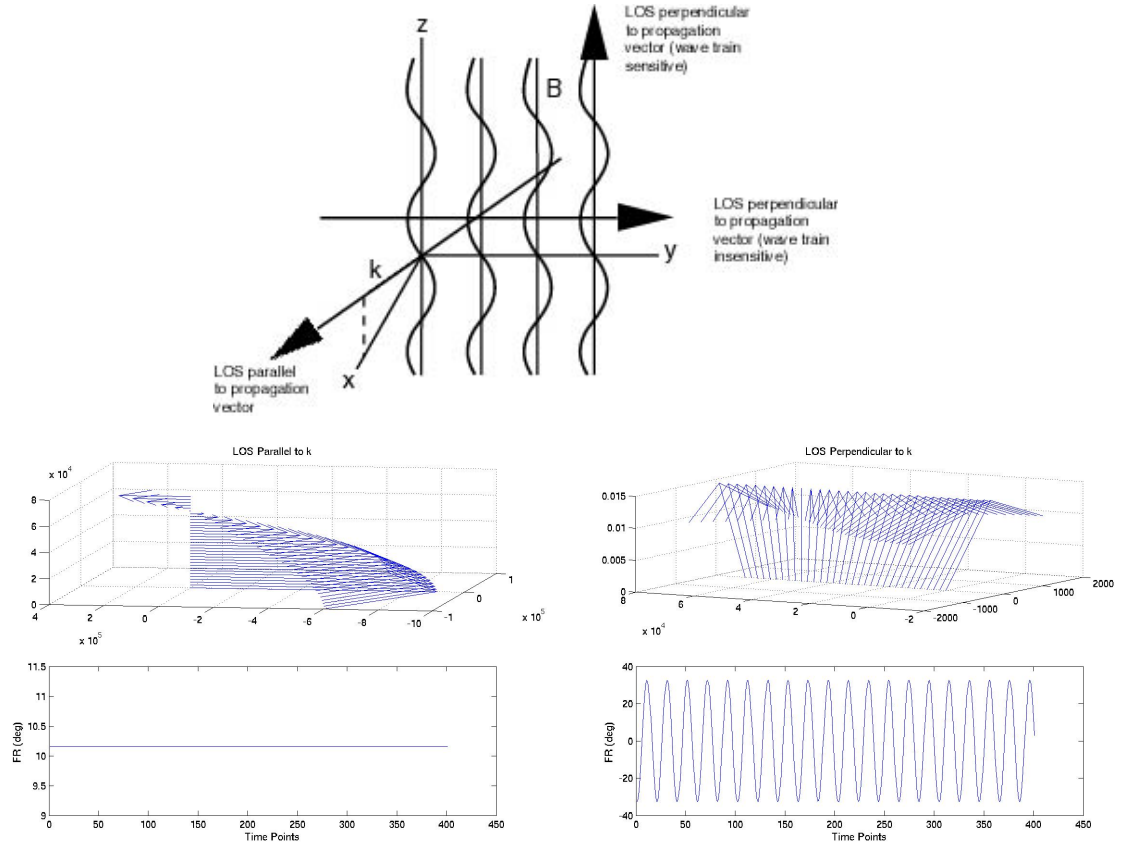
Figure 6.4: *Effects of orientation of Faraday rotation observation through MHD wave propagation. Parallel and perpendicular orientations through an Alfven wave are shown in the upper right hand plot (Kivelson & Russell, 1997). The figures show the resulting Faraday rotation fluctuation from the two extremes of $\vec{k}_{MHD} \cdot \vec{k}_{EM}$. The line of sight is perpendicular to the the wave vector on the left and parallel on the right. Note that the MHD fluctuation perpendicular to the LOS shown is the orientation that is sensitive to the period of the wave present; the wave only extends for half a wavelength. With time, the MHD waves propagate while the line of sight remains fixed.*
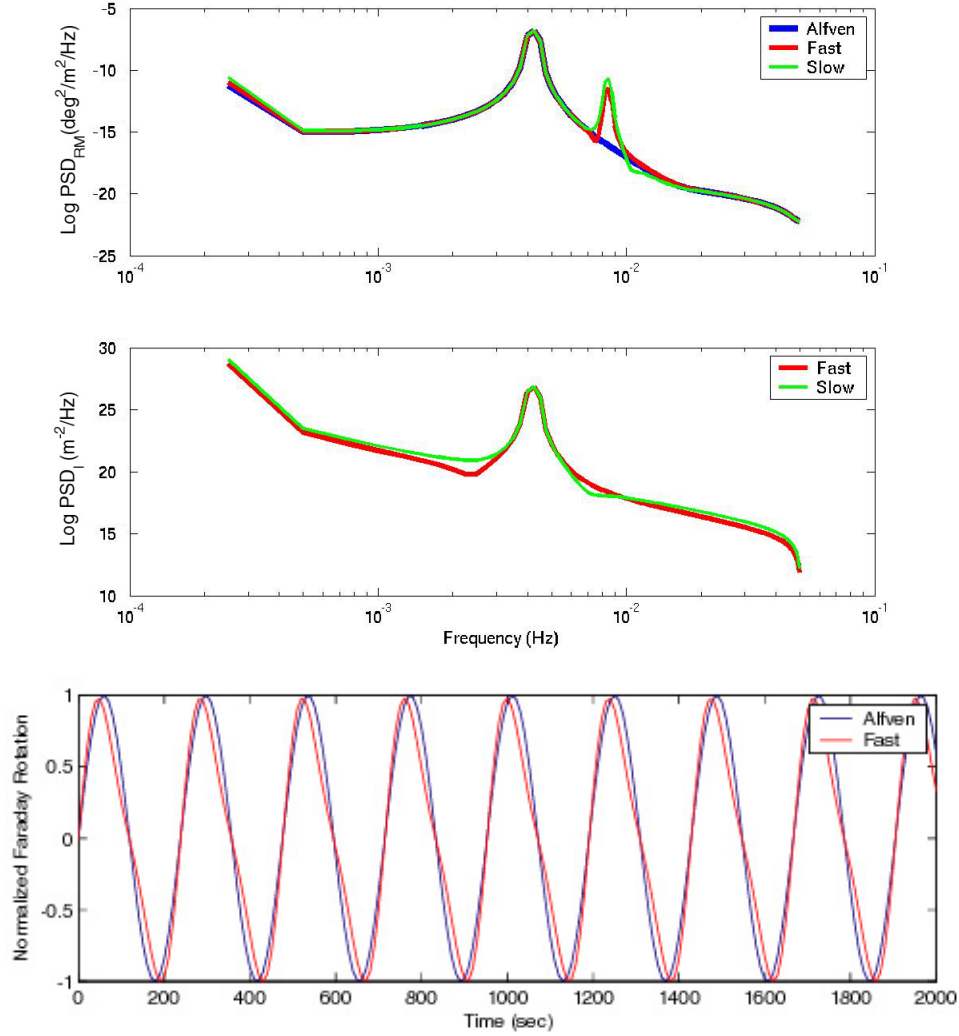
Figure 6.5: *The rotation measure (FR/λ^2_{CF} in the top plot) and columnar electron density FFT spectra (middle plot) generated by the model for three types of MHD waves. The plasma is not compressed in an Alfven wave, and therefore does not produce a fluctuation in electron density. The two magnetosonic modes (fast and slow) produce a second harmonic in the Faraday rotation due to the product of the magnetic field and electron density in the index of refraction. The amplitude of the perturbation in the magnetic field and electron density was set to the product of $V_A \frac{k}{\omega}$ and the background magnetic field or electron density; the box size was set to a single wavelength. The bottom plot shows the affect of the fluctuating electron density on the rotation measurement.*
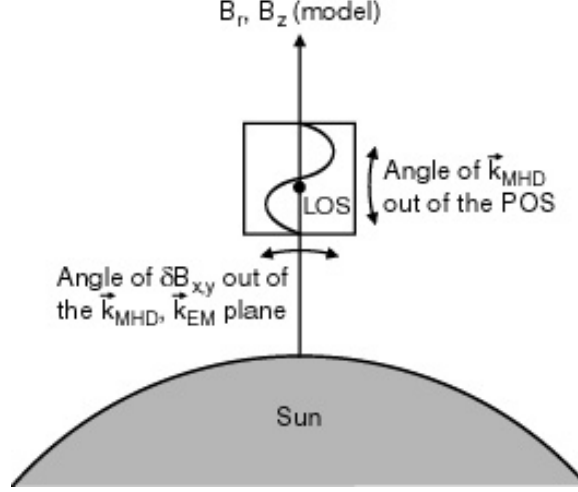
Figure 6.6: *The orientation of the line of sight (LOS) relative to the box model during coronal sounding. If we assume the magnetic field is radial, then the z-axis of the box will be in the radial direction. The y-axis of the box is in the direction in which the magnetic field perturbation moves. In this example, the y-axis is perpendicular to the line of sight. Note that the latitude at which the line of sight passes through the box depends on the angle at which the z-axis tilts out of the plane of the sky (POS).*

x-axis aligned with the line of sight, while the y-axis is perpendicular. Finally, the latitude at which the line of sight passes through the box depends on whether or not the wave is propagating out of the plane of the sky Earthward or anti-Earthward. If it is Earthward/anti-, then the line of sight passes through the box at a small/large colatitude.

6.3.1 Determining the Amplitude of an Alfven Wave

Figure 6.7 shows how the amplitude of the Faraday rotation observation is affected by adjusting its viewing angle through the wave. Along the y-axis of the box, the full perturbation is along the line of sight; as the line of sight rotates towards the x-axis, less of the magnetic field perturbation is measured.
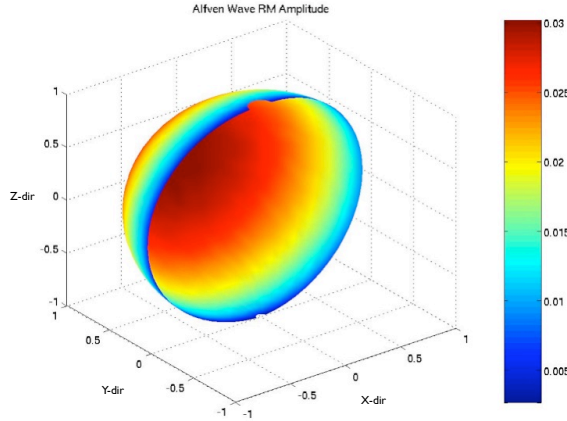
Figure 6.7: *Variation of the amplitude of the magnetic field determined from Faraday rotation observations of an Alfven wave with the direction of the line of sight through the box. The propagation vector is in the z-direction, and the perturbation of the magnetic field is in the y-direction. As the line of sight increasingly passes parallel to the y-axis, the amplitude of the wave is better estimated. The colorbar is represented in units of rotation measure ($RM=FR/\lambda^2$).*

6.3.2 Differentiating Magnetosonic Mode Waves

As discussed in Section 6.2.2, a magnetosonic wave should produce a fundamental and second harmonic in the Faraday rotation frequency spectra, but not in the Doppler ranging (I) measurements. This is the case in the Helios observations on 1985 January 7 and 9, indicating that these are magnetosonic waves. The primary difference between the fast and slow magnetosonic modes are that the magnetic field perturbation is in-phase/out-of-phase with respect to the electron density perturbation in the case of the fast/slow mode.

Figure 6.8 shows how the orientation of the line of sight relative to the box affects the measurement of the phase difference between the Faraday rotation and columnar electron density fluctuations for the magnetosonic waves. If the Faraday rotation and the Doppler fluctuations oscillate in phase we expect that the wave is an in-
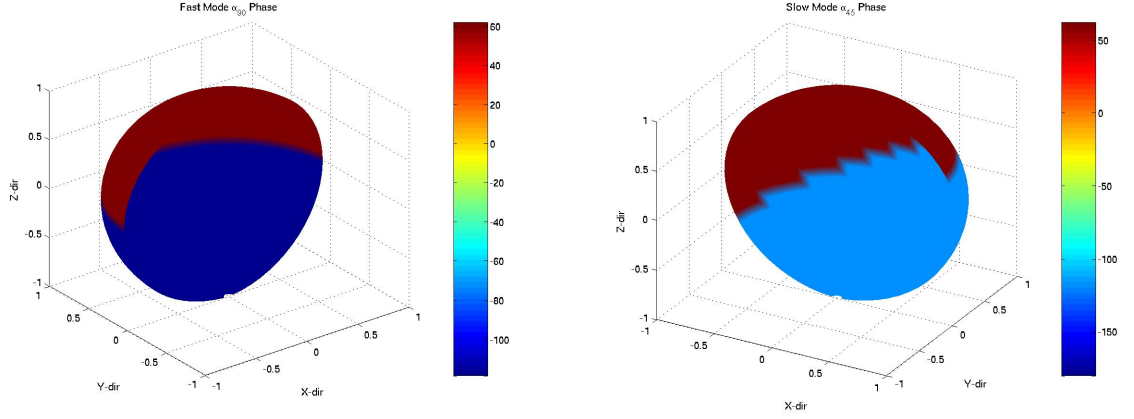
Figure 6.8: *The phase difference between the peaks in Faraday rotation and electron density observations for different lines of sight through fast (left) and slow (right) mode MHD waves.*

phase fast mode wave and if out-of-phase the wave is slow mode. However, Figure 6.8 shows that the difference $(\phi_{FR} - \phi_I)$ depends on the direction of the line of sight relative to the orientation of the wave. The line of phase reversal depends on the propagation angle of the wave relative to the background magnetic field.

6.3.3   Wavelength

The propagation vector is a function of the type of MHD wave, electron density, magnetic field magnitude, temperature, and propagation direction relative to the background magnetic field. Figure 6.9 shows how these parameters interrelate. The wavelength of a wave is given by

$$\lambda = \frac{2\pi}{|k|}$$

Using the 5 minute period oscillations, the solid colored lines show how the wavelength of the wave decreases with distance from the Sun when the propagation

184

vector is along the background magnetic field (solid) and almost perpendicular to the background magnetic field (dashed). This is because of the decreasing temperature, electron density, and magnetic field magnitude of the solar corona with increasing distance from the Sun. The black lines towards the bottom of the figure show the sensitivity of the Cassini X-band 8 Ghz (solid) and the Nagoya, Japan 327 MHz (dashed) radio frequencies based on their Fresnel sizes. Fluctuations smaller than the Fresnel size cannot be measured; the Fresnel size is roughly determined by the signal frequency and separation distance either between the spacecraft and the Earth in the case of Cassini or between the two ground antennas observing the same source in the case of the Nagoya array.

All the spacecraft antenna systems and the Nagoya array should be able to measure MHD waves throughout the heliosphere within their respective sensitivity ranges. The wavelengths of the waves at 1AU are approximately 10 (Alfven or slow) to 100 (fast) times longer than the Fresnel size of spacecraft frequency carriers or the Nagoya array indicating either system should be able to measure the fluctuation.

6.3.4   Amplitude of Alfven Wave Measured By Cassini

Figure 6.7 shows how the amplitude of the Faraday rotation observation is affected by adjusting its viewing angle through the wave. Along the y-axis of the box, the full perturbation is along the line of sight; as the line of sight rotates towards the x-axis, less of the magnetic field perturbation is measured.

On 2002 June 20 (at 2.5 Rs closest approach), the Cassini radio frequency carrier was affected by a passing MHD wave. Figure 6.10 shows the wave, and its Faraday rotation and columnar electron density FFT spectra. The Faraday rotation time
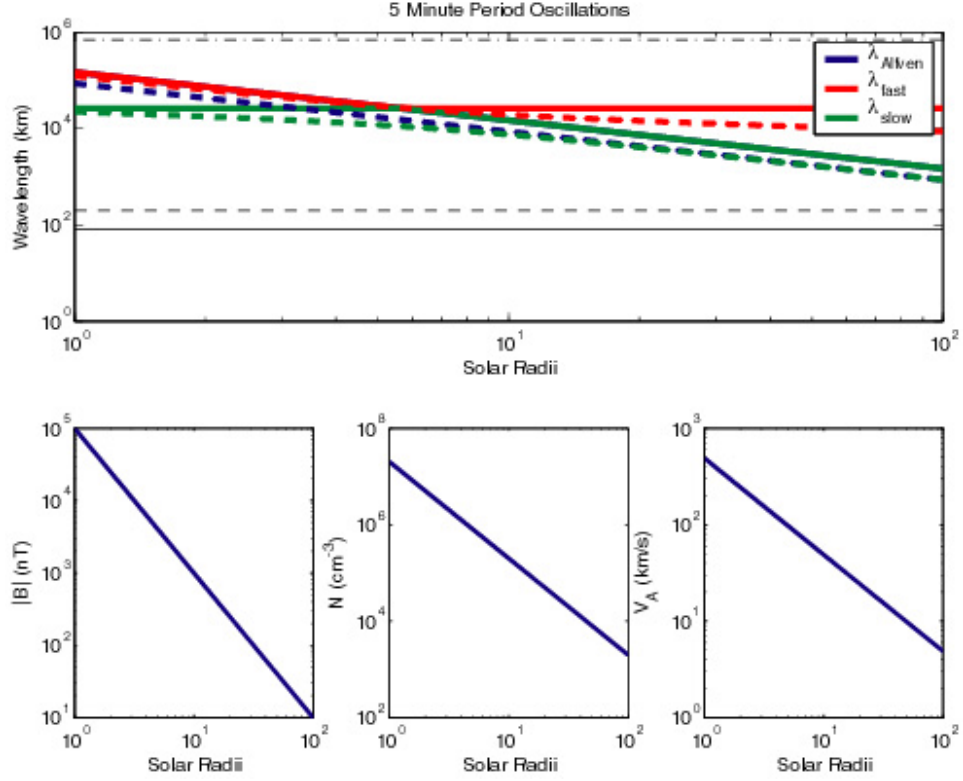
Figure 6.9: *The predicted wavelength of a 5 minute period MHD wave similar to the one measured by Helios with respect to distance from the Sun. The (solid/dashed) colored lines represent the wavelength for the (0/45) degree angle between the propagation vector and the background magnetic field. The top black line is the size of a solar radius, and the solid and dashed black lines at the bottom are the Fresnel sizes for the Cassini 8 GHz X-band carrier and the 327 MHz Nagoya, Japan array.*

series shows that period between 2100UT and midnight are clearly anomalous. In the time series there appears to be two distinct wave packets; these were the time periods used for the FFT analysis. The Faraday rotation FFT spectra shows that the first wave train has a period of approximately 3.5 minutes and the second is between 4.5 and 6 minutes; however, neither time period has a columnar electron density peak at the same frequency. This indicates that the wave is probably an Alfven wave. While the power spectral density of the Cassini Alfven waves are not large, their periods are in the vicinity of the Helios observations.

The determination of the size of the box through which the Alfven wave is being measured is important when estimating the amplitude of the wave based on the Faraday rotation fluctuation. The primary constraint on the size of the box was that the wave coherence be maintained. Figure 6.11 below shows how this was determined. For a radially propagating wave, the component of the wave along the line of sight is destructively combined at distances greater than half of the wavelength along the line of sight. For this reason, we have restricted the size of the box to the region along the line of sight in which the wave coherence is greatest.

The size of the box is therefore determined by the wavelength of the wave; as we have stated previously, the wavelength of the wave is calculated from the wave number. The wave number in the case of an Alfven wave is proportional to the inverse of the Alfven speed, and the Alfven speed is proportional to the magnetic field strength and the square root of the inverse of the electron density. Therefore, the size of the box is determined from the magnetic field strength calculated from the PFSS model and the electron density as determined from the adjusted Tyler model. If we take these values for the time period of the Cassini wave observations, then the background magnetic field strength is 3.7 μT, and the electron density is $1.82 \times 10^{12} m^{-3}$. This gives an Alfven speed of 60 km/s, a wavelength of 14 Mm, and a box size of 220
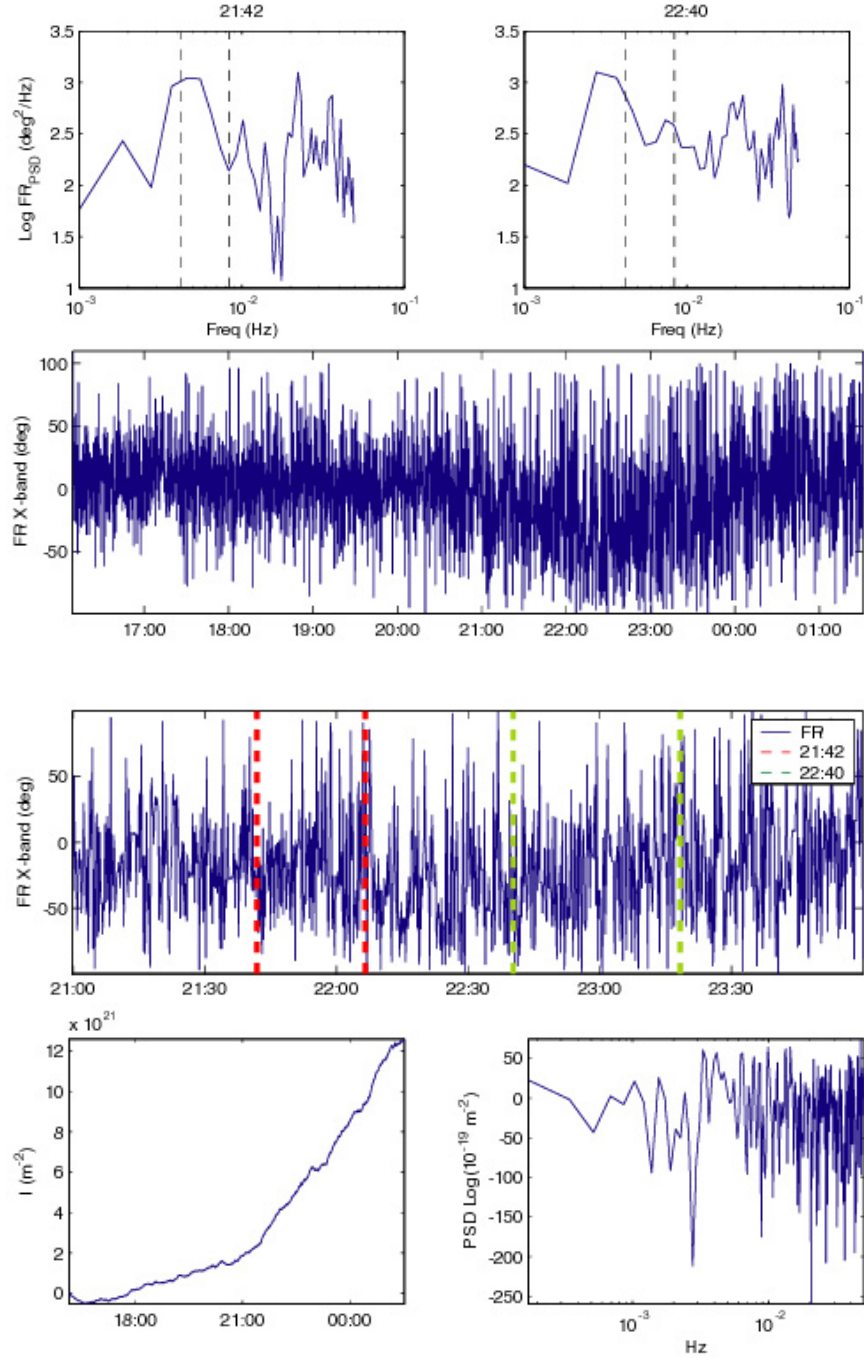
Figure 6.10: *The Faraday rotation time series on 2002 June 21. The red and green dashed lines indicate the time range of observations that were used in the FFT analyses shown in the top two plots (the black dashed lines correspond to 4.2 and 8.4 mHz). There is no associated wave peak in the electron density spectra (bottom right plot) for the same ~2 hour time period. The impact parameter of the point of closest approach of the signal path was 2.5 Rs.*
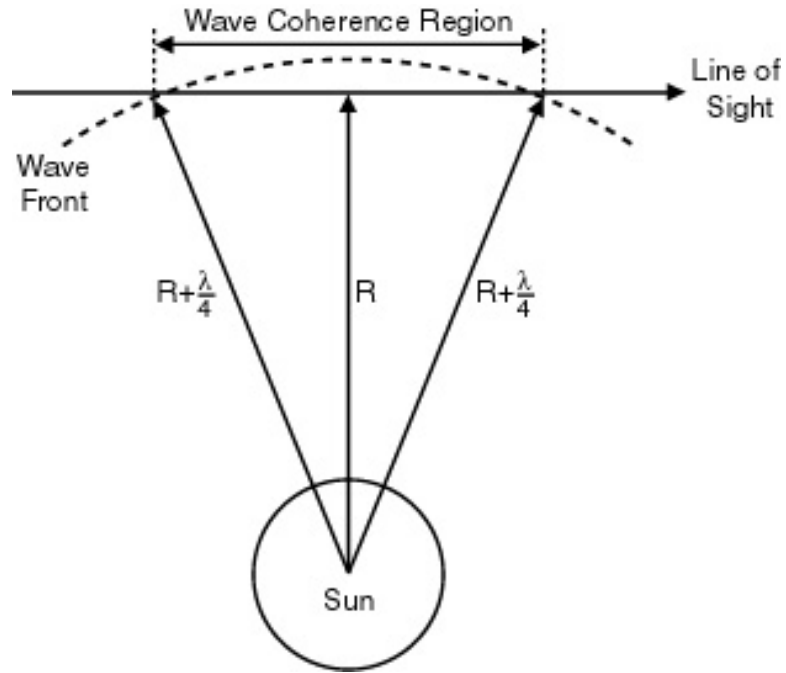
Figure 6.11: *Schematic of the region along the line of sight in which a radially propagating wave is coherent. Along the line of sight, points that are displaced from the radius (R) of the point of closest approach by a distance greater than half a wavelength (λ) interact destructively with the Faraday rotation observation. Therefore, the size of the box is restricted to the region along the line of sight that falls within this distance.*

Mm. If we compare the measurement to the model and assume that the wave vector is radially propagating in the plane of the sky, then we get a minimum amplitude of about 4.3 μT.

Additionally the actual amplitude of the wave depends on the orientation of line of sight relative to the perturbation; Figure 6.7 illustrates how the amplitude of the Faraday rotation perturbation varies with line of sight orientation through the wave for a fixed magnetic field amplitude. The wave amplitude is proportional to the background magnetic field indicating that these are non-linear waves. This amplitude corresponds to 7.3×10^{-6} N/m^2 magnetic pressure $(P_B = B^2/(2\mu_o))$. If we assume that this is a representative value for waves propagating from the Sun over 4π steradians, then the power released in these waves is 1.6×10^{19} W using the values below.

$$
\begin{aligned}
S_{Pynt} &= P_B V_A \\
F_B &= \oint_S S_{Pynt} dA \\
V_A(R &= 2.5Rs) = 60 km/s
\end{aligned}
\tag{6.7}
$$

where the surface S is a sphere centered on the sun with a radius of 2.5 solar radii. The electron density used in determining the Alfven velocity is $N = 1.82 \times 10^{12} m^{-3}$. This is the value at the point of closest approach along the line of sight using the adjusted Tyler et al (1977) electron density model for a total columnar electron density of $4.4 \times 10^{21} m^{-2}$. The technique is described in Chapter 4. The magnetic field strength used in determining the Alfven velocity is $3.7\mu T$ as determined from the adjustment to the Potential Field Source Surface magnetic field model discussed in Chapter 4.

For comparison, the overall optical energy output from the Sun is 4×10^{26} W, the momentum flux at 1AU in the solar wind is 1.7×10^{20} W (Kivelson & Russell, 1997), and the power required to move through the gravitational potential from the solar surface to 1AU is 1.9×10^{23} W ($|GM_{sun}F_{mass}(R_{AU}^{-1} - R_{sun}^{-1})|$, where the mass flux $F_{mass} = 2 \times 10^{30} kg/s$). We note that in observing MHD waves with Faraday rotation requires the wave to be in the proper orientation and coherent, and the fact that these waves are not always detected may be just that the window of detectability is small.

6.4   Summary

Using a simple computer box model through which MHD waves propagate and are measured using Faraday rotation, the sensitivity of FR wave observations in the solar corona is examined. During the years that Helios 1 and 2 Faraday rotation observations were made, numerous MHD waves were observed. The waves generally had periods of 4-5 minutes, and occasionally the waves included a 2nd harmonic. The Alfven wave cannot produce a 2nd harmonic in the Faraday rotation spectrum because it does not have density fluctuations. Using this property alone, a lack of wave power at the same frequency in the columnar electron density power spectra as a wave observed in the Faraday rotation spectra indicates that the mode is either an Alfven wave or a fast wave propagating parallel to the magnetic field ($\alpha = 0$).

We have found that the 2nd harmonic in the Faraday rotation spectra occurs when a magnetosonic wave has a large amplitude. The magnetosonic wave types can be distinguished because of the phase difference between the density and Faraday rotation fluctuations in the fundamental harmonic.

As with all FR observations, there is a viewing angle dependence. The MHD wave must fluctuate with a component of the fluid flow along the line of sight. With the limitations it is possible to put a lower boundary on the amplitude of a wave measured through Faraday rotation assuming that the perturbation is along the line of sight; if the perturbation has a component of the magnetic field perpendicular to the line of sight, then the magnetic field strength in the wave would actually be larger than that observed in the Faraday rotation measurement.

An Alfven wave measured by Cassini had a minimum amplitude of 4.3 μT. If we assume that these waves are typical of the waves propagating in all directions away from the Sun, then the amount of power lost is 1.6×10^{19} W. For comparison, the total power radiated by the Sun is 4×10^{26} W, the power required to pass through the gravitational potential difference from the Sun to 1AU is 1.9×10^{23} W, and the power in the kinetic energy flux at 1AU is 1.7×10^{20} W.

MHD wave observations through Faraday rotation can help estimate the wave energy in the solar corona. The frequency, power, and location of MHD waves can also provide useful parameters for probing the solar corona.

CHAPTER 7

Conclusions

7.1 Results of Investigation

The solar corona is comprised of hot tenuous plasma with the solar magnetic field frozen-in. At 2 solar radii, the plasma of the corona accelerates into the solar wind which directly affects the geomagnetic field when it reaches the Earth. While the solar wind velocity can be predicted with an error of $\pm 15\%$, the polarity of the interplanetary magnetic field frozen-in to the solar wind can be predicted 75% of the time. Between the solar surface and orbiting spacecraft (Messenger en route to Mercury will be as close as 0.4 AU) and outside of solar active regions, the coronal magnetic field can only be measured using Faraday rotation.

High frequency radio sources for Faraday rotation observations include natural and spacecraft sources. Spacecraft observations present special challenges due to power considerations for the the missions. The radio frequency transmitter is designed to use the minimum amount of power to transmit the data with the fewest errors to maximize efficiency. Beginning with Magellan, transmitter were designed to transmit circular polarization for this purpose. However, the polarizer giving this capability is approximately 99% effective and transmits 1% of the signal power in the opposite polarization. Therefore, the signal is elliptically polarized with a plane

of polarization that can be observed for Faraday rotation observations.

The ground receiver similarly uses a polarizer to split the incoming signal into the two opposite polarizations with a similar efficiency. Therefore, plane of polarization observations may be observed to rotate with changes in the ratio of signal power in the two polarizations. To calibrate for this effect, we used the parallactic effect: the rotation in the plane of polarization during a pass from using an altitude-azimuth antenna. This method was successful in the X-band; however, the Ka-band is affected by secondary effects in the antenna which are insignificant in the X-band due to its greater wavelength (4 cm in X, 1 cm in Ka). The gravitational deformation of the alt-az antenna become significant below 7 cm.

The X-band observations in 2002 were collected as the Cassini spacecraft pointing was controlled by reaction wheels. Due to the accelerated deterioration of the reaction wheels, the Cassini spacecraft pointing was controlled by thrusters to preserve the wheels in 2003. The rotation observations from 2003 indicate that the thruster pointing was introducing a limited amount of rotation. Without a stable transmitting platform, the 2003 data could not be used for Faraday rotation observations pending further calibration.

The predictions for solar wind polarity and velocity are based on the Potential Field Source Surface and Wang-Sheeley models for the coronal magnetic field configuration and the solar wind. It has been shown that the PFSS model requires little adjustment to predict the magnitude and direction of Faraday rotation observations outside of the source surface. Within the source surface however, the PFSS-based Faraday rotation model diverges significantly from the observations. This indicates the need for a full MHD based model for the region. From 2 to 3 solar radii, the plasma beta (ratio of the thermal to the magnetic pressure) increased to 1. Beyond

194

three solar radii the sum of the thermal and magnetic pressure gradients are only slightly greater than the gravitational force per volume; this indicates that another source of energy is necessary to accelerate the solar wind.

Periodically, the solar corona releases large scale structures of enhanced mass and magnetic flux called Coronal Mass Ejections. CMEs can have deleterious effects on the surface of the Earth and any communications, satellites, or personnel off the surface of the Earth. Faraday rotation measured both the electron density and the flux rope magnetic field of CMEs. Without multiple lines of sight and electron density information, the orientation of the flux rope with respect to the line of sight can be determined in cone angle. The azimuthal angle of the rope is ambiguous with the handedness. The 'W' shaped Faraday rotation flux ropes were oriented anti-parallel to the line of sight, while the sigmoid and reverse sigmoid were oriented perpendicular to the line of sight. Faraday rotation measurements of CMEs can greatly enhance the determination of risk posed by approaching CMEs.

Coronal heating models need to produce expected observables, but the MHD waves expected in the corona are not observable outside of coronal loops in the "invisible" corona except through Faraday rotation measurements. The Helios and Cassini spacecraft both measured large amplitude, 4-5 minute period MHD waves at 4 and 2.5 solar radii respectively. The Helios MHD wave observations occasionally included a secondary harmonic in the Faraday rotation spectra with a frequency of $2\times$ the primary. We show that this secondary harmonic is expected from a magnetosonic MHD wave due to the fluctuation in electron density; however, we find that identifying the mode of the magnetosonic wave is problematic because of the dependence of Faraday rotation on the orientation of the magnetic field relative to the line of sight. Because the MHD wave observed by Cassini did not show a similar fluctuation in columnar electron density, we identified the wave on 2002

June 20 as an Alfven wave. Using an MHD wave model, we found that the power in the Faraday rotation can be reproduced with a range of amplitudes depending on the orientation of the wave relative to the line of sight. Such MHD waves can be observed by Faraday rotation only with the proper orientation and coherence. For coherent radially propagating waves within the region of coherence in the Faraday rotation measurement defined to be those distances along the line of sight that are a quarter of a wavelength or less farther from the sun than the point of closest approach the observed waves represented a significant energy flux for the solar wind. Using the minimum amplitude, we calculate the energy density of the wave and the power released into the corona assuming the continuous generation of waves in all directions; the resulting power is $1.6 \times 10^{19} W$.

We have shown that high frequency Faraday rotation measurements of the inner corona are important to understand the structure of the coronal magnetic field, the transfer of energy within the corona, and to measure the magnetic structure of CMEs. These observations can improve our predictions of the geoeffectiveness of the solar wind.

7.2 Future Work

I suggest future spacecraft radio systems be designed to allow variable power to the system. Because the observation program at the spacecraft is generally suspended when the spacecraft is occulted by the Sun and solar corona, diverting the power the instruments would usually draw to give an extra boost to the carrier would be really beneficial. If the signal sent from the spacecraft to the Earth can be described by $A_c S(t) \exp(i\omega_c t) + n(t)$ where A_c is the carrier amplitude, $S(t)$ is the telemetry data, and $n(t)$ is the added noise along the transmission path, the standard radio

system is designed to boost power to $S(t)$. I recommend that future designs also be able to boost A_c.

The Stereo spacecraft are moving slowly away from Earth in the pro- and retro-grade directions in the Earth's orbit. By 2014, both spacecraft will be passing behind the solar corona making it possible to obtain Faraday rotation measurements in the same location over several solar rotations. Continuous collection of FR data using the conjunction geometry of the Stereo spacecraft in can allow the resolution of waves of much larger time scales providing a regular observable for coronal heating models.

The effects of the the different amplitudes between polarizations in an elliptically polarized signal on polarization leakage need to be investigated. Beam squint and squash variability with Alt-Az antennas in frequency and power need to be calibrated for determining the antenna component of the Jones matrix.

APPENDIX A

General Faraday Rotation

Faraday rotation is the rotation of the plane of polarization as an electromagnetic signal passed through a magnetic medium such as a magnetized plasma. The equation for Faraday rotation in a magnetized medium is derived from Maxwell's equations. In the presence of an external magnetic field, the electric permittivity is a tensor and Maxwell's equations for an electromagnetic wave in the media become:

$$\nabla X \overrightarrow{E} = i\omega\mu_o \overrightarrow{H}$$

$$\nabla X \overrightarrow{H} = -i\omega\bar{\bar{\epsilon}}\overrightarrow{E}$$

The electric vector is given by

$$\overrightarrow{E} = \overrightarrow{E_o} \exp\left[\mathrm{i}(\overrightarrow{k} \cdot \overrightarrow{r} - \omega\mathrm{t})\right]$$

In Einstein notation, we can solve for the wave:

$$\epsilon_{ijk}\frac{\partial E_j}{\partial i} = i\omega\mu_o H_k$$

$$\epsilon_{lmn}\frac{\partial H_m}{\partial l} = -i\omega\bar{\bar{\epsilon}}E_n$$

$$\epsilon_{lmn}\frac{\partial}{\partial l}\left(\frac{\epsilon_{ijk}\frac{\partial E_j}{\partial i}}{i\omega\mu_o}\right) = -i\omega\bar{\bar{\epsilon}}E_n$$

198

$$\epsilon_{lmn} \frac{\partial}{\partial l} \left(\epsilon_{ijk} \frac{\partial E_j}{\partial i} \right) = \omega^2 \mu_o \bar{\bar{\epsilon}} E_n$$

$$k = m$$

$$\epsilon_{nlm} \epsilon_{ijm} \frac{\partial}{\partial l} \frac{\partial E_j}{\partial i} = \omega^2 \mu_o \bar{\bar{\epsilon}} E_n$$

$$\left(\delta_{nl} \delta_{lj} - \delta_{nj} \delta_{li} \right) \frac{\partial}{\partial l} \frac{\partial E_j}{\partial i} = \omega^2 \mu_o \bar{\bar{\epsilon}} E_n$$

$$\frac{\partial}{\partial l} \frac{\partial E_l}{\partial n} - \frac{\partial}{\partial l} \frac{\partial E_n}{\partial l} = \omega^2 \mu_o \bar{\bar{\epsilon}} E_n$$

Calculating the derivatives and going back to vector notation, we find:

$$k^2 \vec{E_o} - \vec{k} \left(\vec{k} \cdot \vec{E_o} \right) = \omega^2 \mu_o \bar{\bar{\epsilon}} \vec{E_o}$$

This can also be expressed as the wave's dispersion relation (note that $\delta_{ln} E_l = E_n$)

$$\det \left[k^2 \bar{\bar{I}} - \vec{k}\,\vec{k} - \omega^2 \mu_o \bar{\bar{\epsilon}} \bar{\bar{I}} \right] = 0$$

At this point the electric permittivity depends on the medium which gives the index of refraction for the two polarizations in that medium. As we will show for a plasma below.

A.0.1 Faraday Rotation Equation For A Plasma

The electric permittivity vector for a plasma is determined from the equations of motion. If the z-axis is parallel to the applied magnetic field (Stelzried, 1968)

$$\bar{\bar{\epsilon}} = \begin{bmatrix} \epsilon_o(1 - \frac{X}{1-Y^2}) & -i\epsilon_o\frac{XY}{1-Y^2} & 0 \\ i\epsilon_o\frac{XY}{1-Y^2} & \epsilon_o(1 - \frac{X}{1-Y^2}) & 0 \\ 0 & 0 & \epsilon_o(1 - X) \end{bmatrix}$$

(A.1)

$$Y = (-\omega_g e/\omega)$$
$$X = (\omega_{pe}^2/\omega^2)$$

and the general solution to Faraday rotation is:

$$FR = \frac{-XY(\omega/c)}{(1+Y)[(1-Y)(1-Y-X)]^{1/2} + (1-Y)[(1+Y)(1+Y-X)]^{1/2}}$$

(A.2)

$$Y = (-\omega_g e/\omega)$$
$$X = (\omega_{pe}^2/\omega^2)$$

APPENDIX B

Doppler Measurement of Δ I

The quantity I is the integrated density along the line of sight from the spacecraft to the Earth. In this section we present the equations that allow the variation of I to be derived from the Doppler shift. Section B.1 presents the code used to calculate the electron density from the Doppler shift. B. Bertotti and G. Giampieri have derived the equations for the Doppler measurement of electron density (Bertotti & Giampieri, 1997). The electron density causes a Doppler shift through changing the component of the signal propagation vector parallel to the spacecraft and ground antenna line of sight producing a fractional frequency shift as shown in Figure B.1 of $\frac{\Delta f}{f}$.

$$\frac{\Delta f}{f} = \frac{v}{c}\theta$$

where $\frac{v}{c}$ is the orbital velocity of both antennas and θ is the angle of the displacement. Specifically, $v = \frac{v_\oplus l_\oplus + v_{sc} l_{sc}}{l_\oplus + l_{sc}}$; this contribution was on the order of 10^4 m/s.

The deflection of the ray θ was shown to be

$$\theta = \int_{sc}^{\oplus} \delta n\, dx$$
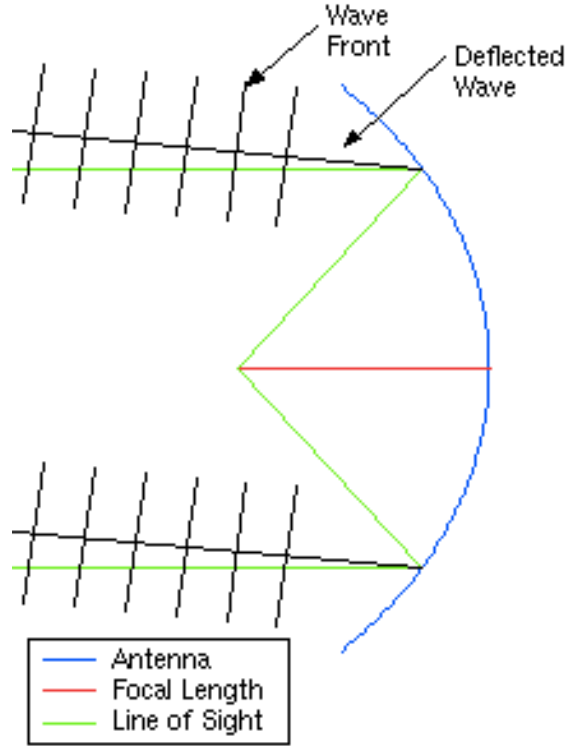
Figure B.1: *Doppler shift from signal refraction by plasma. Following the acquisition of the signal, the antenna pointing is adjusted to maximize signal power. Fluctuations in electron density cause the signal to deflect about this mean position causing a decrease in the signal frequency. The component of the incoming deflected wave parallel to the line of sight of the antenna is passed to the subreflector near the antenna focus. The signal is measured from this component of the deflected wave.*

where n is the index of refraction and x is the axis of propagation

$$n^2 = 1 - \frac{\omega_{pe}^2}{\omega^2}$$

where ω_{pe} $[radians/second]$ is the plasma frequency, and ω $[radians/second]$ is the signal frequency. The plasma frequency is

$$\omega_{pe}^2 = \frac{Ne^2}{\epsilon_o m_e} \left[radians^2/second^2\right]$$

where electron density N $meters^{-3}$, charge $e = 1.6022 \times 10^{-19}$ $Coulombs$, permittivity of free space $\epsilon_o = 8.8542 \times 10^{-12}$ $Coulombs^2/Newton/meters^2$, and electron mass $m_e = 9.1095 \times 10^{-31}$ $kilograms$. In the high freq regime, $\omega \gg \omega_{pe}$ allows the index of refraction to be approximated as

$$n \sim 1 - \frac{1}{2}\frac{\omega_{pe}^2}{\omega^2}$$

which gives $\delta n = -\frac{1}{2}\frac{\omega_{pe}^2}{\omega^2}$ and

$$\delta n = -\frac{1}{2}\frac{e^2}{\epsilon_o m_e 4\pi^2 f^2 c}N \left[seconds\right]$$

where signal frequency $f = \frac{\omega}{2\pi}$ $[Hz]$ and

$$I = \int_{sc}^{\oplus} N ds \left[meters^{-2}\right]$$

203

And so

$$\frac{\Delta f}{f} = \frac{v}{c} \int_{\oplus}^{sc} -\frac{1}{2} \frac{e^2}{\epsilon_o m_e 4\pi^2 f^2 c} N dx$$

However, with every time step that the uplink-locked antenna calculates the new pointing position, it moves to maximize the power in the signal. In other words, it adjusts to point in the direction of the maximum power in the bent ray. Therefore, the equation above needs to be adjusted to

$$\frac{\Delta f}{f} = \frac{v}{c} \left(-\frac{1}{2} \frac{e^2}{\epsilon_o m_e 4\pi^2 f^2 c} \right) \frac{\delta}{\delta t} \int_{\oplus}^{sc} N dx$$

B.1   2002 Doppler Calculation Code

The code `dncorryear.m` which calculates the change in electron density from the Doppler shift in the signal due to the plasma content loads in the frequency predictions files and the observed frequency from FFT calculations and saves the integration of the change in columnar electron density `ndoy` and time `tdoy` in matlab files `nfromdoppyear.mat`. Note in 2003, the predicts were generated with different ratios for the downconversion process requiring the two frequencies to be returned to "skyfrequency", the original signal frequency prior to the downconversion process, before the Doppler shift could be determined. The software is located in the `appb` folder.

B.1.1   Run Commands

First start matlab in the `appb` folder.

From within matlab:

```
>> addpath yourlocaldirtree
>> dncorr2002
>> dncorr2003
```

where `yourlocaldirtree` is the the full directory path to the folder containing all the Matlab `.m` files.

B.1.2   Files Loaded

The `hdr` files contain the header information from within the RSR files are are created using `ReadRSR`. The `phase` files contain the frequency of the carrier wave after the downconversion process. The `predicteffects.txt` files are created using the frequency predictions `dlf` files to calculate the effects of the downconversion process in 2003.

RSR1A1_02_167_162155.1A1.hdr

RSR1A1_02_167_184653.1A1.hdr

RSR4A1_02_167_162155.4A1.hdr

RSR4A1_02_167_184653.4A1.hdr

RSR1A1_02_168_190800.1A1.hdr

RSR1A1_02_168_193204.1A1.hdr

RSR1A1_02_168_195726.1A1.hdr

RSR1A1_02_168_200348.1A1.hdr

RSR1A1_02_168_205256.1A1.hdr

RSR4A1_02_168_190800_R.4A1.hdr

RSR4B1_02_168_193204_R.4B1.hdr

RSR4A1_02_168_195726_R.4A1.hdr

RSR4B1_02_168_200348.4B1.hdr

RSR4B1_02_168_205256.4B1.hdr

RSR1A1_02_169_161054.1A1.hdr

RSR1A1_02_169_174432.1A1.hdr

RSR4B1_02_169_161054.4B1.hdr

RSR4B1_02_169_174432.4B1.hdr

RSR1A1_02_170_142745.1A1.hdr

RSR1A1_02_170_160900.1A1.hdr

RSR4B1_02_170_142745.4B1.hdr

RSR4B1_02_170_160900.4B1.hdr

RSR1A1_02_171_133600.hdr

RSR1A1_02_171_160900.hdr

RSR1A1_02_172_013114.hdr

RSR4B1_02_171_133600.hdr

RSR4B1_02_171_160900.hdr

RSR4B1_02_172_013114.hdr

RSR1A1_02_172_134923.hdr

RSR1A1_02_172_162202.hdr

RSR1A1_02_172_190133.hdr

RSR1A1_02_173_000655.hdr

RSR4B1_02_172_134923.hdr

RSR4B1_02_172_162202.hdr

RSR4B1_02_172_190133.hdr

RSR4B1_02_173_000655.hdr

RSR1A1_02_173_132913.1A1.hdr

RSR1A1_02_173_160820.1A1.hdr

RSR1A1_02_174_010120.1A1.hdr

RSR1A1_02_174_012119.1A1.hdr

RSR4B1_02_173_132913.4B1.hdr

RSR4B1_02_173_160820.4B1.hdr

RSR4B1_02_174_010120.4B1.hdr

RSR4B1_02_174_012119.4B1.hdr

RSR_02_174_133241.1A1.hdr

RSR_02_174_134046.1A1.hdr

RSR_02_174_155336.1A1.hdr

RSR_02_175_000400.1A1.hdr

RSR_02_174_133241.4B1.hdr

RSR_02_174_134046.4B1.hdr

RSR_02_174_155336.4B1.hdr

RSR_02_175_000400.4B1.hdr

RSR1A1_02_175_131424.1A1.hdr

RSR1A1_02_175_155237.1A1.hdr

RSR1A1_02_176_010045.1A1.hdr

RSR4B1_02_175_131424.4B1.hdr

RSR4B1_02_175_155237.4B1.hdr

RSR4B1_02_176_010045.4B1.hdr

RSR1A1_02_176_131930.1A1.hdr

RSR1A1_02_176_155059.1A1.hdr

RSR4B1_02_176_131930.4B1.hdr

RSR4B1_02_176_155059.4B1.hdr

RSR1A1_02_177_131635.1A1.hdr

RSR1A1_02_177_160615.1A1.hdr

RSR1A1_02_177_215846.1A1.hdr

RSR4B1_02_177_131635.4B1.hdr

RSR4B1_02_177_160615.4B1.hdr

RSR4B1_02_177_215846.4B1.hdr

S82D25P2086_03-177-133713.1A1.hdr

S82D25P2086_03-177-165326.1A1.hdr

S82D25P2086_03-177-133713.2B1.hdr

S82D25P2086_03-177-165326.2B1.hdr

S82D13P2087_03-178-140213.1A1.hdr

S82D13P2087_03-178-155401.1A1.hdr

S82D13P2087_03-178-183732.1A1.hdr

S82D13P2087_03-178-140213.2B1.hdr

S82D13P2087_03-178-155401.2B1.hdr

S82D13P2087_03-178-183732.2B1.hdr

S82D13P2088_03-179-134960.1A1.hdr

S82D13P2088_03-179-163857.1A1.hdr

S82D13P2088_03-179-134960.2B1.hdr

S82D13P2088_03-179-163857.2B1.hdr

S82D13P2089_03-180-134500.1A1.hdr

S82D13P2089_03-180-163328.1A1.hdr

S82D13P2089_03-180-134500.2B1.hdr

S82D13P2089_03-180-163328.2B1.hdr

S82D13P2090_03-181-134500.1A1.hdr

S82D13P2090_03-181-163330.1A1.hdr

S82D13P2090_03-181-134500.2B1.hdr

S82D13P2090_03-181-163330.2B1.hdr

S82D13P2091_03-182-132110.1A1.hdr

S82D13P2091_03-182-164627.1A1.hdr

S82D13P2091_03-182-132110.2B1.hdr

S82D13P2091_03-182-164627.2B1.hdr

S82D13P2092_03-183-133500.1A1.hdr

S82D13P2092_03-183-162335.1A1.hdr

S82D13P2092_03-183-133500.2B1.hdr

S82D13P2092_03-183-162335.2B1.hdr

S82D13P2093_03-184-133500.1A1.hdr

S82D13P2093_03-184-162337.1A1.hdr

S82D13P2093_RSR2B1.03-184-133500.hdr

S82D13P2093_RSR2B1.03-184-162337.hdr

S82D13P2094_RSR1A1.03-185-132200.hdr

S82D13P2094_RSR1A1.03-185-162339.hdr

S82D13P2094_RSR2B1.03-185-132200.hdr

S82D13P2094_RSR2B1.03-185-162339.hdr

S82D13P2095_RSR1A1.03-186-131500.hdr

S82D13P2095_RSR1A1.03-186-161339.hdr

S82D13P2095_RSR2B1.03-186-131500.hdr

S82D13P2095_RSR2B1.03-186-161339.hdr

RSR1A1_02_167_162155.1A1.phase

RSR1A1_02_167_184653.1A1.phase

RSR1B1_02_167_162155.1B1.phase

RSR1B1_02_167_184653.1B1.phase

RSR4A1_02_167_162155.4A1.phase

RSR4A1_02_167_184653.4A1.phase

RSR4B1_02_167_162155.4B1.phase

RSR4B1_02_167_184653.4B1.phase

RSR1A1_02_168_190800.1A1.phase

RSR1A1_02_168_193204.1A1.phase

RSR1A1_02_168_195726.1A1.phase

RSR1A1_02_168_200348.1A1.phase

RSR1A1_02_168_205256.1A1.phase

RSR1B1_02_168_190800.1B1.phase

RSR1B1_02_168_193204.1B1.phase

RSR1B1_02_168_195726.1B1.phase

RSR1B1_02_168_200348.1B1.phase

RSR1B1_02_168_205256.1B1.phase

RSR4A1_02_168_190800_R.4A1.phase

RSR4A1_02_168_193204_L.4A1.phase

RSR4A1_02_168_195726_R.4A1.phase

RSR4A1_02_168_200348.4A1.phase

RSR4A1_02_168_205256.4A1.phase

RSR4B1_02_168_190800_L.4B1.phase

RSR4B1_02_168_193204_R.4B1.phase

RSR4B1_02_168_195726_L.4B1.phase

RSR4B1_02_168_200348.4B1.phase

RSR4B1_02_168_205256.4B1.phase

RSR1A1_02_169_161054.1A1.phase

RSR1A1_02_169_174432.1A1.phase

RSR1B1_02_169_161054.1B1.phase

RSR1B1_02_169_174432.1B1.phase

RSR4A1_02_169_161054.4A1.phase

RSR4A1_02_169_174432.4A1.phase

RSR4B1_02_169_161054.4B1.phase

RSR4B1_02_169_174432.4B1.phase

RSR1A1_02_170_142745.1A1.phase

RSR1A1_02_170_160900.1A1.phase

RSR1B1_02_170_142745.1B1.phase

RSR1B1_02_170_160900.1B1.phase

RSR4A1_02_170_142745.4A1.phase

RSR4A1_02_170_160900.4A1.phase

RSR4B1_02_170_142745.4B1.phase

RSR4B1_02_170_160900.4B1.phase

RSR1A1_02_171_133600.phase

RSR1A1_02_171_160900.phase

RSR1A1_02_172_013114.phase

RSR1B1_02_171_133600.phase

RSR1B1_02_171_160900.phase

RSR1B1_02_172_013114.phase

RSR4B1_02_171_133600.phase

RSR4B1_02_171_160900.phase

RSR4B1_02_172_013114.phase

RSR4A1_02_171_133600.phase

RSR4A1_02_171_160900.phase

RSR4A1_02_172_013114.phase

RSR1A1_02_172_134923.phase

RSR1A1_02_172_162202.phase

RSR1A1_02_172_190133.phase

RSR1A1_02_173_000655.phase

RSR1B1_02_172_134923.phase

RSR1B1_02_172_162202.phase

RSR1B1_02_172_190133.phase

RSR1B1_02_173_000655.phase

RSR4B1_02_172_134923.phase

RSR4B1_02_172_162202.phase

RSR4B1_02_172_190133.phase

RSR4B1_02_173_000655.phase

RSR4A1_02_172_134923.phase

RSR4A1_02_172_162202.phase

RSR4A1_02_172_190133.phase

RSR4A1_02_173_000655.phase

RSR1A1_02_173_132913.phase

RSR1A1_02_173_160820.phase

RSR1A1_02_174_010120.phase

RSR1A1_02_174_012119.phase

RSR1B1_02_173_132913.phase

RSR1B1_02_173_160820.phase

RSR1B1_02_174_010120.phase

RSR1B1_02_174_012119.phase

RSR4A1_02_173_132913.phase

RSR4A1_02_173_160820.phase

RSR4A1_02_174_010120.phase

RSR4A1_02_174_012119.phase

RSR4B1_02_173_132913.phase

RSR4B1_02_173_160820.phase

RSR4B1_02_174_010120.phase

RSR4B1_02_174_012119.phase

RSR_02_174_133241.1A1.phase

RSR_02_174_133241.1B1.phase

RSR_02_174_133241.4A1.phase

RSR_02_174_133241.4B1.phase

RSR_02_174_134046.1A1.phase

RSR_02_174_134046.1B1.phase

RSR_02_174_134046.4A1.phase

RSR_02_174_134046.4B1.phase

RSR_02_174_155336.1A1.phase

RSR_02_174_155336.1B1.phase

RSR_02_174_155336.4A1.phase

RSR_02_174_155336.4B1.phase

RSR_02_175_000400.1A1.phase

RSR_02_175_000400.1B1.phase

RSR_02_175_000400.4A1.phase

RSR_02_175_000400.4B1.phase

RSR1A1_02_175_131424.1A1.phase

RSR1A1_02_175_155237.1A1.phase

RSR1A1_02_176_010045.1A1.phase

RSR1B1_02_175_131424.1B1.phase

RSR1B1_02_175_155237.1B1.phase

RSR1B1_02_176_010045.1B1.phase

RSR4B1_02_175_131424.4B1.phase

RSR4B1_02_175_155237.4B1.phase

RSR4B1_02_176_010045.4B1.phase

RSR1A1_02_176_131930.1A1.phase

RSR1A1_02_176_155059.1A1.phase

RSR1B1_02_176_131930.1B1.phase

RSR1B1_02_176_155059.1B1.phase

RSR4A1_02_176_131930.4A1.phase

RSR4A1_02_176_155059.4A1.phase

RSR4B1_02_176_131930.4B1.phase

RSR4B1_02_176_155059.4B1.phase

RSR1A1_02_177_131635.1A1.phase

RSR1A1_02_177_160615.1A1.phase

RSR1A1_02_177_215846.1A1.phase

RSR1B1_02_177_131635.1B1.phase

RSR1B1_02_177_160615.1B1.phase

RSR1B1_02_177_215846.1B1.phase

RSR4A1_02_177_131635.4A1.phase

RSR4A1_02_177_160615.4A1.phase

RSR4A1_02_177_215846.4A1.phase

RSR4B1_02_177_131635.4B1.phase

RSR4B1_02_177_160615.4B1.phase

RSR4B1_02_177_215846.4B1.phase

S82D25P2086_03-177-133713.1A1.phase

S82D25P2086_03-177-165326.1A1.phase

S82D25P2086_03-177-133713.2B1.phase

S82D25P2086_03-177-165326.2B1.phase

S82D13P2087_03-178-140213.1A1.phase

S82D13P2087_03-178-155401.1A1.phase

S82D13P2087_03-178-183732.1A1.phase

S82D13P2087_03-178-140213.2B1.phase

S82D13P2087_03-178-155401.2B1.phase

S82D13P2087_03-178-183732.2B1.phase

S82D13P2088_03-179-134960.1A1.phase

S82D13P2088_03-179-163857.1A1.phase

S82D13P2088_03-179-134960.2B1.phase

S82D13P2088_03-179-163857.2B1.phase

S82D13P2089_03-180-134500.1A1.phase

S82D13P2089_03-180-163328.1A1.phase

S82D13P2089_03-180-134500.2B1.phase

S82D13P2089_03-180-163328.2B1.phase

S82D13P2090_03-181-134500.1A1.phase

S82D13P2090_03-181-163330.1A1.phase

S82D13P2090_03-181-134500.2B1.phase

S82D13P2090_03-181-163330.2B1.phase

S82D13P2091_03-182-132110.1A1.phase

S82D13P2091_03-182-164627.1A1.phase

S82D13P2091_03-182-132110.2B1.phase

S82D13P2091_03-182-164627.2B1.phase

S82D13P2092_03-183-133500.1A1.phase

S82D13P2092_03-183-162335.1A1.phase

S82D13P2092_03-183-133500.2B1.phase

S82D13P2092_03-183-162335.2B1.phase

S82D13P2093_03-184-133500.1A1.phase

S82D13P2093_03-184-162337.1A1.phase

S82D13P2093_RSR2B1.03-184-133500.phase

S82D13P2093_RSR2B1.03-184-162337.phase

S82D13P2094_RSR1A1.03-185-132200.phase

S82D13P2094_RSR1A1.03-185-162339.phase

S82D13P2094_RSR2B1.03-185-132200.phase

S82D13P2094_RSR2B1.03-185-162339.phase

S82D13P2095_RSR1A1.03-186-131500.phase

S82D13P2095_RSR1A1.03-186-161339.phase

S82D13P2095_RSR2B1.03-186-131500.phase

S82D13P2095_RSR2B1.03-186-161339.phase

178predicteffects.txt

179predicteffects.txt

180predicteffects.txt

181predicteffects.txt

183predicteffects.txt

184predicteffects.txt

185predicteffects.txt

B.1.3 Files Generated

These files contain the integration of the change in columnar electron density `ndoy` and time `tdoy` matrices.

nfromdopp2002.mat

nfromdopp2003.mat

APPENDIX C

Range-Data Processing

In this appendix we discuss the process of obtaining integrated electron density data along the line of sight to Cassini using coded square waves sent to Cassini and sent back to Earth with a "bent pipe".

C.1   Range Units to Distance

The square waves that were transmitted on the carrier are correlated with those received from Cassini and their round-trip travel time measures in "ranging units". For an X-band uplink at any tracking stations that has a Block V Exciter (the case for Cassini), one range unit is $749*2/221$ cycles of the X-band transmitted frequency (Moyer, 2000). This means that

$$1RU = \frac{749*2/221 cyc}{f_t cyc/sec} = \frac{749*2}{221 f_t} sec$$

and that therefore the distance for a ranging unit is

$$1RU = \frac{c}{2}\frac{749 * 2}{221 f_t}[meters]$$

where f_t is the transmitted frequency (8.4 GHz).

C.2   Range Units to Electron Density

The following process is applied to measure the total columnar electron density from ranging data:

1) data is received in ranging units

2) converted to distance

3) the minimum distance is subtracted off all of the points

4) the distance values converted to seconds

5) the columnar electron density calculated from the seconds

The third step is to ensure that only the differences in distance due to the plasma remain.

The calculation of the electron density begins with the formula for the group velocity in a plasma

$$v_g = c\sqrt{1 - f_p^2/f^2}$$

where $f >> f_p$, we can do a Taylor expansion to get

$$v_g = c(1 - \frac{1}{2}\frac{f_p^2}{f^2}) = c(1 - \frac{N_e^2}{2*4\pi^2\epsilon_0 mf^2})$$

Now this formula is plugged in to the calculation for the time it takes the signal to travel at group velocity along path s

$$\tau_g = \int \frac{ds}{v_g} = \frac{1}{c} \int \frac{ds}{(1 - \frac{N_e^2}{2*4\pi^2\epsilon_0 mf^2})}$$

This can also be Taylor expanded to give

$$\tau_g = \frac{1}{c} \int (1 + \frac{N_e^2}{2*4\pi^2\epsilon_0 mf^2})ds \sim \frac{s}{c} + \frac{e^2 I}{c8pi^2\epsilon_0 mf^2}$$

and so therefore

$$\Delta\tau \sim \frac{e^2 I}{c8pi^2\epsilon_0 mf^2}$$

From the range units data (residuals), this is calculated as (note that $A = resid\frac{749*2}{221}\frac{c}{2f_t}$)

$$\Delta\tau = \frac{A - min(A)}{c} sec$$

which can then be used to solve for the columnar electron density $I\frac{\#}{m^2}$.

212

C.3 Ranging Code

The matlab program `appc/calc.m` loads the ranging residuals `resid.dat`, and calculates the columnar electron density using the formulas above. Note that ranging measurements were only enabled on the X-band (8.4 GHz).

C.3.1 Usage

Move to the `appc` directory. From within matlab:

```
>> calc
```

C.3.2 Ionosphere Removal

For time series during which the line of sight changes through the ionosphere were dominant, a simple 2nd order polynomial fit was used to obtain an approximate value for the coronal contribution. This operation is performed in the bottom half of the code.

C.3.3 Input/Output Files

`calc.m` loads the range data file `resid.dat` for processing. No output files are specified; the user needs to adjust the code to their needs.

C.3.4 Ancillary Data Files

Three files have been include in `appc` for the user's information. `drvid176.mat` contains the time (matrix `N`) and total columnar electron density values (matrix `range`) for the observation pass on 2002 June 25 (doy 176). Note that the formal time can be obtained using the Matlab command `datevec(N)`. `rangedata.mat` and `rangemod.mat` give the columnar electron density values (matrix `Inew`) with distance from the sun in AU and solar radii (matrix `m`) respectively.

APPENDIX D

Adaptation of Ranging Models

Several papers presenting results from previous ranging experiments have fit global electron density models to the measurements. None took into account that the electron density distribution about the Sun is strongly influenced by its global magnetic field configuration. Ranging measurements can be compared to these models by determining the global field configuration at the time of interest, determining the configuration of the global field during the ranging experiment, calculating the rotation matrix between the two, and rotating the positions of points along the line of sight using the rotation matrix. The problem that this is addressing is the fact that every point along the line of sight in 1976 during the Viking ranging experiment was located at a different latitude in solar dipole coordinates in comparison to every point along the line of sight in 2002 during the Cassini ranging experiment. This is clearly apparent in Muhlemann and Anderson's work showing that the electron density distribution with solar Carrington coordinates is strongly asymmetrical between the limbs of the Sun (Esposito & Anderson, 1977). If the solar dipole field was tilted towards the east limb (ingress), then the line of sight from Mars would have been at distinctly different latitude in solar dipole coordinates between ingress and egress. In contrast, during 2002 the solar dipole was oriented away from the Earth indicating that this model would not provide a good fit.

The Tyler model however was empirically derived from other sources of observation. To use this particular model, the positions of points along the line of sight should be simply rotated into the dipole coordinates. After the new latitudes of the points along the line of sight are determined, the electron density can be calculated for each point, and their integration compared to measurements.

D.0.5   Ranging Models

The available models are listed in Table D.1

D.0.5.1   Adaptation of Ranging Models

The local dipole first need to be determined given the g10, g11, and h11 coefficients for the spherical harmonics Legendre polynomials. Setting the coordinate system such that

$$\vec{z'} = \left[\begin{array}{ccc} h11 & g11 & g10 \end{array} \right]$$

The x-direction simply needs to be consistent, so it was set to the direction of the x-axis in solar (Carrington) coordinates. However for the Tyler model, the x-axis should be set from the center of the Earth to the first point of Aries at the J2000 epoch as discussed in subsection 4.1.2. Finally, the coordinate system for position in the dipole coordinates in terms of Carrington coordinates (unprimed) (or J2000 coordinates) is:

authors	spacecraft	frequency band(s)	time of conjunction	model coordinates	formula
Esposito, Edenhofer, & Lueneburg 1980	Helios 2	S	Mar-Jun 1976	spherical	$N_e(r) = \frac{0.55\times10^6}{r^{2+0.1}}\frac{el}{cm^3} + \frac{1\times10^8}{r^6}$
Tyler, Brenkle, Komarek, & Zygielbaum 1977	Viking	S&X	Oct-Dec 1976	heliographic with rotation axis perpendicular to ecliptic	$N(r,\theta) = \left[\frac{1.55\times10^{14}}{r^6} + \frac{3.44\times10^{11}}{r^2}\right]$ $F(\theta)\frac{\#}{m^3}$ $F(\theta) = \sqrt{\cos\theta^2 + \frac{1}{64}\sin\theta^2}$ Note θ is the heliographic latitude
Berman & Wackley (1977)	Viking	S/X	Oct-Dec 1976	heliographic	$N(r,\theta) = \frac{2.39\times10^{14}}{r^6} + \frac{1.67\times10^{12}}{r^{2.30}}G(\theta)$ $G(\theta) = 10^{-0.9\theta/90}$
D.O. Muhleman&J.D. Anderson 1981	Viking	S/X	Oct-Dec 1976	heliographic	$N_e = \frac{1.32\times10^6}{r^{2.7}}\exp-\phi^2/8o^2 + \frac{2.3\times10^5}{r^{2.04}}$

Table D.1: *Electron density models empirically determined from ranging experiments*

217

$$\vec{z'} X \vec{x} = \vec{y'}$$

and

$$\vec{y'} X \vec{z'} = \vec{x'}$$

Now every position along the line of sight in in J2000 coordinates needs to be rotated into the dipole coordinate system for the Tyler model:

$$\overleftrightarrow{R} \: \overrightarrow{SUN, J2000} = \overrightarrow{Dipole}$$

such that

$$R = \begin{bmatrix} \frac{\frac{g_{10}^2}{n_z^2 n_y} + \frac{g_{11}^2}{n_z^2 n_y}}{n_x} & \frac{-g_{11}h_{11}}{n_z^2 n_y n_x} & \frac{-g_{10}h_{11}}{n_z^2 n_y n_x} \\ 0 & \frac{g_{10}}{n_z n_y} & \frac{-g_{11}}{n_z n_y} \\ \frac{h_{11}}{n_z} & \frac{g_{11}}{n_z} & \frac{g_{10}}{n_z} \end{bmatrix}$$

where

$$n_z = \sqrt{h_{11}^2 + g_{11}^2 + g_{10}^2}, \: n_y = \sqrt{\frac{g_{10}^2}{n_z^2} + \frac{g_{11}^2}{n_z^2}},$$

and

$$n_x = \sqrt{\left(\frac{g_{10}^2}{n_z^2 n_y} + \frac{g_{11}^2}{n_z^2 n_y}\right)^2 + \frac{g_{11}^2 h_{11}^2}{n_z^4 n_y^2} + \frac{g_{10}^2 h_{11}^2}{n_z^4 n_y}}$$

For the Tyler model, this is all that needs to be done before using the new position

radii and colatitudes to calculate electron density at each point along the line of sight.

For the other models, the rotation matrix from the new dipole to the old dipole at the time the models were constructed needs to be determined. To perform this operation, the $\vec{x'}, \vec{y'}, \vec{z'}$ vectors need to be calculated using the old dipole's h11, g11, and g10 harmonics using the same system above (in Carrington coordinates). The new rotation matrix from the current dipole (coordinate system C) to the old dipole (coordinate system M) is then:

$$
R_{c2m} = \begin{bmatrix} \hat{c}_x \cdot \hat{m}_x & \hat{c}_x \cdot \hat{m}_y & \hat{c}_x \cdot \hat{m}_z \\ \hat{c}_y \cdot \hat{m}_x & \hat{c}_y \cdot \hat{m}_y & \hat{c}_y \cdot \hat{m}_z \\ \hat{c}_z \cdot \hat{m}_x & \hat{c}_z \cdot \hat{m}_y & \hat{c}_z \cdot \hat{m}_z \end{bmatrix}
$$

The rotation operation for calculating the positions of points along the line of sight in the coordinate system of the old model is:

$$
\overleftrightarrow{R}_{c2m} \overrightarrow{SUN}_{current} = \overrightarrow{SUN}_{old}
$$

Then the electron density values at these points can be calculated using the old ranging models for comparison to current ranging measurements.

APPENDIX E

The Three Carrington Coordinate Systems

The Heliographic coordinate system is the Carrington system; however, there are three ways to represent the coordinate system. The first system is the synoptic map where longitude is the same as time. The problem with this method is the differential rotation of the Sun causes features at different latitudes to vary in longitude when they actually have not changed position (Figure E.1) (Ulrich & Boyden, 2006). The Differential Rotation Corrected (DRC) synoptic map can be used to construct the grid shown in Figure E.2 to map the data collected at a particular latitude *and time* back to its appropriate longitude creating a "snapshot" map. A comparison is shown in Figure E.3.

For the purposes of the Cassini forward model, it is not significant that the magnetic field predicted by the PFSS model be as accurate as possible in the higher harmonics. The dipole field which rotates the slowest is dominate and should be at least 50% accurate. Faraday rotation observations that are within the equatorial region below the source surface require special attention. Specifically, two phenomena should be addressed: differential rotation at variable heights above the photosphere and the rigid rotation of persistent large-scale features such as coronal holes. The solar surface experiences a differential rotation shown in Figure E.1 and modeling an observation along a line of sight should use a "snapshot" version of the magnetic
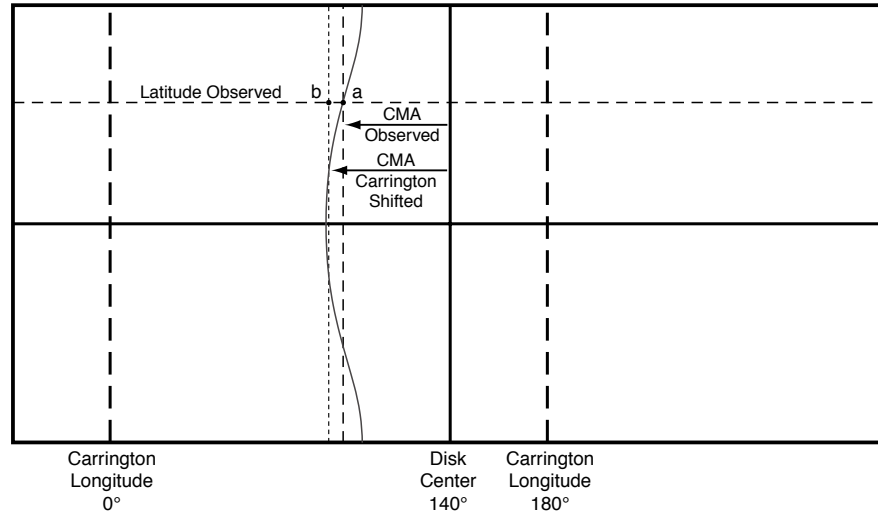
Figure E.1: *Schematic showing how a point (a) observed at the central meridian angle (CMA) and latitude will be observed to cross the central meridian after a time Δt. If the rate of rotation is fixed to the Carrington rate, (a) should be shifted to position (b) so that it crosses the meridian after the same period of time Δt. The thin solid line passes through the points that will reach the central meridian at the same time. This figure illustrates the problem of differential rotation causing "smearing".*
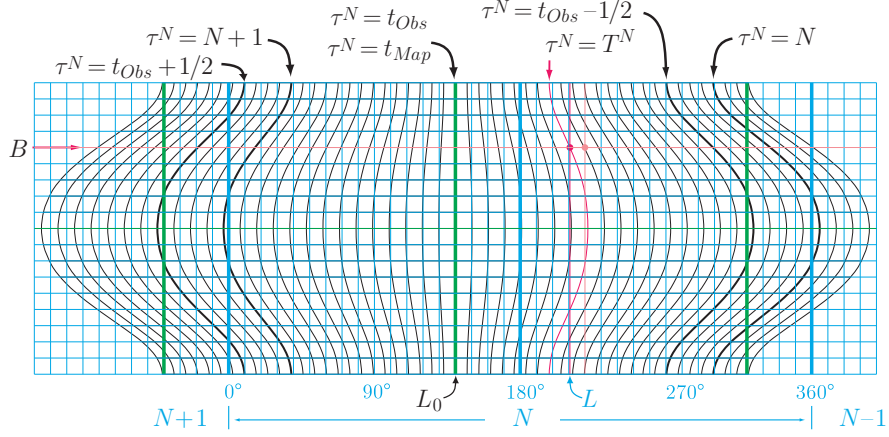
Figure E.2: *A "snapshot" map created using the DRC measurements. A "snapshot" map is created using the DRC measurements to map the magnetic field data to its particular longitude at a specific time. This particular system uses the grid shown in black to adjust the points on the grid shown in blue.*

field as shown in Figure E.2. However, the solar corona is observed to differentially rotate with a weaker latitude dependence relative to the photosphere (Bird & Edenhofer, 1990)

$$\omega_\odot = 13.22 - 0.57 \sin^2 \theta$$

This indicates that the higher latitude plasma is probably expanding equatorially and/or a shear region exists in the corona. Both effects should be studied in the future with Faraday rotation observations.
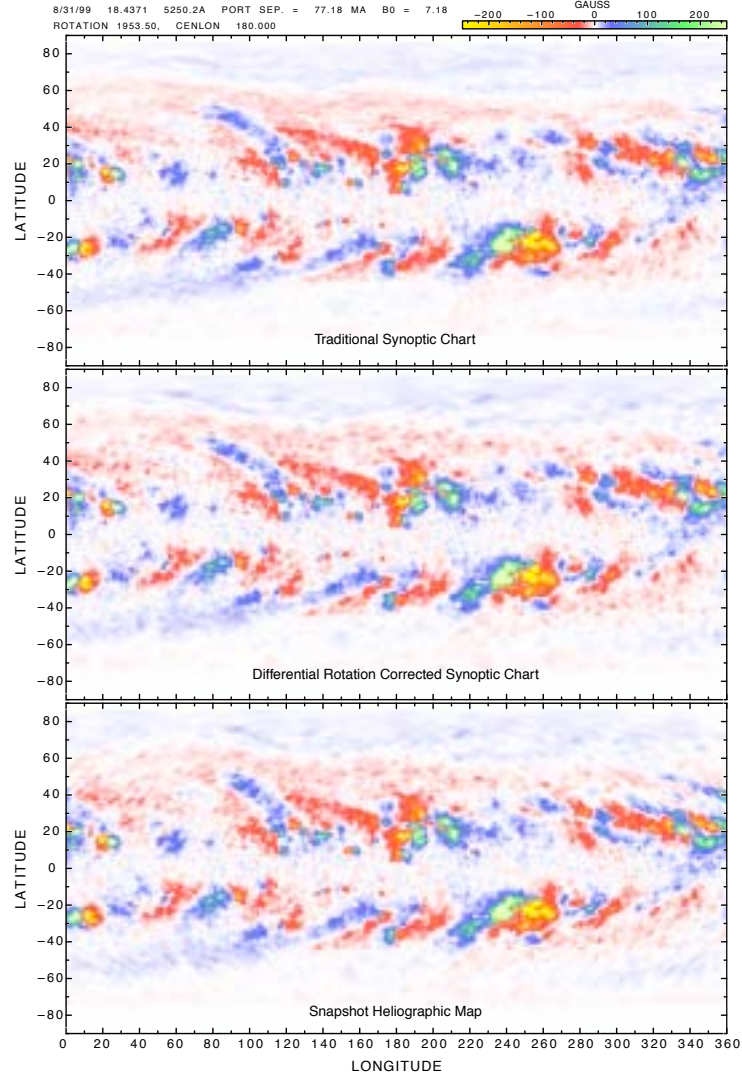
Figure E.3: *Comparison of the three different systems. The traditional synoptic map is on the top, the DRC map is in the middle, and the snapshot map is at the bottom. Notice how the structure at 40 degrees latitude and between 100-120 degrees longitude appears to compress.*

APPENDIX F

Matlab Code For Radio Science Receiver Files

This appendix includes all the source code necessary to read and process radio science receiver (RSR) files. First the RSR needs to be read to strip the headers off of the data and place these in separate files (`readrsr.m`). Then the data should be processed initially to determine if there are data gaps present and whether or not a signal is actually present (`readhdr.m`). If a gap is detected then the data and header files are automatically cut up into separate files to remove the gap (`cutrsr.m`). And finally, the right and left circularly polarized data can be processed for determining the plane of polarization of the signal (`planpolconj.m`). Other handy codes are included as well: FFT (`fftphase.m`), conversion between date (`doy2ymd.m`) and time (`spm2hms.m`) formats, and the ability to quickly scan the header file (`scanhdr.m`) for pertinent information on the data. In general, typing from within matlab `>> help command` will give the user the information for how to run `command.m`. Finally, the user needs to select which plane of polarization will be used; because of the 180 degree ambiguity in polarization, there are two to choose from in the full 360 degrees. These polarization planes were then saved into `filename.xcorr` files. WARNING: BINARY FILES ARE SYSTEM DEPENDENT; DO NOT TRY TO USE BINARY FILES GENERATED ON A UNIX PLATFORM WHEN OPERATING ON A WINDOWS PLATFORM. The archive of data is unix based.

F.1   Separate Headers and Data

`appf/readrsr.m` reads in the RSR file `filename` and creates new files with the extensions `filename.hdr` and `filename.bin` containing the header information and binary data.

F.1.1   Calls

Run matlab inside the appf directory containing the files you are interested in and enter the command:

```
>> addpath yourlocaldirtree
>> readrsr
```

where `yourlocaldirtree` is the the full directory path to the folder containing all the Matlab `.m` files.

The code will prompt for the RSR filename. In the directories, these files can be identified from the lack of extension. All other files in the directories have extensions.

F.2   initial Data Inspection

`appf/readhdr.m` reads in the RSR header file `filename.hdr` and performs two functions. The first is to determine if there are any gaps in the data. If there are, it automatically calls `appf/cutrsr.m` and slices the RSR file into two pieces at the gap and gives the files new names based on their start times. If a gap is detected,

`readhdr.m` performs this function and then exits. In this case, it needs to be rerun to perform its primary function. `readhdr.m` passes the data in `filename.bin` to `appf/fftphase.m` which calculates the frequency for every second in the file. The user must then use the output plot to determine when the signal was actually acquired or lost; this works with a prompt for the number of requested cuts and a cross-hair for selecting the positions of the cuts. When `readhdr.m` has been run on all the RSR files from a pass, the user should then determine the overlap times between the two frequencies and polarizations and run `cutrsr.m` on these files to line them up in time.

F.2.1   Calls

Run matlab inside the appf directory and enter the command:

```
>> addpath yourlocaldirtree
>> readhdr
```

where `yourlocaldirtree` is the the full directory path to the folder containing all the Matlab `.m` files.

The code will prompt for the `hdr` filename.

F.3   Determine Plane of Polarization

Prior to running this code, the user must first run `fftphase.m` on each of the `bin` files and save the output into `filename.phase` files. `fftphase.m` guides the user

through its usage.

`appf/planpolconj.m` loads in the two polarization files and calculates the plane of polarizaiton using the method described in Chapter 3. The code is commented internally to guide the user in the techniques being used including the method described for the day of conjunction in 2003.

F.3.1   Calls

Run matlab inside the appf directory and enter the command:

```
>> addpath yourlocaldirtree
>> planpolconj
```

where `yourlocaldirtree` is the the full directory path to the folder containing all the Matlab `.m` files.

The code will prompt for a series of `bin` filenames (XRCP, XLCP, KaRCP, KaLCP) and ask a series of questions about the quality of the data.

F.3.2   Inputs

`planpolconj.m` automatically loads all `phase` and `bin` files of the same filename.

F.3.3 Output

There is no output; however, the following command must be run from within matlab:

```
>> save filename.mat xvec yvec tvec xplanpol kplanpol
```

APPENDIX G

Matlab Code For Removing Parallactic Effects

The following codes take the output from the plane of polarization calculation (Section 3.1.3) and corrects for the leakage in the polarizer from the stronger RCP channel to the weaker LCP channel. This correction is empirically determined using the formula described in Section 3.2.4. A full calibration of the polarizer should be made in the future using sources of varying polarizations and powers to determine the exact response.

The correction proceeds in two steps: the determination of the parallactic angle for each point in time followed by the calculation for the correction to the plane of polarization necessary to obtain the parallactic angle value (in the case of passes at large distance from the Sun). This allows the calibration of the antenna system for time periods when the plane of polarization is unknown due to Faraday rotation.

G.1 Determine the Parallactic Angle for Each Point in Time

The code `calcpavals.m` calculates what the parallactic angle should be for each point in time a data sample was collected. The values are saved into `padoy` matrices in the output files `pa2002.mat` and `pa2003.mat`

G.1.1 Run Commands

First start matlab in the appg folder.

From within matlab:

```
>> addpath yourlocaldirtree
>> calcpavals
```

where `yourlocaldirtree` is the the full directory path to the folder containing all the Matlab `.m` files.

G.1.2 Files Loaded

The `phase` files contain the times for each data point. The `padoy.dat` and `txt` files contain the parallactic angles calculated for DSS13 given the time periods in the ancillary files of antenna orientation.

RSR1A1_02_167_162155.1A1.phase	RSR1A1_02_169_161054.1A1.phase
RSR1A1_02_167_184653.1A1.phase	RSR1A1_02_169_174432.1A1.phase
RSR1A1_02_176_131930.1A1.phase	RSR1A1_02_170_142745.1A1.phase
RSR1A1_02_176_155059.1A1.phase	RSR1A1_02_170_160900.1A1.phase
RSR1A1_02_168_190800.1A1.phase	RSR1A1_02_171_133600.phase
RSR1A1_02_168_193204.1A1.phase	RSR1A1_02_171_160900.phase
RSR1A1_02_168_195726.1A1.phase	RSR1A1_02_172_134923.phase
RSR1A1_02_168_200348.1A1.phase	RSR1A1_02_172_162202.phase
RSR1A1_02_168_205256.1A1.phase	RSR1A1_02_172_190133.phase

RSR1A1_02_173_000655.phase

RSR1A1_02_173_132913.phase

RSR1A1_02_173_160820.phase

RSR1A1_02_174_010120.phase

RSR1A1_02_174_012119.phase

RSR_02_174_133241.1A1.phase

RSR_02_174_134046.1A1.phase

RSR_02_174_155336.1A1.phase

RSR_02_175_000400.1A1.phase

RSR1A1_02_175_131424.1A1.phase

RSR1A1_02_175_155237.1A1.phase

RSR1A1_02_176_010045.1A1.phase

RSR1A1_02_177_131635.1A1.phase

RSR1A1_02_177_160615.1A1.phase

RSR1A1_02_177_215846.1A1.phase

S82D25P2077_03-168-203059.1A1.phase

S82D25P2084_03-175-164616.1A1.phase

S82D25P2084_03-175-164844.1A1.phase

S82D25P2084_03-175-165926.1A1.phase

S82D25P2084_03-175-204034.1A1.phase

S82D25P2084_03-175-205056.1A1.phase

S82D25P2086_03-177-133713.1A1.phase

S82D25P2086_03-177-165326.1A1.phase

S82D13P2087_03-178-140213.1A1.phase

S82D13P2087_03-178-155401.1A1.phase

S82D13P2087_03-178-183732.1A1.phase

S82D13P2088_03-179-134960.1A1.phase

S82D13P2088_03-179-163857.1A1.phase

S82D13P2089_03-180-134500.1A1.phase

S82D13P2089_03-180-163328.1A1.phase

S82D13P2090_03-181-134500.1A1.phase

S82D13P2090_03-181-163330.1A1.phase

S82D13P2091_03-182-132110.1A1.phase

S82D13P2091_03-182-164627.1A1.phase

S82D13P2092_03-183-133500.1A1.phase

S82D13P2092_03-183-162335.1A1.phase

S82D13P2093_03-184-133500.1A1.phase

S82D13P2093_03-184-162337.1A1.phase

S82D13P2094_RSR1A1.03-185-132200.phase

S82D13P2094_RSR1A1.03-185-162339.phase

S82D13P2095_RSR1A1.03-186-131500.phase

S82D13P2095_RSR1A1.03-186-161339.phase

S82D13P2096_RSR1A1.03-187-132500.phase

S82D13P2096_RSR1A1.03-187-205257.phase

S82D13P2097_RSR1A1.03-188-134500.phase

S82D13P2097_RSR1A1.03-188-144827.phase

S82D13P2097_RSR1A1.03-188-163301.phase

pavals167.dat

pavals176.dat

pavals168.dat

pavals169.dat

pavals170.dat

pavals171.dat   pavals03179.txt

pavals172.dat   pavals03180.txt

pavals173.dat   pavals03181.txt

pavals174.dat   pavals03182.txt

pavals175.dat   pavals03183.txt

pavals177.dat   pavals03184.txt

                                 pavals03185.txt

pavals03168.txt   pavals03186.txt

pavals03175.txt   pavals03187.txt

pavals03177.txt   pavals03188.txt

pavals03178.txt

G.1.3   Files Generated

These files contain the parallactic angle values for each point in time a plane of polarization point was determined.

`pa2002.mat` contains the matrices

`pa167 pa168 pa169 pa170 pa171 pa172 pa173 pa174 pa175 pa176 pa177`

`pa2003.mat` contains the matrices

`pa168 pa175 pa177 pa178 pa179 pa180 pa181 pa182 pa183 pa184 pa185 pa186`
`pa187 pa188`

G.2 Polarizer Leakage Calibration Code

The code `calcdrvals.m` calculates what the polarization correction should be for each point in time a data sample was collected. The values are saved into `drfdoy` and `shiftfdoy` matrices in the output files `dr2002.mat` and `dr2003.mat`. The `shiftfdoy` matrices preserves the original plane of polarization prior to calibration for the Faraday rotation initial plane of polarization.

G.2.1 Run Commands

First start matlab in the appg folder.

From within matlab:

```
>> addpath yourlocaldirtree
>> calcdrvals
```

where `yourlocaldirtree` is the the full directory path to the folder containing all the Matlab `.m` files.

G.2.2 Files Loaded

The `phase` files contain the times for each data point, the power in each frequency, and the power in the background noise for the time period the FFT was calculated. The `payear.mat` and `txt` files contain the parallactic angles calculated for DSS13 given the time periods in the ancillary files of antenna orientation. The `filename.xcorr` files give the plane of polarization values.

pa2002.mat

pa2003.mat

RSR1A1_02_167_162155.1A1.phase

RSR1A1_02_167_184653.1A1.phase

RSR1B1_02_167_162155.1B1.phase

RSR1B1_02_167_184653.1B1.phase

RSR4A1_02_167_162155.4A1.phase

RSR4A1_02_167_184653.4A1.phase

RSR4B1_02_167_162155.4B1.phase

RSR4B1_02_167_184653.4B1.phase

RSR1A1_02_176_131930.1A1.phase

RSR1A1_02_176_155059.1A1.phase

RSR1B1_02_176_131930.1B1.phase

RSR1B1_02_176_155059.1B1.phase

RSR4A1_02_176_131930.4A1.phase

RSR4A1_02_176_155059.4A1.phase

RSR4B1_02_176_131930.4B1.phase

RSR4B1_02_176_155059.4B1.phase

RSR1A1_02_168_190800.1A1.phase

RSR1A1_02_168_193204.1A1.phase

RSR1A1_02_168_195726.1A1.phase

RSR1A1_02_168_200348.1A1.phase

RSR1A1_02_168_205256.1A1.phase

RSR1B1_02_168_190800.1B1.phase

RSR1B1_02_168_193204.1B1.phase

RSR1B1_02_168_195726.1B1.phase

RSR1B1_02_168_200348.1B1.phase

RSR1B1_02_168_205256.1B1.phase

RSR4A1_02_168_190800_R.4A1.phase

RSR4A1_02_168_193204_L.4A1.phase

RSR4A1_02_168_195726_R.4A1.phase

RSR4A1_02_168_200348.4A1.phase

RSR4A1_02_168_205256.4A1.phase

RSR4B1_02_168_190800_L.4B1.phase

RSR4B1_02_168_193204_R.4B1.phase

RSR4B1_02_168_195726_L.4B1.phase

RSR4B1_02_168_200348.4B1.phase

RSR4B1_02_168_205256.4B1.phase

RSR1A1_02_169_161054.1A1.phase

RSR1A1_02_169_174432.1A1.phase

RSR1B1_02_169_161054.1B1.phase

RSR1B1_02_169_174432.1B1.phase

RSR4A1_02_169_161054.4A1.phase

RSR4A1_02_169_174432.4A1.phase

RSR4B1_02_169_161054.4B1.phase

RSR4B1_02_169_174432.4B1.phase

RSR1A1_02_170_142745.1A1.phase

RSR1A1_02_170_160900.1A1.phase

RSR1B1_02_170_142745.1B1.phase

RSR1B1_02_170_160900.1B1.phase

RSR4A1_02_170_142745.4A1.phase

RSR4A1_02_170_160900.4A1.phase

RSR4B1_02_170_142745.4B1.phase

RSR4B1_02_170_160900.4B1.phase   RSR4A1_02_172_190133.phase

RSR1A1_02_171_133600.phase   RSR4A1_02_173_000655.phase

RSR1A1_02_171_160900.phase   RSR1A1_02_173_132913.phase

RSR1A1_02_172_013114.phase   RSR1A1_02_173_160820.phase

RSR1B1_02_171_133600.phase   RSR1A1_02_174_010120.phase

RSR1B1_02_171_160900.phase   RSR1A1_02_174_012119.phase

RSR1B1_02_172_013114.phase   RSR1B1_02_173_132913.phase

RSR4B1_02_171_133600.phase   RSR1B1_02_173_160820.phase

RSR4B1_02_171_160900.phase   RSR1B1_02_174_010120.phase

RSR4B1_02_172_013114.phase   RSR1B1_02_174_012119.phase

RSR4A1_02_171_133600.phase   RSR4A1_02_173_132913.phase

RSR4A1_02_171_160900.phase   RSR4A1_02_173_160820.phase

RSR4A1_02_172_013114.phase   RSR4A1_02_174_010120.phase

RSR1A1_02_172_134923.phase   RSR4A1_02_174_012119.phase

RSR1A1_02_172_162202.phase   RSR4B1_02_173_132913.phase

RSR1A1_02_172_190133.phase   RSR4B1_02_173_160820.phase

RSR1A1_02_173_000655.phase   RSR4B1_02_174_010120.phase

RSR1B1_02_172_134923.phase   RSR4B1_02_174_012119.phase

RSR1B1_02_172_162202.phase   RSR_02_174_133241.1A1.phase

RSR1B1_02_172_190133.phase   RSR_02_174_133241.1B1.phase

RSR1B1_02_173_000655.phase   RSR_02_174_133241.4A1.phase

RSR4B1_02_172_134923.phase   RSR_02_174_133241.4B1.phase

RSR4B1_02_172_162202.phase   RSR_02_174_134046.1A1.phase

RSR4B1_02_172_190133.phase   RSR_02_174_134046.1B1.phase

RSR4B1_02_173_000655.phase   RSR_02_174_134046.4A1.phase

RSR4A1_02_172_134923.phase   RSR_02_174_134046.4B1.phase

RSR4A1_02_172_162202.phase   RSR_02_174_155336.1A1.phase

RSR_02_174_155336.1B1.phase

RSR_02_174_155336.4A1.phase

RSR_02_174_155336.4B1.phase

RSR_02_175_000400.1A1.phase

RSR_02_175_000400.1B1.phase

RSR_02_175_000400.4A1.phase

RSR_02_175_000400.4B1.phase

RSR1A1_02_175_131424.1A1.phase

RSR1A1_02_175_155237.1A1.phase

RSR1A1_02_176_010045.1A1.phase

RSR1B1_02_175_131424.1B1.phase

RSR1B1_02_175_155237.1B1.phase

RSR1B1_02_176_010045.1B1.phase

RSR1A1_02_177_131635.1A1.phase

RSR1A1_02_177_160615.1A1.phase

RSR1A1_02_177_215846.1A1.phase

RSR1B1_02_177_131635.1B1.phase

RSR1B1_02_177_160615.1B1.phase

RSR1B1_02_177_215846.1B1.phase

RSR4A1_02_177_131635.4A1.phase

RSR4A1_02_177_160615.4A1.phase

RSR4A1_02_177_215846.4A1.phase

RSR4B1_02_177_131635.4B1.phase

RSR4B1_02_177_160615.4B1.phase

RSR4B1_02_177_215846.4B1.phase

S82D25P2086_03-177-133713.1A1.phase

S82D25P2086_03-177-165326.1A1.phase

S82D25P2086_03-177-133713.1B1.phase

S82D25P2086_03-177-165326.1B1.phase

S82D25P2086_03-177-133713.2B1.phase

S82D25P2086_03-177-165326.2B1.phase

S82D25P2086_03-177-133713.2A1.phase

S82D25P2086_03-177-165326.2A1.phase

S82D13P2087_03-178-140213.1A1.phase

S82D13P2087_03-178-155401.1A1.phase

S82D13P2087_03-178-183732.1A1.phase

S82D13P2087_03-178-140213.1B1.phase

S82D13P2087_03-178-155401.1B1.phase

S82D13P2087_03-178-183732.1B1.phase

S82D13P2087_03-178-140213.2B1.phase

S82D13P2087_03-178-155401.2B1.phase

S82D13P2087_03-178-183732.2B1.phase

S82D13P2087_03-178-140213.2A1.phase

S82D13P2087_03-178-155401.2A1.phase

S82D13P2087_03-178-183732.2A1.phase

S82D13P2088_03-179-134960.1A1.phase

S82D13P2088_03-179-163857.1A1.phase

S82D13P2088_03-179-134960.1B1.phase

S82D13P2088_03-179-163857.1B1.phase

S82D13P2088_03-179-134960.2B1.phase

S82D13P2088_03-179-163857.2A1.phase

S82D13P2088_03-179-134960.2A1.phase

S82D13P2088_03-179-163857.2B1.phase

S82D13P2089_03-180-134500.1A1.phase

S82D13P2089_03-180-163328.1A1.phase

S82D13P2089_03-180-134500.1B1.phase

S82D13P2089_03-180-163328.1B1.phase

S82D13P2089_03-180-134500.2B1.phase

S82D13P2089_03-180-163328.2B1.phase

S82D13P2089_03-180-134500.2A1.phase

S82D13P2089_03-180-163328.2A1.phase

S82D13P2090_03-181-134500.1A1.phase

S82D13P2090_03-181-163330.1A1.phase

S82D13P2090_03-181-134500.1B1.phase

S82D13P2090_03-181-163330.1B1.phase

S82D13P2090_03-181-134500.2B1.phase

S82D13P2090_03-181-163330.2B1.phase

S82D13P2090_03-181-134500.2A1.phase

S82D13P2090_03-181-163330.2A1.phase

S82D13P2091_03-182-132110.1A1.phase

S82D13P2091_03-182-164627.1A1.phase

S82D13P2091_03-182-132110.1B1.phase

S82D13P2091_03-182-164627.1B1.phase

S82D13P2091_03-182-132110.2B1.phase

S82D13P2091_03-182-164627.2B1.phase

S82D13P2091_03-182-132110.3B1.phase

S82D13P2091_03-182-164627.3B1.phase

S82D13P2092_03-183-133500.1A1.phase

S82D13P2092_03-183-162335.1A1.phase

S82D13P2092_03-183-133500.1B1.phase

S82D13P2092_03-183-162335.1B1.phase

S82D13P2092_03-183-133500.2B1.phase

S82D13P2092_03-183-162335.2B1.phase

S82D13P2092_03-183-133500.3B1.phase

S82D13P2092_03-183-162335.3B1.phase

S82D13P2093_03-184-133500.1A1.phase

S82D13P2093_03-184-162337.1A1.phase

S82D13P2093_03-184-133500.1B1.phase

S82D13P2093_03-184-162337.1B1.phase

S82D13P2093_RSR2B1.03-184-133500.phase

S82D13P2093_RSR2B1.03-184-162337.phase

S82D13P2093_RSR3B1.03-184-133500.phase

S82D13P2093_RSR3B1.03-184-162337.phase

S82D13P2094_RSR1A1.03-185-132200.phase

S82D13P2094_RSR1A1.03-185-162339.phase

S82D13P2094_RSR1B1.03-185-132200.phase

S82D13P2094_RSR1B1.03-185-162339.phase

S82D13P2094_RSR2B1.03-185-132200.phase

S82D13P2094_RSR2B1.03-185-162339.phase

S82D13P2094_RSR3B1.03-185-132200.phase

S82D13P2094_RSR3B1.03-185-162339.phase

S82D13P2095_RSR1A1.03-186-131500.phase

S82D13P2095_RSR1A1.03-186-161339.phase

S82D13P2095_RSR1B1.03-186-131500.phase

S82D13P2095_RSR1B1.03-186-161339.phase

S82D13P2095_RSR2B1.03-186-131500.phase

S82D13P2095_RSR2B1.03-186-161339.phase

S82D13P2095_RSR3B1.03-186-131500.phase

S82D13P2095_RSR3B1.03-186-161339.phase

S82D13P2096_RSR1A1.03-187-132500.phase

S82D13P2096_RSR1A1.03-187-205257.phase

S82D13P2096_RSR1B1.03-187-132500.phase

S82D13P2096_RSR1B1.03-187-205257.phase

S82D13P2096_RSR2B1.03-187-132500.phase

S82D13P2096_RSR2B1.03-187-205257.phase

S82D13P2096_RSR3A1.03-187-132500.phase

S82D13P2096_RSR3A1.03-187-205257.phase

S82D13P2097_RSR1A1.03-188-134500.phase

S82D13P2097_RSR1A1.03-188-144827.phase

S82D13P2097_RSR1A1.03-188-163301.phase

S82D13P2097_RSR1B1.03-188-134500.phase

S82D13P2097_RSR1B1.03-188-144827.phase

S82D13P2097_RSR1B1.03-188-163301.phase

S82D13P2097_RSR2B1.03-188-134500.phase

S82D13P2097_RSR2B1.03-188-144827.phase

S82D13P2097_RSR2B1.03-188-163301.phase

S82D13P2097_RSR3A1.03-188-134500.phase

S82D13P2097_RSR3A1.03-188-144827.phase

S82D13P2097_RSR3A1.03-188-163301.phase

RSRFR_02_167_162155.xcorr

RSRFR1_02_167_184653.xcorr

RSR_02_176_131930.FR.xcorr

RSR_02_176_155059.FR.xcorr

RSRFR1_02_168_190800.xcorr

RSRFR1_02_168_193204.xcorr

RSRFR1_02_168_195726.xcorr

RSRFR1_02_168_200348.xcorr

RSRFR1_02_168_205256.xcorr

RSRFR1_02_169_161054.xcorr

RSRFR1_02_169_174432.xcorr

RSRFR_02_170_142745.xcorr

RSRFR_02_170_160900.xcorr

RSRFR_02_171_133600.xcorr

RSRFR_02_171_160900.xcorr

RSRFR_02_172_013114.xcorr

x172.xcorr

k172.xcorr

k172_2.xcorr

RSRFR_02_172_162202.xcorr

RSRFR_02_172_190133.xcorr

RSRFR_02_173_000655.xcorr

RSRFR_02_173_132913.xcorr

RSRFR_02_173_160820.xcorr

RSRFR_02_174_010120.xcorr

RSRFR_02_174_012119.xcorr

RSR_02_174_133241.FR.xcorr

RSR_02_174_134046.FR.xcorr

RSR_02_174_155336.FR.xcorr

RSR_02_175_000400.FR.xcorr

RSR_02_175_131424.FR.xcorr

RSR_02_175_155237.FR.xcorr   S82D13P2090_03-181-163330.FR.xcorr

RSR_02_176_010045.FR.xcorr   S82D13P2091_03-182-132110.new.xcorr

RSR_02_177_131635.FR.xcorr   S82D13P2091_03-182-164627.new.xcorr

RSR_02_177_160615.FR.xcorr   S82D13P2092_03-183-133500.FR.xcorr

RSR_02_177_215846.FR.xcorr   S82D13P2092_03-183-162335.FR.xcorr

       S82D13P2093_RSRFR.03-184-133500.xcorr

S82D25P2086_03-177-133713.FR.xcorr   S82D13P2093_RSRFR.03-184-162337.xcorr

S82D25P2086_03-177-165326.FR.xcorr   S82D13P2094_RSRFR.03-185-132200.xcorr

S82D13P2087_03-178-140213.FR.xcorr   S82D13P2094_RSRFR.03-185-162339.xcorr

S82D13P2087_03-178-155401.FR.xcorr   S82D13P2095_RSRFR.03-186-131500.xcorr

S82D13P2087_03-178-183732.FR.xcorr   S82D13P2095_RSRFR.03-186-161339.xcorr

S82D13P2088_03-179-134960.FR.xcorr   S82D13P2096_RSRFR.03-187-132500.xcorr

S82D13P2088_03-179-163857.FR.xcorr   S82D13P2096_RSRFR.03-187-205257.xcorr

S82D13P2089_03-180-134500.FR.xcorr   S82D13P2097_RSRFR.03-188-134500.xcorr

S82D13P2089_03-180-163328.FR.xcorr   S82D13P2097_RSRFR.03-188-144827.xcorr

S82D13P2090_03-181-134500.FR.xcorr   S82D13P2097_RSRFR.03-188-163301.xcorr

G.2.3   Files Generated

These files contain the plane of polarization correction values for each point in time.

`dr2002.mat` contains

```
drx167 drx168 drx169 drx170 drx171 drx172 drx173 drx174 drx176 drx177
drk167 drk169 drk170 drk171 drk172 drk173 drk174 drk175 drk176 drk177
drxmap shiftx167 shiftx168 shiftx169 shiftx170 shiftx171 shiftx172
shiftx173 shiftx174 shiftx176 shiftx177 hamin167 hamin168 hamin169
```

```
hamin170 hamin171 hamin172 hamin173 hamin174 hamin176 hamin177
```

`dr2003.mat` contains

```
drx177 drx178 drx179 drx180 drx181 drx182 drx183 drx184 drx185 drx186
drx187 drx188 drk177 drk178 drk179 drk180 drk181 drk182 drk183 drk184
drk185 drk186 drk187 drk188 drxmap shiftx177 shiftx178 shiftx179
shiftx180 shiftx181 shiftx182 shiftx183 shiftx184 shiftx185 shiftx186
shiftx187 shiftx188 hamin177 hamin178 hamin179 hamin180 hamin181
hamin182 hamin183 hamin184 hamin185 hamin186 hamin187 hamin188
```

G.3   Faraday Rotation Calculation Code

This code uses a fit to the polarizer leakage term to calculate what the rotation should be based on the amplitude and noise on the signal combined with the parallactic effect. The difference between this calculation and the measurements is the Faraday rotation. However, remnant effects from the antenna continue to be present and are similarly removed. The left over rotation in time series that should have no rotation is used to estimate the error in the measurement and remove timeseries which fall within the range of the error.

The code `calcfrvals.m` calculates what the Faraday rotation should be for each point in time a data sample was collected. The values are saved into `frdoy` matrices in the output files `fr2002.mat` and `fr2003.mat`.

G.3.1 Run Commands

First start matlab in the appg folder.

From within matlab:

```
>> addpath yourlocaldirtree
>> calcfrvals
```

where `yourlocaldirtree` is the the full directory path to the folder containing all the Matlab `.m` files.

G.3.2 Files Loaded

The `phase` files contain the times for each data point, the power in each frequency, and the power in the background noise for the time period the FFT was calculated. The `payear.mat` files contain the parallactic angles calculated for DSS13 given the time periods in the ancillary files of antenna orientation. The `filename.xcorr` files give the plane of polarization values. The `dryear.mat` files give the values for correcting the plane of polarization values for antenna effects and the original plane of polarization prior to correction.

pa2002.mat	RSR1A1_02_176_131930.1A1.phase
dr2002.mat	RSR1A1_02_176_155059.1A1.phase
pa2003.mat	RSR1B1_02_176_131930.1B1.phase
dr2003.mat	RSR1B1_02_176_155059.1B1.phase
	RSR4A1_02_176_131930.4A1.phase

RSR4A1_02_176_155059.4A1.phase

RSR4B1_02_176_131930.4B1.phase

RSR4B1_02_176_155059.4B1.phase

RSR1A1_02_169_161054.1A1.phase

RSR1A1_02_169_174432.1A1.phase

RSR1B1_02_169_161054.1B1.phase

RSR1B1_02_169_174432.1B1.phase

RSR4A1_02_169_161054.4A1.phase

RSR4A1_02_169_174432.4A1.phase

RSR4B1_02_169_161054.4B1.phase

RSR4B1_02_169_174432.4B1.phase

RSR1A1_02_170_142745.1A1.phase

RSR1A1_02_170_160900.1A1.phase

RSR1B1_02_170_142745.1B1.phase

RSR1B1_02_170_160900.1B1.phase

RSR4A1_02_170_142745.4A1.phase

RSR4A1_02_170_160900.4A1.phase

RSR4B1_02_170_142745.4B1.phase

RSR4B1_02_170_160900.4B1.phase

RSR1A1_02_171_133600.phase

RSR1A1_02_171_160900.phase

RSR1A1_02_172_013114.phase

RSR1B1_02_171_133600.phase

RSR1B1_02_171_160900.phase

RSR1B1_02_172_013114.phase

RSR4B1_02_171_133600.phase

RSR4B1_02_171_160900.phase

RSR4B1_02_172_013114.phase

RSR4A1_02_171_133600.phase

RSR4A1_02_171_160900.phase

RSR4A1_02_172_013114.phase

RSR1A1_02_172_134923.phase

RSR1A1_02_172_162202.phase

RSR1A1_02_172_190133.phase

RSR1A1_02_173_000655.phase

RSR1B1_02_172_134923.phase

RSR1B1_02_172_162202.phase

RSR1B1_02_172_190133.phase

RSR1B1_02_173_000655.phase

RSR4B1_02_172_134923.phase

RSR4B1_02_172_162202.phase

RSR4B1_02_172_190133.phase

RSR4B1_02_173_000655.phase

RSR4A1_02_172_134923.phase

RSR4A1_02_172_162202.phase

RSR4A1_02_172_190133.phase

RSR4A1_02_173_000655.phase

RSR1A1_02_173_132913.phase

RSR1A1_02_173_160820.phase

RSR1A1_02_174_010120.phase

RSR1A1_02_174_012119.phase

RSR1B1_02_173_132913.phase

RSR1B1_02_173_160820.phase

RSR1B1_02_174_010120.phase

RSR1B1_02_174_012119.phase

RSR4A1_02_173_132913.phase

RSR4A1_02_173_160820.phase

RSR4A1_02_174_010120.phase

RSR4A1_02_174_012119.phase

RSR4B1_02_173_132913.phase

RSR4B1_02_173_160820.phase

RSR4B1_02_174_010120.phase

RSR4B1_02_174_012119.phase

RSR_02_174_133241.1A1.phase

RSR_02_174_133241.1B1.phase

RSR_02_174_133241.4A1.phase

RSR_02_174_133241.4B1.phase

RSR_02_174_134046.1A1.phase

RSR_02_174_134046.1B1.phase

RSR_02_174_134046.4A1.phase

RSR_02_174_134046.4B1.phase

RSR_02_174_155336.1A1.phase

RSR_02_174_155336.1B1.phase

RSR_02_174_155336.4A1.phase

RSR_02_174_155336.4B1.phase

RSR_02_175_000400.1A1.phase

RSR_02_175_000400.1B1.phase

RSR_02_175_000400.4A1.phase

RSR_02_175_000400.4B1.phase

RSR1A1_02_175_131424.1A1.phase

RSR1A1_02_175_155237.1A1.phase

RSR1A1_02_176_010045.1A1.phase

RSR1B1_02_175_131424.1B1.phase

RSR1B1_02_175_155237.1B1.phase

RSR1B1_02_176_010045.1B1.phase

RSR1A1_02_167_162155.1A1.phase

RSR1A1_02_167_184653.1A1.phase

RSR1B1_02_167_162155.1B1.phase

RSR1B1_02_167_184653.1B1.phase

RSR4A1_02_167_162155.4A1.phase

RSR4A1_02_167_184653.4A1.phase

RSR4B1_02_167_162155.4B1.phase

RSR4B1_02_167_184653.4B1.phase

RSR1A1_02_177_131635.1A1.phase

RSR1A1_02_177_160615.1A1.phase

RSR1A1_02_177_215846.1A1.phase

RSR1B1_02_177_131635.1B1.phase

RSR1B1_02_177_160615.1B1.phase

RSR1B1_02_177_215846.1B1.phase

RSR4A1_02_177_131635.4A1.phase

RSR4A1_02_177_160615.4A1.phase

RSR4A1_02_177_215846.4A1.phase

RSR4B1_02_177_131635.4B1.phase

RSR4B1_02_177_160615.4B1.phase

RSR4B1_02_177_215846.4B1.phase

S82D25P2086_03-177-133713.1A1.phase

S82D25P2086_03-177-165326.1A1.phase

S82D25P2086_03-177-133713.1B1.phase

S82D25P2086_03-177-165326.1B1.phase

S82D25P2086_03-177-133713.2B1.phase

S82D25P2086_03-177-165326.2B1.phase

S82D25P2086_03-177-133713.2A1.phase

S82D25P2086_03-177-165326.2A1.phase

S82D13P2087_03-178-140213.1A1.phase

S82D13P2087_03-178-155401.1A1.phase

S82D13P2087_03-178-183732.1A1.phase

S82D13P2087_03-178-140213.1B1.phase

S82D13P2087_03-178-155401.1B1.phase

S82D13P2087_03-178-183732.1B1.phase

S82D13P2087_03-178-140213.2B1.phase

S82D13P2087_03-178-155401.2B1.phase

S82D13P2087_03-178-183732.2B1.phase

S82D13P2087_03-178-140213.2A1.phase

S82D13P2087_03-178-155401.2A1.phase

S82D13P2087_03-178-183732.2A1.phase

S82D13P2088_03-179-134960.1A1.phase

S82D13P2088_03-179-163857.1A1.phase

S82D13P2088_03-179-134960.1B1.phase

S82D13P2088_03-179-163857.1B1.phase

S82D13P2088_03-179-134960.2B1.phase

S82D13P2088_03-179-163857.2A1.phase

S82D13P2088_03-179-134960.2A1.phase

S82D13P2088_03-179-163857.2B1.phase

S82D13P2089_03-180-134500.1A1.phase

S82D13P2089_03-180-163328.1A1.phase

S82D13P2089_03-180-134500.1B1.phase

S82D13P2089_03-180-163328.1B1.phase

S82D13P2089_03-180-134500.2B1.phase

S82D13P2089_03-180-163328.2B1.phase

S82D13P2089_03-180-134500.2A1.phase

S82D13P2089_03-180-163328.2A1.phase

S82D13P2090_03-181-134500.1A1.phase

S82D13P2090_03-181-163330.1A1.phase

S82D13P2090_03-181-134500.1B1.phase

S82D13P2090_03-181-163330.1B1.phase

S82D13P2090_03-181-134500.2B1.phase

S82D13P2090_03-181-163330.2B1.phase

S82D13P2090_03-181-134500.2A1.phase

S82D13P2090_03-181-163330.2A1.phase

S82D13P2091_03-182-132110.1A1.phase

S82D13P2091_03-182-164627.1A1.phase

S82D13P2091_03-182-132110.1B1.phase

S82D13P2091_03-182-164627.1B1.phase

S82D13P2091_03-182-132110.2B1.phase

S82D13P2091_03-182-164627.2B1.phase

S82D13P2091_03-182-132110.3B1.phase

S82D13P2091_03-182-164627.3B1.phase

S82D13P2092_03-183-133500.1A1.phase

S82D13P2092_03-183-162335.1A1.phase

S82D13P2092_03-183-133500.1B1.phase

S82D13P2092_03-183-162335.1B1.phase

S82D13P2092_03-183-133500.2B1.phase

S82D13P2092_03-183-162335.2B1.phase

S82D13P2092_03-183-133500.3B1.phase

S82D13P2092_03-183-162335.3B1.phase

S82D13P2093_03-184-133500.1A1.phase

S82D13P2093_03-184-162337.1A1.phase

S82D13P2093_03-184-133500.1B1.phase

S82D13P2093_03-184-162337.1B1.phase

S82D13P2093_RSR2B1.03-184-133500.phase

S82D13P2093_RSR2B1.03-184-162337.phase

S82D13P2093_RSR3B1.03-184-133500.phase

S82D13P2093_RSR3B1.03-184-162337.phase

S82D13P2094_RSR1A1.03-185-132200.phase

S82D13P2094_RSR1A1.03-185-162339.phase

S82D13P2094_RSR1B1.03-185-132200.phase

S82D13P2094_RSR1B1.03-185-162339.phase

S82D13P2094_RSR2B1.03-185-132200.phase

S82D13P2094_RSR2B1.03-185-162339.phase

S82D13P2094_RSR3B1.03-185-132200.phase

S82D13P2094_RSR3B1.03-185-162339.phase

S82D13P2095_RSR1A1.03-186-131500.phase

S82D13P2095_RSR1A1.03-186-161339.phase

S82D13P2095_RSR1B1.03-186-131500.phase

S82D13P2095_RSR1B1.03-186-161339.phase

S82D13P2095_RSR2B1.03-186-131500.phase

S82D13P2095_RSR2B1.03-186-161339.phase

S82D13P2095_RSR3B1.03-186-131500.phase

S82D13P2095_RSR3B1.03-186-161339.phase

S82D13P2096_RSR1A1.03-187-132500.phase

S82D13P2096_RSR1A1.03-187-205257.phase

S82D13P2096_RSR1B1.03-187-132500.phase

S82D13P2096_RSR1B1.03-187-205257.phase

S82D13P2096_RSR2B1.03-187-132500.phase

S82D13P2096_RSR2B1.03-187-205257.phase

S82D13P2096_RSR3A1.03-187-132500.phase

S82D13P2096_RSR3A1.03-187-205257.phase

RSR_02_176_131930.FR.xcorr

RSR_02_176_155059.FR.xcorr

RSRFR1_02_169_161054.xcorr

RSRFR1_02_169_174432.xcorr

RSRFR_02_170_142745.xcorr

RSRFR_02_170_160900.xcorr

RSRFR_02_171_133600.xcorr

RSRFR_02_171_160900.xcorr

RSRFR_02_172_013114.xcorr

x172.xcorr

k172_2.xcorr

RSRFR_02_172_162202.xcorr

RSRFR_02_172_190133.xcorr

RSRFR_02_173_000655.xcorr

RSRFR_02_173_132913.xcorr

RSRFR_02_173_160820.xcorr

RSRFR_02_174_010120.xcorr

RSRFR_02_174_012119.xcorr   S82D13P2088_03-179-134960.FR.xcorr

RSR_02_174_133241.FR.xcorr   S82D13P2088_03-179-163857.FR.xcorr

RSR_02_174_134046.FR.xcorr   S82D13P2089_03-180-134500.FR.xcorr

RSR_02_174_155336.FR.xcorr   S82D13P2089_03-180-163328.FR.xcorr

RSR_02_175_000400.FR.xcorr   S82D13P2090_03-181-134500.FR.xcorr

RSR_02_175_131424.FR.xcorr   S82D13P2090_03-181-163330.FR.xcorr

RSR_02_175_155237.FR.xcorr   S82D13P2091_03-182-132110.new.xcorr

RSR_02_176_010045.FR.xcorr   S82D13P2091_03-182-164627.new.xcorr

RSRFR_02_167_162155.xcorr   S82D13P2092_03-183-133500.FR.xcorr

RSRFR1_02_167_184653.xcorr   S82D13P2092_03-183-162335.FR.xcorr

RSR_02_177_131635.FR.xcorr   S82D13P2093_RSRFR.03-184-133500.xcorr

RSR_02_177_160615.FR.xcorr   S82D13P2093_RSRFR.03-184-162337.xcorr

RSR_02_177_215846.FR.xcorr   S82D13P2094_RSRFR.03-185-132200.xcorr

                                             S82D13P2094_RSRFR.03-185-162339.xcorr

S82D25P2086_03-177-133713.FR.xcorr   S82D13P2095_RSRFR.03-186-131500.xcorr

S82D25P2086_03-177-165326.FR.xcorr   S82D13P2095_RSRFR.03-186-161339.xcorr

S82D13P2087_03-178-140213.FR.xcorr   S82D13P2096_RSRFR.03-187-132500.xcorr

S82D13P2087_03-178-155401.FR.xcorr   S82D13P2096_RSRFR.03-187-205257.xcorr

S82D13P2087_03-178-183732.FR.xcorr

G.3.3   Files Generated

These files contain the plane of polarization correction values for each point in time.

`fr2002.mat` contains `fr167 fr169 fr170 fr171 fr172 fr173 fr174 fr177`

`fr2003.mat` contains `fr178 fr179 fr180 fr181 fr182 fr183 fr185`

APPENDIX H

Faraday Rotation Forward Model C Code

This is the primary code that was used to determine the location of the line of sight, the magnetic field vector, electron density value, and location of every point along the line of sight for a specified period of time. This code also allows the user to generate a CME in different orientations for crossing the line of sight.

Note that the user should adjust the output of the code to their needs. The current setup dumps the position vector, electron density, and magnetic field vectors to the screen which are then dumped into files using the command `> griddoylos.out`. The final output files `griddoy.out` currently are set to give the radius, colatitude, and longitude of the the point of closest approach in columns 4-6 (units are in Rs, radians, radians), the total columnar electron density in column 7 (m^{-3}), and the Faraday rotation prior to the division by frequency squared in column 8 ($FR = col8/f^2$). The command files (`conjyeardoy.cmd`) used to run the forward model are included as examples. Note that the user must have the JPL SPICE codes installed for these programs to run.

Finally, the user must include their own PFSS code. The executables are included to support development.

The inputs are as follows:

H.1   faradayrotation.c

This file is primarily concerned with calculating the Faraday rotation along the line of sight. The flux rope creation routines are ignored; notice in the `conjyeardoy.cmd` files, the CME is generated to cross the line of sight prior to the initial time.

Input the following format:

1)SPICE files (listed in a file)

2)time (in single quotes: year month day hr:mm:ss)

3)WSO file

4)output file

5) center crossing time?

6)angle of dispacement from impact parameter along line of sight _towards the earth_ (rad)

7)angle of displacement from the impact parameter and line of sight plane (rad) CURRENTLY OFF

8)east limb or west? (1.0 or -1.0)

9)clock angle of rope wrt radial vector (rad)

10)cone angle of rope (rad)

11)handedness of rope (-1.0 for right hand, 1.0 for left hand)

12)Magnetic field magnitude of rope (mT)

13)Bessel funtion constant for the Bfield of rope edge

14)time for rope crossing to start (sec)

15)time for rope crossing to stop

16)time step (sec)

17)time finish-time initial (sec)

18) radius of the rope start (km)

19) expansion rate (km/s)

20) filename of the SMEI data

21) Streamer density above local (fraction greater than 1)

22) Streamer start longitude (deg)

23) Streamer stop longitude

24) Streamer start latitude (deg)

25) Streamer stop latitude

26) Increase in density of flux rope

27) Use symmetric density model? (1=yes)

H.2   faradayrotationgse.c

This code was primarily constructed to study flux ropes. The flux rope fit is performed by the matlab code `mr2.m` which calls `faradayrotationgse.c` within the code and feeds it new parameters as it progresses towards a fit. The initial parameters are chosen based on the similarity between the observed CME and the templates shown in Chapter 5. The location of the center point is initialized at the center. After matlab begins its fitting routine, each new set of parameters it test are plotted for review. As the fitting function finishes the initial tests at large offsets in parameter space and begins to refine the best fit, the program is stopped and the center point is offset if it is clear that a good fit can only be achieved through allowing the CME to expand.

Input the following format:

1)SPICE files (listed in a file)

2)time (in single quotes: year month day hr:mm:ss)

3)WSO file

4)output file

5) center crossing time?

6)angle of dispacement from impact parameter along line of sight ‗towards the earth‗
(rad)

7)angle of displacement from the impact parameter and line of sight plane (rad)
CURRENTLY OFF

8)east limb or west limb? (1.0 or -1.0)

9)clock angle of rope wrt radial vector (rad)

10)cone angle of rope (rad)

11)handedness of rope (-1.0 for right hand, 1.0 for left hand)

12)Magnetic field magnitude of rope (mT)

13)Bessel funtion constant for the Bfield of rope edge

14)time for rope crossing to start (sec)

15)time for rope crossing to stop

16)time step (sec)

17)time finish-time initial (sec)

18) Is this a test? 1=yes

19) Are you trying to model 1979 October 23 or 24? [1==23rd,2==24th,0==no]

20) filename of the SMEI data

21) velocity of flux rope (km/sec)?

22)

23)

24)

25) Vary electron density with rope expansion? 1=yes

26) Factor of increase in density of flux rope above Tyler model:

APPENDIX I

Forward Model Fits Analysis

The two codes below perform the functions of adjusting the magnetic field vectors from the PFSS model to fit the Faraday rotation observations through rotation or magnitude adjustments. The results of these fits are then used to determine the magnetic and thermal pressures and the force of gravity. The second code `bccosthetasolutionsplot.m` causes memory problems. Screen prints of figures were necessary in order to be able to create images.

I.1 Fitting Code

`frdatafits.m` is written to query the user for filenames, level of processing, and other parameters involved in the error analysis. The program needs to be run three times: 1) Calculate the electron density values along the line of sight by adjusting the Tyler et al (1977) model. 2) Determine the angle of vector rotation causing the sign of the Faraday rotation to reverse. 3) Stepping through the rotation space available by 1 degree steps, adjust the magnitude of the magnetic field vectors necessary to fit the Faraday rotation observations. It loads up the `griddoylos.out`, `griddoy.out`, `fr2002.mat`, `dr2002.mat`, `nfromdopp2002.mat` files. The user has to manually save the output matrices at each stage (with prompting) by using the Matlab `save`

command.

I.1.1 Within Matlab

Within `appi`, begin Matlab and enter the following command:

```
>> frdatafits.m
```

You will be prompted:

```
Is this a new or old run? [n/o]n
```

In most cases you will enter 'n'; this is mostly to speed things up because loading the `griddoylos.out` file is time consuming. You will then be prompted for the day being processed in year, day of year format. The example below is for 2002 June 21.

```
input the yyyydoy2002172

ans =

loading los calcs

ans =

done loading
```

Then the code will ask you if you about if this is a check in the Faraday rotation error. Note that the error is 1 degree. So if the user has a different value, they should input that value instead.

Then the code requests the Total Electron Content (TEC) in m^{-2}. If the user is also performing an error analysis on the value of the TEC, then this number should be adjusted as well.

Finally the code requires information for the data processing stage. Answering 'n' to the first question (*Did you already run the routine to calculate the densities along the line of sight and recalculate the Faraday rotation?:*) will initiate the electron density analysis. Answering 'y' to the first question and 'n' to the second (*Did you already run the routine to calculate the cos theta boundary where the sign flips?:*) will initiate the second processing stage. And finally answering 'y' to both questions will initiate the third stage. With the exception of the first, the user will be prompted for the `filename.mat` given for the saved data from the previous stage.

At each stage when the program is finished running, the following prompts will be printed:

```
now you should save the elecdeninit elecden steptrack frinit matrices
     for the next step
now you should save the elecdeninit elecden steptrack frinit bmagnitude
     magold adjustval matrices for the next step
now you should save the elecdeninit elecden steptrack frinit bmagnitude
     magold adjustval multvalset adjustvalset frvalset tval matrices
```

Each of these prompts are to remind the user to enter one of the following commands:

```
>> save filename.mat elecdeninit elecden steptrack frinit
>> save filename.mat elecdeninit elecden steptrack frinit bmagnitude
      magold adjustval
>> save filename.mat elecdeninit elecden steptrack frinit bmagnitude
      magold adjustval multvalset adjustvalset frvalset tval
```

I.2 Calculating the currents and plots

`bcosthetasolutionsplot.m` is constructed to minimize the effort required to create the last 3 figures in Chapter 4. The code loads the output file saved from the last stage of running `frdatafits.m` (this is the file being requested by the prompt) and `griddoylos.out`. The latter file is used to determine the location of each point along the line of sight in longitude and radius and the electron density (according to Solar Mass Ejection Imager data) for each of these points (for plotting purposes only).

After loading the necessary files, `bcosthetasolutionsplot.m` calculates the magnetic and thermal pressures (and their radial gradients) and the gravitational force per volume for each point along the line of sight. There are no output files.

I.2.1 Run Command

Within `appi` start Matlab and enter the following command:

```
>> bcosthetasolutionsplot
```

References

Acton, C. H. 1996. Ancillary data services of NASA's Navigation and Ancillary Information Facility. , 44(Jan.), 65–70.

Andreev, V. E., Efimov, A. I., Samoznaev, L. N., Chashei, I. V., & Bird, M. K. 1997. Characteristics of Coronal Alfven Waves Deduced from HELIOS Faraday Rotation Measurements. , 176(Dec.), 387–402.

Antonucci, E., Abbo, L., & Dodero, M. A. 2005. Slow wind and magnetic topology in the solar minimum corona in 1996-1997. , 435(May), 699–711.

Arge, C. N., & Pizzo, V. J. 2000. Improvement in the prediction of solar wind conditions using near-real time solar magnetic field updates. , 105(May), 10465–10480.

Aschwanden, M.J. 2004. *Physics of the Solar Corona.* Springer-Praxis Books in Geophysical Sciences.

Asmar, Sami W. 1996 (May). *Two-Wavelength Faraday Rotation Measurement in the Solar Corona.* M.Phil. thesis, California State University, Northridge, Northridge, CA 91330.

Baumjohann, W., & Treumann, R. A. 1996. *Basic Space Plasma Physics.* Imperial College Press.River Edge, New Jersey. ISBN1-86094-017-X.

Beckers, J. M. 1968. Principles of Operation of Solar Magnetograps. , 5, 15–+.

Belenko, I. A. 2001. Coronal Hole Evolution During 1996-1999. , 199(Mar.), 23–35.

Bertotti, Bruno, & Giampieri, Giacomo. 1997. Solar Coronal Plasma In Doppler Measurements. *Solar Physics*, 178(July), 85–107.

Bilitza, D. 2001. IRI 2000. *Radio Science*, 36, 261–276.

Bird, M. K., & Edenhofer, P. 1990. *Remote Sensing Observations of the Solar Corona*. Physics of the Inner Heliosphere I. Pages 13–+.

Bird, M. K., Volland, H., Howard, R. A., Koomen, M. J., Michels, D. J., Sheeley, N. R., Amstrong, J. W., Seidel, B. L., Stelzried, C. T., & Woo, R. 1985. White-light and radio sounding observations of coronal transients. , 98(Aug.), 341–368.

Cannon, A.R. 1976. *Radio Frequency Probing of the Solar Corona*. Ph.D. thesis, University of California, Berkeley, Berkeley, CA 94704.

Center for Integrated Space Weather Modeling. 2002. *Modeling Space Weather*. webpage. http://www.bu.edu/cism/index.html.

Chapman, S., & Bartels, J. 1940. *Geomagnetism*. Geomagnetism, London: Oxford University Press, 1940, ii. WSO normalized polynomials section 17.4 on page 610.

Chashei, I. V., & Shishov, V. I. 1984. The Turbulence in the Solar Atmosphere and in the Interplanetary Plasma. *Soviet Astronomy*, 28(June), 279–+.

Coffey, H. E. 2005. *NGDC/WDC STP, Boulder-Solar Radio Data via FTP from NGDC*. webpage. http://www.ngdc.noaa.gov/stp/SOLAR/ftpsolarradio.html.

Croft, T. A. 1979. A graphical summary of solar wind electron content observations by Pioneer 6, 8, and 9. , 84(Feb.), 439–449.

Croft, T.A. 1973. Traveling regions of high solar wind density observed in early August 1972. *Journal of Geophysical Research*, 78(16), 3159–66.

Dept. Physics & Astronomy, University of Tennesee. 2006. *Stars, Galaxies, and Cosmology*. webpage. http://csep10.phys.utk.edu/astr162/lect/light/zeeman-split.html.

Dicke, R. H., & Wittke, J. P. 1960. *Introduction to Quantum Mechanics.* Addison-Wesley Publishing Company, Inc.

Dulk, G. A., & McLean, D. J. 1978. Coronal magnetic fields. , 57(Apr.), 279–295.

Efimov, A. I., Samoznaev, L. N., Andreev, V. E., Chashei, I. V., & Bird, M. K. 2000. Quasi-Harmonic Faraday-Rotation Fluctuations of Radio Waves When Sounding the Outer Solar Corona. *Astronomy Letters*, 26(Aug.), 544–552.

Ekelund, P. Tortora L. Iess J.J. Bordi J.E., & Roth, D.C. 2004. Precise Cassini Navigation During Solar Conjunctions Through Multifrequency Plasma Calibrations. *Journal of Guidance, Control, and Dynamics*, 27(Mar.), 251–257.

Elphic, R. C., & Russell, C. T. 1983. Magnetic flux ropes in the Venus ionosphere - Observations and models. , 88(Jan.), 58–72.

Erickson, W. C. 1964. The Radio-Wave Scattering Properties of the Solar Corona. , 139(May), 1290–+.

Esposito, D.O. Muhleman P.B., & Anderson, J.D. 1977. The electron density profile of the outer corona and the interplanetary medium from Mariner-6 and Mariner-7 time-delay measurements. *Astrophysical Journal*, 211(3), 943–57.

Fisher, R., & Sime, D. G. 1984. Rotational characteristics of the white-light solar corona 1965-1983. , 287(Dec.), 959–968.

Frazin, R. A. 2000. Tomography of the Solar Corona. I. A Robust, Regularized, Positive Estimation Method. , 530(Feb.), 1026–1035.

Gamow, G. 1966. *Thirty Years That Shook Physics.* Doubleday & Company, Inc.

Golub, L., & Pasachoff, J. (eds). 1997. *The Solar Corona.* Cambridge University Press.

Graps, A. 1998. *Helioseismology.* webpage. http://soi.stanford.edu/results/heliowhat.html.

Halpern, J., Lax, B., & Nishina, Y. 1964. Quantum Theory of Interband Faraday and Voigt Effects. *Physical Review*, 134(Apr.), 140–153.

Hoeksema, J. T. 2006 (Dec.). *Calculating B from Wilcox spherical harmonics.* Stanford University, Stanford, CA 94305. personal communication.

Hollweg, J. V., Bird, M. K., Volland, H., Edenhofer, P., Stelzried, C. T., & Seidel, B. L. 1982. Possible evidence for coronal Alfven waves. , 87(16), 1–8.

Iess, L., Giampieri, G., Anderson, J. D., & Bertotti, B. 1999. Doppler measurement of the solar gravitational deflection. *Classical and Quantum Gravity*, 16(May), 1487–1502.

Imbriale, W.A. 2003. *Large antennas of the Deep Space Network.* Hoboken, NJ : John Wiley.

Jackson, B. V. 2006. *Time-Dependent Tomographic Reconstruction Using STELab Data.* webpage. http://cassfos02.ucsd.edu/solar/tomography/fast_stel_1965.html.

Jackson, B. V., Hick, P. L., Kojima, M., & Yokobe, A. 1997. Heliospheric tomography using interplanetary scintillation observations. *Advances in Space Research*, 20(Jan.), 23–+.

Jackson, B. V., Hick, P. P., Buffington, A., Kojima, M., Tokumaru, M., Fujiki, K., Ohmi, T., & Yamashita, M. 2003 (Sept.). Time-dependent tomography of hemispheric features using interplanetary scintillation (IPS) remote-sensing observations. *Pages 75–78 of:* Velli, M., Bruno, R., Malara, F., & Bucci, B. (eds), *AIP Conf. Proc. 679: Solar Wind Ten.*

Johnston, D. 2005 (Aug.). *Magellan Data Corruption Problem.* Jet Propulsion Laboratory, Pasadena, CA. personal communication.

Kallenrode, M.-B. 2001. *Space physics : an introduction to plasmas and particles in the heliosphere and magnetospheres.* Space physics : an introduction to plasmas and particles in the heliosphere and magnetospheres, 2nd ed. Berlin: Springer, 2001, xv, 365 p. ISBN 3540412492. figure 6.20 from page 131.

Keil, Stephen L., & Avakyan, Sergey V. (eds). 2003. *Innovative Telescopes and Instrumentation for Solar Astrophysics.* Vol. 4853. Proceedings of SPIE.

Kelso, J.M. 1959. The Determination of Electron Density in Interplanetary Space. *Journal of Atmospheric and Terrestrial Physics*, 16(Mar.), 357–359.

Kirkhorn, J. 1999. *Introduction to IQ-demodulation of RF-data.* Tech. rept. Signalbehandlingsteknikker i ultralyd billeddannelse. IFBT, NTNU (Norwegian University of Science and Technology), http://folk.ntnu.no/htorp/Undervisning/TTK10/.

Kivelson, Margaret G., & Russell, Christopher T. (eds). 1997. *Introduction to Space Physics.* 3 edn. Cambridge University Press.

Klimchuk, J. A. 2006. On Solving the Coronal Heating Problem. , 234(Mar.), 41–77.

Kliore, A. J., Anderson, J. D., Armstrong, J. W., Asmar, S. W., Hamilton, C. L., Rappaport, N. J., Wahlquist, H. D., Ambrosini, R., Flasar, F. M., French, R. G., Iess, L., Marouf, E. A., & Nagy, A. F. 2004. Cassini Radio Science. *Space Science Reviews*, 115(Dec.), 1–4.

Koehler, R.L. 1968. Radio Propagation Measurements of Pulsed Plasma Streams from the Sun Using Pioneer Spacecraft. *Journal of Geophysical Research*, 73(15), 4883–94.

Koutchmy, S., & Livshits, M. 1992. Coronal Streamers. *Space Science Reviews*, 61, 393–+.

Landt, J.A. 1974. Dense solar wind cloud geometries deduced from comparisons of radio signal delay and in situ plasma measurements. *Journal of Geophysical Research*, 79(19), 2761–6.

Lang, K. R. 2003. *The magnetic solar atmosphere.* webpage. http://ase.tufts.edu/cosmos/view_picture.asp?id=852.

Levy, G. S., Sato, T., Seidel, B. L., Stelzried, C. T., Ohlson, J. E., & Rusch, W. V. T. 1969. Pioneer 6: Measurement of Transient Faraday Rotation Phenomena Observed during Solar Occultation. *Science*, 166(Oct.), 596–598.

Luhmann, J. G. 2002. Numerical Simulations Code Access and Data Interpretation. *AGU Spring Meeting Abstracts*, May, B1+.

Luhmann, J. G., Li, Y., Arge, C. N., Gazis, P. R., & Ulrich, R. 2002. Solar cycle changes in coronal holes and space weather cycles. *Journal of Geophysical Research (Space Physics)*, 107(Aug.), 3–1.

Media Relations Office. 2003. *Cassini Significant Event Report For Week Ending 05/23/03.* webpage. http://saturn.jpl.nasa.gov/news/sig-event-details.cfm?newsID=328.

Miralles, M. P., Cranmer, S. R., & Kohl, J. L. 2004. Low-latitude coronal holes during solar maximum. *Advances in Space Research*, 33, 696–700.

Moyer, T.D. 2000. *Formulation for Observed and Computed Values of Deep Space Network Data Types for Navigation.* Tech. rept. Deep Space Communications and Navigation Series Publication 00-7. Jet Propulsion Laboratory, Pasadena, CA 91109.

Mulligan, T. 2002 (Mar.). *Modeling Interplanetary Coronal Mass Ejections.* Ph.D. thesis, University of California, Los Angeles, Los Angeles, CA 90095.

Mulligan, T., Russell, C. T., & Luhmann, J. G. 1998. Solar cycle evolution of the structure of magnetic clouds in the inner heliosphere. , 25(Aug.), 2959–2962.

Myers, S.T. 2004. *Polarization in Interferometry.* webpage. http://www.nrao.edu/ smyers/Synth2004/MyersPolarization04.ppt.

Odstrčil, D., & Pizzo, V. J. 1999. Three-dimensional propagation of coronal mass ejections in a structured solar wind flow 2. CME launched adjacent to the streamer belt. , 104(Jan.), 493–504.

Owens, M. J., Arge, C. N., Spence, H. E., & Pembroke, A. 2005. An event-based approach to validating solar wind speed predictions: High-speed enhancements in the Wang-Sheeley-Arge model. *Journal of Geophysical Research (Space Physics)*, 110(A9), 12105–+.

Parker, E. N. 1958. Dynamics of the Interplanetary Gas and Magnetic Fields. , 128(Nov.), 664–+.

Parthasarathy, R., & Papitashvili, N. 1995. *Description of Coordinate Systems.* webpage. http://nssdc.gsfc.nasa.gov/space/helios/coor_des.html.

Patzold, M., Bird, M. K., Volland, H., Levy, G. S., Seidel, B. L., & Stelzried, C. T. 1987. The mean coronal magnetic field determined from HELIOS Faraday rotation measurements. , 109, 91–105.

Ramaprakash, A. N. 1998 (May). *Development of and Observations with an Astronomical Imaging Polarimeter (IMPOL).* Ph.D. thesis, University of Pune, Ganeshkhind, Pune 114 007, India. Appendix B.

Rueedi, I., Solanki, S. K., Keller, C. U., & Frutiger, C. 1998. Infrared lines as probes of solar magnetic features. XIV. TI i and the cool components of sunspots. , 338(Oct.), 1089–1101.

Russell, C. T. 2000. *Solar Wind and Interplanetary Magnetic Field: A Tutorial.* Tech. rept. IGPP and Dept of ESS, UCLA, Los Angeles, CA 90095. http://www-ssc.igpp.ucla.edu/ssc/tutorial/.

Russell, C. T. 2005. *The Cassini-Huygens Mission.* The Cassini-Huygens Mission, Orbiter In Situ Investigations. Edited by C.T. Russell, University of California, California, U.S.A. Reprinted from Space Science Reviews, volume 114, nos. 1-4, 2004.

Russell, C. T., & Mulligan, T. 2003 (Sept.). The Limitation of Bessel Functions for ICME Modeling. *Pages 125–128 of:* Velli, M., Bruno, R., Malara, F., & Bucci, B. (eds), *AIP Conf. Proc. 679: Solar Wind Ten.*

Samoznaev, V.E. Andreev A.I. Efimov L.N., & Bird, M.K. 1997. Faraday Rotation Fluctuation Spectra Observed during Solar Occultation of the Helios Spacecraft. *00*, 0(Sept.), 34–37.

Scherrer, P. H., Wilcox, J. M., Svalgaard, L., Duvall, T. L., Dittmer, P. H., & Gustafson, E. K. 1977. The mean magnetic field of the sun - Observations at Stanford. , 54(Oct.), 353–361.

Scudder, Jack D. 1992. Why All Stars Should Possess Circumstellar Temperature Inversions. *The Astrophysical Journal*, 398(Oct.), 319–349.

Staelin, D. 2003. *Receivers, Antennas, and Signals.* MIT OpenCourseWare.

Stelzried, C. T. 1968 (Nov.). *A Faraday Rotation Measurement of a 13-cm Signal in*

the Solar Corona. Tech. rept. 32-1401. Jet Propulsion Laboratory, Pasadena, CA 91109.

Stelzried, J.V. Hollweg M.K. Bird H. Volland P. Edenhofer C.T., & Seidel, B.L. 1982. Possible Evidence for Coronal Alfven Waves. *Journal of Geophysical Research, A*, 87(1), 1–8.

Svalgaard, L. 2005. Magnetograph Saturation: Comparison of WSO and SOLIS. *AGU Spring Meeting Abstracts*, May, C5+.

Swanson, Donald G. 1989. *Plasma Waves.* 1 edn. Institute of Physics Publishing.

Tinto, M., & Sniffin, R.W. 2000. *Open-Loop Radio Science.* Tech. rept. DSMS Telecommunications Link Design Handbook 810-005, Revision E. Jet Propulsion Laboratory, Pasadena, CA 91109.

Tolstov, G. P. 1962. *Fourier Series.* Prentice Hall.Eaglewood Cliffs, New Jersey.

Tran, T. V., Bertello, L., Ulrich, R. K., & Boyden, J. E. 2005. Potential Field Source Surface analysis from high resolution synoptic and heliographic maps. *AGU Spring Meeting Abstracts*, May, A11+.

Tyler, G. L., Brenkle, J. P., Komarek, T. A., & Zygielbaum, A. I. 1977. The Viking solar corona experiment. *Journal of Geophysical Research*, 82(Sept.), 4335–4340.

Ulrich, R. K., & Boyden, J. E. 2006. Carrington Coordinates and Solar Maps. , 235(May), 17–29.

Unno, W. 1956. Line Formation of a Normal Zeeman Triplet. , 8, 108–+.

Volland, H., Bird, M. K., Levy, G. S., Stelzried, C. T., & Seidel, B. L. 1977. Helios-1 Faraday rotation experiment - Results and interpretations of the solar occultations in 1975. *Journal of Geophysics Zeitschrift Geophysik*, 42, 659–672.

Walker, R. 2000. *ESS154 Solar Terrestrial Physics.* webpage. http://lucid.igpp.ucla.edu/lessons/ess154.

Wang, Y.-M., Sheeley, N. R., Socker, D. G., Howard, R. A., & Rich, N. B. 2000. The dynamical nature of coronal streamers. , 105(Nov.), 25133–25142.

Webb, D. F., & Howard, R. A. 1994. The solar cycle variation of coronal mass ejections and the solar wind mass flux. *Journal of Geophysical Research*, 99(Mar.), 4201–4220.

Yizengaw, E. 2004. *Imaging the Ionosphere.* Ph.D. thesis, La Trobe University, Bundoora, Victoria 3086, Australia.